The induced mean flow of surface, internal and interfacial gravity wave groups

T.S. van den Bremer

New College

University of Oxford

Thesis submitted in partial fulfilment of the requirements for the degree of Doctor of Philosophy at the University of Oxford

Michaelmas 2014

Abstract

Although the leading-order motion of waves is periodic − in other words backwards and forwards − many types of waves including those driven by gravity induce a mean flow as a higher-order effect. It is the induced mean flow of three types of gravity waves that this thesis examines: surface (part I), internal (part II) and interfacial gravity waves (part III). In particular, this thesis examines wave groups. Because they transport energy, momentum and other tracers, wave-induced mean flows have important consequences for climate, environment, air traffic, fisheries, offshore oil and other industries. In this thesis perturbation methods are used to develop a simplified understanding of the physics of the induced mean flow for each of these three types of gravity wave groups. Leading-order estimates of different transport quantities are developed.

For surface gravity wave groups (part I), the induced mean flow consists of two components: the Stokes drift dominant near the surface and the Eulerian return flow acting in the opposite direction and dominant at depth. By considering subsequent orders in a separation of scales expansion and by comparing to the Fourier-space solutions of Longuet-Higgins and Stewart (1962), this thesis shows that the effects of frequency dispersion can be ignored for deep-water waves with realistic bandwidths. An approximate depth scale is developed and validated above which the Stokes drift is dominant and below which the return flow wins: the transition depth. Results are extended to include the effects of finite depth and directional spreading.

Internal gravity wave groups (part II) do not display Stokes drift, but a quantity analogous to Stokes transport for surface gravity waves can still be developed, termed the "divergent-flux induced flow" herein. The divergent-flux induced flow it itself a divergent flow and induces a response. In a three-dimensional geometry, the divergent-flux induced flow and the return flow form a balanced circulation in the horizontal plane with the former transporting fluid through the centre of the group and the latter acting in the opposite direction around the group. In a two-dimensional geometry, stratification inhibits a balanced circulation and a second type of waves are generated that travel far ahead and in the lee of the wave group. The results in the seminal work of Bretherton (1969b) are thus validated, explicit expressions for the response and return flow are developed and compared to numerical simulations in the two-dimensional case.

Finally, for interfacial wave groups (part III) the induced mean flow is shown to behave analogously to the surface wave problem of part I. Exploring both pure interfacial waves in a channel with a closed lid and interacting surface and interfacial waves, expressions for the Stokes drift and return flow are found for different configurations with the mean set-up or set-down of the interface playing an important role.

Acknowledgements

First and foremost, I would like to thank my supervisor Professor Paul Taylor for academic guidance and support completing the research for this thesis. I would like to thank Paul for being a very dedicated and committed supervisor, for the many fruitful discussions and his warm approach. Part of the work on internal waves presented herein was completed when visiting the Woods Hole Oceanographic Institution as part of the 2013 WHOI Geophysical Fluid Dynamics Program under the supervision of Professor Bruce Sutherland. I would like to thank Bruce for outstanding academic guidance and his encouraging, often jolly, supervision.

I acknowledge financial support from an Engineering and Physical Sciences Research Council Doctoral Training Award, New College Oxford, the National Science Foundation (Grant No. OCE-0824636) and the Office of Naval Research (Grant No. N00014-09-1-0844) through their support of the 2013 WHOI Geophysical Fluid Dynamics Program where the work on internal waves presented herein was first undertaken. I would like to thank Professors Stefan Llewellyn Smith and Eric Chastignet and Dr Claudia Cenedese for organizing the 2013 WHOI Geophysical Fluid Dynamics Program.

I would like to thank colleagues at Keble College and in the Environmental Fluid Mechanic group, notably Dr Colm Fitzgerald and Professor Thomas Adcock and the members of my transfer and confirmation committee Professors Byron Byrne and Richard Willden. I would like to thank my Oxford friends Bas van Schaik, Irem Guceri, Mathias Kruetli, Andreas Tischbirek, Max Roser and Sebastian Königs, the former also for occasionally fixing my computer. Finally, I am grateful to my parents and sister.

As a researcher, I have learnt important lessons from different people. I am indebted to Professor Rick van der Ploeg, who taught me time is scarce and selecting the right question can often be as important as getting the right answer. I am indebted to Professor Gary Hunt, who first sparked my interest in fluid mechanics as an undergraduate and with whom I wrote my first academic publications.

Ton van den Bremer, December 2014

Contents

List of Figures

List of Tables

Chapter 1

Introduction

1.1 Background

Although the leading-order motion of waves is periodic – in other words backwards and forwards – many types of waves including those driven by gravity induce a mean flow as a higher-order effect. Unlike the wave motion, the induced mean flow is not periodic and can therefore transport tracers such as particles, momentum and energy. This thesis examines the induced mean flow of three types of gravity waves that manifest themselves in different parts of the world's oceans and atmosphere. Surface gravity waves, as can be observed on the beach, a lake, or the open ocean, are familiar to many and can mainly be understood by ignoring the effect of the layer of air that overlies the body of fluid underneath, typically water, with a much higher density, except of course when it concerns their generation by wind. Interfacial waves can form on the interface between fluids of comparable but unequal density and occur, for example, when a fresh river flows out into a salty sea. Density differences can also arise because of temperature differences, such as in fresh water lakes and the (seasonal) thermocline most prominent in tropical oceans. When the variation of density is more gradual and a distinct interface can no longer be distinguished, the now continuously stratified medium can still sustain waves: internal gravity waves. Such waves are ubiquitous in the stratified ocean and atmosphere (see for example Sutherland (2010) for a review).

With different governing equations and boundary conditions, the induced mean flows of these three types of gravity waves are different and depend on the geometry of the problem, with the depth of the fluid and the number of dimensions considered (two versus three) playing important roles. Yet, there are many similarities, which are explored in this thesis. Crucially, this thesis examines wave groups or packets instead of monochromatic or periodic waves. Not only does the finite spatial extent of the group lead to different physical behaviour of the induced mean flow, groups are also more representative of the real world, as real waves are rarely monochromatic.

Because they transport energy and momentum and cause turbulence where they break, gravity waves and their induced mean flows have important consequences for climate, environment, air traffic, fisheries, offshore oil and other industries. Stokes drift for surface gravity waves is thought to play an important role in the physics of ocean surfaces and hence constitutes an important component of oceanic general circulation models. In such models the individual waves are typically too small to be resolved by even the most powerful computational models and the effect of Stokes drift must be parameterized before inclusion. Such parameterizations have only recently begun to be extended to include the non-monochromatic or packet nature of the waves (e.g. Breivik et al. (2014)). Other applications include the dispersion of pollutants by waves, such as those resulting from an offshore oil spill (e.g. Röhrs et al. (2013)). More generally, the wave-induced transport of momentum and mass by different types of waves plays an important role in the evolution of the atmospheric and oceanic circulation at global scales. Internal waves may, for example, play a significant role in horizontal dispersion in the ocean (Banyte et al. 2013). The ability to understand and adequately parameterize these effects for inclusion in large-scale numerical models ultimately determines the ability of such models to predict the climate.

Wave-induced mean flow is a problem that stretches across many branches of physics with applications in acoustics, plasma physics, condensed matter physics and, most notably, geophysical fluid dynamics. Perhaps one of the first to describe wave-induced mean flow was George Gabriel Stokes (1819-1903), who predicted for periodic surface gravity waves that "in addition to the motion of oscillation the particles are transferred forwards, that is, in the direction of propagation, with a constant velocity" (Stokes (1847), p. 207). Figure 1.1 illustrates his predictions. Shown are the trajectories of Lagrangian particles underneath periodic free surface gravity waves. Provided the water depth is sufficiently large relative to the length of the waves and to leading-order of approximation, the particle trajectories are circular with the radius of the circles declining exponentially with depth. Near the surface the orbits do not close perfectly and a small net drift in the direction of wave propagation can be observed. The effect is typically small and arises at a higher order of approximation than linear.

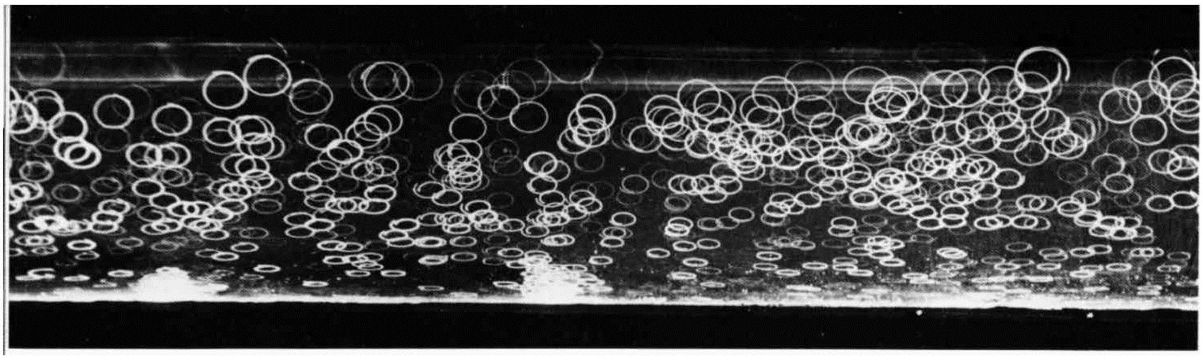

Figure 1.1: Lagrangian particle trajectories underneath two-dimensional deep-water periodic surface gravity waves from Wallet and Ruellan (1950) reproduced in van Dyke (1982). The waves are only moderately non-linear and the net horizontal drift is only visually apparent for a few orbits near the surface. *[Reproduced with permission.]*

This phenomenon, in which Lagrangian particles undergo a mean transport despite the absence of an Eulerian mean flow, is known as Stokes drift. Stokes drift is most conveniently defined as the difference between the Lagrangian and the Eulerian flow field:

$$\text{Lagrangian} = \text{Euler} + \text{Stokes}. \tag{1.1}$$

In terms of net transport, the concept of 'Lagrangian mean' is often required in a more general sense than its classical sense of the mean following a single fluid particle. What is of interest is the Lagrangian-mean flow described in terms of equations in Eulerian form, namely as a function of coordinates x, y and z and time t and not in terms of the initial particle position, as in a traditional Lagrangian framework. The framework of Lagrangian-mean flow, which underlies these early results by Stokes, was formalized in Andrews and McIntyre (1978), who provided a generalized theory for the back effect of oscillatory disturbances upon the mean state termed the 'generalized Lagrangian-mean' (GLM) (see Bühler (2009) for a review of state-of-the-art wave mean flow interaction theory).

As first shown by Longuet-Higgins and Stewart (1962), Stokes drift for surface waves is complemented by another physical process when one considers a wave group or a multichromatic set of waves instead of a monochromatic wave. In the case of a wave group, particles are transported by the Stokes drift as well as by an Eulerian flow that acts in the opposite direction: the return flow. Although interfacial waves behave much like surface waves with the density difference between the two fluids now becoming an important factor, internal waves are different. As the phase and group velocities of internal waves are orthogonal, such waves do not display Stokes drift. Nevertheless, a mean flow can be induced by such waves, as first studied by Francis Bretherton (Bretherton 1969a,b).

1.2 Synopsis

The thesis consists of three parts: the induced mean flow by surface gravity wave groups (part I), internal gravity wave groups (part II) and interfacial gravity wave groups (part III). Part I on surface gravity waves is further subdivided into two chapters: waves in deep water and two-dimensional seas (chapter 2) and an extension to include two additional but important physical effects: finite depth and directional spreading (chapter 3). Part II on internal gravity waves is also subdivided into two chapters: two-dimensional internal waves (chapter 4) and an extension to three dimensions (chapter 5). Finally, part III on interfacial waves consists of one chapter (chapter 6) on two-dimensional gravity interfacial waves distinguishing both pure interfacial waves in a two-layer fluid with closed lids and their interaction with surface waves in a two-layer fluid with a free surface.

This thesis uses perturbation methods to simplify the non-linear partial differential equations, both governing equations and boundary conditions, of the three problems. In particular, it uses a combination of Stokes expansions (after Stokes (1847)) in the non-dimensional amplitude of the wave envelope and separation of scales or multiple-scales expansion. The separation of scales expansions take advantage of the difference in magnitude between the fast scales of the individual waves (the short wave lengths) that make up a wave group and the slow scale of the group itself in a quasi-monochromatic wave group, defined as the much longer length of the envelope.

In doing so, this thesis aims to develop a simplified understanding of the physics of wave-induced mean flow for these three types of gravity wave groups. In particular, the induced mean flow always consists of two components and their interaction can be understood from the simple principle of mass conservation. The first component can be calculated entirely based on linear theory and transports fluid in the direction of the group velocity vector. For surface and interfacial gravity waves this first quantity corresponds to the Stokes drift and its associated Stokes transport. For internal waves this first quantity is termed the 'divergent-flux induced flow' herein, as it can be calculated from the divergence of the advective components in the momentum equation written in flux form. The divergent-flux induced flow is also known as the pseudo-momentum (per unit mass). The divergent-flux induced flow for internal waves and the Stokes transport for surface and interfacial waves are themselves divergent: they transport mass in the direction of the group velocity vector. A second mean-flow component is needed to ensure mass is conserved and the entire flow field at second order is divergence-free. This is the Eulerian

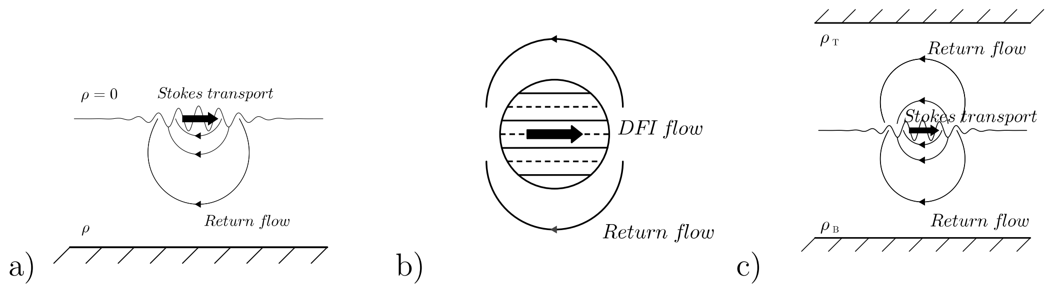

Figure 1.2: Illustration of the two components of wave-induced mean flow for (a) two-dimensional surface gravity wave groups, (b) three-dimensional internal gravity wave groups and (c) two-dimensional interfacial gravity wave groups with top and bottom fluids of density ρ_T and ρ_B, respectively. Divergent-flux induced flow is abbreviated as DFI-flow in panel b and the horizontal lines are lines of constant phase. Panels a and c show a vertical plane, whereas panel b shows a horizontal plane. The divergent-flux induced flows are denoted by bold block arrows through the centre of the group, whereas the return flows are denoted by small arrows around the group.

return flow, another non-linear quantity that transports fluid in the opposite direction.

For two-dimensional surface gravity wave groups the return flow acts at depth below the group, as illustrated in figure 1.2a. For three-dimensional surface gravity wave groups the return flow is three-dimensional and is also located spatially below and around the group. For three-dimensional internal gravity wave groups, an analogous irrotational balance between divergent-flux induced flow and return flow exists, but any mean flows are confined to the horizontal plane by the stratification. Figure 1.2b illustrates the balanced circulation that holds in any horizontal plane. The absence of the third dimension necessary for a balanced circulation in the two-dimensional case leads to a markedly different response for two-dimensional internal gravity wave groups. Then long waves are generated both ahead of the group and in its lee. For interfacial waves, a return flow exists on both sides of the interface, as illustrated in figure 1.2c. A detailed synopsis of the contribution to the literature made in each chapter is provided below.

This thesis does not examine the effects of non-linearity above the order of the wave-induced mean flow (second-order in amplitude) and thus does not capture the instability of the wave train through interaction with the mean flow nor any other non-linear aspects of the evolution of the group. Furthermore, the effect of earth's rotation and the induced mean flow of inertial waves (e.g. Longuet-Higgins (1969)) are not considered herein, nor are the effects of surface tension, viscous drag in the boundary layer or turbulent drag in the Ekman layer.

1.2.1 Surface gravity waves – part I (chapters 2 and 3)

Chapter 2: Stokes drift and return flow for 2D groups in deep water

The Lagrangian trajectories of neutrally buoyant particles underneath focussed surface gravity wave groups are dictated by two physical phenomena: the well-known Stokes drift results in a net displacement of particles in the direction of propagation of the group, whereas the less widely appreciated Eulerian return flow transports such particles in the opposite direction. This chapter develops simple expressions for the net Lagrangian displacement of particles as a function of steepness, bandwidth and depth in a two-dimensional deep-water environment. This chapter does so by pursuing a separation of scales expansion and, by comparing to the multi-chromatic wave theory of Longuet-Higgins and Stewart (1962), it shows that to a very good level of approximation the effects of frequency dispersion can be ignored for realistic sea states. Solutions at all orders are provided in terms of continuous spectra, so that standard asymptotic methods can be employed, instead of the discrete series solutions of Longuet-Higgins and Stewart (1962), which are numerically difficult to integrate to sufficient precision. Finally, this chapter develops a characteristic depth scale, the transition depth, above which net Lagrangian particle transport is forwards and dominated by the Stokes drift and below which the net transport is negative and dominated by the return current.

Chapter 2 is based on a paper entitled "Lagrangian transport by Stokes drift and the return flow for deep-water surface gravity wave packets", co-authored by P.H. Taylor and submitted to the Journal of Fluid Mechanics.

Chapter 3: The effects of directionality and finite depth

The results in chapter 2 rely crucially on the two-dimensionality and deep-water assumptions, which are limiting in real seas. This chapter extends the estimates of the net Lagrangian transport and transition depth in the previous chapter to include the effects of finite depth and directional spreading. This chapter shows that from the perspective of the return flow, almost all seas are of finite depth, invalidating the ubiquitous deep-water approximation. In fact, many seas can be shown to be "shallow" from the perspective of the return flow with little variation of this flow with depth. In addition to the Stokes transport, the mean set-down of the free surface now also has to be taken into account when calculating the return flow. Even a small amount of directional spreading has a large influence on the magnitude of the horizontal transport by the return flow. As the return flow is now localized around as well as underneath the group, the transition depth becomes a transition curve in the two-dimensional plane, for which approximate expressions are found and validated.

1.2.2 Internal gravity waves – part II (chapters 4 and 5)

Chapter 4: The mean flow and long waves induced by 2D groups

Through theory supported by numerical simulations, this chapter examines the induced local and long-range response flows associated with a two-dimensional Boussinesq internal gravity wave group in a uniformly stratified ambient. This chapter shows that stratification inhibits a mean flow in the vertical direction to leading-order and that, instead, the wave group generates another type of wave in its lee. In doing so, this chapter validates the results in the seminal work of Bretherton (1969b). These solutions are explored and, thereby, the structure of the response waves showing that a number of results that lend great physical insight into the problem can be obtained at lower order in the perturbation expansion. For example, the induced flow resulting from the vertical gradient of the vertical flux of horizontal momentum is responsible for all the momentum contained in the long-wave response. Qualitatively different from horizontally periodic internal waves, the vertical profile of the induced horizontal flow across the horizontally localized wave group is positive at the leading edge and negative at the trailing edge. These results are validated by the results of numerical simulations.

Chapter 4 is based on a paper entitled "The mean flow and long waves induced by two-dimensional internal gravity wavepackets", co-authored with B.R. Sutherland and published in Physics of Fluids (2014, Volume 26, 106601.)

Chapter 5: The balanced circulation induced by 3D groups

The results obtained in chapter 4 depend crucially on the geometry of the problem. The absence of a third direction, in which a mean flow is not inhibited by stratification, prohibits a balanced circulation and leads to the generation of a long-wave response. This chapter derives the simplest possible model of the balanced circulation in the horizontal plane for three-dimensional internal gravity groups consisting of the induced mean flow resulting from momentum-flux divergence (the divergent-flux induced flow) and a return flow to ensure mass is conserved. We show these two flows are analogous to the Stokes transport and the return flow for surface gravity wave groups, respectively.

1.2.3 Interfacial gravity waves – part III (chapter 6)

Chapter 6: Stokes drift and return flow for interfacial wave groups

This chapter extends the framework developed for surface gravity waves in chapters 2 and 3 to two-dimensional interfacial gravity wave groups in a stably stratified two-layer fluid. The induced mean flow for interfacial gravity waves, which has not previously been studied, is analogous to the surface gravity wave case, but with return flows on both sides of the interface. As for finite depth surface gravity waves, the return flow can be driven by both the divergence of the Stokes transport and the mean set-up or set-down of the interface. For pure interfacial wave groups in a two-dimensional channel three cases are examined in turn: the case of two infinitely deep fluids, the case of two fluids of finite and equal depth and the asymmetric case of a finite depth fluid overlying an infinitely deep fluid. Finally, the induced mean flow of coupled free surface and interfacial waves is considered, distinguishing the barotropic and the baroclinic solutions to the dispersion relationship.

Chapter 7: Conclusions

Finally, results are summarized and conclusions drawn in chapter 7, outlining future work and containing suggestions how the analytical modelling approach developed in this thesis can be applied to a wider range of geophysical problems.

Part I

Surface gravity waves

Chapter 2

Stokes drift and return flow for two-dimensional surface gravity waves groups in deep water

The Lagrangian trajectories of neutrally buoyant particles underneath focussed surface gravity wave groups are dictated by two physical phenomena: the well-known Stokes drift results in a net displacement of particles in the direction of propagation of the group, whereas the less widely appreciated Eulerian return flow transports such particles in the opposite direction. Generally, the Stokes drift is the larger of the two near the surface, whereas the effects of the return flow dominate at depth and can be thought of as a flow that balances the divergent mass flux associated with the Stokes transport, hence the 'return' flow. It is described by the second-order frequency difference components in second-order multi-chromatic wave theory as first developed by Longuet-Higgins and Stewart (1962), but more simply by solving potential flow subject to a distribution of sources and sinks located at the still water level, as shown herein. This chapter sets out to examine the variation of this return flow with depth. It does so explicitly by pursuing a separation of scales expansion to study the effects of frequency dispersion on wave groups of different bandwidths in a two-dimensional deep-water environment. This chapter develops simple expressions for the net Lagrangian displacement of particles as a function of steepness and bandwidth and studies its variation with depth. Finally, a characteristic depth scale is developed: the transition depth, above which Lagrangian particles are transported forwards by the Stokes drift and below which such particles are transported backwards by the return current.

2.1 Introduction

The net horizontal movement that a fluid particle undergoes in a water wave, named Stokes drift after George Gabriel Stokes who first derived a theoretical description for this drift in 1847, has been studied extensively. As Stokes noted in his 1847 study, "*in addition to the motion of oscillation the particles are transferred forwards, that is, in the direction of propagation, with a constant velocity depending on the depth, and decreasing rapidly as the depth increases*" (Stokes (1847), p. 207). Taking a Lagrangian approach, Stokes (1847) found the following expression for the horizontal drift velocity for regular waves in deep water and to second order of approximation:

$$u_{\mathrm{SD}}(z_0) = \frac{1}{T}\int_t^{t+T} u\big(x(t), z(t), t\big)\,dt = c(ka)^2 e^{2kz_0}, \tag{2.1}$$

where $c = \sqrt{g/k} =$ is the wave celerity or phase speed, g is the gravitational constant, $k = 2\pi/\lambda$ is the wave number of the regular wave, a its amplitude and z_0 the initial vertical position of the particle with $z_0 = 0$ corresponding to the still water level. Stokes drift is thus a non-linear phenomenon (cf. $(ka)^2$) that can be derived entirely from linear theory. Stokes (1847) considered both the effect of horizontal displacement $x(t) = x_0 + \Delta x(t)$ and the vertical displacement $z(t) = z_0 + \Delta z(t)$ on the drift velocity u_{SD}, equal to the net displacement per wave period T, and found that half of the drift arose from each. The resulting close to circular particle orbits with orbits near the surface not quite closing are best illustrated by Wallet & Ruellan's (1950) image reproduced in van Dyke's (1982) Album of Fluid Motion (see figure 1.1). Compatible results were first derived in an Eulerian framework by Starr (1947). In an Eulerian framework, a net mass flux is identified by integrating the (linear) horizontal velocity from the bottom $z \to -\infty$ up to the (linear) free surface $z = \eta(x,t)$. Because the horizontal velocity is higher at a crest than at a trough, the result gives a mean depth-integrated horizontal flux consistent with the flux obtained by depth integration of (2.1):

$$Q_{\mathrm{ST}} = \frac{1}{T}\int_t^{t+T}\int_{-\infty}^{\eta(x,t)} u\big(x(t), z(t), t\big)\,dz\,dt = \frac{1}{2}\sqrt{\frac{g}{k^3}}(ka)^2, \tag{2.2}$$

a volume flux that is sometimes referred to as the "Stokes transport" and is thence abbreviated by the subscript ST.

The framework of Lagrangian-mean flow, which underlies these early results, was not formalized until Andrews and McIntyre (1978), who provided a generalized theory for the back effect of oscillatory disturbances upon the mean state termed the 'generalized Lagrangian-mean' (GLM). As noted by these authors, the concept of 'Lagrangian mean' is often required in a more general sense than its classical sense of the mean following a single fluid particle. What is of interest is the Lagrangian-mean flow described in terms of equations in Eulerian form, i.e. potentially as a function of position (x, z) and time t. When we refer to the Stokes drift velocity (cf. equation (2.1), which is not a function of the horizontal coordinate and time here only because the wave considered is periodic) or the mass flux at a certain position x and time t, it is in fact the 'generalized Lagrangian-mean' of Andrews and McIntyre (1978), a hybrid Eulerian-Lagrangian description of wave mean-flow interaction, we implicitly adopt.

Stokes drift is thought to play an important role in the physics of ocean surfaces and hence constitutes an important component of oceanic general circulation models (OGCMs) (McWilliams and Restrepo 1999). In particular, it is now widely accepted that the interaction between Stokes drift induced by surface waves and vertical shear in turbulent fluid is responsible for Langmuir circulation (Craik and Leibovich 1976), the formation of a series of shallow, slow, counter-rotating vortices at the ocean's surface with characteristic bands of floating seaweed, foam and debris accumulating in the convergence zones between the vortices, at scales of 2m-1km (Thorpe 2004). In turn, the Langmuir circulation is a large contributor of turbulent kinetic energy to the upper mixed layer of the ocean surface, much larger than for example wave breaking (Kantha and Clayson 2004). Many authors have estimated Stokes drift and its geographical spatial distribution across the world's seas and oceans from oceanographic datasets (e.g. Smith (2006), Ardhuin et al. (2009) and Tamura et al. (2012)). Typically, such studies are concerned with the dynamics at the surface only and are based on linear wave theory.

Other authors have considered Stokes drift in experimental wave flumes (e.g. Swan (1990), Hudspeth and Sulisz (1991), Monismith et al. (2007)) and have found that in such closed domains in which the zero net mass flux constraint is automatically satisfied, Stokes drift has to be accompanied by an Eulerian return current, typically driven by a setup in the direction downstream of wave propagation.

For particles with a density different than that of sea water, such as sediment, organic material or pollutants, drag forces, inertial forces and added mass all have to be taken into account. Eames (2008), who investigated the transport of small particles and bubbles by progressive water waves and took into account inertial forces and added mass but not viscous effects, concluded that, to leading order, the average motion of dense particles can be determined by the combination of their settling velocity and Stokes drift. Eames (2008) also points to the wider body of literature on multiphase fluid flow in which Stokes drift effects play an important role (cf. Hunt et al. (1994)). Stokes drift is also intimately related to Darwin drift (Eames et al. 1994), the particle displacement in irrotational fluids due to moving objects. Specifically, the particle displacement due to a finite group of waves may be compared to a finite string of spherical pearls moving through an irrotational fluid (Eames and McIntyre 1999).

Although the literature has examined Stokes drift in periodic surface gravity waves in great detail, the motion of fluid particles transported by a wave group has received considerably less attention. Such wave groups or wave groups form a localized display of wave action that travels as an albeit dispersive unit or group and can be represented by the summation of a series of sinusoidal waves with different wave numbers or by means of a standard separation of scales representation, in which the individual waves evolve on a fast scale making up an amplitude envelope that evolves slowly in comparison. In practice, the wave field on the open sea often has a group-like structure. Smith (2006) not only finds significant variation of his estimates of Stokes drift across the area studied in line with the occurrence of compact wave groups, but also identifies counter flows at depth that cancel the estimated Stokes drift at the surface completely. In oceanic general circulation models, in which the shear of the Stokes drift velocity needs to be included to model Langmuir turbulence, it is customary to replace the full Stokes drift velocity profile by a monochromatic profile matched to the transport and the surface Stokes velocity to avoid expensive computations (Breivik et al. 2014), leading these authors to propose alternative simple approximations based on the deep-water assumption but taking into account the group structure of real seas.

In real seas, a focused wave group occurs when a set of multi-chromatic wave components focus at a single position in space and time. Focussed wave groups are relevant, because they can be used to describe the average shape of an extreme wave crest in a random sea as a set of independent sinusoids of random amplitude (Tromans et al. 1991). Boccotti (1983) has shown that the average shape of an extreme wave crest corresponds to a scaled autocorrelation function of the underlying spectrum.

The structure of the wave-induced mean flow is fundamentally different for wave groups compared to regular waves. In wave groups the divergent volume flux associated with Stokes transport (2.2) must induce a return flow. In mathematical terms, the different wave number components, which make up the linear multi-chromatic wave group, interact to produce frequency-sum and frequency-difference components at the next order in amplitude. The frequency difference components, in turn, are responsible for the return

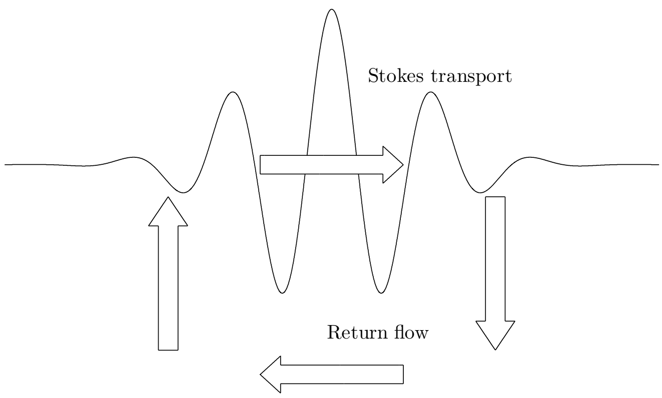

Figure 2.1: Illustration of the irrotational circulation that moves with the travelling wave group and in which Stokes transport, located near the free surface, transports fluid in the direction in which the group travels and the return flow acts to balance this by returning the flow at depth below the free surface. All four fluxes are equal.

flow, as first described by Longuet-Higgins and Stewart (1962). In physical terms, the dynamic free surface boundary condition, requiring a uniform pressure on the free surface and the satisfaction of Bernoulli's law for energy conservation, prevent a net deposition (extraction) of fluid at the leading (trailing) edge of the group due to the horizontal convergence (divergence) of the Stokes transport flux. For deep water, a spatial separation of the two effects takes place, as illustrated in figure 2.1: the Stokes transport dominates at the free surface over the e-folding depth $(2k_0)^{-1}$ with k_0 now denoting the peak of the wave number spectrum; the magnitude of the return flow decreases much more slowly with depth and consequently dominates far below the free surface. Combining the (local) Stokes transport and the (non-local) return flow leads to zero vertically-integrated mass transport at the centre of the group and hence there is zero vertically-integrated momentum associated with the centre of a surface gravity wave group, as emphasized by McIntyre (1981).

This chapter explores Lagrangian trajectories of neutrally buoyant particles underneath focussed surface gravity wave groups. It does so for irrotational, inviscid surface gravity waves in a semi-infinite two-dimensional unstratified and incompressible fluid. Instead of integrating the velocity profiles obtained from standard multi-chromatic second-order theories (Longuet-Higgins and Stewart 1962, Sharma and Dean 1981, Dalzell 1999), we do so by explicitly by pursuing a separation of scales expansion to study the effects of frequency dispersion on the net Lagrangian displacement by wave groups of different bandwidths in a two-dimensional deep-water environment. We develop simple expressions for the net Lagrangian displacement of particles as a function of steepness and bandwidth and study its variation with depth. Finally, we develop a characteristic length scale, the transition depth, above which Lagrangian particles are transported forwards by the Stokes drift and below which such particles are transported backwards by the return flow.

This chapter is laid out as follows. The governing equations and notation are introduced in §2.2 followed by a discussion of well-known results for periodic waves in §2.3, which are extended to higher order herein. The perturbation expansion framework in which the Stokes drift and the return flow are studied in this chapter is set up in §2.4. The equations describing the Stokes drift and the return flow are solved and discussed in §2.5 first ignoring the effects of dispersion (§2.5.1), then including leading-order dispersion (§2.5.2) and finally including all linear (in amplitude) dispersion to reproduce the Fourier-space solutions of Longuet-Higgins and Stewart (1962) (§2.5.3). Lagrangian particle trajectories are then examined in §2.6 followed by a discussion in §2.7 of a characteristic depth above which Stokes drift and below which the return flow are the dominant features of the flow. Finally, conclusions are drawn in §2.8.

2.2 Governing equations

A two-dimensional body of water of infinite depth and indefinite lateral extent is assumed with a coordinate system (x,z), where x denotes the horizontal coordinate and z the vertical coordinate measured from the undisturbed water level upwards. Inviscid, incompressible and irrotational flow is assumed and, as a result, the velocity vector can be defined as the gradient of the velocity potential $\mathbf{u} = \nabla\phi$ and the horizontal and vertical velocity as $u = \partial\phi/\partial x$ and $w = \partial\phi/\partial z$, respectively. The governing equation within the domain of the fluid is then Laplace:

$$\nabla^2\phi = 0 \quad \text{for } z \leq \eta(x,t), \tag{2.3}$$

where $\eta(x,t)$ denotes the free surface. The kinematic free surface boundary condition, which defines the free surface as moving with the particles located at the free surface, and the dynamic free surface boundary condition, which states that pressure at the free surface is constant and zero, are:

$$w - \frac{\partial\eta}{\partial t} - u\frac{\partial\eta}{\partial x} = 0, \quad g\eta + \frac{\partial\phi}{\partial t} + \frac{1}{2}\left(u^2 + w^2\right) = 0 \quad \text{at } z = \eta(x,t), \tag{2.4a,b}$$

where gravity g acts in the negative z direction. Finally, there is a no-flow bottom boundary condition requiring that $\partial\phi/\partial z = 0$ as $z \to -\infty$. We combine the two free surface boundary conditions (2.4a,b) into one equation in terms of ϕ:

$$\frac{\partial^2\phi}{\partial t^2} + g\frac{\partial\phi}{\partial z} + \frac{\partial}{\partial t}\Big(\Big(\frac{\partial\phi}{\partial x}\Big)^2 + \frac{1}{2}\Big(\frac{\partial\phi}{\partial z}\Big)^2\Big) + \frac{1}{2}\frac{\partial\phi}{\partial x}\frac{\partial}{\partial x}(\nabla\phi)^2 = 0 \quad \text{at } z = \eta(x,t), \tag{2.5}$$

where $(\nabla\phi)^2 = (\nabla\phi)\cdot(\nabla\phi) = u^2 + w^2$ denotes an inner product. Equation (2.5) can be solved in combination with a second (diagnostic) equation relating η to ϕ.

2.3 Periodic waves

2.3.1 Lagrangian particle displacement: Stokes drift

As a Lagrangian particle undergoes its orbital motion in periodic waves, Stokes drift arises due to two components: one due to vertical displacement and one due to horizontal displacement. For deep-water waves the two contributions are equal. The net horizontal motion of a particle located at $x = x_0$ and $z = z_0$ at $t = 0$ can be approximated by:

$$\frac{dx}{dt} = u(x_0, z = z_0, t) + \sum_{i=1}^{n}\sum_{j=1}^{n-i}\frac{(x-x_0)^i}{i!}\frac{(z-z_0)^j}{j!}\frac{\partial^{i+j}u(x,z,t)}{\partial x^i\partial z^j}\Big|_{x=x_0,z=z_0,t} + O(\alpha^{n+1}), \tag{2.6}$$

where we expand about the initial vertical and horizontal position of the particle z_0 and x_0 up to nth order in the small parameters α, which denotes the wave steepness α. To obtain the horizontal velocity $u(x,z,t)$ and the surface elevation $\eta(x,t)$ (for particles at the free surface), we use the 5th order Stokes expansion of Fenton (1985) (see appendix A). For consistency with Fenton's (1985) series, which are normalized so that $\max(\eta) - \min(\eta) = H$, we define $\alpha = kH/2$ with $k = 2\pi/\lambda$ denoting the wave number and H the full, non-linear wave height and not the (smaller) component of underlying linear wave height.

To find an approximate expression for the net displacement Δx in one Eulerian period T, we solve the differential equation (2.6) retaining only the non-periodic terms. This must be done iteratively with increasing order of approximation including all the possible interactions between velocity and displacement terms of different order, ultimately only retaining terms up to and including fifth order. Using Fenton's (1985) non-linear dispersion equation (A.3), we obtain after very considerable manipulation for a particle at the free surface:

$$\frac{\Delta x_{\mathrm{SD,E}}}{\lambda} = \alpha^2 + \frac{1}{2}\alpha^4 + O(\alpha^6) \quad \text{per Eulerian period } T. \tag{2.7}$$

It is important here to make a distinction between the two characteristic periods of the motion: the Eulerian period $T = \lambda/c$ associated with the periodic motion in a stationary reference frame and the Lagrangian period $T_{\mathrm{L}} = \lambda/(c-u_{\mathrm{SD}})$ (cf. Doppler shift) associated with the completion of the particle orbits in a Lagrangian frame of reference (Longuet-Higgins 1986), where $c = \sqrt{g/k}(1+\alpha^2/2+\alpha^4/8)$ (Fenton 1985) and u_{SD} are the phase speed and the horizontal drift velocity in the stationary frame of reference. We therefore have (Longuet-Higgins 1986):

$$\frac{T_{\mathrm{L}}-T}{T} = \frac{u_{\mathrm{SD}}/c}{1-u_{\mathrm{SD}}/c}, \tag{2.8}$$

and thus a longer period associated with the orbital motion compared to the period of the wave. We obtain:

$$\frac{\Delta x_{\mathrm{SD,L}}}{\lambda} = \alpha^2+\alpha^4+O\big(\alpha^6\big), \quad \frac{T_{\mathrm{L}}}{T} = 1+\alpha^2+\alpha^4+O\big(\alpha^6\big). \tag{2.9a,b}$$

From (2.9a) and (2.9b) we then obtain the horizontal Stokes drift velocity at the free surface:

$$\frac{u_{\mathrm{SD}}}{c} = \frac{\Delta x_L/\lambda}{T_L/T} = \alpha^2+O(\alpha^6), \tag{2.10}$$

which extends the validity of Stokes's (1847) original result ($u_{\mathrm{SD}}/c = \alpha^2$) obtained up to $O(\alpha^3)$ to higher order. It is noteworthy that up to fifth order of approximation, only second-order terms in the wave steepness are retained in the expression for the horizontal Stokes drift velocity for regular waves (2.10). Figure 2.2a validates (2.10) by comparing to the horizontal Stokes drift velocity obtained from numerical integration of $dx/dt = u(x,z,t)$ and $dz/dt = v(x,z,t)$ with velocities provided by Fenton's (1985) 5th order Stokes expansion. The small difference between the two lines is consistent with the inclusion of some but not all $O(\alpha^6)$ terms in the results from numerical integration.

2.3.2 Eulerian transport: Stokes transport

An Eulerian wave-induced volume flux, known as the Stokes transport, arises from integration of the (linear) time-varying horizontal velocity $u(x,z,t)$ with respect to depth z from the bottom at $z \to -\infty$ up to the (linear) time-varying free surface $z = \eta(x,t)$. Using Fenton's (1985) 5th order Stokes solution (appendix A) and retaining only non-periodic terms, the net volume flux (L^2T^{-1}) is given by:

$$Q_{\mathrm{ST}} = \frac{1}{T}\int_t^{t+T}\int_{-\infty}^{\eta(x,t)} u(x,z,t)dzdt = \sqrt{\frac{g}{k^3}}\Big(\frac{1}{2}\alpha^2-\frac{1}{4}\alpha^4+O(\alpha^6)\Big), \tag{2.11}$$

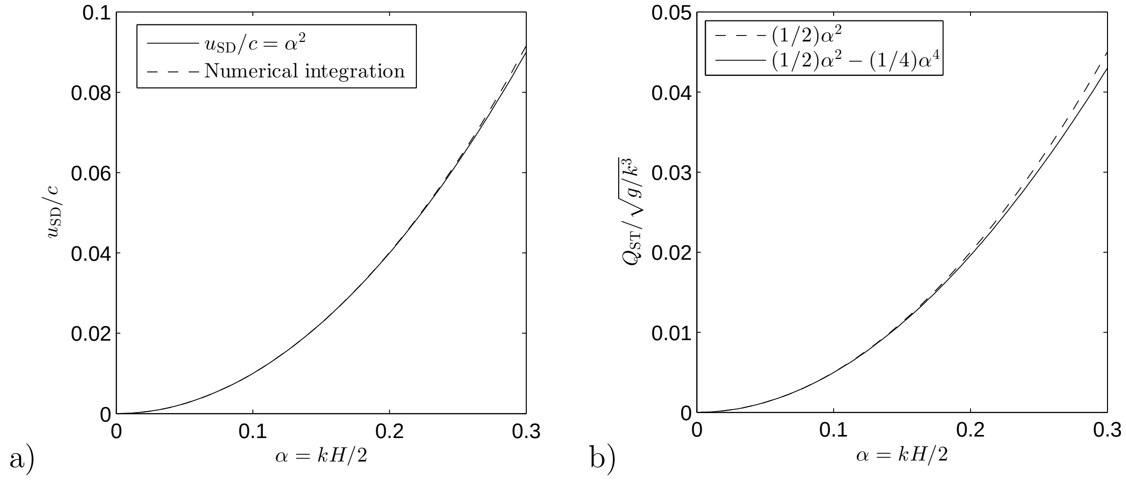

Figure 2.2: Stokes drift for regular waves showing (a) the Lagrangian horizontal Stokes drift velocity at the free surface (2.10) compared to results from numerical integration and (b) the associated Eulerian depth-integrated volume flux (2.11) known as the Stokes transport.

and is shown in figure 2.2b. Although it has to be emphasized that the volume flux (2.11) in itself does not arise from Stokes drift, but from the in-phase relationship of the integrand (the horizontal velocity) and the upper limit (the free surface elevation), an identical volume flux (at least to leading order) can be obtained by integrating the horizontal Stokes drift velocity (2.10) with depth.

2.4 Perturbation expansion for wave groups

2.4.1 Perturbation expansion in two small parameters

Whereas one small parameter (the wave steepness α) is sufficient to examine periodic waves, two small parameters are required for the study of wave groups by means of a perturbation expansion: a steepness (or sometimes amplitude) parameter α and a bandwidth parameter ϵ separating slow and fast scales. We define $\alpha = k_0|A_0|$, where $|A_0|$ is the magnitude (of the leading-order component in bandwidth, see §2.4.1.1) of the complex envelope of the surface elevation η and k_0 is the wave number of the (fast) carrier wave. The fast spatial and temporal scales are denoted by x, z and t and the slow scales by:

$$X = \epsilon(x - c_g t), \quad Z = \epsilon z, \quad T = \epsilon^2 t, \tag{2.12a,b,c}$$

where the slow scale X moves with the group velocity and the effects of frequency dispersion occur on the higher order time scale T. The slow scale X simply captures translation of the group at the group velocity, whereas the higher order time scale T captures changes of shape of the group. We keep track of both the order in the bandwidth parameter ϵ, which we denote by a subscript, and the order in the steepness of the signal, which we denote by a superscript. For example, $\eta^{(2)}_{(1)}$ denotes the component of the surface elevation that is first order in bandwidth ϵ and second order in steepness α. We do not make the assumption that $\epsilon = \alpha$, an assumption that is commonly made to derive equations of the non-linear Schrödinger type (e.g. Dysthe (1979)).

We note different authors have adopted different symbols and conventions to denote the group. For example, in Yuen and Lake (1975), a denotes the magnitude of the complex amplitude of the surface elevation A so that $A = a\exp(i\tilde{\theta})$, whereas in Dysthe (1979) A denotes the complex amplitude of the velocity potential and B denotes the complex amplitude of the surface elevation. Yuen and Lake (1975) then continue to express their equations in terms of the (complex) amplitude of the surface elevation, whereas Dysthe (1979) has his in terms of the (complex) amplitude of the velocity potential. Herein, we adopt the following inelegant but correct notation. We let B denote the complex amplitude envelope of the velocity potential ϕ (with dimensions L^2T^{-1}). Similarly, A_n denotes the complex amplitude of the surface elevation (with dimensions L) at nth order in bandwidth ϵ. We then use $\partial/\partial x$ to denote the combined effect of slow and fast derivatives, but let the subscripts in ∂_x and ∂_X denote only fast or slow derivatives, respectively (this distinct notation is not retained in future chapters). We restrict our attention to first and second order in amplitude α, which we consider in turn.

2.4.1.1 Linear in amplitude $O(\alpha)$

We consider the following linear (in steepness) velocity potential:

$$\phi^{(1)}(x,z,t) \equiv \phi^{(1)}_{(0)}(x,z,t) \equiv \mathrm{Re}\big[B(X,Z,T)e^{k_0 z}e^{i(k_0 x - \omega_0 t)}\big], \tag{2.13}$$

where we have set $\phi^{(1)}_{(n)} \equiv 0$ for $n \geq 1$. Equation (2.13) automatically satisfies Laplace (2.3) at $O(\alpha^1\epsilon^0)$ and for subsequent orders in ϵ we obtain: $\partial_Z B = -i\partial_X B$ and $\partial_{ZZ}B = -\partial_{XX}B$ for $z \leq 0$. From the combined free surface boundary condition (2.5) we obtain, at subsequent orders in ϵ, the linear dispersion relationship $(\alpha^1\epsilon^0)$, the group velocity at which the envelope travels without changing shape $(\alpha^1\epsilon^1)$ and the modification to this shape due to leading-order dispersion $(\alpha^1\epsilon^2)$:

$$\underbrace{\left(gk_0 - \omega_0^2\right)}_{=0} B + 2i\epsilon\omega_0 \underbrace{\left(c_{g,0} - \frac{g}{2\omega_0}\right)}_{=0} \partial_X B + \epsilon^2 \underbrace{\left(c_{g,0}^2\partial_{XX} - 2i\omega_0\partial_T\right)}_{=0} B = 0 \quad \text{at } z = 0, \tag{2.14}$$

where we have used $\partial_Z B|_{z=0} = -i\partial_X B|_{z=0}$ from Laplace at $O(\alpha^1\epsilon^1)$. The linearized (in α) version of (2.4a), $\partial\eta/\partial t = \partial\phi/\partial z|_{z=0}$, provides a relationship between $\phi^{(1)}$ in (2.13) and $\eta^{(1)}$. The latter is defined as:

$$\eta^{(1)} \equiv \sum_{n=0}^{\infty} \eta^{(1)}_{(n)} \equiv \sum_{n=0}^{\infty} A_n \epsilon^n e^{i(k_0 x - \omega_0 t)}, \tag{2.15}$$

where A_n (with units L) denotes the envelope of the $O(\alpha\epsilon^n)$ component of the surface elevation $\eta^{(1)}_{(n)}$. From (2.4a) we then have:

$$\Big(\partial_t - \epsilon c_{g,0}\partial_X + \epsilon^2\partial_T\Big) \sum_{n=0}^{\infty} \eta^{(1)}_{(n)} = \Big(k_0 - i\epsilon\partial_X\Big) B|_{z=0} e^{i(k_0 x - \omega_0 t)}, \tag{2.16}$$

where we have used $\partial_Z B|_{z=0} = -i\partial_X B|_{z=0}$ from Laplace at $O(\alpha^1\epsilon^1)$. In order to satisfy (2.4a) at first order in α and all orders in ϵ, it can be shown that we need an infinite number of terms in (2.15). Following some manipulation, it can be shown that the first three terms are:

$$A_0 = i\frac{k_0}{\omega_0} B|_{z=0}, \quad A_1 = \frac{1}{2}\frac{1}{\omega_0}\partial_X B|_{z=0}, \quad A_2 = \frac{1}{\omega_0^2}\Big(\frac{i}{2}c_{g,0}\partial_{XX} + k_0\partial_T\Big) B|_{z=0}. \tag{2.17a,b,c}$$

2.4.1.2 Second-order in amplitude $O(\alpha^2)$

At $O(\alpha^2)$ we have from (2.4):

$$\begin{aligned} \frac{\partial\phi^{(2)}}{\partial z} + \frac{\partial^2\phi^{(1)}}{\partial x^2}\eta^{(1)} - \frac{\partial\eta^{(2)}}{\partial t} - \frac{\partial\phi^{(1)}}{\partial x}\frac{\partial\eta^{(1)}}{\partial x} &= 0 \quad \text{at } z = 0, \\ g\eta^{(2)} + \frac{\partial\phi^{(2)}}{\partial t} + \frac{\partial^2\phi^{(1)}}{\partial t\partial z}\eta^{(1)} + \frac{1}{2}\bigg(\Big(\frac{\partial\phi^{(1)}}{\partial x}\Big)^2 + \Big(\frac{\partial\phi^{(1)}}{\partial z}\Big)^2\bigg) &= 0 \quad \text{at } z = 0. \end{aligned} \tag{2.18a,b}$$

We have from combination of (2.18a) (2.18b) and at $O(\alpha^2)$:

$$\Big(\frac{\partial}{\partial z} + \frac{1}{g}\frac{\partial^2}{\partial t^2}\Big)\phi^{(2)} = \frac{\partial}{\partial x}\Big(\eta^{(1)}\frac{\partial\phi^{(1)}}{\partial x}\Big) - \frac{1}{g}\frac{\partial}{\partial t}\bigg(\frac{\partial^2\phi^{(1)}}{\partial z\partial t}\eta^{(1)} + \frac{1}{2}\bigg(\Big(\frac{\partial\phi^{(1)}}{\partial x}\Big)^2 + \Big(\frac{\partial\phi^{(1)}}{\partial z}\Big)^2\bigg)\bigg) \quad \text{at } z = 0, \tag{2.19}$$

where we have used $\partial^2\phi^{(1)}/\partial z^2 = -\partial^2\phi^{(1)}/\partial x^2$ from Laplace. Equation (2.19) can be understood as the "forcing equation" of the return flow with its right-hand side terms representing a "forcing" by the first-order (in steepness) wave terms that gives rise to a mean flow on the left hand side. In fact, it can be shown by substituting the $O(\alpha)$ solutions at the various orders in ϵ into the right hand side that the "forcing" only gives rise to mean flow terms and that there are no higher harmonics for the potential (at least up to $O(\alpha^2\epsilon^3)$). Equation (2.19) becomes:

$$\Big(\epsilon\partial_Z + \frac{1}{g}\epsilon^2 c_{g,0}^2 \partial_{XX}\Big)\phi_{\mathrm{RF}}^{(2)}(X,Z,T) = \frac{\epsilon k_0^2}{2\omega_0}\partial_X |B|^2 + O(\alpha^2\epsilon^3) \quad \text{at } z=0, \tag{2.20}$$

where we note that the forcing term at $O(\alpha^2\epsilon^2)$, the order of leading-order dispersion in (2.14), is equal to zero. The return flow potential $\phi_{\mathrm{RF}}^{(2)}$ in (2.20) only caputures the slowly varying terms in (2.19) and arises from averaging the right hand side over the fast scales. The return flow can thus be found by solving its governing equation $(\partial_{XX} + \partial_{ZZ})\phi_{\mathrm{RF}}^{(2)} = 0$ subject to (2.20) and the bottom boundary condition. We note that our (2.20) up to $O(\epsilon^2)$ is equivalent to (2.20-2.21) of Dysthe (1979), who sets $\alpha = \epsilon$ and only considers terms up to 4th order in the combined small parameter.

2.5 Stokes drift, transport and the return flow for wave groups

Having derived a forcing equation for the return flow (2.20) in the previous section, this section evaluates the explicit solutions for the Stokes drift and transport and the return flow at the different orders in ϵ thereby first ignoring the effects of dispersion (§2.5.1), then including leading-order dispersion (§2.5.2) and finally including all linear (in amplitude) dispersion to reproduce the Fourier-space solutions of Longuet-Higgins and Stewart (1962), Sharma and Dean (1981) and Dalzell (1999) (§2.5.3). To assess the effect of frequency dispersion, comparisons are made between the three solutions for a Gaussian spectrum that is reasonably broad-banded ($\epsilon = 0.16$). The value $\epsilon = 0.16$ is representative of a severe sea state and is obtained by fitting a Gaussian distribution to the peak of a JONSWAP spectrum obtained from measurements of real seas (Hasselmann et al. 1980) with a peak enhancement factor $\gamma = 3.3$ (Gibbs and Taylor 2005).

2.5.1 Wave groups without dispersion $O(\alpha^2\epsilon^1)$

2.5.1.1 Stokes drift and transport for groups without dispersion $O(\alpha^2\epsilon^0)$

By substituting the leading-order ($\alpha^1\epsilon^0$) solutions for the horizontal and vertical velocity u and w into (2.6), a leading-order ($\alpha^2\epsilon^0$) expression for the Stokes drift and transport can be derived. The horizontal Stokes drift velocity and the Stokes transport become:

$$u_{\mathrm{SD}}(x,z,t) = \omega_0 k_0 e^{2k_0 z}|A_0(X)|^2, \quad Q_{\mathrm{ST}}(x,t) = \frac{1}{2}\omega_0 |A_0(X)|^2. \tag{2.21a,b}$$

Comparison with (2.10) and (2.11) for periodic waves immediately reveals that (2.21a) and (2.21b) are direct extensions of the periodic case with the amplitude envelope A_0, which varies on the slow scales, replacing the constant amplitude $H/2$. The Stokes transport Q_{ST} now increases (with increasing x) at the trailing edge of the group and decreases at the leading edge. It does so at the slow length scale X associated with the group and in doing so, it effectively "absorbs" fluid at the trailing edge, transports it through the centre of the group and deposits it at the leading edge of the group. In other words, the Stokes transport is not divergence-free. The excess quantity of fluid thus generated near the free surface is given by $-\partial Q_{\mathrm{ST}}/\partial x$ (see figure 2.3). In physical terms, this excess (or deficit) necessitates a return flow.

2.5.1.2 Return flow for groups without dispersion $O(\alpha^2\epsilon^1)$

At leading order in ϵ, the return flow can be found by solving for the potential flow field in the infinite half-space subject to the boundary conditions $w_{\mathrm{RF}} \to 0$ as $z \to -\infty$ and from (2.20):

$$w_{\mathrm{RF}}(X, Z=0) = \frac{1}{2}\omega_0\epsilon\frac{\partial|A_0(X)|^2}{\partial X} = \epsilon\frac{\partial Q_{\mathrm{ST}}(X)}{\partial X}, \tag{2.22}$$

where the second equality follows from (2.21b). It is evident then (cf. figure 2.3) that the Stokes transport acts as a sink (and the return flow as a source) with fluid flowing upwards ($w_{\mathrm{RF}}(X, Z=0) > 0$ when the volume flux transported by Stokes transport along the free surface increases ($\partial_X Q_{\mathrm{ST}} > 0$ for $X < 0$). Conversely, the Stokes transport acts as a source (and the return flow as a sink) with excess fluid flowing downwards ($w_{\mathrm{RF}}(X, Z=0) < 0$ for $X > 0$) when the volume flux transported by the Stokes transport along the free surface decreases ($\partial_X Q_{\mathrm{ST}} < 0$ for $X > 0$).

Using separation of variables and a Fourier sine transform for a Gaussian wave group $A_0(x,t) = a_0\exp(-(x-c_{g,0}t)^2/2\sigma^2)$ to solve the boundary value problem $(\partial_{XX}+\partial_{ZZ})\phi^{(2)}_{\mathrm{RF}} = 0$ subject to (2.22) and the bottom boundary condition, we obtain for the potential of the return flow:

$$\phi_{\mathrm{RF}}(x,z,t) = -\frac{1}{2\sqrt{\pi}}|a_0|^2\omega_0\sigma\int_0^\infty e^{-\frac{1}{4}(k\sigma)^2+kz}\sin\big(k(x-c_{g,0}t)\big)dk. \tag{2.23}$$

We note that the envelope of $\eta^{(1)}_{(0)}$ (A_0) and, consequently, the envelope of $\phi^{(1)}$ (B) has a Gaussian shape, but the envelope of $\eta^{(1)}$ (A) does not. The corresponding velocity components are given by:

$$
\begin{aligned}
u_{\mathrm{RF}}(x,z,t) &= -\frac{1}{2\sqrt{\pi}}|a_0|^2\omega_0\sigma\int_0^\infty ke^{-\frac{1}{4}(k\sigma)^2+kz}\cos\big(k(x-c_{g,0}t)\big)dk,\\
w_{\mathrm{RF}}(x,z,t) &= -\frac{1}{2\sqrt{\pi}}|a_0|^2\omega_0\sigma\int_0^\infty ke^{-\frac{1}{4}(k\sigma)^2+kz}\sin\big(k(x-c_{g,0}t)\big)dk.
\end{aligned}
\tag{2.24a,b}
$$

An alternative method of deriving an equation for the return flow equivalent to (2.24) that lends more physical insight into the problem (but is mathematically entirely equivalent) is illustrated in figure 2.3. At the trailing edge, the Stokes transport provides a sink of fluid, whereas at the leading edge it acts as a source with strength of the source given by $-\epsilon\partial_X Q_{\mathrm{ST}}$. The contribution to the horizontal velocity field at (x,z) of a dipole with its source located at ($l + c_{g,0}t$,0) and its sink at ($-l + c_{g,0}t$,0) and strength M per unit length dl is given by:

$$
du_{\mathrm{RF}} = \frac{M}{\pi}\Big[\frac{x-l-c_{g,0}t}{(x-l-c_{g,0}t)^2+z^2} - \frac{x+l-c_{g,0}t}{(x+l-c_{g,0}t)^2+z^2}\Big]dl,
\tag{2.25}
$$

Summing all the potential-flow contributions of the sources and sinks located at $z = 0$ then gives for the horizontal component of the return flow:

$$
\begin{aligned}
u_{\mathrm{RF}}(x,z,t) &= \int_0^\infty \frac{M(l)}{\pi}\Big[\frac{x-l-c_{g,0}t}{(x-l-c_{g,0}t)^2+z^2} - \frac{x+l-c_{g,0}t}{(x+l-c_{g,0}t)^2+z^2}\Big]dl,\\
&= \frac{|a_0|^2\omega_0}{\pi\sigma^2}\int_0^\infty \Big[\frac{x-l-c_{g,0}t}{(x-l-c_{g,0}t)^2+z^2} - \frac{x+l-c_{g,0}t}{(x+l-c_{g,0}t)^2+z^2}\Big]l\exp(-(l/\sigma)^2)dl,
\end{aligned}
\tag{2.26}
$$

where the strength is given by $M(l) = (\omega_0|a_0|^2/\sigma)(l/\sigma)\exp(-(l/\sigma)^2)$, as evaluated from (2.21b) for a Gaussian group. Equation (2.26) can be shown to be equivalent to (2.24a).

Figure 2.4 illustrates the spatial distribution of the horizontal and the vertical component of the return flow field, which at leading order are steady in the frame of reference of the group. It is evident from figure 2.4b that the return flow consist of downward and upward flowing bodies of fluid on, respectively, the leading and trailing edge of the group, consistent with the idea of a "return" flow. From figure 2.4a it is evident that the return flow not only consists of a large backward flow underneath the centre of the group $|x - c_{g,0}t| \lesssim 0.5\sigma$, but also sizeable forwards flow centered around $x - c_{g,0}t = \sqrt{2}\sigma$ at the leading edge and $x - c_{g,0}t = -\sqrt{2}\sigma$ at the trailing edge.

To examine the variation of the return flow with depth, consider the horizontal component of the return flow u_{RF} at the centre of the group $x = c_{g,0}t$, where $w_{\mathrm{RF}} = 0$. From either

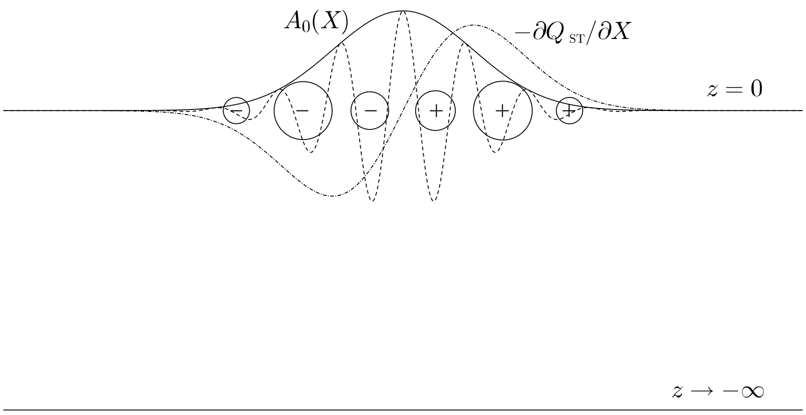

Figure 2.3: Illustration of the boundary conditions the spatial distribution of Stokes transport near the free surface poses for the return flow in the underlying body of fluid for a wave group without dispersion. At the trailing edge, the Stokes transport provides a sink of fluid, whereas at the leading edge it acts as a source with strength of the source given by $M(X) = -\epsilon\partial Q_{\rm ST}/\partial X$, located at the still water level $z = 0$ and denoted graphically by circles with radii proportional to the local strength of the source or sink. Also shown are the individual waves that make up the group.

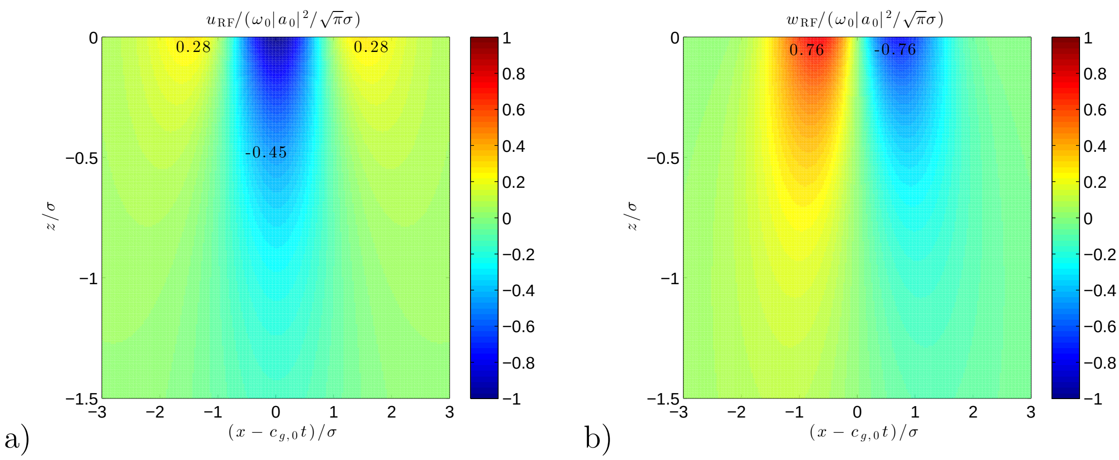

Figure 2.4: Return flow velocity field for wave groups without dispersion showing (a) the horizontal velocity (2.24a) and (b) the vertical velocity (2.24b) for $\epsilon = 0.16$. It is evident from panel a that the "return" flow does not only consist of negative horizontal velocities.

(2.24a) or (2.26) we have at this location, the only location at which a non-trivial closed-form solution is available:

$$u_{\mathrm{RF}}(x = c_{g,0}t, z) = -\frac{\omega_0|a_0|^2}{\sqrt{\pi}\sigma}\left(1 + \sqrt{\pi}\frac{z}{\sigma}\left(1 + \mathrm{erf}\left(\frac{\mathrm{z}}{\sigma}\right)\right)\mathrm{e}^{\frac{z^2}{\sigma^2}}\right), \tag{2.27}$$

which has the near-surface limit $|z| \ll \sigma$ and the deep-down limit $|z| \gg \sigma$:

$$u_{\mathrm{RF}}(x = c_{g,0}t, z) = \begin{cases} -\frac{\omega_0|a_0|^2}{\sqrt{\pi}\sigma} & \text{for } |z| \ll \sigma, \\ -\frac{\omega_0|a_0|^2}{\sqrt{\pi}\sigma}\frac{1}{2}\left(\frac{z}{\sigma}\right)^{-2} & \text{for } |z| \gg \sigma. \end{cases} \tag{2.28}$$

More generally, we can derive the following limiting behaviour of the horizontal component of the return flow in the far-field of large $|x - c_{g,0}t|$ or large $|z|$ (see appendix B):

$$u_{\mathrm{RF}}(x, z, t) = \frac{|a_0|^2\sigma\omega_0}{2\sqrt{\pi}}\frac{(x - c_{g,0}t)^2 - z^2}{\left((x - c_{g,0}t)^2 + z^2\right)^2}, \tag{2.29}$$

from which we can obtain the two far-field limits: $u_{\mathrm{RF}} \sim -z^{-2}$ for $|z| \gg |x - c_{g,0}t|$ and $u_{\mathrm{RF}} \sim (x - c_{g,0}t)^{-2}$ for $|x - c_{g,0}t| \gg |z|$, where we emphasize the difference in sign. In the first limit, namely deep down in the fluid below the group, the horizontal flow velocity is negative, whereas near the surface, either far in front or far behind the group, the horizontal flow velocity is positive. The horizontal flow is zero in the far field along 45° lines drawn from the centre of the group (2.29). It is also instructive here to note the difference in depth decay between the Stokes drift and the return flow: the Stokes drift (2.21) decays very rapidly (exponentially) with depth on the scale of the wave length of the individual waves λ_0 (cf. $\exp(2k_0z)$) as opposed to the return flow which asymptotically decays much more slowly with depth (cf. $(z/\sigma)^{-2}$) on the scale of the width of the group σ. Figure 2.5 compares the depth decay of the Stokes drift and the return flow at two different locations.

We note from comparison of (2.21a) and (2.28) that the Stokes drift velocity is $O(\alpha^2\epsilon^0)$, whereas the return flow is always one order higher in ϵ, namely $O(\alpha^2\epsilon^1)$. The difference is explained by the length scales over which both velocities act: the Stokes drift decays more rapidly (cf. $\exp(2k_0z)$) with (a fraction of) the wave length as the characteristic scale over which it acts ($1/(2k_0) = \lambda_0/(4\pi)$) than the return flow, which decays more slowly on the scale of the half-width of the wave group σ. In fact, the horizontal velocity of the return flow (2.24a) can be integrated with depth to obtain the total volume flux by the return flow:

$$Q_{\mathrm{RF}} = \int_{-\infty}^{0} u_{\mathrm{RF}} dz = -\frac{1}{2}|a_0|^2\omega_0 e^{\frac{(x-c_{g,0}t)^2}{\sigma^2}}, \tag{2.30}$$

thereby confirming the result, emphasized by McIntyre (1981), that $Q_{\mathrm{RF}}(x, t) + Q_{\mathrm{ST}}(x, t) =$

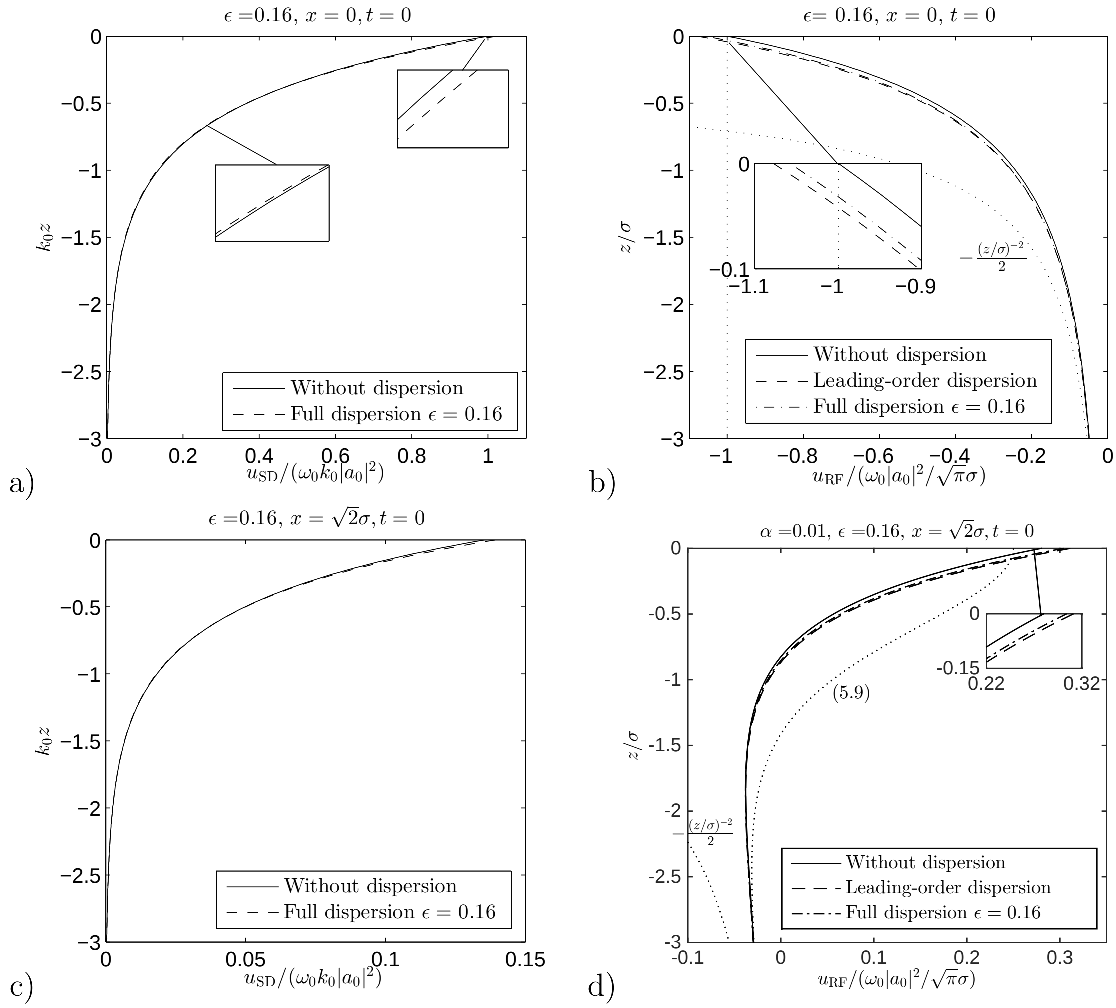

Figure 2.5: Stokes drift (a,b) and return flow (c,d) velocities for wave groups as a function of depth at the centre of the group $x = 0$ (a,c) and at $x = \sqrt{2}\sigma$ (b,d) at $t = 0$, the time of focus as $t = 0$, comparing the solutions for groups without dispersion, with leading-order dispersion and with full dispersion. Note the different scales on the axes: $z/\sigma = \epsilon(k_0 z)$ with $\epsilon = 0.16$ here. The dotted lines in panels b and d correspond to the asymptotic limits (2.28) (a) and (2.29) (b).

0, a (non-dispersive) surface gravity wave group is associated with zero depth-integrated momentum, as illustrated in figure 2.6.

2.5.2 Wave groups with leading-order dispersion $O(\alpha^2\epsilon^2)$

From inspection of (2.20) it is clear that at the next order in bandwidth ($\alpha^2\epsilon^2$), the order at which the leading-order effects of dispersion cause the group to change shape as it travels, the "forcing term" of the return flow is zero. It can indeed be confirmed from integrating (2.6) over the fast time scale but allowing for leading-order slow variation in Δx and Δz that no additional Stokes drift arises at order $\alpha^2\epsilon$. Leading-order dispersion,

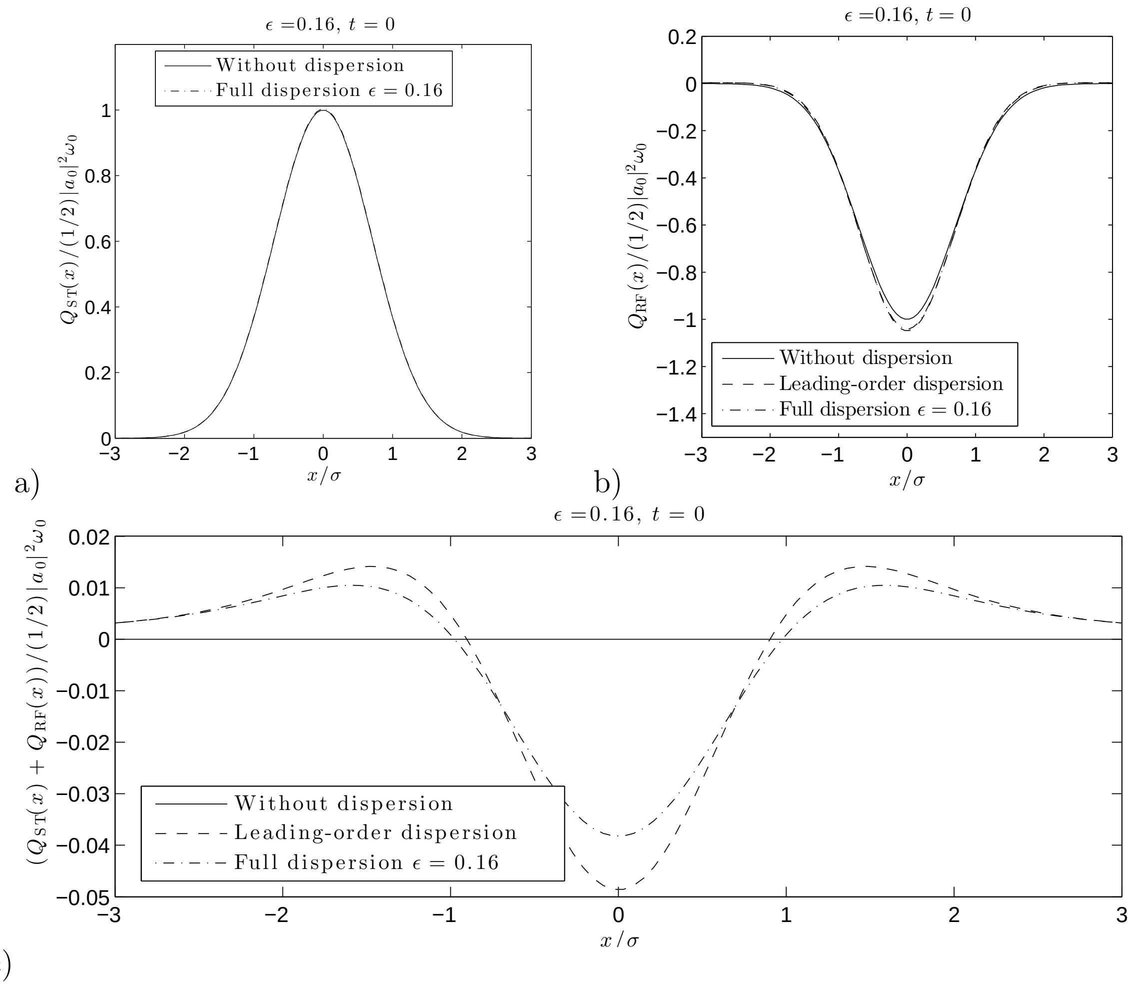

Figure 2.6: Depth-integrated volume flux by (a) Stokes transport (Q_{ST}), (b) the return flow (Q_{RF}) and (c) the sum of both ($Q_{\mathrm{ST}} + Q_{\mathrm{RF}}$) as a function of x for $t = 0$ (the time of focus is $t = 0$) for wave groups without dispersion, with leading-order dispersion and with full dispersion.

however, causes the group to evolve differently in space and time. As time progresses the group becomes wider due to dispersion and the third term in (2.14) must now also be satisfied to reflect this. At this order we have for a Gaussian group (Kinsman 1984):

$$B(x,z,t)|_{z=0} = -i\frac{\omega_0}{k_0}A_0(x,t) = b_0\frac{1}{\sqrt{1+\frac{i\,\gamma_0\,t}{\sigma^2}}}e^{-\left(\frac{1}{1+\gamma_0^2t^2/\sigma^4}\frac{(x-c_{g,0}t)^2}{2\sigma^2}\right)}e^{i\left(\frac{\gamma_0 t/\sigma^2}{1+\gamma_0^2t^2/\sigma^4}\frac{(x-c_{g,0}t)^2}{2\sigma^2}\right)}, \tag{2.31}$$

where we have $\gamma_0 = d^2\omega/dk^2|_{k=k_0} = -\sqrt{g/k_0^3}/4$ with $\omega(k)$ obtained from the linear dispersion relationship. More simply, we have for the magnitude of B:

$$|B(x,t)| = |\tilde{b}|e^{-\frac{(x-c_{g,0}t)^2}{2\tilde{\sigma}^2}}, \tag{2.32}$$

with $|\tilde{b}| = |b_0|/(1+\gamma_0^2 t^2/\sigma^4)^{1/4}$ denoting the effective amplitude and $\tilde{\sigma} = \sigma\sqrt{1+\gamma_0^2 t^2/\sigma^4}$ the effective Gaussian half-width of the group. As the group disperses with time, the group widens ($\partial\tilde{\sigma}/\partial t > 0$) and its effective amplitude decreases ($\partial|\tilde{b}|/\partial t < 0$). At any point in time, the forcing term on the right hand side of (2.20) can be modified to include the effects of leading-order dispersion by replacing σ by $\tilde{\sigma}$ and $|b|$ by $|\tilde{b}|$. We note in passing that (2.31) satisfies the linear part of the non-linear Schrödinger equation often used to model weakly non-linear, narrow-banded, deep-water wave groups (Adcock and Taylor 2009).

Although the right hand side of (2.20) is not, the left hand side of (2.20) is affected by leading-order dispersion. Including the $O(\epsilon^2)$ term, we obtain without further approximation:

$$\phi_{\mathrm{RF}}(x,z,t) = -\frac{1}{2\sqrt{\pi}}|\tilde{a}_0|^2\omega_0\tilde{\sigma}\int_0^\infty \frac{e^{-\frac{1}{4}(k\tilde{\sigma})^2+kz}\sin\big(k(x-c_{g,0}t)\big)}{1-kc_{g,0}^2/g}dk, \qquad (2.33)$$

where $|\tilde{a}_0| = |a_0|/(1+\gamma_0^2 t^2/\sigma^4)^{1/4}$ is the effective amplitude. Comparison with the non-dispersive and the fully dispersive solution is made in §2.5.3.

2.5.3 Fully dispersive wave groups $O(\alpha^2\epsilon^\infty)$

For completeness, we also follow the frequency domain approach of Longuet-Higgins and Stewart (1962) (see also Sharma and Dean (1981), Dalzell (1999)). In doing so, we not only capture the effect of leading-order frequency dispersion of the group (§2.5.2), but effectively include all orders in ϵ. Instead of discretizing the spectrum (Longuet-Higgins & Stewart 1962), we define the following linear (in steepness) velocity potential and surface elevation using a continuous spectrum:

$$\phi^{(1)}(x,z,t) = \int_{-\infty}^{\infty}\hat{b}(k)e^{|k|z}e^{i[kx-\omega(k)t]}dk, \quad \eta^{(1)}(x,t) = \int_{-\infty}^{\infty}\hat{a}(k)e^{i[kx-\omega(k)t]}dk, \quad (2.34\text{a,b})$$

where all spectral terms satisfy the linear dispersion relationship $\omega = \sqrt{g|k|}$ and $\hat{a}(k) = i|k|\hat{b}(k)/\omega(k)$ in order to satisfy the (linearized in α) free surface boundary conditions (2.5-2.4a). For consistency with the separation of scales approach, we choose $\hat{b}(k)$ so that $\phi^{(1)}(x, z = 0, t)$ in (2.34) has a Gaussian spatial distribution equivalent to (2.13), namely $\hat{b}(k) = (\sigma b_0/\sqrt{2\pi})\exp(-\sigma^2(k-k_0)^2/2)$. In turn, we set $b_0 = -i\omega_0 a_0/k_0$, so that the surface elevation envelope is focussed at $x = 0$ and $t = 0$. We let f denote the Gaussian wave number spectrum with unit amplitude: $f(k) = (\sigma/\sqrt{2\pi})\exp(-\sigma^2(k-k_0)^2/2)$.

2.5.3.1 Stokes drift and transport for fully dispersive wave groups $O(\alpha^2\epsilon^\infty)$

By substituting linear expressions for $\partial u^{(1)}/\partial x$, $\partial u^{(1)}/\partial z$, $\Delta x^{(1)}$ and $\Delta z^{(1)}$ obtained from (2.34a) into (2.6), we obtain for the horizontal Stokes drift up to 2nd order in steepness:

$$u_{\mathrm{SD}}(x,z,t) = \frac{|b_0|^2}{2}\int_{-\infty}^{\infty}\int_{-\infty}^{\infty} f(k_1)f(k_2)\frac{k_1^2k_2 + k_1|k_1||k_2|}{\omega(k_2)}e^{(|k_1|+|k_2|)z}\cos(\theta_2-\theta_1)dk_1dk_2, \tag{2.35}$$

where $\theta_j = k_jx - \omega_jt + \mu_j$ for $j = 1, 2$. Although (2.35) does not appear to have a closed-form solution, it can be readily confirmed that it reduces to (2.21) in the limit of narrow band-width ($\epsilon \ll 1$). Finally, we note we have deliberately chosen a continuous over a discrete spectral representation, so that the (small) Lagrangian displacements can be evaluated to the required accuracy using standard numerical integration techniques and the solutions without dispersion (§2.5.1) and with leading-order dispersion (§2.5.2) can be recovered in the limit of small ϵ. For the same reason and to allow for Gaussian groups, we have allowed for both positive and negative wave numbers, although the contribution from the latter is numerically negligibly small for the bandwidth considered herein ($\epsilon = 0.16$).

2.5.3.2 Return flow for fully dispersive wave groups $O(\alpha^2\epsilon^\infty)$

By substituting the linear solutions (2.34), the right hand side of (2.19) becomes:

$$\left(\tfrac{\partial}{\partial z} + \tfrac{1}{g}\tfrac{\partial^2}{\partial t^2}\right)\phi_{\mathrm{RF}}^{(2)} = \tfrac{|b_0|^2}{2}\int_{-\infty}^{\infty}\int_{-\infty}^{\infty}\frac{f(k_1)f(k_2)\big(\sqrt{|k_1|}-\sqrt{|k_2|}\big)\big(|k_1||k_2|+k_1k_2\big)}{\sqrt{g}}\sin(\theta_2-\theta_1)dk_1dk_2. \tag{2.36}$$

The solution to Laplace subject to the "forcing" (2.36) and the bottom boundary condition is then:

$$\phi_{\mathrm{RF}}(x,z,t) = \tfrac{|b_0|^2}{2\sqrt{g}}\int_{-\infty}^{\infty}\int_{-\infty}^{\infty}\frac{f(k_1)f(k_2)\big(\sqrt{|k_1|}-\sqrt{|k_2|}\big)\big(|k_1||k_2|+k_1k_2\big)}{|k_2-k_1|-(\sqrt{k_2}-\sqrt{k_1})^2}e^{|k_2-k_1|z}\sin(\theta_2-\theta_1)dk_1dk_2. \tag{2.37}$$

For a spectrum with only positive wave numbers, (2.37) reduces to the more familiar (see the deep-water limit of Longuet-Higgins and Stewart (1962) evaluated explicitly by Sharma and Dean (1981) and Dalzell (1999)):

$$\phi_{\mathrm{RF}}(x,z,t) = \int_0^{\infty}\int_{k_2>k_1}^{\infty}\hat{a}(k_1)\hat{a}(k_2)\omega(k_2)e^{(k_2-k_1)z}\sin(\theta_2-\theta_1)dk_2dk_1. \tag{2.38}$$

In §2.5.2 we have already shown that leading-order frequency dispersion does not affect the Stokes drift velocities. It is evident from figures 2.5a,c that for reasonable values of the bandwidth ($\epsilon = 0.16$) the effect of full dispersion is negligible too. Focussing on the return flow, it has been shown in §2.5.2 that leading-order dispersion generally increases the magnitude of the horizontal return flow velocities. It can be confirmed from figures 2.5b,d that leading-order dispersion is in good agreement with full dispersion for $\epsilon = 0.16$. The effect remains small with magnitudes of the return flow velocity at $z = 0$ approximatively 10% larger at the centre of the group (figure 2.5b) and 7% at $x = \sqrt{2}\sigma$ (figure 2.5d) when allowing for dispersion.

The physical explanation for the larger return flow velocities is most easily understood by considering the "forcing" equation (2.20). Without any dispersion ($O(\epsilon)$) (2.20) is simply a steady mass balance argument: the divergence of the volume flux on the right hand side results in an up- and downflow on either side of the group. Including leading-order dispersion ($O(\epsilon^2)$), the "forcing"-term on the right hand side of (2.20) is not affected. The only difference is that the problem is no longer steady as the group disperses and an extra term is introduced on the left hand side. In loose terms, although the volume deficit and excess associated with the Stokes transports remains unaffected, on the same time scale the group appears to have become more broad spatially thus requiring larger return flow velocities to "return" the fluid and ensure that the total induced mean flow, the sum of the Stokes transport and the return flow, is divergence free.

Finally, we turn to figure 2.6 confirming the depth integrated volume fluxes of the Stokes transport and the return flow are equal and opposite ($Q_{\text{ST}} + Q_{\text{RF}} = 0$) without dispersion, but the latter is not the case with dispersion simply reflecting a redistribution of fluid away from the group as the group ($\eta^{(2)}$) disperses and becomes wider.

2.6 Particle trajectories

In this section we use the kinematics for groups without dispersion, with leading-order dispersion and a fully dispersive wave group evaluated in §2.5.1-§2.5.3 to determine the scaling and shape of the Lagrangian particle trajectories at and below the free surface, as well as their final displacements. The total Lagrangian velocity of a particle $\mathbf{u}_{\text{L}}$ is determined by the sum of its Stokes drift $\mathbf{u}_{\text{SD}}$, a Lagrangian phenomenon, and the Eulerian return flow field $\mathbf{u}_{\text{RF}}$ (Andrews and McIntyre 1978):

$$\underbrace{\mathbf{u}_{\text{L}}}_{\text{Lagrangian}} = \underbrace{\mathbf{u}_{\text{SD}}}_{\text{Stokes drift}} + \underbrace{\mathbf{u}_{\text{RF}}}_{\text{Euler}}. \tag{2.39}$$

We first consider the net contribution by each in turn.

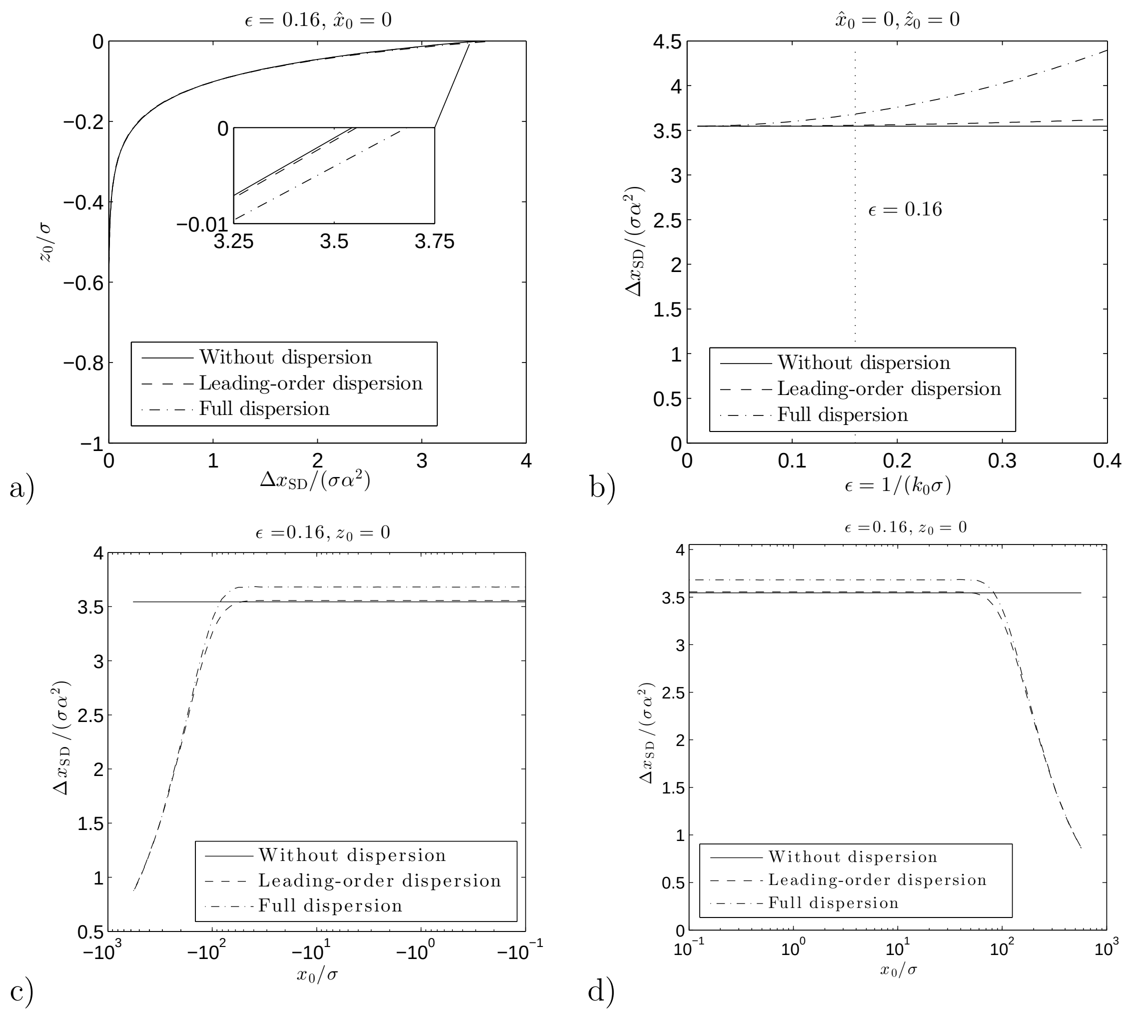

Figure 2.7: Net horizontal particle displacement due to Stokes drift $\Delta x_{\rm SD}$ (a) as a function of depth, (b) as a function of the bandwidth parameter ϵ and (c,d) as a function of the initial position of the particle x_0 relative to the focus point of the group $x = 0$ (at $t = 0$) for (c) negative x_0 and (d) positive x_0. Three solutions are compared in each panel: the separation of scales solution without dispersion (2.40), with leading-order dispersion (2.41) and the Fourier-space solution with full dispersion. The three solutions in (c,d) are in fact symmetric around $x_0 = 0$.

2.6.1 Particle displacement by Stokes drift

From (2.21a) we obtain for the net horizontal displacement due to Stokes drift for a particle as a function of its initial vertical position z_0 and for a Gaussian group:

$$\frac{\Delta x_{\rm SD}(z_0)}{\sigma} = \frac{\displaystyle\int_{-\infty}^{\infty} u_{\rm SD}(x_0, z_0, t)dt}{\sigma} = 2\sqrt{\pi}\alpha^2 e^{2k_0 z_0} \quad \text{without dispersion,} \tag{2.40}$$

where we have ignored the effects of dispersion. The horizontal particle displacement is thus only a function of the steepness (cf. α^2) and the half-width of the wave group σ, but decays rapidly with depth, as would be expected. Including the leading-order effect of dispersion, we obtain from (2.21) in combination with the leading-order dispersive group (2.32):

$$\frac{\Delta x_{\mathrm{SD}}(x_0, z_0)}{\sigma} = 2\alpha^2 e^{2k_0 z_0} \int_{-\infty}^{\infty} \frac{1}{\sqrt{1+\epsilon^2\hat{t}^2/4}} e^{\frac{-(\hat{x}_0-\hat{t})^2}{1+\epsilon^2\hat{t}^2/4}} d\hat{t} \quad \text{with leading-order dispersion,} \tag{2.41}$$

where the right-hand side integral has been non dimensionalized by defining $\hat{x}_0 = x_0/\sigma$ and $\hat{t} = c_{g,0}t/\sigma$. The net horizontal displacement due to Stokes drift is now both a function of the initial horizontal and the initial vertical position of the particle. Finally, the fully dispersive solution (2.35) can be integrated numerically. Figure 2.7 compares the three solutions.

It is evident then from figure 2.7a that dispersion does not non-negligibly affect the horizontal displacement by Stokes drift for $\epsilon = 0.16$. In fact, the effects of dispersion only become apparent at very high ϵ (figure 2.7b). These differences then arise from higher-order and not leading-order dispersion (figure 2.7b). The effects of dispersion only play a role through the initial position of the particle (figure 2.7c,d). Particles located very far away from the centre of the group ($|x_0| \gtrsim 10^2\sigma$) simply undergo motion corresponding to a group that has dispersed and is of much reduced amplitude.

2.6.2 Particle displacement by the return flow

From the identity of the Stokes transport and the opposite and equal return flow volume flux $Q_{\mathrm{ST}}(x,t) = -Q_{\mathrm{RF}}(x,t)$ for a non-dispersive wave group, it follows that equal and opposites (two-dimensional) volumes of fluid V_{ST} and V_{RF} are transported horizontally by each:

$$\underbrace{\int_{-\infty}^{\infty} Q_{\mathrm{ST}}(x,t)dt}_{\equiv V_{\mathrm{ST}}} = -\underbrace{\int_{-\infty}^{\infty} Q_{\mathrm{RF}}(x,t)dt}_{\equiv V_{\mathrm{RF}}}. \tag{2.42}$$

The horizontal transport can be found by integrating the horizontal return flow velocity with respect to time. For a wave group without dispersion we obtain from (2.24a):

$$\frac{\Delta x_{\mathrm{RF}}(z_0)}{\sigma} = -\frac{\alpha^2\epsilon}{\sqrt{\pi}} \int_{-\infty}^{\infty}\int_{0}^{\infty} \hat{k} e^{-\frac{\hat{k}^2}{4}+\hat{k}\hat{z}_0} \cos(\hat{k}\hat{t}) d\hat{k} d\hat{t} \quad \text{without dispersion,} \tag{2.43}$$

where the double integral on the right hand side is non-dimensional with $\hat{k} = k\sigma$, $\hat{t} = c_{g,0}t/\sigma$ and only a function of the scaled depth $\hat{z}_0 = z_0/\sigma$. Explicitly, we have from

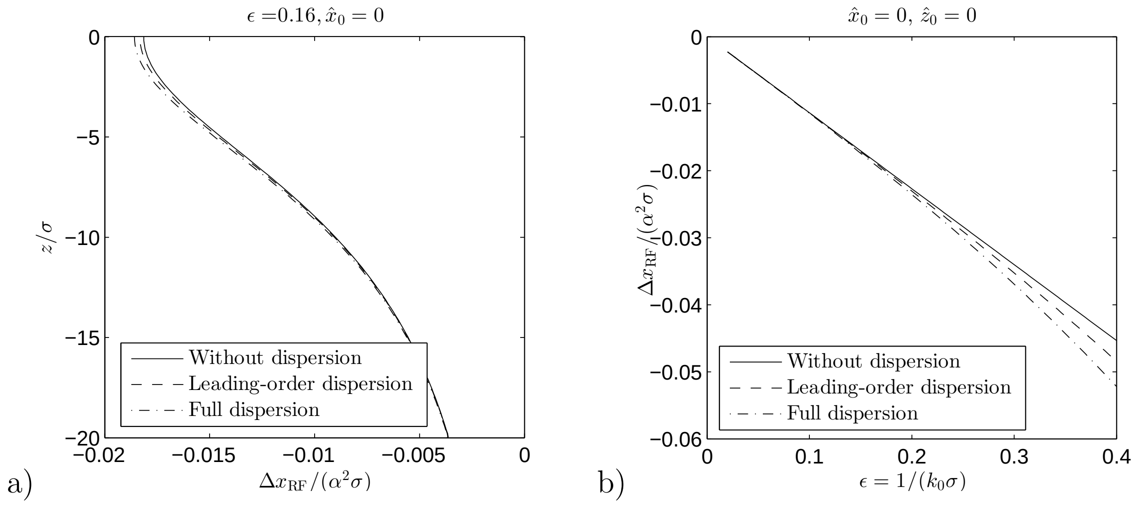

Figure 2.8: Net horizontal particle displacement due to the return flow Δx_{RF} (a) as a function of depth and (b) as a function of the bandwidth parameter ϵ. Three solutions are compared in each panel: the separation of scales solution without dispersion, with leading-order dispersion and the Fourier-space solution with full dispersion.

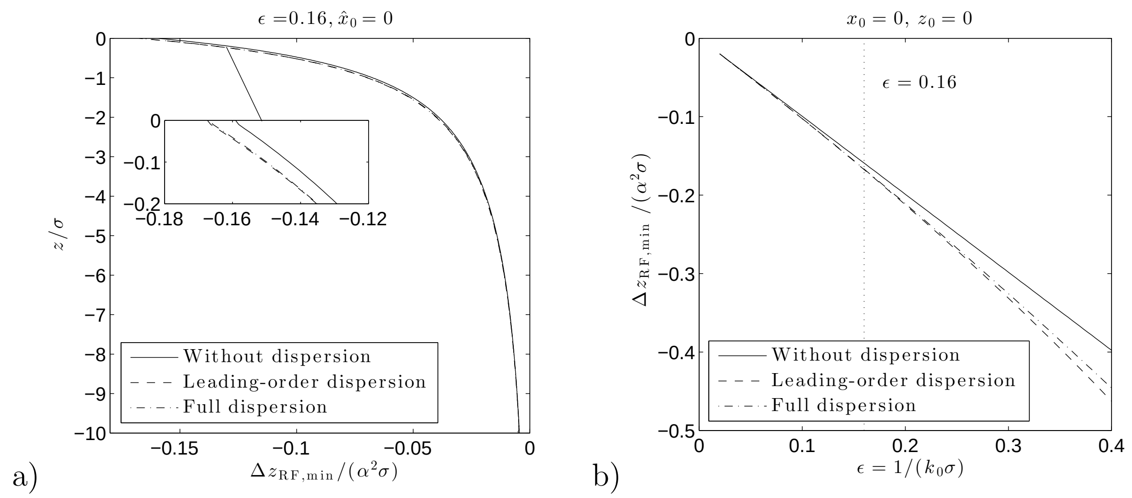

Figure 2.9: Maximum vertical particle displacement due to the return flow $\Delta z_{\mathrm{RF,min}}$ (a) as a function of depth and (b) as a function of the bandwidth parameter ϵ. Three solutions are compared in each panel: the separation of scales solution without dispersion, with leading-order dispersion and the Fourier-space solution with full dispersion.

numerical evaluation of the double integral for a particle located at $z_0 = 0$:

$$\frac{\Delta x_{\mathrm{RF}}(z_0 = 0)}{\sigma} \approx -0.1134\alpha^2\epsilon \quad \text{without dispersion.} \tag{2.44}$$

From comparison of (2.40) and (2.44) for $z_0 = 0$ we thus have a positive horizontal displacement due to Stokes drift that is a factor $\approx 31.3/\epsilon$ (≈ 195 for $\epsilon = 0.16$) larger compared to the opposite horizontal displacement due to the return flow. Equation (2.43) can be readily modified to allow for the effects of leading-order dispersion. From (2.33) we obtain:

$$\frac{\Delta x_{\mathrm{RF}}(x_0, z_0)}{\sigma} = -\frac{\alpha^2\epsilon}{\sqrt{\pi}} \int_{-\infty}^{\infty} \int_0^{\infty} \frac{\hat{k}}{1 - \epsilon\hat{k}/4} e^{-\frac{\hat{k}^2}{4} + \hat{k}\hat{z}_0} \cos(\hat{k}(\hat{x}_0 - \hat{t})) d\hat{k} d\hat{t}, \tag{2.45}$$

which is now additionally a function of the non-dimensional initial horizontal position $\hat{x}_0 = x_0/\sigma$. Finally, the net horizontal displacement by the fully dispersive return flow can be obtained by means of numerical integration of the horizontal velocity corresponding to (2.37).

It turns out that the double integrals in (2.43) and (2.45) are very difficult to evaluate using standard numerical quadratures in part due to the very slow decay of the large time tails of the integrand (cf. $u_{\mathrm{RF}} \sim t^{-2}$, see appendix B). The horizontal displacements are in practice evaluated by first calculating the depth-integrated transported volume $V_{\mathrm{RF}}(z_0) = \int_{-\infty}^{z_0} u_{\mathrm{RF}} dz$ as a function of intial particle depth z_0 followed by numerical differentiation of this quantity with respect to z_0. An alternative method that gives the same result is to integrate numerically for small time and analytically for large time using the far-field solutions in appendix B and combine both contributions.

Figure 2.8a then shows the net horizontal displacement as a function of depth displaying an even slower variation than the horizontal return flow velocity (figure 2.5a,c). The (small) magnitude of the displacement at $z = -10\sigma$ is still approximately half the value at the still water level. It can be shown that the far-field solution (2.29) does not result in a net displacement (appendix B). In agreement with the larger return flow velocities in figure 2.5a,c dispersion slightly increases the magnitude of the (negative) displacement (figure 2.8a) and more so for large ϵ (figure 2.8b). We emphasize that, as opposed to the Stokes drift, the net displacement due to the return flow for non-dispersive groups is not a direct function of σ, but the dependence is only through the dependence on the vertical position z_0/σ , which scales on σ. The small parameter ϵ only appears in (2.43) because of the scaling of the left hand side by σ. It goes without saying that the depth integral of the displacement due to Stokes drift and the return flow despite their very different distribution with depth are equal and opposite (2.42). A very small backwards displacement that decays extremely slowly with depth thus compensates a very much larger forward displacement concentrated near the still water level.

Although no net vertical displacement of particles arises due to the return flow, we can evaluate the maximum vertical displacement to obtain a sense of the vertical scale of the motion associated with the return flow. At $z_0 = 0$ we have from (2.24b):

$$\frac{\Delta z_{\mathrm{RF,min}}(z_0 = 0)}{\sigma} = -\alpha^2 \epsilon \quad \text{without dispersion,} \tag{2.46}$$

and similarly for the leading-order and fully dispersive solution. Figure 2.9 evaluates this maximum vertical displacement as a function of depth and ϵ. We note from comparison of figures 2.8a and 2.9a that maximum vertical displacement is approximately 10 times larger than the net horizontal displacement.

2.6.3 Lagrangian trajectories

Having obtained expressions for the net displacement due to Stokes drift and the return flow, figure 2.10 shows the trajectories of Lagrangian particles obtained from numerical integration of the equations of motion $d\mathbf{x}/dt = \mathbf{u}^{(1)} + \mathbf{u}^{(2)}$ for a group without dispersion for particles initially located at different depths (rows) and different values of ϵ (columns).

The behaviour of particles with initial positions at the still water level (top row) is dominated by Stokes drift with smaller values of ϵ corresponding to more individual waves making up the group and thus more orbits contributing to the net horizontal displacement. For particles at great depth (bottom row) the particle trajectories are dominated by the return flow with the individual waves only giving rise to small deflections of the horse-shoe shaped particle trajectory. We note that for deep water the magnitude of the horse-shoe shaped return flow trajectory is in fact very small, so small in fact that it might be difficult to observe in reality. At intermediate depths both the effect of Stokes drift and the return flow play a role.

The trajectories in figure 2.10 correspond to focused crests, whereas those in 2.11 correspond to focused troughs. Although the net displacements are not affected, as shown in §2.6.1 and §2.6.2, the trajectory of particles whose motion is dominated by Stokes drift is affected, whereas the trajectory of particles whose motion is dominated by the return

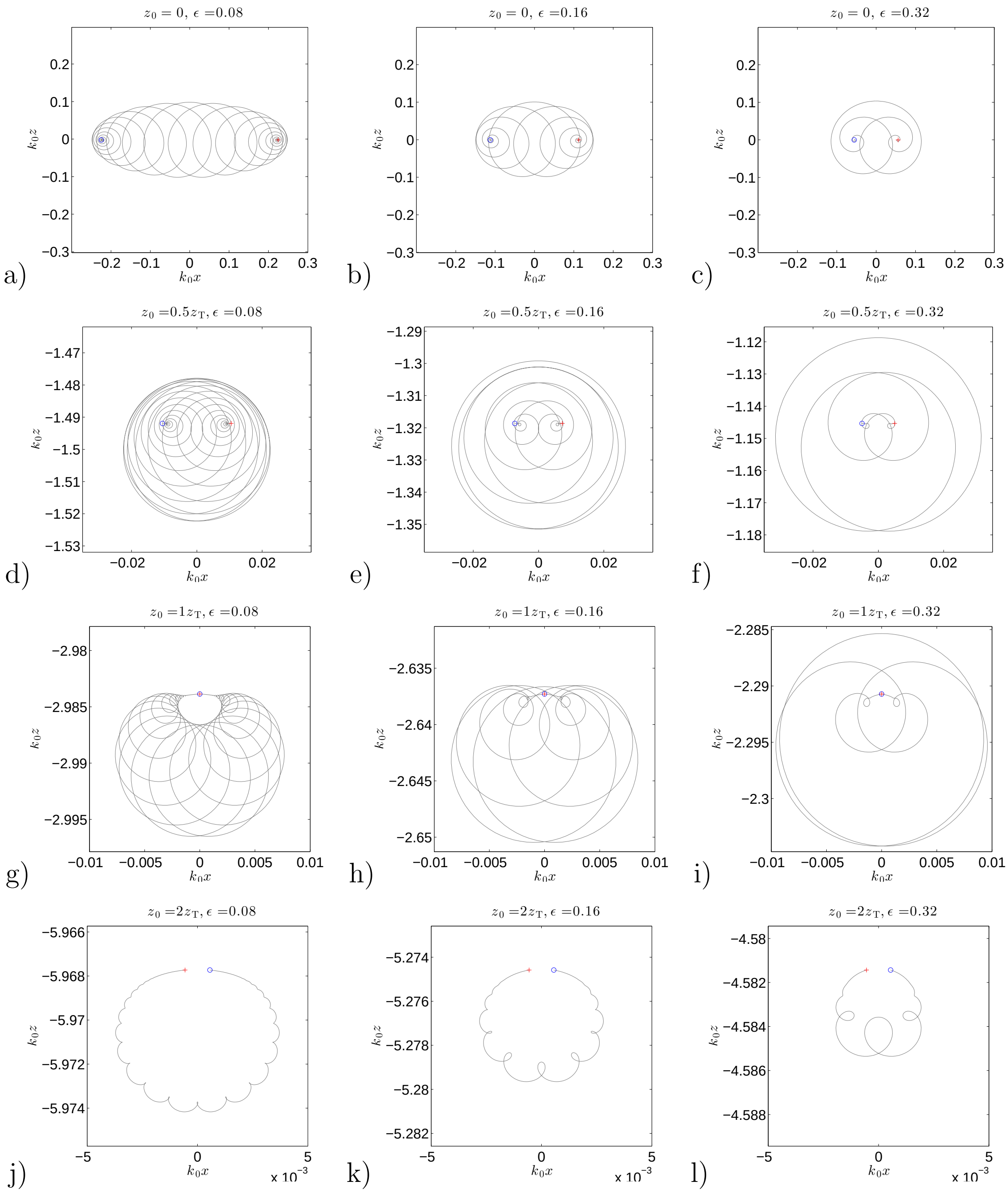

Figure 2.10: Lagrangian trajectories of neutrally buoyant particles at different depths below a focussed crest wave group and for different values of the bandwidth parameter $\epsilon = 1/(k_0\sigma)$. The rows correspond to initial particle depths $z_0 = \{0, 0.5, 1, 2\}z_{\rm T}$ with $z_{\rm T}$ denoting the approximate transition depth of (2.49), where the net horizontal Lagrangian transport is zero. The columns correspond to values of $\epsilon = 0.08$, 0.16 and 0.32, respectively. The trajectories shown correspond to the solutions without dispersion with the blue open circle corresponding to the initial position of the particle and the red cross corresponding to the final position of the particle. The waves are of steepness $\alpha = 0.1$.

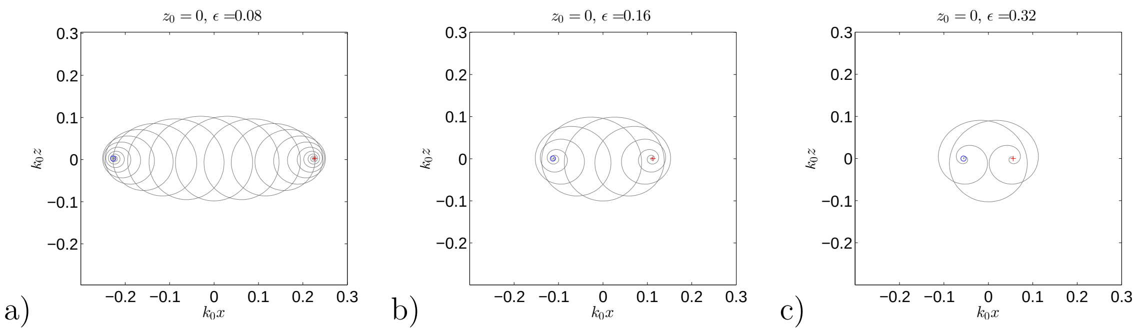

Figure 2.11: Lagrangian trajectories of neutrally buoyant particles at the still water level of a focussed trough wave group and for different values of the bandwidth parameter $\epsilon = 1/(k_0\sigma)$. The columns correspond to values of $\epsilon = 0.08$, 0.16 and 0.32, respectively. The trajectories shown correspond to the solutions without dispersion with the blue open circle corresponding to the initial position of the particle and the red cross corresponding to the final position of the particle. The waves are of steepness $\alpha = 0.1$.

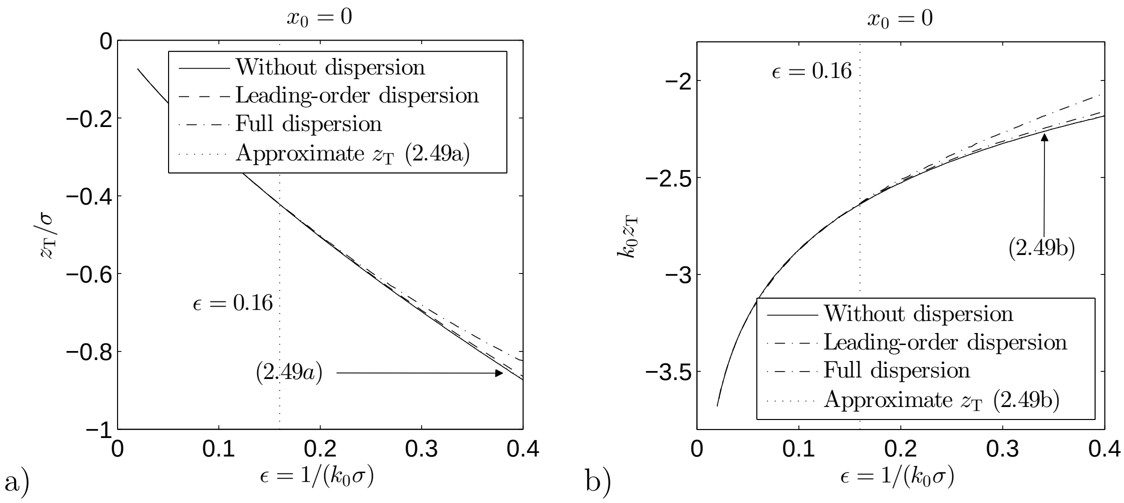

Figure 2.12: The transition depth between positive horizontal particle transport by the Stokes drift and negative horizontal particle transport by the return flow. Note all the lines (almost) overlap.

flow is not. The difference in motion is evident from comparison of figures 2.10a,b,c and 2.11a,b,c for particles at the still water level.

2.7 The transition depth

In order to classify when either type of motion described in §2.6.3 occurs, a transition depth z_{T} can be defined as the depth at which the positive horizontal displacement of a particle by the Stokes drift is equal to the negative horizontal displacement of a particle by the return flow so that the net Lagrangian displacement is zero:

$$\Delta x_{\mathrm{L}}(z_0 = z_{\mathrm{T}}) = \Delta x_{\mathrm{SD}}(z_0 = z_{\mathrm{T}}) + \Delta x_{\mathrm{RF}}(z_0 = z_{\mathrm{T}}) = 0 \quad \text{transition depth.} \tag{2.47}$$

Above this depth ($z_0 > z_{\mathrm{T}}$) particles will be transported in the direction of positive x and below this depth ($z_0 < z_{\mathrm{T}}$) particles will be transported in the opposite direction. Ignoring the generally small effects of dispersion and making use of the fact that Stokes drift decays much faster with depth than the return flow, an approximate expression for the transition depth $z_{\mathrm{T,\,APPROX}}$ can be obtained by finding the depth at which the net horizontal Stokes drift displacement (2.40) has decreased to the surface value of the return flow displacement at $z_0 = 0$ (2.44), which is assumed not to decay over that same depth:

$$\Delta x_{\mathrm{RF}}(z_0 = 0) + \Delta x_{\mathrm{SD}}(z_0 = z_{\mathrm{T,\,APPROX}}) = 0, \tag{2.48}$$

which has the solution:

$$\frac{z_{\mathrm{T,APPROX}}}{\sigma} \approx \frac{1}{2}\epsilon\big(-3.442 + \log(\epsilon)\big), \quad \text{or} \quad k_0 z_{\mathrm{T,APPROX}} \approx \frac{1}{2}\big(-3.442 + \log(\epsilon)\big). \tag{2.49a,b}$$

Figure 2.12 compares the approximate transition depth with transition depths obtained from solving $\Delta x_{\mathrm{L}} = 0$ (2.47) implicitly without dispersion, with leading-order dispersion (at $x_0 = 0$) and with full dispersion (at $x_0 = 0$). It is evident then that the approximate transition depth (2.49) provides an excellent prediction of the actual transition depth even including the effects of dispersion at large values of ϵ, much larger than the representative value of $\epsilon = 0.16$.

As the steepness of the wave $\alpha = |A_0|k_0$ affects both the magnitude of the displacement due to Stokes drift and the displacement due to the return flow in the same way, the transition depth is only a function of the bandwidth parameter $\epsilon = 1/(k_0\sigma)$. As we keep the wave length of the peak spectral component k_0 fixed and shrink the width of the group σ (and thus let ϵ increase), the magnitude of the displacement due to the return flow near the free surface is unaffected $\Delta x_{\mathrm{RF}} \approx -0.1134\alpha^2 k_0^{-1}$ (from (2.44)), but the magnitude of the displacement due to Stokes drift $\Delta x_{\mathrm{SD}} = 2\sqrt{\pi}\sigma\alpha^2 \exp(2k_0 z_0)$ (from (2.40)) decreases, as the group is simply shorter. The point at which the net displacement is equal to zero must then occur at smaller depth and z_T approaches zero as ϵ increases (figure 2.12 b).

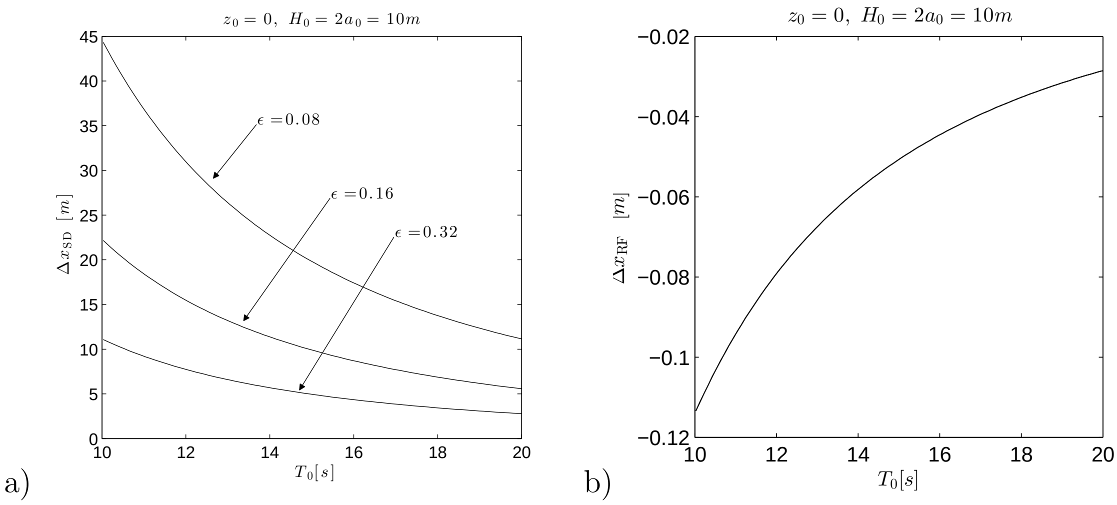

Figure 2.13: Dimensional net horizontal particle displacement at the surface $z_0 = 0$ (a) due to Stokes drift and (b) due to the return flow as a function of the peak period of the spectrum T_0 for a wave group with linear wave height $H_0 = 2a_0 = 10$m. Note that solutions are only plotted for $\alpha < 0.2$ corresponding to $T_0 > 2\pi\sqrt{a_0/(g\alpha)} \approx 10.0s$. The solution in (a) is a function of ϵ, the solution in (b) is not.

2.8 Conclusions

The Lagrangian trajectories of neutrally buoyant particles underneath focussed surface gravity wave groups have been examined and simple leading-order expressions for the net displacement resulting from Stokes drift and the return flow have been developed. In the deep-water limit, both the Stokes drift, the mean velocity that arises due to the waves when tracking Lagrangian particles and ignoring the effect of Eulerian flows, and the Stokes transport, the Eulerian volume flux that arises at the same order (second order) in steepness occur in the vicinity of the still water level. The much smaller return flow, on the other hand, varies much more slowly with depth, to the extent that its variation in the near surface region, where Stokes drift takes place, can be ignored. A separation of the physical domains in which the two physical phenomena occur thus takes place. Frequency dispersion is found to only marginally affect both phenomena for realistic sea states and, to good approximation, the problem can be studied using a leading-order separation of scales approximation, in which the wave-induced mean flow is steady in the frame of reference of the group without resorting to more complicated frequency domain representations (Longuet-Higgins and Stewart 1962, Sharma and Dean 1981, Dalzell 1999). To obtain a sense of the magnitude of the displacements in real seas, figure 2.13, shows the particle displacements predicted as a function of the peak period of the spectrum T_0 for a group with linear wave height $H_0 = 2a_0 = 10$m. Whereas displacements of the order 10^1-10^2m are predicted for the Stokes drift, the return flow only results in displacements of the order 10^{-2}-10^{-1}m.

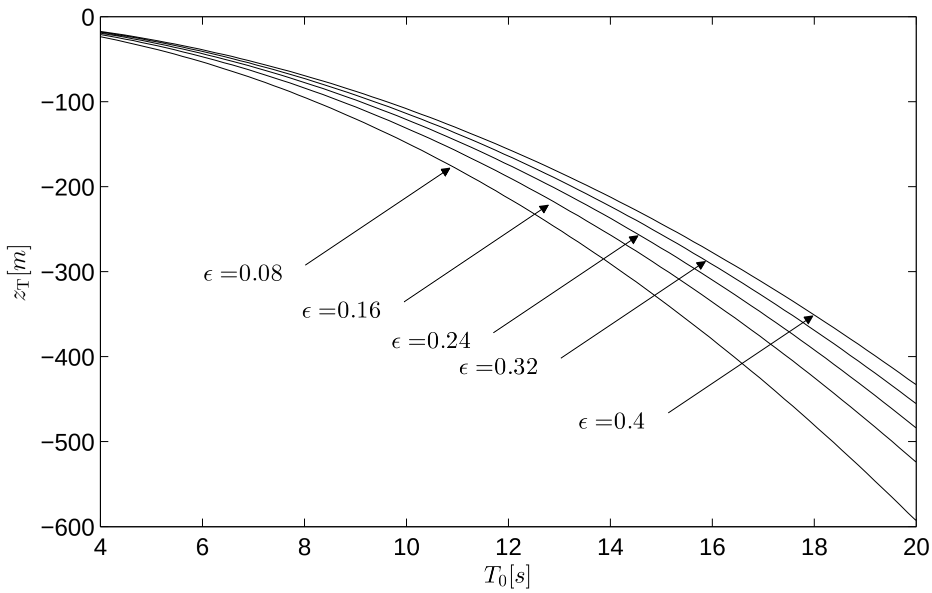

Figure 2.14: The dimensional transition depth z_{T} between positive horizontal particle transport by the Stokes drift and negative horizontal particle transport by the return flow. Shown is the approximate transition depth $z_{\mathrm{T,\ APPROX}}$ (2.49) as a function of the peak period of the spectrum T_0 for different values of the bandwidth parameter $\epsilon = 1/(k_0\sigma)$.

Based on the very different depth decay of Stokes drift and the return flow, an approximate transition depth has been proposed above which Lagrangian particles are transported forwards by the Stokes drift and below which such particles are transported backwards by the return current. The transition depth is only a function of the peak wave number k_0 and the half-width of the group σ decreasing (in absolute terms) with the former and increasing (in absolute terms) with the latter. To obtain a sense of the magnitude of this transition depth for real seas, figure 2.14 shows the transition depth as a function of the peak period of the spectrum T_0 for different values of the bandwidth parameter $\epsilon = 1/(k_0\sigma)$. It is not a function of steepness. The transition point only occurs close to the surface for short period waves.

The results presented herein rely crucially on the deep-water assumption. Although a typical engineering criterion for an oscillatory wave to be in deep water is $k_0 d \gtrsim 3$, a much larger depth may be required for the return flow of a group not to "feel" the presence of the bottom. For example, for $\epsilon = 0.16$, we have $k_0 d = 3$ corresponding to $d/\sigma = 3\epsilon = 0.48$, whereas the Lagrangian displacement due to the return current may still be a significant share of its surface value at $z/\sigma = -20$ (cf. figure 2.8a). A sea that is deep for a $T_0 = 10$ s wave, namely $d \approx 75$ m so that $k_0 d = 3$, may require a much greater depth for the return flow to be unaffected by the bottom boundary condition, namely $d \gtrsim 3$ km (taking $z/\sigma = -20$ as a criterion with $\epsilon = 0.16$). The presence of the bottom boundary in what can reasonably be considered infinite depth for the oscillatory components of the wave group but is in fact finite depth for the return flow, is then likely to increase the magnitude of the return flow near the still water level. This, in turn, has important effects on the stability properties of the wave train through interaction with the mean flow as first captured by Dysthe (1979) for truly infinite depth (see Janssen (1983) for a discussion) and first extended to finite depth by Brinch-Nielsen and Jonsson (1986) and more recently in an Hamiltonian framework by Craig et al. (2010) and Gramstad and Trulsen (2007). On finite depth the return flow enters the non-linear Schrödinger equation describing the evolution and stability of the group at lower order than on deep water.

As a final caveat, we note that, although the results presented herein for Gaussian spectra can be readily extended to different spectra, they rely on the ignoring the third dimension evidently present in real seas, which will affect the return flow and the transition depths. The analysis presented here for two-dimensional waves on deep water will be extended to finite depth in three-dimensional seas in the next chapter.

Chapter 3

The effects of directionality and finite depth on the induced mean flow of surface gravity wave groups

As explored in the previous chapter, two physical phenomena drive the Lagrangian trajectories of neutrally buoyant particles underneath surface gravity wave groups: the Stokes drift results in a net displacement of particles in the direction of propagation of the group, whereas the Eulerian return flow transports such particles in the opposite direction. Generally, the Stokes drift is the larger of the two near the surface, whereas the effects of the return flow dominate at depth. A transition depth can be defined that separates the two regimes. Using a multiple-scales expansion we provide leading-order estimates of the forward transport, the backward transport and the transition depth for realistic sea states. Starting from an idealized Gaussian deep-water wave group in a two-dimensional sea, we consider the effects of both finite depth and the directionally spread nature of the waves in a three-dimensional sea on our estimates of these three quantities. We show that from the perspective of the return flow, almost all seas are of finite depth invalidating the ubiquitous deep-water approximation. In fact, many seas can be shown to be "shallow" from the perspective of the return flow with little variation of this flow with depth. Furthermore, even small degrees of directional spreading can considerably reduce the magnitude of the return flow and its transport.

3.1 Introduction

As explored in the previous chapter, surface gravity waves have an associated a wave-induced mean flow known as the Stokes drift. The drift manifests itself most evidently as the mean horizontal velocity of fluid parcels (Lagrangian particles) that are displaced by a finite horizontal distance over each wave cycle. During one cycle beneath a wave on deep water, at leading order in the steepness of the wave the particle follows a circular trajectory with the size of the circle decreasing exponentially with depth. At the next order, it is clear these orbits do not close resulting from the displacement of the Lagrangian particle from its initial position:

$$u_{\mathrm{SD}} = \overline{\frac{\partial u^{(1)}}{\partial x}\Delta x^{(1)} + \frac{\partial u^{(1)}}{\partial x}\Delta z^{(1)}}, \tag{3.1}$$

where the over-line denotes averaging over the individual waves and the superscripts denote the order in wave steepness. In an Eulerian framework, a surface gravity wave can be shown to have an associated net volume flux resulting from integration of the linear horizontal velocity with depth up to the linear free surface $\eta^{(1)}$, known as the Stokes transport:

$$Q_{\mathrm{ST}} = \overline{\int_{-d}^{\eta^{(1)}(x,t)} u^{(1)}(x,z,t)dz}. \tag{3.2}$$

Real seas consist of a spectrum of different frequency components thus constituting a packet or group structure. Making use of the separation of scales between the fast variation of the individual waves and the slow variation of the group's modulation for a quasi-monochromatic or narrow-banded group, the expressions for the Stokes drift (3.1) and the Stokes transport (3.2) still hold. The averaging denoted by the over-lines is over the fast scales, the individual waves. The Stokes transport (3.2) for groups varies with the (square of the) local amplitude of the group and is therefore divergent. It must induce a return flow ($\mathbf{u}_{\mathrm{RF}}$) first described by Longuet-Higgins and Stewart (1962) that in some sense returns the fluid deposited by the Stokes transport at the group's leading edge to be absorbed again by the Stokes transport at its trailing edge. For sufficiently deep-water, a spatial separation of the two effects takes place: Stokes drift dominates near the free surface and the return flow dominates at depth. In physical terms, the dynamic free surface boundary condition, requiring a uniform pressure on the free surface and the satisfaction of Bernoulli's law for energy conservation, prevent a net deposition (extraction) of fluid at the leading (trailing) edge of the group due to the horizontal convergence (divergence) of the Stokes transport.

Broadly, two oceanographic applications of Stokes drift can be distinguished: its effect on Lagrangian tracers such as pollutants and buoys on the one hand and its part in the physics of the ocean surface mixed layer on the other. Regarding the first, Stokes drift play an important role in trajectory forecasts for search and rescue operations, oil spill mitigation and the interpretation of in situ observations obtained from tracking buoys (Röhrs et al. 2013). These authors use data to estimate the effects on Lagrangian displacement of a submerged tracking buoy (in water depths of 220-700 m) distinguishing the effects of the Stokes drift and the wave-induced Eulerian fluxes as well as the Coriolis-Stokes forcing.

Secondly, Stokes drift plays an important role in the ocean surface boundary (or "mixed") layer, the approximately 100 m thick layer that controls the exchange of heat, momentum and gases between the atmosphere and the ocean and is therefore critical in determining the role of the global ocean circulation on climate (see Belcher et al. (2012) for a review). With lines of constant vorticity moving with Lagrangian fluid particles in an inviscid fluid, the sheared depth profile of the Stokes drift velocity with depth stretches initially vertically orientated vorticity into the horizontal plane (Polton et al. 2005). Two sources of vertical vorticity can be distinguished: the three-dimensional turbulent vorticity that give rise to Langmuir circulation and the planetary vorticity that interacts with the Stokes drift and gives rise to the Stokes-Coriolis force.

With both Langmuir turbulence and the Stokes-Coriolis forcing included in oceanic general circulation models, the magnitude of the Stokes drift and its variation with depth (cf. shear) must also be included. In such models the individual waves are typically too small to be resolved by even the most powerful computational models and the effect of Stokes drift must be parameterized before inclusion. Such parameterizations have only recently begun to be extended to include the non-monochromatic or group nature of the waves (Breivik et al. 2014).

An important assumption is often that the sea is deep, in other words, that the product of the wave number k_0 and the water depth d is large, typically taken as $k_0 d \gtrsim 3$. Variation of the (linear) properties can then be assumed to be exponential with depth, considerably simplifying the analysis. Whereas the variation of the linear dynamics with depth scales on the inverse of the wave number k_0^{-1}, the return flow varies on the horizontal scale of the wave group σ. For the return flow to be unaffected by the bottom boundary condition, we thus require $d/\sigma = \epsilon k_0 d$ to be large, a more restrictive assumption. For a quasi-monochromatic group, the parameter $\epsilon = 1/(k_0\sigma)$ is assumed to be small. A sea that is deep for a $T_0 = 10$ s wave, namely $d \approx 75$ m so that $k_0 d = 3$, may require a much greater depth for the return flow to be unaffected by the bottom boundary condition, namely $d \gtrsim 3$ km (taking $z/\sigma = -20$ as a criterion with $\epsilon = 0.16$) (see chapter 2). Furthermore, the magnitudes of the return flow are expected to reduce considerably when the spectrum is directionally spread and the group become spatially localised in both horizontal directions. The return flow can then both "return" underneath as well as around the sides of the group. The motivation for this chapter is thus to study the behaviour of the return flow and its contribution to Lagrangian transport for realistic sea states: sea states in finite depth and with directional spreading.

Focussing on two-dimensional deep-water waves and second-order in steepness α, chapter 2 has shown that a leading-order expansion in the bandwidth parameter $\epsilon = 1/(k_0\sigma)$ is adequate for capturing the Lagrangian dynamics by both the Stokes drift and the return flow for a realistic value of bandwidth obtained by fitting a Gaussian spectrum to the enhanced peak of a Jonswap spectrum (Gibbs and Taylor (2005)). In other words, such a leading-order expansion correctly captures the Lagrangian dynamics underneath a wave group, where the effects of frequency dispersion on the shape of the group can be ignored and the group can be assumed to translate at the group speed without changes in shape. An approximate transition depth is proposed, above which Lagrangian particles are transported forwards and below which the transport is in the opposite direction. Moreover, chapter 2 shows that for the return flow not to be affected by finite depth effects, the water depth may have to be unrealistically large.

In this chapter, we follow the approach of chapter 2 and extend it to three dimensions and finite depth. Using a leading-order multiple scales approach, we thus set out to examine the effect of finite depth and the directional nature of the spectrum in a three-dimensional sea on three quantities: the net horizontal transport by the Stokes drift, the net horizontal transport by the return flow and the transition depth that separates these two regimes. Since the effect of frequency dispersion reduces as the water depth becomes less deep and motivated by the results of chapter 2, we only consider leading-order contribution in the small parameter ϵ: the order at which the group travels without changing shape. Finally, an important effect of reducing the depth from infinite to finite needs to be taken into account. This is the wave-induced set-down, a slowly varying quantity that has non-negligible effects on the mean flow field for finite depth, but can be ignored for deep-water (McIntyre (1981)).

This chapter is laid out as follows. §3.2 introduces the governing equations and boundary conditions and briefly summarizes the findings of chapter 2 for infinitely deep two-dimensional seas. §3.3 considers the effects of finite depth for two-dimensional seas. This is followed by a discussion of three-dimensional effects in §3.4, with realistic directional distributions being considered in §3.4.3. Finally, conclusions are drawn in §3.5.

3.2 Governing equations and separation of scales model

3.2.1 Governing equations

Assuming irrotational and incompressible flow in a fluid of constant density, the governing equation $\nabla^2\phi = 0$ can be expressed in terms of the velocity potential ϕ defined here in a three-dimensional coordinate system (x, y, z) with velocity components $u = \partial\phi/\partial x$, $v = \partial\phi/\partial y$ and $w = \partial\phi/\partial z$. In vector notation we have $\mathbf{x} = (x, y, z)$ and $\mathbf{u} = (u, v, w)$. Gravity $\mathbf{g}$ acts in the negative z-direction and the still water level corresponds to $z = 0$. The governing equation is solved subject to the linear no-flow bottom boundary condition $w(z = -d) = 0$ and the kinematic and dynamic boundary conditions at the free surface $z = \eta(x, y, t)$:

$$\frac{D}{Dt}\Big(\eta(x,y,t) - z\Big) = 0, \quad g\eta + \frac{\partial\phi}{\partial t} + \frac{1}{2}(\nabla\phi)^2 = 0 \text{ at } z = \eta, \tag{3.3a,b}$$

where $D/Dt = \partial_t + \mathbf{u}\cdot\nabla$ denotes a total derivative and $(\nabla\phi)^2 = (\nabla\phi)\cdot(\nabla\phi) = u^2+v^2+w^2$ the inner product.

3.2.2 A leading-order two-dimensional separation of scales model for deep water (review of chapter 2)

Solving potential flow subject to its non-linear boundary conditions (3.3a-3.3b) for a wave group, two small parameters can be defined: the steepness $\alpha = k_0|a_0|$, the product of a characteristic wave number k_0 and the magnitude of the amplitude $|a_0|$ of the surface elevation envelope $A(X)$, and a bandwidth parameter $\epsilon = 1/(k_0\sigma)$, a measure of the bandwidth of the spectrum with $\epsilon \to 0$ corresponding to a periodic wave and σ an estimate of the characteristic spatial scale of the group. In the deep-water limit ($d \to -\infty$) and a two-dimensional sea, the dimensional linear signal ($O(\alpha^1\epsilon^0)$) is given by:

$$\eta^{(1)} = A(X)e^{i(k_0x-\omega_0t)}, \quad \phi^{(1)} = B(X,Z)e^{k_0z}e^{i(k_0x-\omega_0t)}, \tag{3.4a,b}$$

where the real part is understood. The envelopes $A(X)$ (L) and $B(X,Z)$ (L^2T^{-1}) are a function of the slow scales:

$$X = \epsilon(x - c_{g,0}t), \quad Z = \epsilon z, \tag{3.5a,b}$$

where the linear dispersion equation $\omega_0^2 = gk_0$, $c_{g,0} = d\omega_0/dk_0 = \sqrt{g/k_0}/2$ and $A = i(k_0/\omega_0)B|_{z=0}$ ensure the linear (in α) parts of the boundary conditions (3.3a-3.3b) are satisfied.

The Stokes drift, defined as the net horizontal velocity of a Lagrangian particle due to the linear wave motion (3.1), and the Stokes transport, defined as the net depth-integrated horizontal Eulerian volume flux associated with linear wave motion (3.2), are given by:

$$u_{\text{SD}} = \omega_0 k_0 e^{2k_0 z}|A(X)|^2, \quad Q_{\text{ST}} = \frac{1}{2}\omega_0 |A(X)|^2. \tag{3.6a,b}$$

At leading order in ϵ, the return flow is forced by the divergence of the Stokes transport:

$$\frac{\partial \phi_{\text{RF}}}{\partial z} = \epsilon \frac{\partial Q_{\text{ST}}}{\partial X} \quad \text{at } z = 0. \tag{3.7}$$

The return flow is governed by Laplace $\nabla^2 \phi_{\text{RF}} = 0$, subject to the bottom boundary condition $w_{\text{RF}} \to 0$ as $z \to -\infty$ and the "forcing" equation (3.7), to give for the horizontal velocity:

$$u_{\text{RF}} = -\frac{\omega_0 |a_0|^2}{2\pi\sigma} \int_0^\infty \hat{k} f(\hat{k}) e^{\hat{k}\hat{z}} \cos(\hat{k}\hat{x}) d\hat{k}, \tag{3.8}$$

where the hats denote non-dimensional variables, $\hat{k} = k\sigma$, $\hat{z} = z/\sigma$, $\hat{x} = (x - c_{g,0}t)/\sigma$ defined as the horizontal coordinate centered around the middle of the wave group, and $f(\hat{k})$ is the normalized Fourier transform of the squared amplitude envelope:

$$f(\hat{k}) = \frac{\displaystyle\int_{-\infty}^{\infty} |A(x)|^2 e^{-ikx} dx}{\sigma |a_0|^2}. \tag{3.9}$$

For a Gaussian group $A = |a_0| \exp(-\hat{x}^2/2)$, $f(\hat{k}) = \sqrt{\pi} \exp(-\hat{k}^2/4)$. In the far-field ($|x - c_{g,0}t| \gg \sigma$, $|z| \gg \sigma$ or both) we can obtain a dipole approximation to the horizontal velocity field. For a Gaussian group, we have from (3.8) (see appendix D.1):

$$u_{\text{RF}} = \frac{1}{2\sqrt{\pi}} \frac{\omega_0 |a_0|^2}{\sigma} \frac{\hat{x}^2 - \hat{z}^2}{(\hat{x}^2 + \hat{z}^2)^2}. \tag{3.10}$$

At the centre of the group $\hat{x} = 0$ the horizontal velocity thus decays as $(z/\sigma)^{-2}$ with depth.

3.2.2.1 Lagrangian transport

The total Lagrangian velocity of a particle $\mathbf{u}_{\text{L}}$ is determined by the sum of its Stokes drift $\mathbf{u}_{\text{SD}}$, a Lagrangian phenomenon, and the Eulerian return flow field $\mathbf{u}_{\text{RF}}$ (Andrews and McIntyre

1978):

$$\underbrace{\mathbf{u}_{\mathrm{L}}}_{\text{Lagrangian}} = \underbrace{\mathbf{u}_{\mathrm{SD}}}_{\text{Stokes drift}} + \underbrace{\mathbf{u}_{\mathrm{RF}}}_{\text{Eulerian}} . \tag{3.11}$$

The net horizontal displacement by the Stokes drift (3.6) for a particle as a function of its initial vertical position z_0 and for a Gaussian group is given by:

$$\Delta x_{\mathrm{SD}}(z_0) = 2\sqrt{\pi}\sigma\alpha^2 e^{2k_0 z_0}. \tag{3.12}$$

The net horizontal transport by the return flow can be found by integrating the horizontal return flow velocity (3.8) with respect to time. For a wave group without dispersion we obtain from (3.8):

$$\Delta x_{\mathrm{RF}}(z_0) = -\frac{\alpha^2}{\pi k_0}\int_{-\infty}^{\infty}\int_{0}^{\infty} \hat{k} f(\hat{k}) e^{\hat{k}\hat{z}_0}\cos(\hat{k}\hat{t}) d\hat{k} d\hat{t}, \tag{3.13}$$

where the double integral on the right hand side is non-dimensional ($\hat{t} = c_{g,0}t/\sigma$) and only a function of the scaled initial particle depth $\hat{z}_0 = z_0/\sigma$. Explicitly, we have from numerical evaluation of the double integral for a particle located at $z_0 = 0$ and a Gaussian group $\Delta x_{\mathrm{RF}}(z_0 = 0) \approx -0.1134\alpha^2/k_0$. Comparing magnitudes, we thus have at the surface:

$$\Delta x_{\mathrm{L}}(z_0 = 0) \approx \sigma\alpha^2\big(2\sqrt{\pi} - 0.1134\epsilon\big). \tag{3.14}$$

For $\epsilon = 0.16$, a representative value obtained from fitting an idealized Gaussian spectrum to the peak of a Jonswap spectrum Gibbs and Taylor (2005), the contribution due to Stokes drift is a factor ~ 200 larger than the contribution due to the return flow, provided the sea is two-dimensional and the depth is large relative to both the length of the individual waves λ_0 and the length of the group σ.

3.2.2.2 The transition depth

The transition depth, below which Lagrangian particles are transported backwards by the return flow and above which such particles are transported forwards by Stokes drift, is defined by:

$$\Delta x_{\mathrm{L}}(z_0 = z_{\mathrm{T}}) = \Delta x_{\mathrm{SD}}(z_{\mathrm{T}}) + \Delta x_{\mathrm{RF}}(z_{\mathrm{T}}) = 0. \tag{3.15}$$

Ignoring the generally small effects of dispersion and making use of the fact that Stokes drift decays much faster with depth than the return flow for deep water, an approximate expression for the transition depth z_{T}^* can be obtained. This is achieved by finding the depth at which the net horizontal Stokes drift displacement (3.12) has decreased to the surface value ($z_0 = 0$) of the return flow displacement, which can be assumed not to decay over that same depth:

$$\Delta x_{\text{RF}}(z_0 = 0) + \Delta x_{\text{SD}}(z_0 = z^*_{\text{T,DRF}}) = 0, \tag{3.16}$$

which has the solution:

$$z^*_{\text{T,DRF}} \approx \frac{1}{2k_0}\big(-3.442 + \log(\epsilon)\big). \tag{3.17}$$

Provided the fluid is very deep ($d/\sigma \gg 1$), chapter 2 has shown that (3.17) provides a near perfect approximation to the transition depth for realistic bandwidths (using $\epsilon = 0.16$ as a representative value).

3.3 The effect of finite depth

It is evident from (3.8) that for the return flow not to feel the effect of finite depth, not only $k_0 d$ needs to be large, but so does $d/\sigma = \epsilon k_0 d$, which is one order in ϵ smaller than the former. Without taking the $d \to -\infty$ limit, the linear solution ($O(\alpha^1\epsilon^0)$) in (3.4) becomes:

$$\eta^{(1)} = A(X)e^{i(k_0 x - \omega_0 t)}, \quad \phi^{(1)} = B(X,Z)\frac{\cosh\left(k_0(z+d)\right)}{\cosh(k_0 d)}e^{i(k_0 x - \omega_0 t)}, \tag{3.18a,b}$$

where the slow scales are defined as in (3.5). From the linear ($O(\alpha^1\epsilon^0)$) free surface boundary conditions (3.3a-3.3b) we have $B = -igA/\omega_0$ and $\omega_0^2 = gk_0\tanh(k_0 d)$, the linear dispersion relationship. At next order in ϵ, the linear (in α) signals are defined such that the envelope travels at the group velocity $c_{g,0} = d\omega_0/dk_0$.

From the linear signal (3.18), leading-order expressions for the Stokes drift and the Stokes transport can be obtained:

$$u_{\text{SD}} = \frac{\omega_0 k_0}{2}\frac{\cosh(2k_0(d+z))}{\sinh^2(k_0 d)}|A(X)|^2, \quad Q_{\text{ST}} = \frac{\omega_0}{2\tanh(k_0 d)}|A(X)|^2. \tag{3.19a,b}$$

It is evident then from (3.19) and from figure 3.1, which shows the variation of the Stokes drift with depth for a number of different depths, that both the magnitude of the Stokes drift and that of the Stokes transport are larger for shallower depth, the latter equal in magnitude to the depth integral of the former.

At second-order in steepness, the free surface boundary conditions (3.3a-3.3b) can be

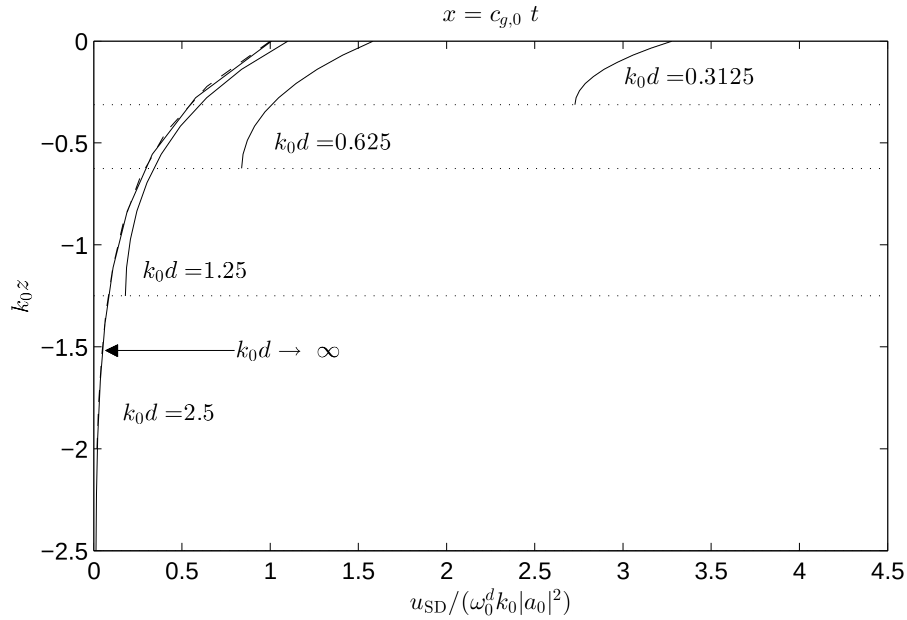

Figure 3.1: Depth decay of the Stokes drift (3.19a) for different values of the non-dimensional depth $k_0 d = \{\infty, 2.5, 1.25, 0.625, 0.3125\}$ ($d/\sigma = \{\infty, 0.4, 0.2, 0.1, 0.05\}$ for $\epsilon = 0.16$) for a Gaussian group. The asymptotic limit for infinite depth $k_0 d_0 \to \infty$ (3.6a) is denoted by a dashed line visually not distinguishable from $k_0 d = 2.5$ here. The values are correct for two-dimensional seas ((3.6a) and (3.19a)) as well as for three-dimensional seas ((3.33a) and (3.44a)) at the centre of the group ($y = 0$). To enable comparison, the wave number $\omega_0^d = \sqrt{g k_0}$ used in the scaling of the horizontal axis is the deep-water value, so not a function of depth.

combined to give a "forcing" equation for the Eulerian flow field at second order:

$$\Big(\frac{\partial}{\partial z} + \frac{1}{g}\frac{\partial^2}{\partial t^2}\Big)\phi^{(2)}_{\mathrm{RF}} = \overline{\underbrace{\nabla_{\mathrm{H}} \cdot \big(\mathbf{u}^{(1)}\eta^{(1)}\big)}_{\nabla_{\mathrm{H}}\cdot\mathbf{Q}_{\mathrm{ST}}} \underbrace{-\frac{1}{g}\frac{\partial}{\partial t}\Big(\frac{\partial^2\phi^{(1)}}{\partial t \partial z}\eta^{(1)} + \frac{1}{2}(\nabla\phi^{(1)})^2\Big)}_{\partial\eta^{(2)}/\partial t}} \text{ at } z = 0, \qquad (3.20)$$

where we have used $\partial_z w = -\partial_x u - \partial_y v$ from conservation of volume and $\nabla_{\mathrm{H}} = (\partial_x, \partial_y, 0)$. Equation (3.20) is referred to as the return flow forcing equation and constitutes the boundary condition subject to which the Laplace equation has to be solved to obtain the Eulerian flow at second order. Implicitly, we only include terms that contribute to the mean flow here. Hence the terms on the right hand side are averaged over the fast scales. The forcing consists of two terms: the divergence of the Stokes transport ($\nabla_{\mathrm{H}} \cdot \mathbf{Q}_{\mathrm{ST}}$) and the variation of the slowly varying set-down of the free surface associated with the group ($\partial\eta^{(2)}/\partial t$). We will refer to the mean flow driven by both these effects as the return flow.

It can be readily verified from the polarization relationships of the linear wave solutions ($O(\alpha^1\epsilon^0)$), showing the relative phases of the different linear components and included in appendix C for completeness, that only the first term of the mean-flow forcing equation

$(\nabla_{\text{H}} \cdot \mathbf{Q}_{\text{ST}})$ is non-zero at leading-order $(O(\alpha^2\epsilon^1))$ for deep water. In words, the mean set-down associated with the group is too small to non-negligibly affect the underlying mean flow field when the fluid is deep and we assume a slowly-varying wave group. The free surface then "appears rigid to the local mean flow", as observed by McIntyre (1981) (p. 339) based on taking a limit of the solutions by Longuet-Higgins and Stewart (1962). When the fluid is of finite depth, both terms contribute and we have (see appendix C) for the set-down $(O(\alpha^2\epsilon^0))$ and the return flow potential at leading order $(O(\alpha^2\epsilon^0))$:

$$\eta^{(2)} = -\frac{1}{2\sinh(2k_0d)}k_0A^2, \tag{3.21}$$

$$\left.\frac{\partial\phi_{\text{RF}}}{\partial z}\right|_{z=0} = \big(1+\delta_{\text{FD}}(k_0d)\big)\frac{\partial Q_{\text{ST}}}{\partial x}, \tag{3.22}$$

where Q_{ST} is given by (3.19b) and $\delta_{\text{FD}}(k_0d) = c_{g,0}\omega_0/(g\sinh(2k_0d))$. Explicitly, the term arising from the mean set-down $\delta_{\text{FD}}(k_0d)$ can be written as:

$$\delta_{\text{FD}}(k_0d) = \frac{k_0d\,\text{sech}^2(k_0d) + \tanh(k_0d)}{2\sinh(2k_0d)}, \tag{3.23}$$

where, to avoid confusion, we note that δ does not denote a Dirac delta function in this chapter. In the deep-water limit $k_0d \to \infty$, $\delta_{\text{FD}}(k_0d) \to 0$ and we recover the deep-water return flow forcing equation (3.7). In the limit $k_0d \to 0$, $\delta_{\text{FD}}(k_0d) \to 1/2$. The corresponding set-down for deep water is $\eta^{(2)} = -\epsilon k_0A^2/4$, one order higher in ϵ than (3.21).

Solving the boundary value problem subject to the bottom boundary condition and the new forcing equation (3.22), we obtain for the return flow:

$$u_{\text{RF}} = \frac{-\omega_0|a_0|^2(1+\delta_{\text{FD}}(k_0d))}{2\pi\sigma\tanh(k_0d)}\int_0^\infty \frac{\hat{k}f(\hat{k})\cosh(\hat{k}(\hat{z}+\hat{d}))}{\sinh(\hat{k}\hat{d})}\cos(\hat{k}\hat{x})d\hat{k}, \tag{3.24}$$

where $\hat{d} = d/\sigma$ is an additional non-dimensional parameter and $f(\hat{k})$ is defined as in (3.9). By taking the limit $d/\sigma \gg 1$ (and hence $k_0d \gg 1$), we recover the deep-water limit (3.8). With ϵ small, it is however possible for the water to be shallow with respect to the return flow which varies on the scale σ but of intermediate depth or even deep with respect to the individual waves that scale on $\lambda = 2\pi/k_0$ (the shallow-water limit $k_0d \to 0$ is considered in appendix E for completeness). In this limit ($\hat{d} = d/\sigma \to 0$), (3.24) reduces to a uniform flow:

$$u_{\text{RF}} = -\frac{\omega_0|A(X)|^2(1+\delta_{\text{FD}}(k_0d))}{2\tanh(k_0d)d}, \tag{3.25}$$

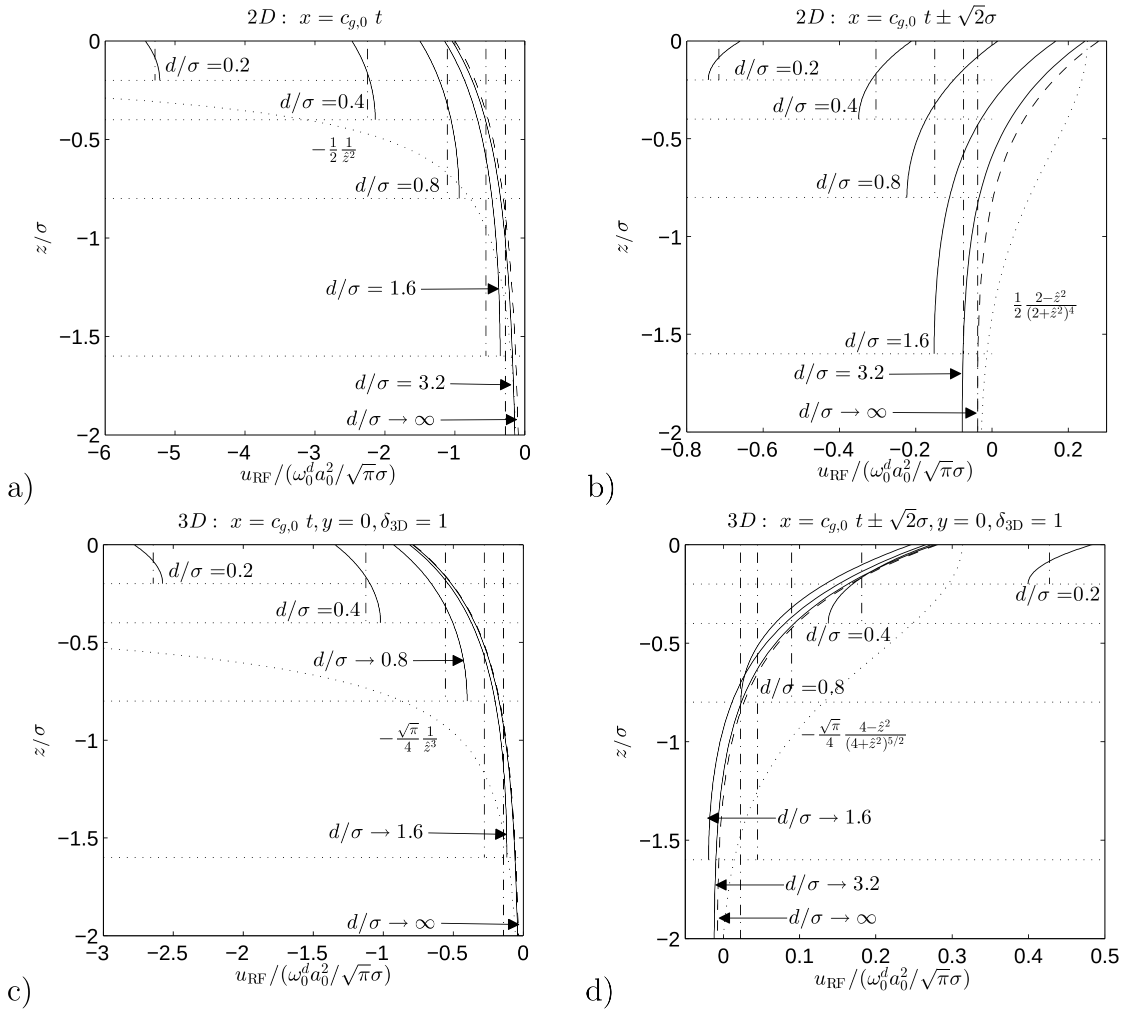

Figure 3.2: Depth decay of the return flow for (a,b) two-dimensional groups and (c,d) three-dimensional groups with equal group widths in both directions ($\sigma = \sigma_x = \sigma_y$) at the centre of the group (a,c) and at its edge (b,d). The different lines correspond to different depths $d/\sigma = \{\infty, 3.2, 1.6, 0.8, 0.4, 0.2\}$ ($k_0 d = \{\infty, 20, 10, 5, 2.5, 1.25\}$ for $\epsilon = 0.16$). The deep-water limit ($d/\sigma \to \infty$) is denoted by a dashed line and the shallow return flow limits ((3.25) and (3.46)) are denoted by dash-dotted lines.

for a general spectrum. Figure 3.2 compares the horizontal velocity (3.24) for different depths with the shallow return flow limit (3.25) at two different locations: at the centre of the group $x = c_{g,0}t$ and at the trailing and leading edge $x = c_{g,0}t \pm \sqrt{2}\sigma$.

3.3.1 Lagrangian transport

For the net horizontal displacement due to Stokes drift by a Gaussian group, we obtain from (3.19a) as a function of the initial vertical position of the particle z_0:

$$\Delta x_{SD}(z_0) = 2\sqrt{\pi}\alpha^2\sigma\delta_{SD}(k_0 d)\cosh(2k_0(d + z_0)), \tag{3.26}$$

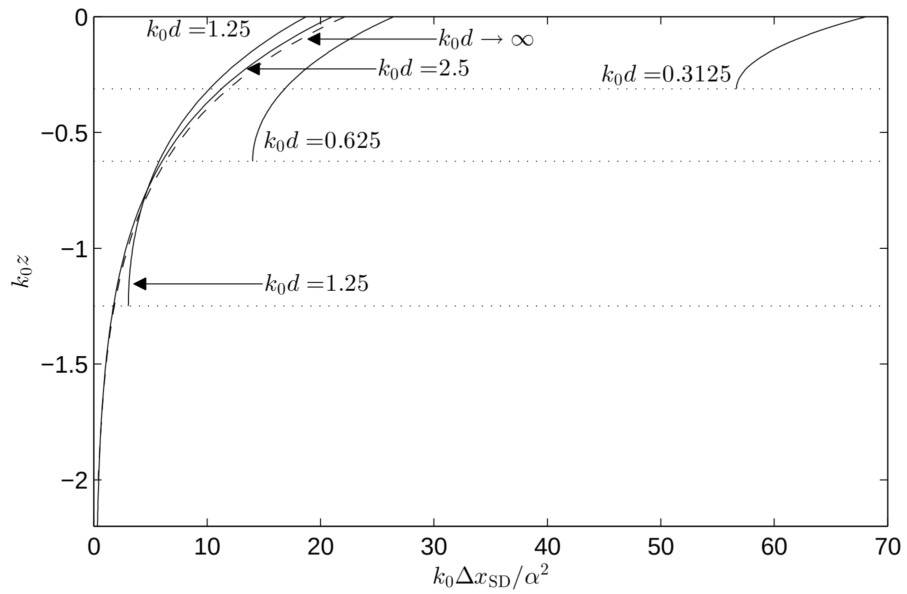

Figure 3.3: Depth decay of the net horizontal transport by Stokes drift (3.26) for different values of the non-dimensional depth $k_0d = \{\infty, 2.5, 1.25, 0.625, 0.3125\}$ ($d/\sigma = \{\infty, 0.4, 0.2, 0.1, 0.05\}$ for $\epsilon = 0.16$) for Gaussian groups. The asymptotic limit for infinite depth $k_0d_0 \to \infty$ (3.12) is denoted by a dashed line. The values are correct for two-dimensional seas ((3.12) and (3.26)) as well as for three-dimensional seas ((3.39) and (3.47)) at the centre of the group ($y = 0$).

where $\delta_{\text{SD}}(k_0d) = \coth(k_0d)/(2k_0d + \sinh(2k_0d))$, so that $\delta_{\text{SD}}(k_0d)\cosh(2k_0(d + z)) \to \exp(2k_0z)$ as $k_0d \to \infty$ and we recover the deep-water limit (3.12). Figure 3.3 examines the depth decay of the net displacement by Stokes drift for different values of k_0d. The overall form is of course very similar to the Stokes drift velocity profiles in figure 3.1.

From (3.24) we have for the net horizontal displacement by the return flow as a function of the initial vertical position of the particle z_0:

$$\Delta x_{\text{RF}}(z_0) = \frac{-\alpha^2\delta_{\text{RF}}(k_0d)}{\pi k_0} \int_{-\infty}^{\infty}\int_{0}^{\infty} \frac{\hat{k}f(\hat{k})\cosh(\hat{k}(\hat{z}_0 + \hat{d}))}{\sinh(\hat{k}\hat{d})} \cos(\hat{k}\hat{t})d\hat{k}d\hat{t}, \tag{3.27}$$

where $\delta_{\text{RF}}(k_0d) = \delta_{\text{SD}}(k_0d)(1 + \delta_{\text{FD}}(k_0d))\sinh(2k_0d)$ so that $\delta_{\text{RF}}(k_0d) \to 1$ as $k_0d \to \infty$ and we recover (3.13). Explicitly, we have for $\delta_{\text{RF}}(k_0d)$:

$$\delta_{\text{RF}}(k_0d) = \delta_{\text{SD}}(k_0d)(1 + \delta_{\text{FD}}(k_0d))\sinh(2k_0d) = \frac{2k_0d + 3\sinh(2k_0d) + \sinh(4k_0d)}{2\sinh^2(k_0d)\big(2k_0d + \sinh(2k_0d)\big)}. \tag{3.28}$$

If the depth is sufficiently small ($d/\sigma \to 0$), (3.27) reduces to:

$$\Delta x_{\text{RF}} = -2\sqrt{\pi}\alpha^2\sigma\frac{\delta_{\text{RF}}(k_0d)}{2k_0d}. \tag{3.29}$$

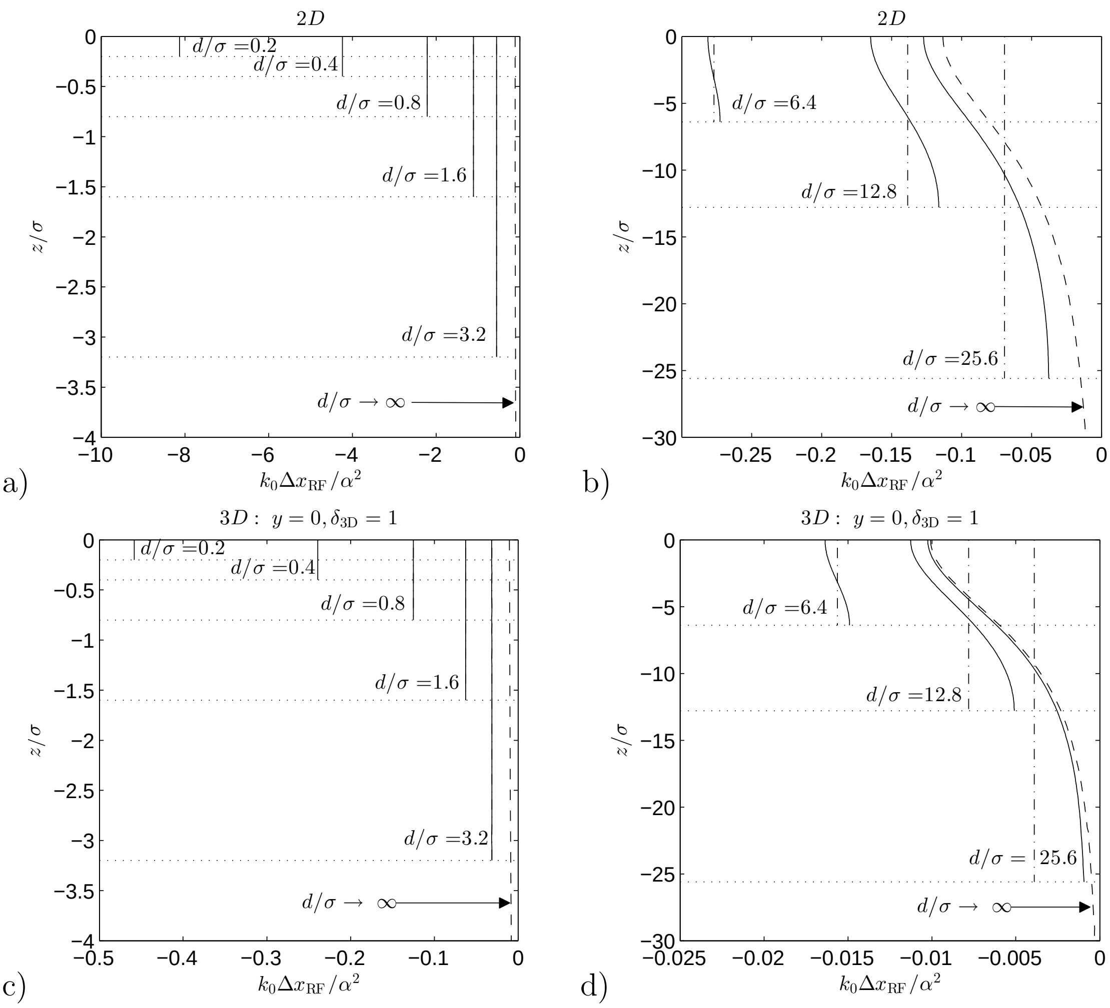

Figure 3.4: Depth decay of the net horizontal transport by the return flow for different depths for (a,b) two-dimensional groups and (c,d) three-dimensional groups with equal group widths in both directions ($\sigma = \sigma_x = \sigma_y$). The panels on the left show intermediate values of depth $d/\sigma = \{3.2, 1.6, 0.8, 0.4, 0.2\}$ ($k_0 d = \{20, 10, 5, 2.5, 1.25\}$ for $\epsilon = 0.16$) and the panels on the right show very large depths $d/\sigma = \{\infty, 25.6, 12.8, 6.4\}$ ($k_0 d = \{\infty, 160, 80, 40\}$ for $\epsilon = 0.16$). Also shown (dash-dotted lines) is the shallow return flow limit (3.29). The difference is only visible for really large depths (right panels).

We note that in this shallow water regime the net displacement is a (linear) function of σ, whereas for deep water there is no dependence on σ apart from through the dependence on depth $\hat{z} = z/\sigma$ (cf. (3.13)). In other words, unlike in the deep-water case, the net displacement by Stokes drift (3.26) and by the return flow (3.29) scale equivalently, namely with σ. The net displacement is evidently no longer a function of the initial vertical particle position. Figure 3.4 shows the variation of the net horizontal displacement (3.27) by the return flow as a function as a function of depth. Comparison with the shallow return flow limit (3.29) confirms that the return flow can be approximated as a shallow uniform flow for all except for extremely large depths.

3.3.2 The transition depth

Although it is not possible to develop an explicit expression for the transition depth for general depth $k_0 d$, the expression for the net transport in the limit in which the water is shallow with respect to the return flow (3.29) but not with respect to the individual waves (3.27) gives:

$$\Delta x_{\mathrm{L}} = 2\sqrt{\pi}\alpha^2\sigma\delta_{\mathrm{SD}}(k_0 d)\Big(\cosh(2k_0(z_0+d)) - \frac{\sinh(2k_0 d)}{2k_0 d}\big(1+\delta_{\mathrm{FD}}(k_0 d)\big)\Big). \tag{3.30}$$

We can obtain a corresponding estimate of the transition depth by setting $\Delta x_{\mathrm{L}} = 0$:

$$z^*_{\mathrm{T,SRF}} = \frac{1}{2k_0}\cosh^{-1}\Big(\frac{\sinh(2k_0 d)}{2k_0 d}\big(1+\delta_{\mathrm{FD}}(k_0 d)\big)\Big) - d. \tag{3.31}$$

Figure 3.5 compares this approximate transition depth (3.31) to the implicit solution of $\Delta x_{\mathrm{L}}(z_{\mathrm{T}}) = 0$ showing its large domain validity.

Furthermore, it is evident from (3.22) that for sufficiently small depth, when both the Stokes drift and the return flow start start to behave like a uniform flow with depth (see appendix E), the return flow becomes larger than the Stokes drift. Setting $z^*_{\mathrm{T,SRF}} = 0$, equation (3.31) can be solved implicitly to give $k_0 d = 0.53$ independently of the spectrum as an approximate criterion for $\Delta x_{\mathrm{SD}} = -\Delta x_{\mathrm{RF}}$ at $z_0 = 0$. The transition depth in figure 3.5 is thus only shown for $k_0 d > 0.53$.

3.4 The effect of directionality

Realistic sea states are directionally spread and comparison with field measurements by Donelan et al. (1985) and Ewans (1998) to a wrapped normal distribution gives a rms spreading parameter of $15° - 30°$ (Gibbs and Taylor 2005). Assuming the spreading angle is small, we assume the rms spreading parameter (in radians) corresponds directly to the ratio of the two horizontal scales of the group σ_x and σ_y. We then have $\delta_{\mathrm{3D}} \equiv \sigma_x/\sigma_y = 1.6 - 3.3$. In order to make analytical progress, we assume the effect of directionality is sufficiently small for it to only affect the slow dynamics. Defining two small parameters $\epsilon_x = 1/(k_0\sigma_x)$ and $\epsilon_y = 1/(k_0\sigma_y)$, where k_0 remains the wave number of the fast waves in the x-direction, we assume $O(\epsilon_x) = O(\epsilon_y)$, but not necessarily $\epsilon_x = \epsilon_y$. For rms spreading parameters towards the lower end of the range $15° - 30°$ this assumption is evidently supported by the data. We have $\epsilon_y = 0.26 - 0.52$, setting $\epsilon_x = 0.16$. In words, the group is typically somewhat longer than it is wide, but, more importantly, the length scales are

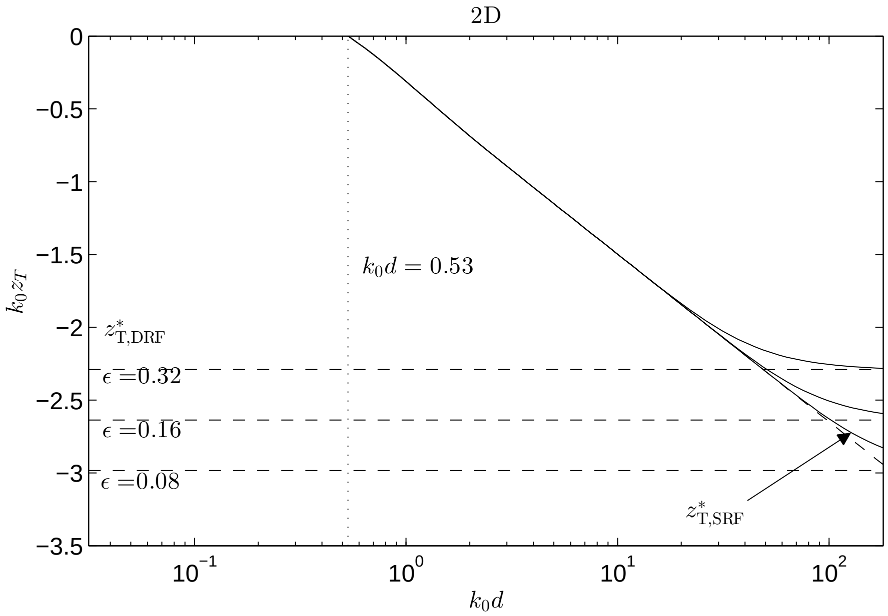

Figure 3.5: Transition depth for two-dimensional seas comparing the approximate transition depth for deep water ($z^*_{\mathrm{T,DRF}}$) (3.17) and the approximate transition depth for a shallow return flow ($z^*_{\mathrm{T,SRF}}$) (3.31) to the implicit solution of $\Delta x_{\mathrm{L}}(z_{\mathrm{T}}) = 0$ for three values of $\epsilon = 1/(k_0\sigma)$.

of the same order of magnitude. To study the effect of introducing a third dimension in the simplest possible way, §3.4.1 and §3.4.2 initially proceed under the assumption that $\sigma_y = \sigma_x$ (and $\delta_{\mathrm{3D}} = 1$). §3.4.3 then relaxes this assumption and examines different degrees of spreading within the reported range. Corresponding solutions for $\delta_{\mathrm{3D}} \neq 1$ are given in appendix F.

3.4.1 Infinite depth ($\sigma_y = \sigma_x$)

In the deep-water limit ($d \to \infty$) and a three-dimensional sea (x, y, z), the linear signal ($O(\alpha^1\epsilon^0)$) is given by:

$$\eta^{(1)} = A(X,Y)e^{i(k_0x-\omega_0t)}, \quad \phi^{(1)} = B(X,Y,Z)e^{k_0z}e^{i(k_0x-\omega_0t)}, \tag{3.32a,b}$$

where we have defined an additional slow scale $Y = \epsilon_y y$ with $\epsilon_y = 1/(k_0\sigma_y)$ and we have assumed the fast carrier wave travels in the x-direction without loss of generality. For uni-directional seas we have $\delta_{\mathrm{3D}} = 0$ ($\sigma_y \to \infty$) and we return to the two-dimensional solutions presented above. To simplify the analysis, we start by considering the case of a group that is as wide as it is long: $\sigma \equiv \sigma_x = \sigma_y$, $\delta_{\mathrm{3D}} = 1$, and thus $\epsilon = \epsilon_x = \epsilon_y$. §3.4.3 considers more realistic directional distributions.

We have for the Stokes drift and the Stokes transport per unit width at leading order:

$$u_{\text{SD}} = \omega_0 k_0 e^{2k_0 z}|A(X,Y)|^2, \quad Q_{\text{ST}} = \frac{1}{2}\omega_0 |A(X,Y)|^2, \tag{3.33}$$

where the only difference with the two-dimensional result (3.6) is the additional dependence on the slow scale Y. We note that at leading order there is only a Stokes drift and transport in the x-direction. Although the Stokes drift and Stokes transport are unaffected at leading order in ϵ ($v^{(1)} = \partial\phi^{(1)}/\partial y = 0$ at $O(\epsilon^0)$), the return flow is affected at leading order by the introduction of the third dimension. The "forcing" equation (3.7) remains unchanged, but the governing equation has an additional dimension and we thus have for the return flow:

$$u_{\text{RF}} = -\frac{\omega_0|a_0|^2}{8\pi^2\sigma}\int_{-\infty}^{\infty}\int_{-\infty}^{\infty}\frac{\hat{k}^2 f(\hat{k},\hat{l})}{\sqrt{\hat{k}^2+\hat{l}^2}}e^{\sqrt{\hat{k}^2+\hat{l}^2}\hat{z}+i(\hat{k}\hat{x}+\hat{l}\hat{y})}d\hat{k}d\hat{l}, \tag{3.34}$$

$$v_{\text{RF}} = -\frac{\omega_0|a_0|^2}{8\pi^2\sigma}\int_{-\infty}^{\infty}\int_{-\infty}^{\infty}\frac{\hat{k}\hat{l} f(\hat{k},\hat{l})}{\sqrt{\hat{k}^2+\hat{l}^2}}e^{\sqrt{\hat{k}^2+\hat{l}^2}\hat{z}+i(\hat{k}\hat{x}+\hat{l}\hat{y})}d\hat{k}d\hat{l}, \tag{3.35}$$

$$w_{\text{RF}} = \frac{\omega_0|a_0|^2}{8\pi^2\sigma}\int_{-\infty}^{\infty}\int_{-\infty}^{\infty} i\hat{k} f(\hat{k},\hat{l})e^{\sqrt{\hat{k}^2+\hat{l}^2}\hat{z}+i(\hat{k}\hat{x}+\hat{l}\hat{y})}d\hat{k}d\hat{l}, \tag{3.36}$$

where $\hat{x} = (x - c_{g,0}t)/\sigma_x$, $\hat{y} = y/\sigma_y$, $\hat{z} = z/\sigma_x$ and $f(\hat{k},\hat{l})$ is now a bivariate function defined as:

$$f(\hat{k},\hat{l}) = \frac{\displaystyle\int_{-\infty}^{\infty}\int_{-\infty}^{\infty}|A(x,y)|^2 e^{-i(kx+ly)}dxdy}{\sigma^2|a_0|^2}, \tag{3.37}$$

where $\hat{k} = k\sigma$ and $\hat{l} = l\sigma$. We have $f(\hat{k},\hat{l}) = \pi\exp(-(\hat{k}^2+\hat{l}^2)/4)$ for a bivariate Gaussian group $A(x,y) = a_0\exp(-(\hat{x}^2+\hat{y}^2)/2)$. Obviously, the third dimension generally reduces the magnitude of the return flow (see figure 3.2), as the mass imbalance caused by the Stokes transport can be remedied by a return flow in three dimensions rather than one constrained to a plane.

The far-field behaviour of the horizontal velocity for such a group (see appendix D.2) is given by a dipole solution in three dimensions:

$$u_{\text{RF}} = \frac{\omega_0|a_0|^2}{4\sigma}\frac{2\hat{x}^2-\hat{y}^2-\hat{z}^2}{(\hat{x}^2+\hat{y}^2+\hat{z}^2)^{5/2}}. \tag{3.38}$$

At the centre of the group ($\hat{x} = 0$, $\hat{y} = 0$), the horizontal velocity decays with depth as $\hat{z}^{-3}$, evidently a faster rate of decay with depth compared to the two-dimensional case ($\hat{z}^{-2}$). At the surface ($\hat{z} = 0$) and at the centre of the group ($\hat{x} = 0$), the far-field decay with the span-wise coordinate y is equivalent to the decay with depth: $\hat{y}^{-3}$. It is evident from figure 3.6 that the horizontal velocity generally decays faster with depth for the

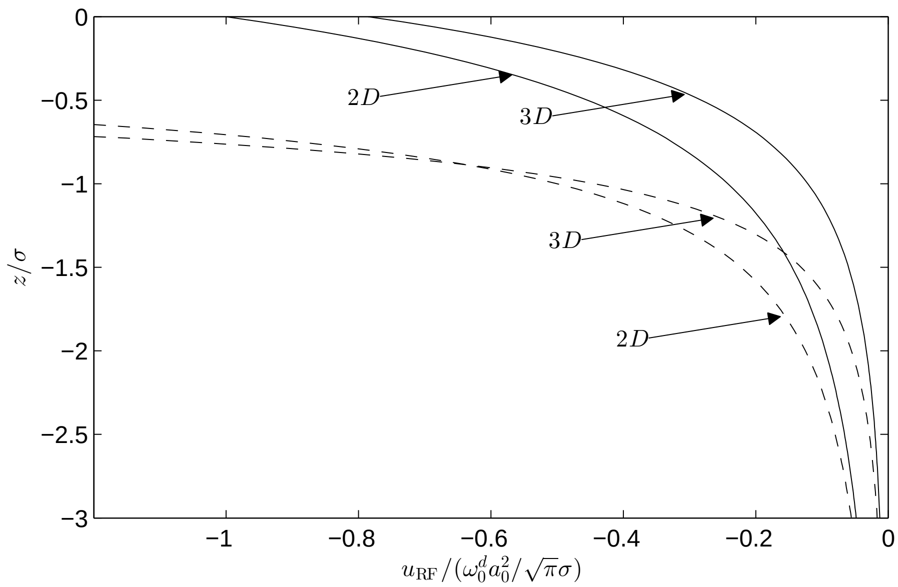

Figure 3.6: Far-field depth decay of the return flow (dashed lines) and the full deep-water solutions for two- and three-dimensional seas (continuous lines) with $\sigma \equiv \sigma_x = \sigma_y$ at the centre of the group ($x = 0$, $y = 0$) and for $\epsilon = 0.16$.

three-dimensional case and is also generally smaller in magnitude.

3.4.1.1 Lagrangian transport

From (3.33) we can obtain for the total horizontal Lagrangian transport by the Stokes drift alone, as a function of the initial particle coordinates y_0 and z_0:

$$\Delta x_{\mathrm{SD}}(y_0, z_0) = 2\sqrt{\pi}\sigma\alpha^2 e^{2k_0 z_0} e^{-(y_0/\sigma)^2}, \tag{3.39}$$

where the only difference with the analogous two-dimensional result (3.12) is the additional dependence on transverse (across group) direction y, given here for a Gaussian group. From (3.34), we obtain for the net horizontal transport by the return flow as a function of the initial particle coordinates y_0 and z_0:

$$\Delta x_{\mathrm{RF}}(y_0, z_0) = -\frac{\alpha^2}{4\pi^2 k_0}\int_{-\infty}^{\infty}\int_{-\infty}^{\infty}\int_{-\infty}^{\infty} \frac{\hat{k}^2 f(\hat{k},\hat{l})}{\sqrt{\hat{k}^2+\hat{l}^2}} e^{\sqrt{\hat{k}^2+\hat{l}^2}\hat{z}_0 + i(\hat{k}\hat{x}+\hat{l}\hat{y}_0)} d\hat{k}\,d\hat{l}\,d\hat{x}. \tag{3.40}$$

At the still water level ($z_0 = 0$) and at the centre of the group ($y_0 = 0$), we obtain from numerical integration of (3.40): $\Delta x_{\mathrm{RF}} \approx -0.0101\alpha^2/k_0$, approximately a factor of 11.3 smaller than the two-dimensional case (cf. $\Delta x_{\mathrm{RF}} \approx -0.1134\alpha^2/k_0$ for 2D) thus illustrating the strong weakening effect of three-dimensionality on the return flow.

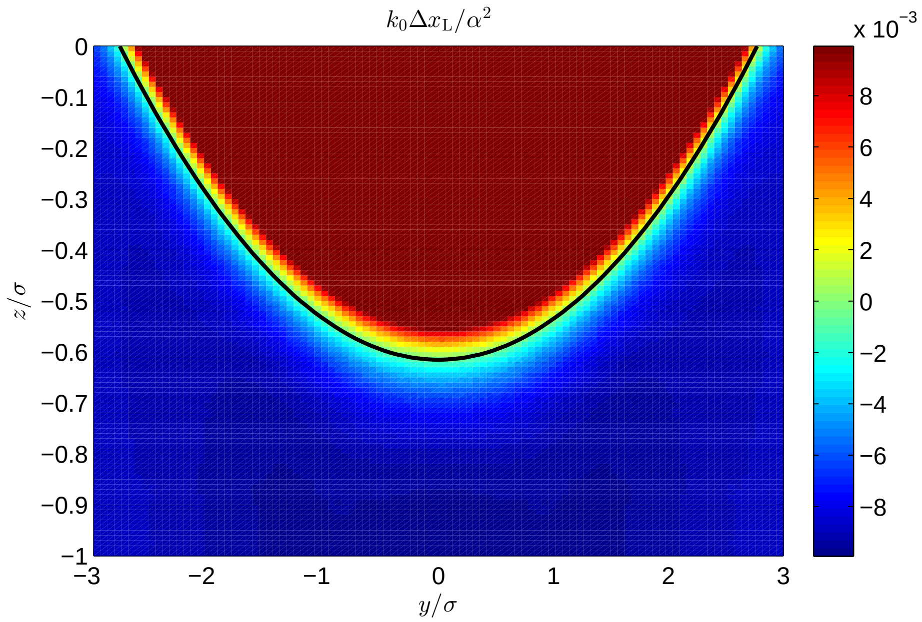

Figure 3.7: Net displacement by a three-dimensional wave group in infinitely deep water with $\sigma \equiv \sigma_x = \sigma_y$ for $\epsilon = 0.16$ showing the approximate transition curve (3.41) (black line) for infinitely deep water. Note that the colour scale saturates for positive Δx_L.

3.4.1.2 The transition depth and width

Upon introducing a third dimension, one length scale, i.e. the transition depth, is no longer sufficient to sufficient to map out the transition between forward transport by Stokes drift and backward transport by the return flow. Assuming that the return flow varies much more slowly spatially than the Stokes drift, an assumption which was shown to be valid for the transition depth of two-dimensional seas, we obtain a parabolic relationship for the transition curve $\Delta x_{\mathrm{L}} \approx \Delta x_{\mathrm{SD}}(y_0^*, z_0^*) + \Delta x_{\mathrm{RF}}(0,0) = 0$:

$$k_0 z_0^* - \frac{1}{2}\epsilon^2 (k_0 y_0^*)^2 = \frac{1}{2}\log(\epsilon) - 2.93, \tag{3.41}$$

which is illustrated in figure 3.7. Comparing to the full (y, z) field of Δx_{L} without making this assumption finds excellent agreement. We define the transition depth and the transition width as intersections with the z-axis and the x-axis, respectively:

$$z^*_{\mathrm{T,DRF,3D}} = \frac{1}{2k_0}\Big(\log(\epsilon) - 5.86\Big), \quad y^*_{\mathrm{T,DRF,3D}} = \pm\sigma\sqrt{5.86 - \log(\epsilon)}. \qquad (3.42\mathrm{a,b})$$

Figure 3.8 compares these approximate length scales to the full solutions of $\Delta x_{\mathrm{L}} = 0$, obtained implicitly, demonstrating near perfect agreement for a broad range of bandwidths similar to the results in chapter 2.

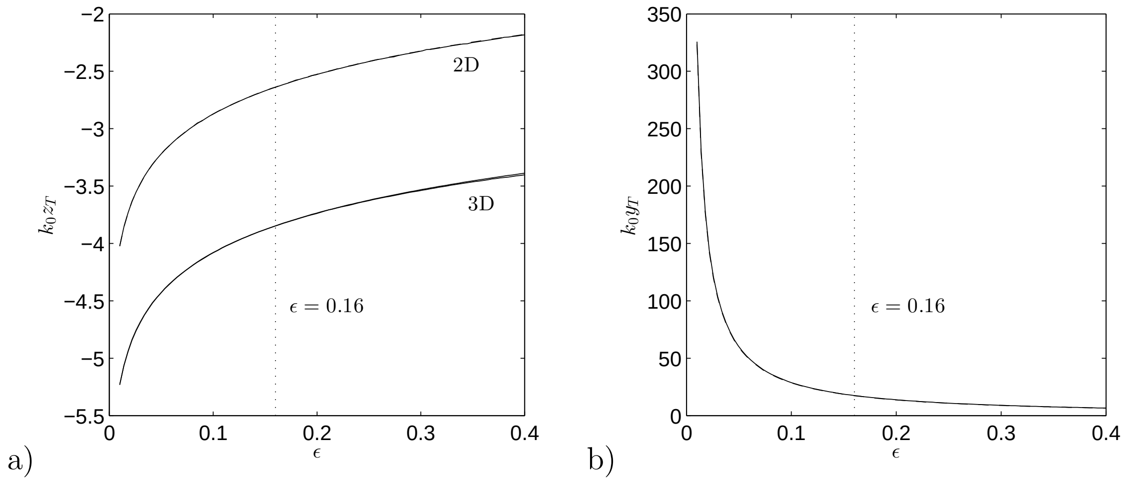

Figure 3.8: Approximate deep return flow transition depth (a) $z^*_{\mathrm{T,DRF,3D}}$ and width (b) $y^*_{\mathrm{T,DRF,3D}}$ (3.42) (dashed lines) compared to the full solutions (continuous lines) for infinite depth and in three-dimensional seas ($\sigma_x = \sigma_x$, $\delta_{\mathrm{3D}} = 1$). Note the full solutions are indistinguishable from the approximate solutions.

3.4.2 Finite depth ($\sigma_y = \sigma_x$)

Combining the effects of finite depth (§3.3) and that of adding the third dimension (§3.4.1), gives for the linear signal ($O(\alpha^1\epsilon^0)$):

$$\eta^{(1)} = A(X,Y)e^{i(k_0x-\omega_0t)}, \quad \phi^{(1)} = B(X,Y,Z)\frac{\cosh\left(k_0(z+d)\right)}{\cosh(k_0d)}e^{i(k_0x-\omega_0t)}, \qquad \text{(3.43a,b)}$$

where the slow scales are defined as in (3.5) and $Y = \epsilon_y y$ with $\epsilon_y \equiv 1/(k_0\sigma_y) = \epsilon_x = \epsilon$ as in §3.4.1. From the linear (in α) free surface boundary conditions (3.3) we have $B = -igA/\omega_0$ and $\omega_0^2 = gk_0\tanh(k_0d)$, the linear dispersion relationship.

From the linear signal (3.43), expressions for the Stokes drift and the Stokes transport can be obtained:

$$u_{\mathrm{SD}} = \frac{\omega_0k_0}{2}\frac{\cosh(2k_0(d+z))}{\sinh^2(k_0d)}|A(X,Y)|^2, \quad Q_{\mathrm{ST}} = \frac{\omega_0}{2\tanh(k_0d)}|A(X,Y)|^2. \qquad \text{(3.44a,b)}$$

where the only difference with their two-dimensional analogues is an additional dependence on y. The leading-order Stokes drift and Stokes transport are only non-zero in the x-direction. The return flow is given by:

$$u_{\mathrm{RF}} = -\frac{\omega_0|a_0|^2(1+\delta_{\mathrm{FD}}(k_0d))}{8\pi^2\tanh(k_0d)\sigma}\int_{-\infty}^{\infty}\int_{-\infty}^{\infty}\frac{\hat{k}^2f(\hat{k},\hat{l})}{\sqrt{\hat{k}^2+\hat{l}^2}}\frac{\cosh(\sqrt{\hat{k}^2+\hat{l}^2}(\hat{z}+\hat{d}))}{\sinh(\sqrt{\hat{k}^2+\hat{l}^2}\hat{d})}e^{i(\hat{k}\hat{x}+\hat{l}\hat{y})}d\hat{k}d\hat{l}, \qquad \text{(3.45)}$$

where $\hat{k} = k\sigma$, $\hat{l} = l\sigma$, $\hat{x} = x/\sigma$, $\hat{y} = y/\sigma$, $\hat{z} = z/\sigma$, $\hat{d} = d/\sigma$, $\delta_{\mathrm{FD}}(k_0 d)$ defined in (3.23) and $f(\hat{k}, \hat{l})$ in (3.37). Taking the limit $d/\sigma \to 0$, we obtain a flow that is uniform with depth but varies spatially according to:

$$u_{\mathrm{RF}} = -\frac{\omega_0 |a_0|^2 (1 + \delta_{\mathrm{FD}}(k_0 d))}{8\pi^2 \tanh(k_0 d) d} \int_{-\infty}^{\infty} \int_{-\infty}^{\infty} \frac{\hat{k}^2 f(\hat{k}, \hat{l})}{\hat{k}^2 + \hat{l}^2} e^{i(\hat{k}\hat{x} + \hat{l}\hat{y})} d\hat{k} d\hat{l}. \tag{3.46}$$

3.4.2.1 Lagrangian transport

The net horizontal transport by Stokes drift alone can be found from integrating (3.44a) with respect to time for a Gaussian group. As a function of the initial particle coordinates y_0 and z_0, we obtain:

$$\Delta x_{\mathrm{SD}}(y_0, z_0) = 2\sqrt{\pi}\alpha^2 \sigma \delta_{\mathrm{SD}}(k_0 d) \cosh(2k_0(d + z_0)) \exp(-(y_0/\sigma)^2), \tag{3.47}$$

where $\delta_{\mathrm{SD}}(k_0 d) = \coth(k_0 d)/(2k_0 d + \sinh(2k_0 d))$. The only difference with the two-dimensional solution (3.26) is the additional dependence on $\hat{y}_0 = y_0/\sigma$. Similarly, the net displacement by the return flow is given by:

$$\Delta x_{\mathrm{RF}}(y_0, z_0) = -\frac{\alpha^2 \delta_{\mathrm{RF}}(k_0 d)}{4\pi^2 k_0} \int_{-\infty}^{\infty} \int_{-\infty}^{\infty} \int_{-\infty}^{\infty} \frac{\hat{k}^2 f(\hat{k}, \hat{l})}{\sqrt{\hat{k}^2 + \hat{l}^2}} \frac{\cosh(\sqrt{\hat{k}^2 + \hat{l}^2}(\hat{z}_0 + \hat{d}))}{\sinh(\sqrt{\hat{k}^2 + \hat{l}^2}\hat{d})} e^{i(\hat{k}\hat{x} + \hat{l}\hat{y}_0)} d\hat{k} d\hat{l} d\hat{x}, \tag{3.48}$$

with $\delta_{\mathrm{RF}}(k_0 d) = \delta_{\mathrm{SD}}(k_0 d) \sinh(2k_0 d)(1 + \delta_{\mathrm{FD}}(k_0 d))$ as before. We consider the shallow-water limit $d/\sigma \to 0$ and obtain from (3.48):

$$\Delta x_{\mathrm{RF}}(y_0) = -\frac{\alpha^2 \sigma}{4\pi^2} \frac{\delta_{\mathrm{RF}}(k_0 d)}{k_0 d} \int_{-\infty}^{\infty} \int_{-\infty}^{\infty} \int_{-\infty}^{\infty} \frac{\hat{k}^2 f(\hat{k}, \hat{l})}{\hat{k}^2 + \hat{l}^2} e^{i(\hat{k}\hat{x} + \hat{l}\hat{y}_0)} d\hat{k} d\hat{l} d\hat{x}, \tag{3.49}$$

where we note that the net transport by the return flow is constant with depth, but remains a function of the transverse coordinate y_0. Figure 3.4 shows the variation with depth of the net displacement by the return flow for different depths at the centre of the group $y = 0$, whereas figure 3.9 examines its variation with the transverse coordinate y at the still water level $z = 0$. It is evident from these figures that the shallow return flow approximation (3.49) is valid except for extremely large water depths ($k_0 d \gtrsim 20$ for $\epsilon = 0.16$).

3.4.2.2 The transition depth and width

As before, we can obtain the following approximate relationship for the transition curve: $\Delta x_{\mathrm{L}} \approx \Delta x_{\mathrm{SD}}(y_0^*, z_0^*) + \Delta x_{\mathrm{RF}}(0, 0) = 0$ based on the shallow return flow limit (3.49).

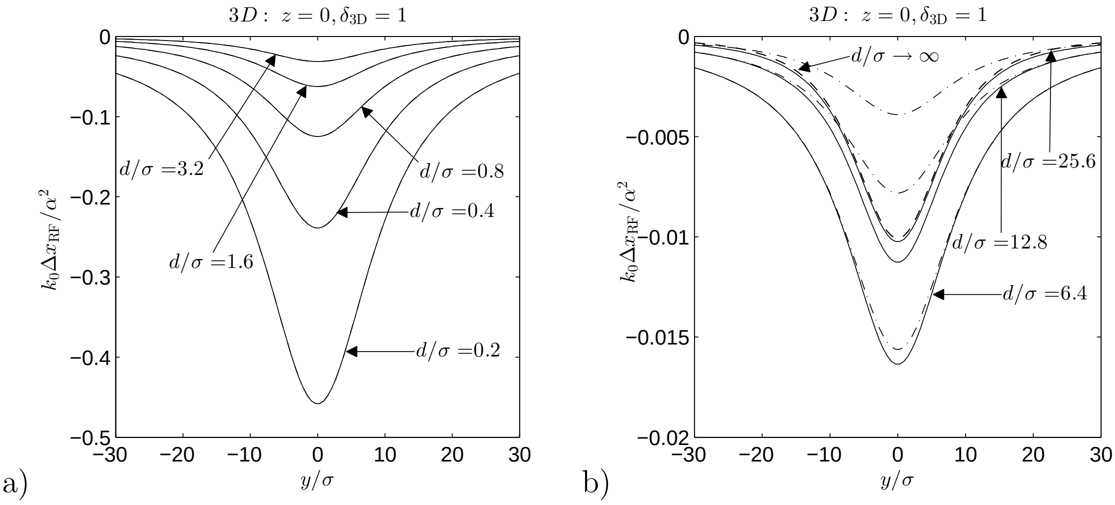

Figure 3.9: Variation of the net horizontal transport by the return flow in the vertical plane orthogonal to the direction of propagation for different depths. The panel on the left shows intermediate values of depth $d/\sigma = \{3.2, 1.6, 0.8, 0.4, 0.2\}$ ($k_0d = \{20, 10, 5, 2.5, 1.25\}$ for $\epsilon = 0.16$) and the panel on the right shows very large depths $d/\sigma = \{\infty, 25.6, 12.8, 6.4\}$ ($k_0d = \{\infty, 160, 80, 40\}$ for $\epsilon = 0.16$). Also shown (dash-dotted lines) is the shallow return flow limit (3.29). The difference is only visible for really large depths (right panels).

Explicitly, this can be rewritten as:

$$z_0^* = \frac{1}{2k_0}\left(\cosh^{-1}\left(C_{\text{SRF,3D}}(\delta_{\text{3D}}=1)\frac{\sinh(2k_0d)(1+\delta_{\text{FD}}(k_0d))}{2k_0d}e^{(y_0^*/\sigma)^2}\right)-d\right), \tag{3.50}$$

where the non-dimensional constant c is given by:

$$C_{\text{SRF,3D}}(\delta_{\text{3D}}=1) = \frac{1}{4\pi^{5/2}}\int_{-\infty}^{\infty}\int_{-\infty}^{\infty}\int_{-\infty}^{\infty}\frac{\hat{k}^2 f(\hat{k},\hat{l})}{\hat{k}^2+\hat{l}^2}e^{i(\hat{k}\hat{x}+\hat{l}\hat{y})}d\hat{k}d\hat{l}d\hat{x} \approx 0.056, \tag{3.51}$$

with the second approximate equality holding for a Gaussian group with $\sigma_x = \sigma_y$.

Figure 3.10 illustrates the topology of the transition curve for different depths comparing the finite depth solutions for the net Lagrangian transport Δx_{L} with the approximate transition curve (3.50). It is evident from figure 3.10 that the transition "curve" is no longer a continuous curve when finite depth effects are considered. In fact, for shallow enough depths and sufficiently spread groups the Stokes drift dominates the return flow at all depths in terms of its net horizontal transport underneath the centre of the group. For the case $\delta_{\text{3D}} = 1$ considered here, this depth criterion corresponds to $k_0d \approx 2.6$ (from $\sinh(2k_0d)(1+\delta_{\text{3D}})/(2k_0d) = 1/C_{\text{SRF,3D}}(\delta_{\text{3D}} = 1)$). The separation of physical domains that is observed for deep water, in which the Stokes drift dominates near the surface and the return flow at depth, is transformed for shallow water provided the group

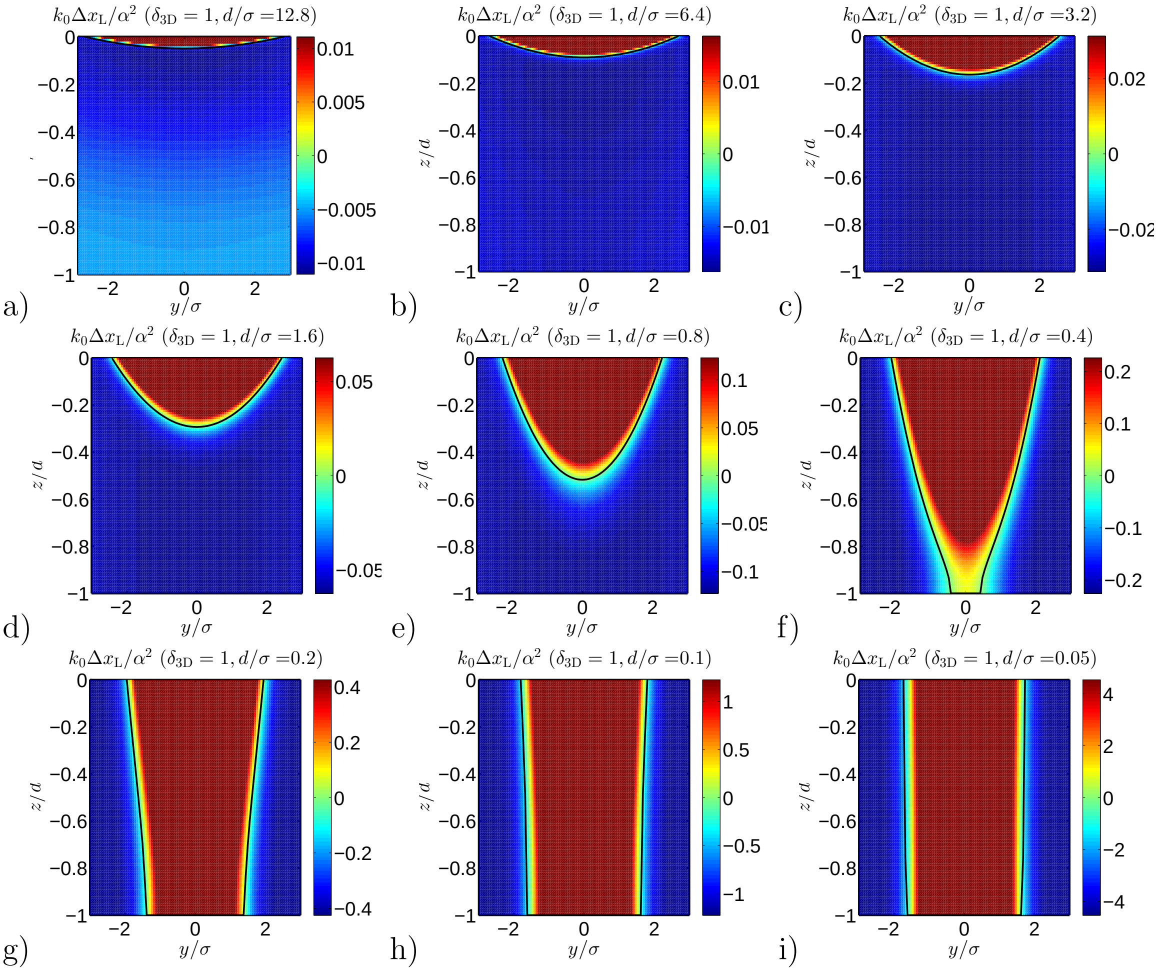

Figure 3.10: Net horizontal Lagrangian displacement by a three-dimensional wave group with $\sigma \equiv \sigma_x = \sigma_y$ for $\epsilon = 0.16$ and different values for depth $d/\sigma = \{12.8, 6.4, 3.2, 1.6, 0.8, 0.4, 0.2, 0.1, 0.05\}$ ($k_0 d = \{80, 40, 20, 10, 5, 2.5, 1.25, 0.625, 0.3125\}$ for $\epsilon = 0.16$) showing the approximate transition curve (3.50) (black line). Note that the colour scale saturates for positive Δx_L.

has some directional spreading. In that case, the Stokes drift is dominant everywhere underneath the group ($|y/\sigma| \lesssim 2$) and the return flow dominates everywhere else ($|y/\sigma| \gtrsim 2$). Although we no longer have a parabola, we still define the vertical and horizontal scales of the transition curve as $z^*_{\mathrm{T,SRF,3D}} \equiv z^*_0(y^*_0 = 0$ and $y^*_{\mathrm{T,SRF,3D}} \equiv y^*_0(z^*_0 = 0)$:

$$z^*_{\mathrm{T,SRF,3D}} = \begin{cases} \frac{1}{2k_0}\cosh^{-1}\left(C_{\mathrm{SRF,3D}}(\delta_{\mathrm{3D}}=1)\frac{\sinh(2k_0d)}{2k_0d}\right) - d & \text{for} \quad \frac{\sinh(2k_0d)}{2k_0d} \geq \dfrac{1}{C_{\mathrm{SRF,3D}}(\delta_{\mathrm{3D}}=1)}, \\ -d & \text{for} \quad \frac{\sinh(2k_0d)}{2k_0d} < \dfrac{1}{C_{\mathrm{SRF,3D}}(\delta_{\mathrm{3D}}=1)}, \end{cases} \tag{3.52}$$

$$y^*_{\mathrm{T,SRF,3D}} = \sigma\sqrt{\log\left(\frac{1}{C_{\mathrm{SRF,3D}}(\delta_{\mathrm{3D}}=1)}\frac{2k_0d}{\tanh(2k_0d)}\right)}. \tag{3.53}$$

3.4.3 Realistic directional spectra

Considering more realistic degrees of directional spreading, appendix F shows the solutions for the three-dimensional return flow field for $\sigma_y \neq \sigma_x$ (and $\delta_{\mathrm{3D}} \neq 1$). For different degrees of directional spreading representative of real world seas, this section then compares the deep and shallow return flow limit to the net displacements of a particle at the free surface and transition depths and width than can be obtained from the velocity fields in appendix F. We first consider the two limits in turn for $\delta_{\mathrm{3D}} \neq 1$.

3.4.3.1 The deep-water return flow limit

In deep water ($d/\sigma \to \infty$), the net transport by Stokes drift and return flow associated with a directionally spread group are given by:

$$\Delta x_{\mathrm{SD}}(y_0, z_0) = 2\sqrt{\pi}\sigma_x \alpha^2 \exp\left(2k_0 z_0 - \left(\frac{y_0}{\sigma_y}\right)^2\right), \tag{3.54}$$

$$\Delta x_{\mathrm{RF}}(y_0 = 0, z_0 = 0) = -\frac{2\sqrt{\pi} C_{\mathrm{DRF,3D}}(\delta_{\mathrm{3D}})\alpha^2}{k_0}, \tag{3.55}$$

where $C_{\mathrm{DRF,3D}}(\delta_{\mathrm{3D}})$ is given by:

$$C_{\mathrm{DRF,3D}}(\delta_{\mathrm{3D}}) = \frac{1}{8\pi^{5/2}} \int_{-\infty}^{\infty}\int_{-\infty}^{\infty}\int_{-\infty}^{\infty} \frac{\hat{k}^2 f(\hat{k},\hat{l})}{\sqrt{\hat{k}^2 + \delta_{\mathrm{3D}}^2 \hat{l}^2}} e^{i(\hat{k}\hat{x} + \hat{l}\hat{y}_0)} d\hat{k} d\hat{l} d\hat{x}. \tag{3.56}$$

From numerical evaluation of the numerical integral for a Gaussian group, we have for the constant $C_{\mathrm{DRF,3D}} = \{0.032, 0.0056, 0.0028, 0.0014, 0.0010\}$ for $\delta_{\mathrm{3D}} = \{0, 0.5, 1, 2, 3\}$ with corresponding values of $\Delta x_{\mathrm{RF}}(y_0 = 0, z_0 = 0) = \{0.1134, 0.0197, 0.0101, 0.0051, 0.0034\}\alpha^2/k_0$ illustrating the dramatic effect of even small degrees of directional spreading on the net transport by the return flow. The approximate transition curve remains parabolic:

$$k_0 z_0 - \frac{1}{2}\left(\frac{y_0}{\sigma_y}\right)^2 = \frac{1}{2}\log\left(C_{\mathrm{SRF,3D}}(\delta_{\mathrm{3D}})\epsilon_x\right). \tag{3.57}$$

Approximate transition depths and widths are:

$$z^*_{\mathrm{T,DRF,3D}} = \frac{1}{2k_0}\Big(\log(\epsilon_x) + \log(C_{\mathrm{SRF,3D}}(\delta_{\mathrm{3D}}))\Big), \quad y^*_{\mathrm{T,DRF,3D}} = \sigma_y\sqrt{-\log(C_{\mathrm{SRF,3D}}(\delta_{\mathrm{3D}})) - \log(\epsilon_x)}. \tag{3.58a,b}$$

3.4.3.2 The shallow-water return flow limit

Under the shallow return flow approximation ($d/\sigma \to 0$), the net transport by Stokes drift and return flow associated with a directionally spread group are given by:

$$\Delta x_{\mathrm{SD}}(y_0, z_0) = 2\sqrt{\pi}\alpha^2\sigma_x\delta_{\mathrm{SD}}(k_0 d)\cosh(2k_0(d+z_0))\exp(-(y_0/\sigma_y)^2), \tag{3.59}$$

$$\Delta x_{\mathrm{RF}}(y_0 = 0, z_0 = 0) = -2\sqrt{\pi}\sigma_x\delta_{\mathrm{SD}}(k_0 d)(1+\delta_{\mathrm{FD}}(k_0 d))\frac{\sinh(2k_0 d)}{2k_0 d}C_{\mathrm{SRF,3D}}(\delta_{\mathrm{3D}}), \tag{3.60}$$

where $C_{\mathrm{SRF,3D}} =$ is given by:

$$C_{\mathrm{SRF,3D}}(\delta_{\mathrm{3D}}) = \frac{1}{4\pi^{5/2}}\int_{-\infty}^{\infty}\int_{-\infty}^{\infty}\int_{-\infty}^{\infty}\frac{\hat{k}^2 f(\hat{k},\hat{l})}{\hat{k}^2+\delta_{\mathrm{3D}}^2\hat{l}^2}e^{i\hat{k}\hat{x}}d\hat{k}d\hat{l}d\hat{x}. \tag{3.61}$$

From numerical evaluation of the numerical integral for a Gaussian group, we have for the constant $C_{\mathrm{SRF,3D}} = \{1, 0.11, 0.056, 0.028, 0.019\}$ for $\delta_{\mathrm{3D}} = \{0, 0.5, 1, 2, 3\}$. The approximate transition curve is given by:

$$z_0 = \frac{1}{2k_0}\cosh^{-1}\left(\frac{\sinh(2k_0 d)}{2k_0 d}C_{\mathrm{SRF,3D}}(\delta_{\mathrm{3D}})\exp((y_0/\sigma_y)^2)\right) - d. \tag{3.62}$$

Approximate transition depths and widths are:

$$z^*_{\mathrm{T,SRF,3D}} = \frac{\cosh^{-1}\left(\frac{\sinh(2k_0 d)}{2k_0 d}(1+\delta_{\mathrm{FD}}(k_0 d))C_{\mathrm{SRF,3D}}(\delta_{\mathrm{3D}})\right)}{2k_0} - d, \tag{3.63}$$

$$y^*_{\mathrm{T,SRF,3D}} = \sigma_y\sqrt{-\log(C_{\mathrm{SRF,3D}}(\delta_{\mathrm{3D}})) - \log\left(\frac{\tanh(2k_0 d)(1+\delta_{\mathrm{FD}}(k_0 d))}{2k_0 d}\right)}, \tag{3.64}$$

where the transition depth is only defined for $\sinh(2k_0 d)(1+\delta_{\mathrm{FD}}(k_0 d)/(2k_0 d) \geq 1/C_{\mathrm{SRF,3D}}(\delta_{\mathrm{3D}})$. For smaller depths, the Stokes drift is always larger underneath the centre of the group.

Figure 3.11a and 3.11b compare the transition depth, defined as the solution to $\Delta x_{\mathrm{L}}(y_0 = 0, z_0 = z_{\mathrm{T}}) = 0$, and the transition width, defined as the solution to $\Delta x_{\mathrm{L}}(y_0 = y_{\mathrm{T}}, z_0 = 0) = 0$, to the approximate scales in the deep return flow ($d/\sigma \to \infty$) (3.58) and the shallow return flow limit ($d/\sigma \to 0$) (3.63-3.64) for different degrees of directional spreading. It is evident from these figures that the shallow return flow limit provides an excellent approximation except for very large depths. Unless the sea state is perfectly uni-directional, a transition depth cannot be defined for $k_0 d \lesssim 2$ with all net transport positive below the

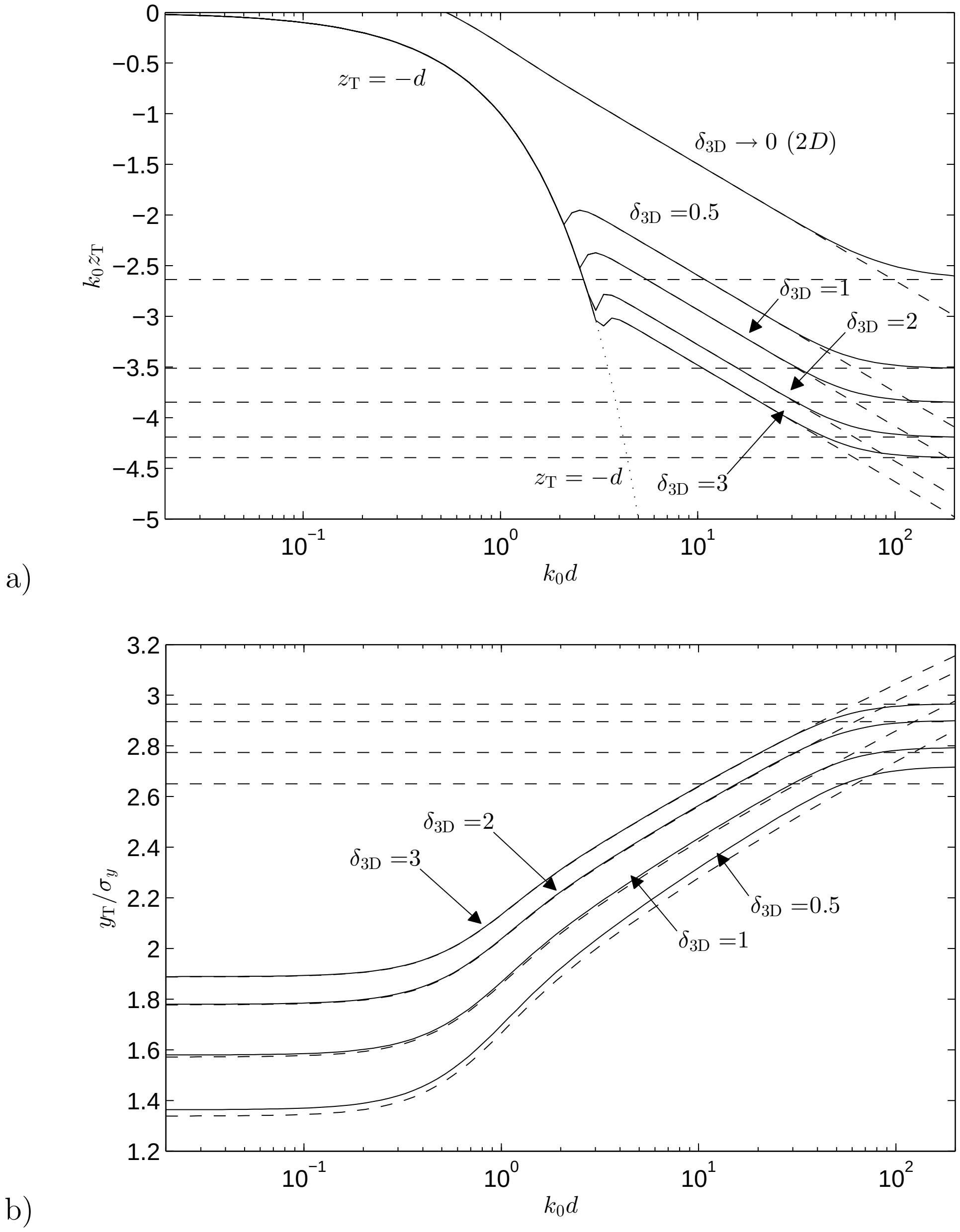

Figure 3.11: Transition depth (a) and width (b) for three-dimensional seas with different degrees of directionality $\delta_{3\mathrm{D}} = \sigma_x/\sigma_y$ and as a function of water depth $k_0 d$. Shown are the deep return flow limit (3.58) (horizontal dashed lines), the shallow return flow limit (3.63-3.64) (dashed lines) and the implicit solution for intermediate depth (continuous lines).

					$\sigma_{\text{RMS}} = 0°$	$\sigma_{\text{RMS}} = 5°$	$\sigma_{\text{RMS}} = 10°$	$\sigma_{\text{RMS}} = 20°$	$\sigma_{\text{RMS}} = 30°$
Location	d	$k_0 d$	$\lvert a_0 \rvert$ [m]	Δx_{SD} [m]	Δx_{RF} [m]	Δx_{RF} [m]	Δx_{RF} [m]	Δx_{RF} [m]	Δx_{RF} [m]
					−11.9	−1.2	−0.62	−0.31	−0.21
Coastal	10 m	0.68	2.9	14.4	**−11.9**	**−1.2**	**−0.62**	**−0.31**	**−0.21**
					−0.07	−0.01	−0.005	−0.003	−0.002
					−8.0	−0.82	−0.41	−0.21	−0.14
Coastal	20 m	1.0	3.9	14.9	**−8.0**	**−0.82**	**−0.41**	**−0.21**	**−0.14**
					−0.09	−0.01	−0.007	−0.004	−0.002
					−5.4	−0.56	−0.28	−0.14	−0.09
S. North Sea	40 m	1.7	4.7	18.1	**−5.4**	**−0.56**	**−0.28**	**−0.14**	**−0.09**
					−0.11	−0.02	−0.009	−0.004	−0.003
					−3.3	−0.34	−0.17	−0.09	−0.06
C. North Sea	80 m	3.2	5.0	21.6	**−3.3**	**−0.34**	**−0.17**	**−0.09**	**−0.06**
					−0.11	−0.02	−0.009	−0.005	−0.003
					−1.7	−0.17	−0.09	−0.04	−0.03
N. North Sea	160 m	6.4	5.0	22.0	**−1.7**	**−0.18**	**−0.09**	**−0.04**	**−0.03**
					−0.11	−0.02	−0.009	−0.005	−0.003
					−0.55	−0.06	−0.03	−0.01	−0.01
Continental Slope	500 m	20	5.0	22.0	**−0.55**	**−0.06**	**−0.03**	**−0.01**	**−0.01**
					−0.11	−0.02	−0.009	−0.005	−0.003
					−0.27	−0.03	−0.01	−0.007	−0.005
Continental Slope	1.0 km	40	5.0	22.0	**−0.28**	**−0.03**	**−0.02**	**−0.008**	**−0.0058**
					−0.11	−0.02	−0.009	−0.005	−0.003
					−0.09	−0.009	−0.005	−0.002	−0.001
Abyssal Plane	3.0 km	$1.2 \cdot 10^2$	5.0	22.0	**−0.14**	**−0.02**	**−0.01**	**−0.005**	**−0.003**
					−0.11	−0.02	−0.009	−0.005	−0.003
					−0.05	−0.005	−0.002	−0.002	−0.0008
Abyssal Plane	6.0 km	$2.4 \cdot 10^2$	5.0	22.0	**−0.12**	**−0.02**	**−0.009**	**−0.005**	**−0.003**
					−0.11	−0.02	−0.009	−0.005	−0.003
					−0.03	−0.003	−0.001	−0.0006	−0.0004
Mariana Trench	11 km	$4.4 \cdot 10^2$	5.0	22.0	**−0.11**	**−0.02**	**−0.009**	**−0.005**	**−0.003**
					−0.11	−0.02	−0.009	−0.005	−0.003

Table 3.1: Net horizontal transport for particles at the free surface and at the centre of the group ($z_0 = 0$, $y_0 = 0$) for different depths (rows) and different degrees of directional spreading (columns). We set $T_0 = 10s$, $\alpha = 0.2$ and $\epsilon_x = 0.16$. Three values are reported. The top value of Δx_{RF} corresponds to the shallow-water return flow limit, the bold value to the full finite depth solution and the bottom value to the deep-water return flow limit. The root mean square spreading parameters $\sigma_{\text{RMS}} = \{0°, 5°, 10°, 20°, 30°\}$ correspond to $\delta_{3\text{D}} = \{0, 0.54, 1.1, 2.2, 3.3\}$. If $z_{\text{T}} < -d$, the Stokes drift dominates the return flow at all depths below the centre of the group.

centre of the group. The kinks in figure 3.11a arise because of the change in topology of the transition curve as shown in moving from figure 3.10e to 3.10f.

3.5 Conclusions

This chapter has examined the Lagrangian transport by wave groups in finite depth and directionally spread seas driven by two opposing effects: the Stokes transport transporting fluid particles in one direction and the return flow opposing this by transporting fluid particles in the opposite direction. Both the effect of finite depth and the effect of directional spreading are crucial factors in determining the magnitude and physical importance of the net transport.

			$\sigma_{\mathrm{RMS}} = 0°$	$\sigma_{\mathrm{RMS}} = 5°$	$\sigma_{\mathrm{RMS}} = 10°$	$\sigma_{\mathrm{RMS}} = 20°$	$\sigma_{\mathrm{RMS}} = 30°$
Location	d	k_0d	z_{T} [m]	z_{T} [m]	z_{T} [m]	z_{T} [m]	z_{T} [m]
			-1.6	$< -d$	$< -d$	$< -d$	$< -d$
Coastal	10 m	0.68	$\mathbf{-1.6}$	$< -\mathbf{d}$	$< -\mathbf{d}$	$< -\mathbf{d}$	$< -\mathbf{d}$
			-38.8	-52.2	-57.2	-62.3	-65.2
			-6.4	$< -d$	$< -d$	$< -d$	$< -d$
Coastal	20 m	1.0	$\mathbf{-6.4}$	$< -\mathbf{d}$	$< -\mathbf{d}$	$< -\mathbf{d}$	$< -\mathbf{d}$
			-50.9	-68.6	-75.1	-81.7	-85.6
			-14.1	$< -d$	$< -d$	$< -d$	$< -d$
S. North Sea	40 m	1.7	$\mathbf{-14.1}$	$< -\mathbf{d}$	$< -\mathbf{d}$	$< -\mathbf{d}$	$< -\mathbf{d}$
			-61.4	-82.8	-90.6	-98.7	-103
			-23.1	-51.5	-60.3	-70.9	$< -d$
C. North Sea	80 m	3.2	$\mathbf{-23.1}$	$\mathbf{-51.5}$	$\mathbf{-60.3}$	$\mathbf{-70.9}$	$< -\mathbf{d}$
			-65.3	-88.0	-96.4	-105	-110
			-31.8	-60.1	-68.5	-77.1	-82.1
N. North Sea	160 m	6.4	$\mathbf{-31.8}$	$\mathbf{-60.1}$	$\mathbf{-68.5}$	$\mathbf{-77.1}$	$\mathbf{-82.1}$
			-65.5	-88.3	-96.7	-105	-110
			-45.9	-74.2	-82.7	-91.3	-96.3
Continental slope	500 m	20	$\mathbf{-45.9}$	$\mathbf{-74.2}$	$\mathbf{-82.7}$	$\mathbf{-91.3}$	$\mathbf{-96.3}$
			-65.5	-88.3	-96.7	-105	-110
			-54.5	-80.9	-91.3	-99.9	-105
Continental slope	1.0 km	40	$\mathbf{-54.3}$	$\mathbf{-80.3}$	$\mathbf{-90.7}$	$\mathbf{-99.3}$	$\mathbf{-104}$
			-65.5	-88.3	-96.7	-105	-110
			-68.2	-96.5	-105	-113	-119
Abyssal Plane	3.0 km	$1.2 \cdot 10^2$	$\mathbf{-63.2}$	$\mathbf{-87.9}$	$\mathbf{-96.3}$	$\mathbf{-105}$	$\mathbf{-110}$
			-65.5	-88.3	-96.7	-105	-110
			-76.8	-105	-114	-122	-127
Abyssal Plane	6.0 km	$2.4 \cdot 10^2$	$\mathbf{-64.9}$	$\mathbf{-88.3}$	$\mathbf{-96.7}$	$\mathbf{-105}$	$\mathbf{-110}$
			-65.5	-88.3	-96.7	-105	-110
			–	–	–	–	–
Mariana Trench	11 km	$4.4 \cdot 10^2$	$\mathbf{-65.5}$	$\mathbf{-88.3}$	$\mathbf{-96.7}$	$\mathbf{-105}$	$\mathbf{-110}$
			-65.5	-88.3	-96.7	-105	-110

Table 3.2: Transition depth at the centre of the group ($z_0 = 0$, $y_0 = 0$) for different depths (rows) and different degrees of directional spreading (columns). We set $T_0 = 10s$ and $\epsilon_x = 0.16$. Three values are reported. The top value of Δx_{RF} corresponds to the shallow return flow limit, the bold value to the full finite depth solution and the bottom value to the deep return flow limit. The root mean square spreading parameters $\sigma_{\mathrm{RMS}} = \{0°, 5°, 10°, 20°, 30°\}$ correspond to $\delta_{\mathrm{3D}} = \{0, 0.54, 1.1, 2.2, 3.3\}$.

To illustrate these findings, table 3.1 shows estimates of the net transport of a particle located at the still water level for a broad range of water depths ranging from shallow coastal regions ($d = 10$ m) to the deepest point in the ocean ($d = 11$ km). The values shown correspond to a wave group of steepness $\alpha = k_0|a_0| = 0.2$, a bandwidth parameter of ϵ_x corresponding to the best fit of a Gaussian to a Jonswap spectrum (Gibbs and Taylor 2005) and a peak period of $T_0 = 10$ s. It is evident from this table that the effects of depth on the magnitude of the transport by the return flow are large. Evidently, the limits of validity of a Stokes expansion are reached for sufficiently small depth, when the ratio of depth and wave amplitude d/a_0 is no longer large. Different authors have studied the range of validity of Stokes theory (Dean 1970, Hedges 1995, Fenton 1990, Sobey 2012). Typically, the shallow-water limit of validity can be expressed in terms of the Ursell number (Ursell 1953):

$$U_r = \frac{H\lambda_0^2}{d^3}, \tag{3.65}$$

where $H = 2a_0$ is the wave height. Hedges (1995), for example, shows that $U_r = 40$ gives a good boundary between the validity of Stokes and Cnoidal theory. Using the small parameters in this chapter, we have from (3.65): $U_r = 8\pi^2\alpha/(k_0d)^3$. Therefore $U_r = 40$ and $\alpha = 0.2$ corresponds to $k_0d \approx 0.73$ and only our estimates for $d = 10$ m in table 3.1 are perhaps marginally outside of the domain of validity of Stokes theory. Furthermore, by comparing estimates based on the shallow return flow limit and the deep return flow limit to the general finite depth solution, we show that the return flow can be modelled a uniform flow with depth (the shallow return flow limit) for water depths up to $0.5 - 1$ km for the case considered in table 3.1.

Also shown in table 3.1 is the effect of directional spreading on the return flow, demonstrating the large decreasing effect of even a small degree of directional spreading on the magnitude of the transport by the return flow. The values of the rms spreading parameter ($15° - 30°$) shown correspond to the typical range observed in field measurements for storm driven waves (Donelan et al. 1985, Ewans 1998).

Finally, table 3.2 provides an overview of estimates of the transition depth, defined as the depth at which the Lagrangian transport by the Stokes drift and the return flow exactly balance and $\Delta x_L = 0$, for a broad range of water depths. Again, the effect of directional spreading is significant. For sufficiently shallow water the transition depth cannot be defined, as the return flow is located around instead of below the group.

Part II

Internal gravity waves

Chapter 4

The mean flow and long waves induced by two-dimensional internal gravity waves groups

Through theory supported by numerical simulations, this chapter examines the induced local and long-range response flows resulting from the momentum-flux divergence associated with a two-dimensional Boussinesq internal gravity wave group in a uniformly stratified ambient. The theoretical approach performs a perturbation analysis that takes advantage of the separation of scales between waves and the amplitude envelope of a quasi-monochromatic wave group. The approach is first illustrated by applying it to the case of the deep water surface gravity waves of chapter 2, showing that the induced flow, u_{DF}, resulting from the divergence of the horizontal momentum flux is equal to the Stokes drift. For a localized surface wave group, u_{DF} is itself a divergent flow and so there is the non-local response manifest in the form of a deep return flow beneath the wave group. The focus of this chapter is on internal wave groups that are localized in the horizontal and vertical. This chapter derives an expression for the divergent-flux induced flow that, as in this case of surface wave groups, is itself a divergent flow. This chapter then shows that the response is a horizontally long internal wave that translates vertically with the wave group at its group velocity. Scaling relationships are used to estimate the wave number, horizontal extent and amplitude of this induced long wave. At higher order in perturbation theory, an explicit integral formulation for the induced long wave is derived.

This chapter thus provides validation of Bretherton's (1969b) analysis of flows induced by two-dimensional internal wave groups and provides further analysis that gives intuitive insights into the physics governing the properties of the induced long wave. In particular, consistent with momentum conservation, this chapter shows that the horizontally-integrated horizontal flow associated with the long wave is given exactly by the horizontal integral of u_{DF}. However,

qualitatively different from horizontally periodic internal waves, the vertical profile of the induced horizontal flow across the horizontally localized wave group is positive at the leading edge and negative at the trailing edge. These results are validated by the results of numerical simulations of a Gaussian wave group initialized in an otherwise stationary ambient fluid.

4.1 Introduction

Internal waves propagate vertically through the atmosphere and ocean moving under the influence of buoyancy forces in a stratified medium. Where they break, the consequent momentum-flux divergence irreversibly accelerates the ambient fluid. Cumulatively in the atmosphere, this non-negligibly affects the zonal wind speeds and, through thermal wind balance, the mean temperatures (Palmer et al. 1986, McFarlane 1987, McLandress 1998). Despite their importance, the mechanism for momentum transport and deposition by internal waves remains unclear. Although linear theory is sometimes employed to predict where anelastic internal waves break (Lindzen 1981), it is now clear that weakly non-linear effects can significantly change the evolution and breaking levels (Sutherland 2006b, Dosser and Sutherland 2011a, Rieper et al. 2013). Most studies into vertically propagating weakly non-linear internal waves have examined wave groups that are vertically localized and horizontally periodic. Such wave groups have a well-defined wave-induced mean flow that translates vertically with the wave group at its group velocity, before being irreversibly deposited to the background when the waves break. Even before breaking, the wave-induced mean flow Doppler shifts the waves as they grow to large amplitude giving rise to modulational stability or instability (Sutherland 2006b).

If an internal wave group is horizontally as well as vertically localized, the direct counterpart to the induced flow for horizontally periodic waves is a horizontally divergent flow field. And so there must be a response flow that ensures the total flow field is incompressible. Using the concept of wave-action conservation, Bretherton (1969b) examined the wave-induced flow resulting from two- and three-dimensional internal wave groups. He predicted that a small-amplitude localized two-dimensional wave group should excite a horizontally long disturbance while a three-dimensional (span-wise localized) wave group should generate a horizontal recirculation, which in itself could have a far-field influence on the ambient fluid (Bühler and McIntyre 2005, Bühler 2009).

This chapter revisits the theory for the flow induced by two-dimensional internal wave groups. The objectives are threefold. Firstly, rather than relying on wave-action conservation, we develop a wave group-based theory to derive intuitive expressions for the (local) divergent-flux induced flow and the (non-local) induced long wave associated with a localized quasi-monochromatic wave group. Secondly, we derive approximate scaling estimates and an analysis of the integral equation describing the induced long wave that provides insight into the structure of the non-local motion induced by the wave group. Thirdly, we compare the theoretical predictions with fully non-linear numerical simulations of a small-amplitude wave group initialized in a stationary ambient.

To lay the theoretical groundwork, we first review the theory for the wave-induced flow of surface wave groups as discussed in chapter 2 and of horizontally periodic, vertically localized internal wave groups. Even without breaking, surface gravity waves have associated with them a wave-induced flow known commonly as the Stokes drift (Stokes 1847). From a Lagrangian perspective, the flow is a consequence of fluid parcels being advected further in the wave-direction at the top of their orbits than they propagate in the opposite direction at the bottom of their orbits, as well as an equivalent effect during motion in the horizontal direction. The expression for the vertical integral of the Stokes drift is equal to the pseudo-momentum per unit mass. But the latter is conceptually distinct, arising from consideration of conservation laws.

In this chapter, we present another perspective, showing that the pseudo-momentum per unit mass is identical to the flow arising from the divergence of the horizontal flux of horizontal momentum associated with a quasi-monochromatic wave group. This we refer to as the "divergent-flux induced flow". If the surface wave group has finite horizontal extent, the Stokes drift is zero ahead and behind the wave group resulting in a convergence and divergence of the horizontal flow at the wave group's leading and trailing edge, respectively. This results in a response flow that moves opposite to the direction of the Stokes drift, and is hence referred to as the return flow. For deep water it extends far below the surface (Longuet-Higgins and Stewart 1962) (see chapter 2). The vertically integrated volume flux of this response flow is equal and opposite to the volume flux associated with the Stokes drift. It is for this reason that the Stokes drift is sometimes referred to as the *pseudo*-momentum per unit mass, a reminder that the actual momentum of the wave group (which includes the return flow) is zero (cf. McIntyre (1981) and discussion in chapter 2).

For internal waves in a uniformly stratified fluid, the properties of their associated wave-induced flow are not so well understood. It is well known that plane periodic Boussinesq internal waves are an exact solution of the fully non-linear equations of motion. The mean Lagrangian displacement of fluid parcels due to the waves is zero: there is no Stokes drift. However, the pseudo-momentum, inferred through wave-action conservation (Bretherton and Garrett 1969, Bretherton 1969b, Acheson 1976) or derived through the principles of Hamiltonian fluid dynamics (Scinocca and Shepherd 1992), is non-zero (Bühler 2009). Indeed, for horizontally periodic, vertically localized internal wave groups, the pseudo-momentum per mass gives the wave-induced mean flow Sutherland (2001). This is a transient, horizontally uniform flow that translates vertically with the wave group at the vertical group velocity. Through a separate theoretical approach that examines momentum transport by quasi-monochromatic wave groups, the origin of the wave-induced mean flow for horizontally periodic wave groups is clear: the flow results from the vertical divergence of the horizontal momentum flux (Sutherland 2010, Dosser and Sutherland 2011b).

If a two-dimensional internal wave group is horizontally as well as vertically localized, the divergence of the pseudo-momentum is non-zero. And so, as in the case of surface wave groups, there must be a response flow. However, this flow cannot simply return above and below the wave group because stratification inhibits vertical motions associated with such a re-circulation. Different from the approach of Bretherton (1969b), we use a wave-group approach to derive what we call the "divergent-flux induced flow" for localized internal wave groups. We show that the divergent-flux induced flow itself induces a response flow such that the total wave-induced flow extends broadly in the horizontal to either side of the wave group. Higher-order perturbation theory reveals that the flow induced by the wave group is a horizontally long internal wave that moves vertically with the wave group.

This chapter is laid out as follows. Governing equations for two-dimensional internal gravity waves are introduced in §4.2. §4.3 then reviews the theory of wave-induced mean flow associated with surface waves and horizontally periodic internal waves introducing the concept of divergent-flux induced flow. In §4.4 the concept of divergent-flux induced flow is used to describe the induced mean flow of two-dimensional internal gravity waves. In §4.5 these predictions are compared with numerical simulations of a quasi-monochromatic horizontally periodic and horizontally localized wave groups showing that the theory well captures the flow induced by a small-amplitude internal wave after a transient start-up time. Finally, conclusions are drawn and implications discussed in §4.6.

4.2 Governing equations

We begin by making the usual Boussinesq approximation, that is, we ignore variation of density in the conservation equations except where it is responsible for the existence of the buoyancy force itself. In a two-dimensional coordinate system in which x and z denote the horizontal and vertical coordinates, respectively, the corresponding momentum equations are:

$$\frac{Du}{Dt} = -\frac{1}{\rho_0}\frac{\partial p}{\partial x}, \quad \frac{Dw}{Dt} = -\frac{1}{\rho_0}\frac{\partial p}{\partial z} - g\frac{\rho}{\rho_0}, \tag{4.1a,b}$$

where u and w denote the horizontal and vertical velocity, respectively, p the fluctuation pressure, and gravity g acts in the negative z direction. In the Boussinesq approximation ρ_0 is the (constant) characteristic density. The total density of the fluid is the sum of background density $\overline{\rho}(z)$ and small variations from the background ρ, so that $\rho_T = \overline{\rho} + \rho$. The fluid is assumed to be incompressible. Together with mass conservation this requires the flow to be non-divergent:

$$\nabla \cdot \mathbf{u} = 0. \tag{4.2}$$

We further assume the ambient is uniformly stratified with a corresponding positive and constant squared buoyancy frequency:

$$N^2 = -\frac{g}{\rho_0}\frac{d\overline{\rho}}{dz}. \tag{4.3}$$

Neglecting diffusion of heat and salinity, internal energy conservation gives the following evolution equation for the perturbation density ρ:

$$\frac{D\rho}{Dt} = -w\frac{d\overline{\rho}}{dz}. \tag{4.4}$$

In a uniformly stratified Boussinesq fluid it is convenient to re-express ρ in terms of the vertical displacement field ξ through:

$$\xi = -\frac{\rho}{\overline{\rho}'(z)}, \tag{4.5}$$

where the prime denotes a z-derivative. Then (4.4) can be rewritten as:

$$\frac{D\xi}{Dt} = w. \tag{4.6}$$

From (4.2), one may define a stream function $\psi(x, z, t)$, so that:

$$u = -\partial\psi/\partial z \quad \text{and} \quad w = \partial\psi/\partial x. \tag{4.7a,b}$$

It is convenient to combine the horizontal and vertical momentum equations (4.1) into one equation in terms of ψ and ξ. By taking the span-wise component of the curl of momentum equation and using (4.5), we obtain the equation for baroclinic generation of (span-wise) vorticity:

$$\frac{D\nabla^2\psi}{Dt} = -N^2\frac{\partial\xi}{\partial x}. \tag{4.8}$$

in which the material derivative acts on the vorticity, defined by:

$$\zeta = -\nabla^2\psi. \tag{4.9}$$

Finally, (4.6) and (4.8) are combined and written in the form with a linear differential operator L acting on ψ on the left-hand side and the divergence of a non-linear vector $\mathbf{F}$ on the right-hand side:

$$\underbrace{\left[\frac{\partial^2}{\partial t^2}\left[\frac{\partial^2}{\partial x^2}+\frac{\partial^2}{\partial z^2}\right]+N^2\frac{\partial^2}{\partial x^2}\right]}_{\equiv\, L}\psi = \nabla\cdot\underbrace{\left[\frac{\partial}{\partial t}\left[\zeta\ \mathbf{u}\right]+N^2\frac{\partial}{\partial x}\left[\xi\ \mathbf{u}\right]\right]}_{\equiv\,\mathbf{F}}. \tag{4.10}$$

Equations (4.6) and (4.10), together with (4.7) and (4.9), comprise two coupled fully non-linear equations in ξ and ψ.

4.3 Surface waves and horizontally periodic internal waves

In this section we begin by reviewing the theory for the wave-induced mean flow associated with surface wave, already explored in chapter 2. We show that the Stokes drift is equal (but not equivalent) to the pseudo-momentum per unit mass and that both are reproduced by consideration of the divergence of the horizontal flux of horizontal momentum associated with quasi-monochromatic surface wave groups. Likewise, we show that the divergence of the vertical transport of horizontal momentum associated with horizontally periodic internal wave groups reproduces the pseudo-momentum. With this physically intuitive derivation of the wave-induced flow, which is local to the wave group, we go on to examine the divergent-flux induced flow and the total wave-induced flow associated with horizontally and vertically localized wave groups, which are non-local to the wave group.

4.3.1 Surface gravity waves

The purpose of this section is not only to review the theory for surface waves, but also to establish the mathematical terminology in a familiar setting. Plane surface gravity waves in deep water of horizontal wave number k (assumed positive) have frequency $\omega = \sqrt{gk}$, in which g is gravity and we have assumed $\omega > 0$ corresponding to rightward-propagating waves. Assuming the waves have vertical-displacement amplitude A_0, the polarization relations give the horizontal and vertical velocities:

$$u = \omega A_0 e^{kz} e^{i(kx-\omega t)}, \quad w = -i\omega A_0 e^{kz} e^{i(kx-\omega t)}, \tag{4.11a,b}$$

and the corresponding horizontal and vertical displacement fields:

$$\Delta x = iA_0 e^{kz} e^{i(kx-\omega t)}, \quad \Delta z = A_0 e^{kz} e^{i(kx-\omega t)}, \tag{4.12a,b}$$

in which it is understood that the actual fields are the real part of the right-hand expressions. Averaging these fields in time over one period gives zero. However, performing a Taylor-series expansion of the horizontal velocity up to order amplitude squared (thus following particles in their leading-order Lagrangian motion) and averaging gives (Stokes 1847):

$$u_{\text{SD}} = \overline{u + \Delta x\,\frac{\partial u}{\partial x} + \Delta z\,\frac{\partial u}{\partial z}} = (\omega/k)\alpha^2 e^{2kz}, \tag{4.13}$$

in which $\alpha \equiv A_0 k$ is the wave steepness and the over-line denotes averaging over either a period or a wavelength. This is the Stokes drift, which corresponds to the mean Lagrangian advection of fluid parcels by a surface wave in the absence of any background (i.e. Eulerian) flow. The corresponding Lagrangian volume flux is given by vertically integrating (4.13). Multiplied by the density of water ρ_0 the Stokes drift of periodic surface gravity waves has an associated vertically integrated momentum:

$$M = \rho_0 \frac{\omega}{2k^2}\alpha^2. \tag{4.14}$$

An analogous result was first derived in an Eulerian framework by Starr (1947). In an Eulerian framework, a net mass flux is identified by integrating the horizontal velocity from the bottom up to the free surface. Because the flow is higher at a crest than at a trough, the result gives a mean depth-integrated horizontal flux consistent with the flux obtained by depth integration of (4.13).

The vertically integrated energy associated these waves is $E = \rho_0(g/2){A_0}^2$. The analogy to momentum as a conserved quantity for fluids is the so-called "pseudo-momentum", which, from the principle of conservation of wave-action (Bretherton and Garrett 1969), is given generally for waves in a stationary ambient by:

$$P = kE/\omega. \tag{4.15}$$

Substituting the expression for E into (4.15) and using the dispersion relation reveals that $P = M$: the pseudo-momentum is equal to the momentum computed from the Stokes drift.

These results have assumed an infinitely periodic wave train. Perhaps a more physically intuitive appreciation of the near-surface momentum associated with surface waves comes from consideration of quasi-monochromatic surface wave groups. By analogy with (4.11), we suppose the horizontal and vertical velocity fields are given by:

$$u^{(1)} = \omega A(X,T)e^{kz}e^{i(kx-\omega t)}, \quad w^{(1)} = -i\omega A(X,T)e^{kz}e^{i(kx-\omega t)}, \tag{4.16a,b}$$

in which A is the amplitude envelope with initial magnitude $A_0 \equiv |A|$, and the superscripts on the left-hand side emphasize that these are velocities given to $O(\alpha^1)$. The amplitude envelope is assumed to vary slowly in space and time compared to the fast scales k^{-1} and ω^{-1}, respectively. The leading-order evolution of the wave group is its translation at the group velocity. This is captured by setting $X \equiv \epsilon(x - c_g t)$ with $\epsilon = 1/(\sigma k) \ll 1$, in which σ represents the spatial extent of the wave group and $c_g = (\sqrt{g/k})/2$ is the group velocity. The dispersion of the wave group is a slower process that depends on the curvature of the amplitude envelope, as represented by $T = \epsilon^2 t$. Because our examination is not concerned with weakly non-linear effects, we need not provide a scaling between α and ϵ for the multiple-scales asymptotic expansion that follows, as in the previous chapters.

Now consider the flux-form of the horizontal momentum equation:

$$\frac{\partial u}{\partial t} = -\frac{\partial(uu)}{\partial x} - \frac{\partial(uw)}{\partial z} - \frac{\partial(p/\rho_0)}{\partial x}. \tag{4.17}$$

Substituting (4.16) into the advective terms on the right-hand side and keeping only the slowly varying terms we find that the vertical divergence term vanishes because $u^{(1)}$ and $w^{(1)}$ are 90° out of phase. The remaining flux term is:

$$-\partial_x \overline{u^{(1)}u^{(1)}} \to -\epsilon\partial_X \left[\frac{\omega^2}{2}\left|A(X,T)\right|^2 e^{2kz}\right]. \tag{4.18}$$

Here the over-line denotes effective averaging over the fast scales so as to retain only slowly varying terms. As a result, we have retained the x-derivative term in (4.18), which represents the horizontal transport of horizontal momentum per unit mass.

The order α^2 divergent flux in (4.18) results in an acceleration which itself must be order α^2. The resulting divergent-flux induced flow we denote by $u_{\text{DF}}(X,T)$, an $O(\alpha^2)$ quantity that translates at the group velocity of the surface wave group. Substituting u_{DF} on the left-hand side of (4.17) and taking the time derivative gives $-\partial_t u_{\text{DF}} \simeq -\epsilon c_g \partial_X u_{\text{DF}}$, in which we have retained terms of order ϵ alone. Equating this to the divergent-flux term and integrating in X gives the explicit expression for the divergent-flux induced flow:

$$u_{\text{DF}} = \frac{1}{c_g}\overline{u^{(1)}u^{(1)}} = \omega k |A|^2\, e^{2kz}. \tag{4.19}$$

For plane waves $|A| = A_0$ and (4.19) becomes equal to the equation for the Stokes drift (4.13). The vertical integral of (4.19) after multiplying by density gives the pseudo-momentum, given by generally (4.15) and specifically by (4.14). The physics of the near-surface flow are clear under this macroscopic examination of the momentum conservation law, which reveals that the horizontal flow results from the divergence of the horizontal flux of horizontal momentum per unit mass.

Of course, this is not the whole story. Because u_{DF} for horizontally localized wave groups is itself a horizontally divergent flow, there must also be a response flow in order to ensure volume is conserved. This is taken care of by the pressure gradient term in (4.17). The divergence of u_{DF} gives rise to an order α^2 pressure $p^{(2)}$ that drives a return flow $\mathbf{u}_{\text{RF}}$ below the wave group. The structure of this flow was first computed by Longuet-Higgins & Stewart (1962) (see chapter 2) through a spectral analysis that extracted a mean flow resulting from wave-wave interactions within the wave group. The perspective provided by our wave group analysis reveals that, ignoring dispersion, this return flow results from an effective mass source-sink dipole acting at the upper boundary of an irrotational fluid (see chapter 2).

The total wave-induced flow associated with surface waves is the sum of the divergent-flux induced flow and the return flow: $\mathbf{u}^{(2)} = u_{\text{DF}}\hat{\mathbf{i}} + \mathbf{u}_{\text{RF}}$, where $\hat{\mathbf{i}}$ is the unit vector in the x-direction.

4.3.2 Horizontally periodic internal waves

Plane periodic two-dimensional internal waves in Boussinesq fluid have a dispersion relation $\omega = Nk_x/|\mathbf{k}|$, in which $\mathbf{k} = (k_x, k_z)$ is the wave number vector and $N = \sqrt{-(g/\rho_0)d\bar{\rho}/dz}$ is the buoyancy frequency, which is a function of the background density gradient $\bar{\rho}$. The polarization relations for these waves expressed in terms of the vertical-displacement amplitude A_0 give the velocities:

$$u = i\frac{k_z}{k_x}\omega A_0 e^{i(k_x x + k_z z - \omega t)}, \quad w = -i\omega A_0 e^{i(k_x x + k_z z - \omega t)}. \tag{4.20a,b}$$

Using these expressions to compute the Lagrangian horizontal displacement of fluid parcels at order amplitude-squared, as in (4.13), gives zero. Thus there is no Stokes drift for internal waves. However, from the energy density, $E = \rho_0 N^2 {A_0}^2/2$, one can determine the pseudo-momentum:

$$\mathcal{P} \equiv \frac{k_x}{\omega}E = \text{sgn}(k_x)\frac{1}{2}\rho_0 N|\mathbf{k}|{A_0}^2, \tag{4.21}$$

in which $\text{sgn}(k_x)$ denotes the sign of the horizontal wave number. And so one can infer a corresponding induced flow:

$$u_P \equiv \text{sgn}(k_x)\frac{1}{2}N|\mathbf{k}|{A_0}^2. \tag{4.22}$$

From Hamiltonian fluid mechanics (Scinocca and Shepherd 1992) or through consideration of the circulation associated with isopycnals displaced by periodic internal waves (cf. §3.4.5 of Sutherland (2010)), the wave-induced flow is alternately expressed by $-\langle\xi\zeta\rangle_x$, the negative correlation of the vertical displacement (ξ) and span-wise vorticity (ζ) fields. Using the polarization relations, it is straightforward to show that this expression is equivalent to that given by u_P in (4.22).

As above, we reconsider this problem by examining the evolution of quasi-monochromatic internal wave groups (Sutherland 2006b, Dosser and Sutherland 2011a) (cf. §3.4.5 of Sutherland (2010)). In this section we suppose the wave group is horizontally periodic but vertically localized with vertical displacement field is given by:

$$\xi^{(1)} = A(Z,T)e^{i(k_x x + k_z z - \omega t)}, \tag{4.23}$$

in which $A(Z,T)$ is the (complex) amplitude envelope of the wave group that translates at the vertical group velocity c_{gz}, as represented by the choice of the slow scale $Z = \epsilon_z(z - c_{gz}t)$, in which $\epsilon_z \equiv 1/(k_x\sigma_z)$ where σ_z measures the vertical extent of the wave group. The effects of dispersion, which come in at higher order in ϵ_z, are expressed through the long time scale $T = \epsilon_z^2\, t$.

As in (4.20), the corresponding horizontal and vertical velocity fields at leading order in ϵ are:

$$u^{(1)} = i\frac{k_z}{k_x}\omega A(Z,T)\, e^{i(k_x x + k_z z - \omega t)}, \quad w^{(1)} = -i\omega A(Z,T)\, e^{i(k_x x + k_z z - \omega t)}, \qquad (4.24\text{a,b})$$

in which it is understood that the actual fields are the real parts of the expressions on the right-hand side. Again we consider the flux-form of the horizontal momentum equation (4.17). Because the wave group is horizontally periodic, the x-average of (4.17) gives the usual expression for momentum transport per unit mass:

$$\frac{\partial}{\partial t}\langle u\rangle_x = -\frac{\partial}{\partial z}\langle uw\rangle_x, \qquad (4.25)$$

where we let the angular brackets with the subscript x denote averaging over x. It is important to appreciate that u on the left-hand side of (4.25) does not represent the fluctuation horizontal velocity due to waves. If it were, the average would give zero. Instead $\langle u\rangle_x$ represents the horizontal mean flow that is induced by a wave group whose amplitude envelope varies in the vertical. This is not the irreversible mean flow that results from wave breaking. Rather, it is transient: it translates with the vertical group velocity of the wave group, the flow accelerating at the wave group's leading edge and decelerating at its trailing edge according to (4.25).

With this in mind, we expect $\langle u\rangle_x$ to depend on the slow variables Z and T. And so, continuing the informal separation of scales argument, the time derivative on the left-hand side of (4.25) is replaced by Z and T derivatives according to $\partial_t = -\epsilon_z c_{gz}\partial_Z + \epsilon_z^2\partial_T$, and the second of these is neglected under the assumption that ϵ_z is small. Likewise, $\partial/\partial z$ on the right-hand side of (4.25) becomes the slow vertical derivative $\epsilon_z\partial_Z$. And so we have to leading order in ϵ_z:

$$\langle u^{(2)}\rangle_x = \frac{1}{c_{gz}}\langle u^{(1)}w^{(1)}\rangle_x. \qquad (4.26)$$

The induced mean flow $\langle u^{(2)}\rangle$ is $O(\alpha^2)$, hence the superscript. Note that (4.26) is analogous to the well-known result that the mean energy of a wave times its group velocity is just the energy flux. Multiplying both sides of (4.26) by the background density ρ_0

and by c_{gz} gives the statement that the horizontal momentum times the vertical group velocity equals the vertical flux of horizontal momentum.

Substituting the horizontal and vertical velocities from (4.24), we obtain an explicit expression for the divergent-flux induced flow in terms of the amplitude envelope of the vertical displacement field:

$$u_{\mathrm{DF}} \equiv \langle u^{(2)} \rangle_x = \mathrm{sgn}(k_x) \frac{1}{2} N |\mathbf{k}| \, |A|^2. \tag{4.27}$$

For vertically as well as horizontally periodic waves, $A(Z,T) = A_0$, in which case u_{DF} reduces to the (4.22) for the wave-induced mean flow derived from the pseudo-momentum. Because (4.27) was derived for horizontally periodic wave groups, u_{DF} is independent of x and so itself is a divergence-free flow. Indeed, being derived from the horizontally averaged horizontal momentum equation (4.25), we see there is no additional induced flow that would result from an order amplitude-squared pressure field. For horizontally periodic internal wave groups, the divergent-flux induced flow (hence the pseudo-momentum per unit mass) is the total wave-induced flow.

4.4 Horizontally localized internal wave groups

4.4.1 The divergent-flux induced flow

Vertically and horizontally localized wave groups translate in the x-z plane at the group velocity $\mathbf{c}_g = (c_{gx}, c_{gz})$. As such, in addition to the slow variable $Z = \epsilon_z(z - c_{gz}t)$ used above, we introduce the slow scale in a frame translating at the horizontal group velocity $X = \epsilon_x(x - c_{gx}t)$, in which $\epsilon_x \equiv 1/(k_x\sigma_x)$ and σ_x measures the horizontal extent of the wave group. For convenience, we suppose $\sigma \equiv \sigma_x \sim \sigma_z$ so that $\epsilon \equiv \epsilon_x \sim \epsilon_z$. The slow variables are thus defined to be:

$$X = \epsilon(x - c_{gx}t), \quad Z = \epsilon(z - c_{gz}t), \quad T = \epsilon^2 t. \tag{4.28a,b,c}$$

Similar to (4.23), the leading-order vertical displacement field is:

$$\xi^{(1)}_{(0)} = A(X,Z,T) e^{i(k_x x + k_z z - \omega t)}, \tag{4.29}$$

in which the subscript and superscript emphasize that the term is $O(\epsilon^0 \alpha^1)$. Corresponding expressions for the horizontal and vertical velocity are found as in (4.24), respectively, but with the arguments to A additionally involving the slow variable X.

The flux-form of the horizontal momentum equation is again given by (4.17). But now we cannot meaningfully average in the horizontal. Neglecting pressure for now, we focus on the flow resulting from the vertical divergence of the horizontal momentum flux u_{DF}:

$$\partial_t u_{\mathrm{DF}} = -\partial_x \overline{u_{(0)}^{(1)} u_{(0)}^{(1)}} - \partial_z \overline{u_{(0)}^{(1)} w_{(0)}^{(1)}}. \tag{4.30}$$

As in (4.18), the over-line denotes the operation of effectively averaging with respect to the fast scales keeping only the slow variations.

Following the same procedure, we write the vertical momentum equation in flux-form and consider the slowly varying, order amplitude-squared terms crucially neglecting the mean pressure gradient and buoyancy forcing that arise at the same order. The resulting equation for the vertical component of the divergent-flux induced flow is thus given by:

$$\partial_t w_{\mathrm{DF}} = -\partial_x \overline{u_{(0)}^{(1)} w_{(0)}^{(1)}} - \partial_z \overline{w_{(0)}^{(1)} w_{(0)}^{(1)}}. \tag{4.31}$$

We now recast these equations in terms of the slow variables, keeping terms of order ϵ alone. In particular, at $O(\epsilon)$, the partial time-derivative on the left-hand sides of (4.30) and (4.31) becomes $\partial_t \sim -\epsilon c_{gx}\partial_X - \epsilon c_{gz}\partial_Z$. Thus we arrive at the pair of equations:

$$\mathbf{c}_g u_{\mathrm{DF}} = \overline{u_{(0)}^{(1)} \mathbf{u}_{(0)}^{(1)}}, \quad \mathbf{c}_g w_{\mathrm{DF}} = \overline{w_{(0)}^{(1)} \mathbf{u}_{(0)}^{(1)}}. \tag{4.32a,b}$$

Finally, using the polarization relations of the form (4.24), we derive an explicit expression for the divergent-flux induced flow of horizontally and vertically localized internal gravity wave groups:

$$(u_{\mathrm{DF}}, w_{\mathrm{DF}}) = \mathrm{sgn}(k_x)\frac{1}{2c_{gx}} N|\mathbf{k}|\,|A|^2 \mathbf{c}_g = \mathrm{sgn}(k_x)\frac{1}{2} N|\mathbf{k}|\,|A|^2 \Big(1, -\frac{k_z}{k_x}\Big). \tag{4.33}$$

The horizontal component is the same as that found for horizontally periodic wave groups in (4.27). But it is now evident that the divergent-flux induced flow has a vertical component as well. By way of illustration, figures 4.1a and b show the vertical displacement field and divergent-flux induced flow associated with a Gaussian wave group centered at the origin whose vertical displacement field is given by:

$$\xi = A_0 \exp\left[-\frac{1}{2}\left(\frac{x^2}{{\sigma_x}^2} + \frac{z^2}{{\sigma_z}^2}\right)\right] \cos(k_x x + k_z z), \tag{4.34}$$

with $k_z = -k_x$, $\sigma_x = \sigma_z = 20{k_x}^{-1}$ and $A_0 = 0.01{k_x}^{-1}$. The divergent-flux induced flow in

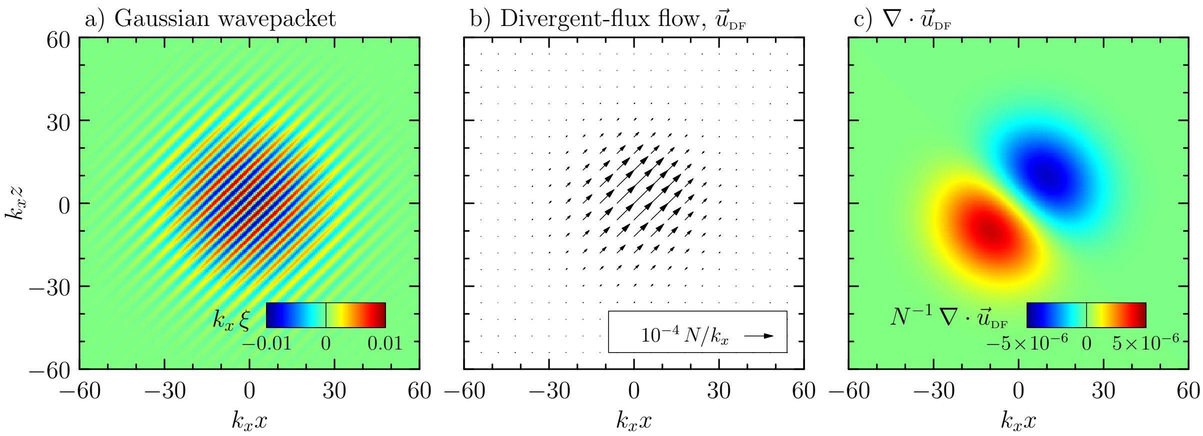

Figure 4.1: Vertical displacement field (a) associated with a localized internal wave group defined to propagate upward and to the right, its corresponding divergent-flux induced flow (b) given by (4.33) and the negative divergence of this induced flow field (c). The wave group is defined with $\mathbf{k} = k_x(1, 1)$, envelope width $\sigma = \sigma_x = \sigma_z = 20{k_x}^{-1}$ and amplitude $A_0 = 0.01k_x^{-1}$. The legend in panel b indicates the magnitude of the displayed arrow.

figure 4.1b is negligible except within the wave group itself and the direction of the flow is everywhere parallel to the group velocity vector.

Unlike the case of horizontally periodic waves, (4.33) cannot represent the total wave-induced flow. Computing the negative divergence of (4.33), shown in figure 4.1c, we see that there is a net transport of mass away from the trailing edge of the group and a net deposition of mass at the leading edge. The flow is not divergence free. So, as in the case of horizontally localized surface gravity wave groups, there must be a response flow that results in a divergence-free total wave-induced flow.

4.4.2 Total wave-induced flow and leading-order response flow

Here we derive an expression that predicts the leading-order, divergence-free, wave-induced flow that is the sum of the divergent-flux induced flow (4.33) and the response flow. After finding the total flow, it is straightforward to find the response flow.

As in §4.4.1, we consider a horizontally and vertically localized wave group whose vertical displacement field $\xi_{(0)}^{(1)}$ is given by (4.29), in which the slow variables are defined by (4.28). The polarization relations of plane waves give corresponding equations at first order in amplitude for the velocity $\mathbf{u}_{(0)}^{(1)}$ and the vorticity $\zeta_{(0)}^{(1)}$. Substituting these relations in the right-hand side of (4.10), gives the second-order amplitude equation:

$$L\psi^{(2)} = \nabla \cdot \Big[\partial_t\big(\zeta^{(1)}\mathbf{u}^{(1)}\big) + N^2\partial_x\big(\xi^{(1)}\mathbf{u}^{(1)}\big)\Big], \tag{4.35}$$

where the linear operator L is defined in (4.10) and, for now, we have included terms at all orders in ϵ arising from the various slow derivatives. If we substitute plane-wave solutions, for which $A(X, Z, T) = A_0$ is constant, into the right-hand side of (4.35), we find the operator is identically zero. This demonstrates the well-known result that plane periodic internal gravity waves satisfy the non-linear equations exactly. The total wave-induced flow, derived from the $O(\alpha^2)$ stream function $\psi^{(2)}$, is a consequence of the internal wave group having finite spatial extent as expressed by the small but non-zero value of ϵ.

However, if we use the $O(\alpha^1\epsilon^0)$ wave group equations for $\xi^{(1)}_{(0)}$, $\zeta^{(1)}_{(0)}$ and $\mathbf{u}^{(1)}_{(0)}$, as in (4.29), to compute the slowly varying products $\overline{\zeta^{(1)}_{(0)}\mathbf{u}^{(1)}_{(0)}}$ and $\overline{\xi^{(1)}_{(0)}\mathbf{u}^{(1)}_{(0)}}$ in (4.35), again we obtain zero. This is because the vertical displacement and vorticity fields associated with plane waves are 90° out of phase with the components of the velocity field. As shown in §4.4.4 and appendix G, the leading-order non-zero terms resulting from the products of vorticity and vertical displacement with velocity are $O(\alpha^2\epsilon)$. Therefore, the scales of each term in (4.35) are given as follows:

$$\Big[\underbrace{\partial_{tt}\big(\partial_{xx} + \partial_{zz}\big)}_{O(\alpha^0\epsilon^4)} + \underbrace{N^2\partial_{xx}}_{O(\alpha^0\epsilon^2)}\Big]\underbrace{\psi^{(2)}(X, Z)}_{O(\alpha^2\epsilon^0)} = \underbrace{\nabla \cdot \Big[\partial_t\big(\zeta^{(1)}\ \mathbf{u}^{(1)}\big) + N^2\partial_x\big(\xi^{(1)}\ \mathbf{u}^{(1)}\big)\Big]}_{O(\alpha^2\epsilon^3)}, \tag{4.36}$$

where we have assumed the divergence on the right-hand side induces a response expressed in terms of the stream function $\psi^{(2)}$, which is a function of the slow scales X and Z. Extracting the leading-order term, gives the differential equation $\epsilon^2\partial_{XX}\psi^{(2)}(X, Z) = 0$, which has the general solution:

$$\psi^{(2)} = f(Z)X - g(Z), \tag{4.37}$$

where $f(Z)$ and $g(Z)$ are arbitrary functions of the slow scale Z. Using (4.7), we find that the general velocity field for the leading-order total wave-induced flow in a frame of reference moving with the wave group is $(u^{(2)}, w^{(2)}) = (-f'(Z)X + g'(Z), f(Z))$. Requiring bounded horizontal flows as $X \to \pm\infty$, we must have $f'(Z) = 0$. And so $f(Z)$ is constant. But the additional requirement that the wave-induced vertical velocity must be zero as $Z \to \pm\infty$ means $f(Z) = 0$. Therefore at this order of approximation the total wave-induced flow is:

$$u^{(2)} = G(Z), \quad w^{(2)} = 0, \tag{4.38a,b}$$

in which $G(Z) \equiv g'(Z)$ is some function of Z. Thus we have shown that at $O(\alpha^2\epsilon^1)$ the total wave-induced flow has no vertical motion but extends horizontally far from the wave group.

These equations for the total wave-induced flow, together with the equations (4.33) for the divergent-flux induced flow of internal waves, give equations for the response flow $(u_{\mathrm{RF}}, w_{\mathrm{RF}})$. To satisfy (4.38b), we must have:

$$w_{\mathrm{RF}} = -w_{\mathrm{DF}} = \frac{1}{2}\frac{N^2 k_z}{\omega}\,|A|^2. \tag{4.39}$$

Because the total horizontal wave-induced flow $u^{(2)} = G(Z)$ is independent of x, momentum conservation dictates that the response flow at this order must act to spread the local divergent-flux induced flow u_{DF} horizontally uniformly in x. Explicitly, the horizontal component of the response flow is:

$$u_{\mathrm{RF}} = -u_{\mathrm{DF}} + \frac{1}{L_x}\int u_{\mathrm{DF}}\,dx, \tag{4.40}$$

in which the integral is performed over the horizontal extent of the domain L_x. Combining these results, the total wave-induced flow at $O(\alpha^2\epsilon)$ is:

$$\mathbf{u}^{(2)} = \Big(\frac{1}{L_x} I_{u,\mathrm{DF}}, 0\Big), \tag{4.41}$$

in which

$$I_{u,\mathrm{DF}} = \int u_{\mathrm{DF}}\,dx \tag{4.42}$$

is the horizontally integrated horizontal component of the divergent-flux induced flow. In particular, for a Gaussian wave group centered at the origin with vertical displacement given by (4.34), equations (4.33) and (4.42) give:

$$I_{u,\mathrm{DF}} = \mathrm{sgn}(k_x)\frac{1}{2}\sqrt{\pi}\,\sigma_x\; N|\mathbf{k}|A_0^2\,e^{-z^2/\sigma_z{}^2}. \tag{4.43}$$

4.4.3 Horizontal long wave response: scaling considerations

At first glance, (4.41) suggests the counter-intuitive prediction that the wave-induced flow decreases to zero as the horizontal extent of the domain in which the wave group propagates extends to infinity. Yet, it must be kept in mind that the prediction (4.38) arises as a result of truncating the perturbation expansion on the right-hand side of (4.36) at $O(\alpha^2\epsilon^2)$. As we will show in §4.4.4, by considering terms at $O(\alpha^2\epsilon^3)$ on the right-hand side of (4.36), the wave-induced flow at higher order in ϵ is in fact a horizontally long internal wave that translates vertically with the wave group.

This insight does not negate the usefulness of results in §4.4.2. In the wave group's immediate surroundings, the wave-induced flow does appear to be horizontally uniform. Only in the far field to either side of the wave group does the horizontal flow gradually decrease to zero. Nonetheless, the horizontal extent of the induced flow is finite. And so it is not useful to compute the average of a localized horizontal flow over the domain as in (4.41). It is useful, however, to characterize the magnitude of the induced horizontal flow in terms of the integral given by (4.42). Here we use this diagnostic and physical reasoning to make order-of-magnitude estimates for the structure of the long wave induced by the wave group. The estimates will be compared with the long wave properties derived more rigorously in §4.4.4.

We imagine the wave group as a translating body force in a stratified ambient that excites a long, hence hydrostatic, internal wave. This part of the induced flow we describe as the "response wave". Its spatio-temporal structure (denoted by 'r' subscripts) is described by the following three relationships:

$$\omega_r = N\frac{k_{xr}}{|k_{zr}|}, \qquad \frac{\omega_r}{k_{zr}} = c_{gz}, \qquad |k_{zr}| \simeq \frac{2\pi}{4\sigma_z}. \tag{4.44a,b,c}$$

The first identity is the dispersion relation for long waves ($|k_{xr}| \ll |k_{zr}|$). The second identity equates the vertical phase speed of the response wave to the vertical group velocity of the localized wave group c_{gz}, which is the source of the response waves. Finally, assuming the localized wave group travels rightward, the horizontal velocity field associated with the response wave near the localized wave group must be positive over the total vertical extent $\sim 2\sigma_z$ of the localized wave group. This gives rise to the third expression for the approximate vertical wave number of the response wave.

Combining the expressions in (4.44) gives the horizontal wave number of the response wave and the lateral extent of the disturbance L_i, estimated to be half a horizontal wavelength of the response wave:

$$|k_{xr}| = \frac{|c_{gz}|}{N}\,k_{zr}^2 \simeq \Big(\frac{\pi^2}{4}\frac{k_x^2|k_z|}{|\mathbf{k}|^3}{\epsilon_z}^2\Big)\;k_x, \quad L_i = \pi/|k_{xr}| \simeq \Big(\frac{4}{\pi}\frac{|\mathbf{k}|^3}{k_x^2|k_z|}\;\epsilon_x{\epsilon_z}^{-2}\Big)\;\sigma_x. \tag{4.45a,b}$$

The scaling for $|k_{xr}|$ emphasizes that the response wave is long compared to the horizontal wave number of the waves k_x, and the scaling for L_i emphasizes that the horizontal extent of the long wave is indeed much wider than the wave group extent σ_x, under the assumption that $\epsilon_x \sim \epsilon_z$. The scaling relationship for L_i is alternatively found by considering the distance travelled by a long wave at its horizontal group velocity $|c_{gxr}| \simeq N|k_{xr}|/{k_{zr}}^2$ over the time, σ_z/c_{gz}, in which the wave group travels vertically at its group velocity over its vertical extent. Likewise, by examining characteristic velocity and time scales, Bretherton (1969b) proposed the scaling $L_i \sim \epsilon^{-1} N {\sigma_z}^2/c_{gz}$, in which $\epsilon = \epsilon_x \sim \epsilon_z$. By matching the dispersion characteristics of the wave group and the response wave, (4.45) is more explicit in the dependence of L_i on the vertical and horizontal extents of the wave group.

The response wave should emanate from the localized wave group qualitatively like a bow wave. The corresponding magnitude of the slope of lines of constant phase of the response wave is:

$$\left|\frac{k_{xr}}{k_{zr}}\right| = \frac{\pi}{2}\cos^2\theta \sin|\theta|\ \epsilon_z, \tag{4.46}$$

which, being small, is consistent with this being a long wave.

The amplitude of the response wave is estimated by the requirement that the horizontal integral of the horizontal flow over a crest of the long wave should equal $I_{u,\mathrm{DF}}$, given by (4.42). Thus the amplitude of the horizontal velocity associated with the long wave is:

$$A_{0ur} \simeq \frac{1}{2} k_{xr} I_{u,\mathrm{DF}}. \tag{4.47}$$

In particular, for the Gaussian wave group given by (4.34), we estimate:

$$A_{0ur} \simeq \frac{\pi^2}{16}(\sqrt{\pi}\sigma_x)\frac{N k_x^3 |k_z|}{|\mathbf{k}|^2}\ |A_0|^2 {\epsilon_z}^2 = \frac{\pi^{5/2}}{16}\frac{N|k_z|}{|\mathbf{k}|^2}\ \alpha^2 {\epsilon_x}^{-1} {\epsilon_z}^2, \tag{4.48}$$

in which we have used (4.43). Because the divergent-flux induced flow has spread laterally over a distance of order L_i, the total wave-induced flow within the wave group, estimated by A_{0ur}, is smaller than u_{DF} by a factor ${\epsilon_x}^{-1}{\epsilon_z}^2$.

4.4.4 Estimation of the horizontal long wave response

In §4.4.2 we derived the fully non-linear equation (4.10) expressed in terms of a linear response $L\psi$ to non-linear forcing $\nabla\cdot\mathbf{F}$. There we showed that substitution of the leading-order fields associated with the wave group into the quadratic terms of $\mathbf{F}$ gives zero. One must express the fields associated with the wave group to next order in ϵ in order to produce a non-trivial non-linear forcing term. The details of this calculation are provided in appendix G. Therein we derive expressions for $\mathbf{u}$, ξ and ζ at $O(\alpha^1\epsilon^1)$ and from these we find $\nabla\cdot\mathbf{F}$ at $O(\alpha^2\epsilon^3)$.

With the insight provided in §4.4.3, we expect the non-linear forcing given by (G.6) to excite a disturbance that is long compared to the horizontal extent of the forcing region. Following Bretherton (1969b), we therefore approximate the x-dependent forcing by a Dirac delta function. Explicitly, we write the non-linear forcing term as:

$$(\nabla\cdot\mathbf{F})_3^{(2)} \simeq \mathcal{N}(\tilde{z})\delta(k_x\tilde{x}), \tag{4.49}$$

in which:

$$\mathcal{N}(\tilde{z}) = k_x\int_{-\infty}^{\infty}(\nabla\cdot\mathbf{F})_3^{(2)}\,d\tilde{x}. \tag{4.50}$$

For later convenience, we have written the result in terms of the fast variables in a reference frame translating at the group velocity of the wave group $\tilde{x} = X/\epsilon = x - c_{gx}t$ and $\tilde{z} = Z/\epsilon = z - c_{gz}t$. In particular, if the amplitude envelope of the vertical displacement field is a Gaussian in the horizontal so that $A(\tilde{x},\tilde{z}) = A_0\exp[-\tilde{x}^2/(2\sigma_x^2)]\ \mathcal{A}(\tilde{z})$ with $||\mathcal{A}|| = 1$, then (4.50) together with (G.6) gives:

$$\mathcal{N}(\tilde{z}) = -\frac{1}{2}(\sqrt{\pi}\,\sigma_x)\,N^3\frac{k_x^3k_z^2}{|\mathbf{k}|^5}A_0^2\partial_{\tilde{z}\tilde{z}\tilde{z}}|\mathcal{A}|^2. \tag{4.51}$$

In deriving this result we note that the integral in $\tilde{x}$, hence in X, eliminates all terms in (G.6) that involve at least one X derivative. The term that remains results from the vertical divergence of $\partial_t(\overline{\zeta w})$. Transforming from Z- to $\tilde{z}$-derivatives results in the implicit appearance of $\epsilon_z^3 = (k_x\sigma_z)^{-3}$.

To find the induced long wave response at $O(\alpha^2)$ to the non-linear forcing of a horizontally Gaussian wave group, we solve for the stream function $\psi^{(2)}$ by substituting (4.49) and (4.51) on the right-hand side of (4.10). On the left-hand side we solve in the vertically translating frame and make use of the long wave approximation so that $\partial_{tt}\sim -c_{gz}^2\partial_{\tilde{z}\tilde{z}}$ and $\partial_{xx}+\partial_{zz}\sim\partial_{\tilde{z}\tilde{z}}$. Explicitly, we have:

$$\left(c_{gz}^2\partial_{\tilde{z}\tilde{z}\tilde{z}\tilde{z}} - N^2\partial_{\tilde{x}\tilde{x}}\right)\psi^{(2)} = \mathcal{N}(\tilde{z})\delta(k_x\tilde{x}). \tag{4.52}$$

The solution is found by taking the double Fourier transform in $\tilde{x}$ and $\tilde{z}$ of the resulting differential equation. We begin by taking the Fourier transform of the right-hand side

(4.49) with $\mathcal{N}(\tilde{z})$ given by (4.51):

$$\int_{-\infty}^{\infty}\int_{-\infty}^{\infty}(\nabla\cdot\mathbf{F})_3^{(2)}e^{-i(\kappa\tilde{x}+\mu\tilde{z})}d\tilde{x}d\tilde{z}=\frac{i\pi}{2}N^3\frac{k_x^2k_z^2}{|\mathbf{k}|^5}A_0^2\sigma_x\sigma_z\;\mu^3\widehat{|\mathcal{A}|^2},\tag{4.53}$$

in which $\widehat{|\mathcal{A}|^2}(\mu)$ is the Fourier transform of $|\mathcal{A}|^2(\tilde{z})$. In particular, if the wave group is a Gaussian in the vertical as well as horizontal such that $\mathcal{A}=\exp(-\tilde{z}^2/2\sigma_z^2)$, we have the Fourier transform pair:

$$|\mathcal{A}|^2=\exp(-\tilde{z}^2/\sigma_z^2),\quad \widehat{|\mathcal{A}|^2}=\exp(-(\mu\sigma_z)^2/4).\tag{4.54}$$

The solution to (4.52) in Fourier space is given generally by:

$$\hat{\psi}^{(2)}(\kappa,\mu)=\frac{i\pi}{2}N^3\frac{k_x^2k_z^2}{|\mathbf{k}|^5}A_0^2\sigma_x\sigma_z\;\frac{\mu^3\widehat{|\mathcal{A}|^2}}{c_{gz}^2\mu^4-N^2\kappa^2}.\tag{4.55}$$

While inverting the double Fourier transform to obtain the solution for $\psi^{(2)}$ in real space, the integral with respect to κ can be evaluated explicitly. In doing so, it is necessary to select the branch cut corresponding to outgoing waves (Bretherton 1969b). Thus we find:

$$\psi^{(2)}(\tilde{x},\tilde{z})=-\frac{1}{8}N\frac{k_xk_z}{|\mathbf{k}|^2}A_0^2\sigma_x\sigma_z\;\int_0^{\infty}\widehat{|\mathcal{A}|^2}\mu\cos\big(\mu\tilde{z}+\mu^2\frac{c_{gz}|\tilde{x}|}{N}\big)d\mu,\tag{4.56}$$

which corresponds to the solution given by (3.15-3.16) in Bretherton (1969b). Therefore the horizontal flow associated with the induced long wave is:

$$u^{(2)}(\tilde{x},\tilde{z})=-\frac{1}{8}N\frac{k_xk_z}{|\mathbf{k}|^2}A_0^2\sigma_x\sigma_z\;\int_0^{\infty}\widehat{|\mathcal{A}|^2}\mu^2\sin\big(\mu\tilde{z}\;+\;\mu^2\frac{c_{gz}|\tilde{x}|}{N}\big)d\mu,\tag{4.57}$$

In particular, for a bivariate Gaussian wave group, according to (4.54) we have

$$\psi^{(2)}(\tilde{x},\tilde{z})=-\frac{1}{8}N\frac{k_xk_z}{|\mathbf{k}|^2}A_0^2\frac{\sigma_x}{\sigma_z}\;\int_0^{\infty}e^{-\hat{\mu}^2/4}\hat{\mu}\cos\big(\hat{\mu}\frac{\tilde{z}}{\sigma_z}+\hat{\mu}^2\frac{c_{gz}|\tilde{x}|}{N\sigma_z^2}\big)d\hat{\mu}\tag{4.58}$$

and

$$u^{(2)}(\tilde{x},\tilde{z})=-\frac{1}{8}N\frac{k_xk_z}{|\mathbf{k}|^2}A_0^2\frac{\sigma_x}{\sigma_z^2}\;\int_0^{\infty}e^{-\hat{\mu}^2/4}\hat{\mu}^2\sin\big(\hat{\mu}\frac{\tilde{z}}{\sigma_z}+\hat{\mu}^2\frac{c_{gz}|\tilde{x}|}{N\sigma_z^2}\big)d\hat{\mu}.\tag{4.59}$$

where $\hat{\mu}=\mu\sigma_z$, so that the integral-terms in (4.58-4.59) are non-dimensional.

Figure 4.2 plots the predicted stream function and horizontal velocity associated with the long wave induced by an upward-propagating Gaussian wave group given by (4.34). Clearly the induced wave is significantly longer than the horizontal extent of the wave group, which is $\sigma_x=20k_x^{-1}$. From (4.45b), the predicted horizontal extent of the wave

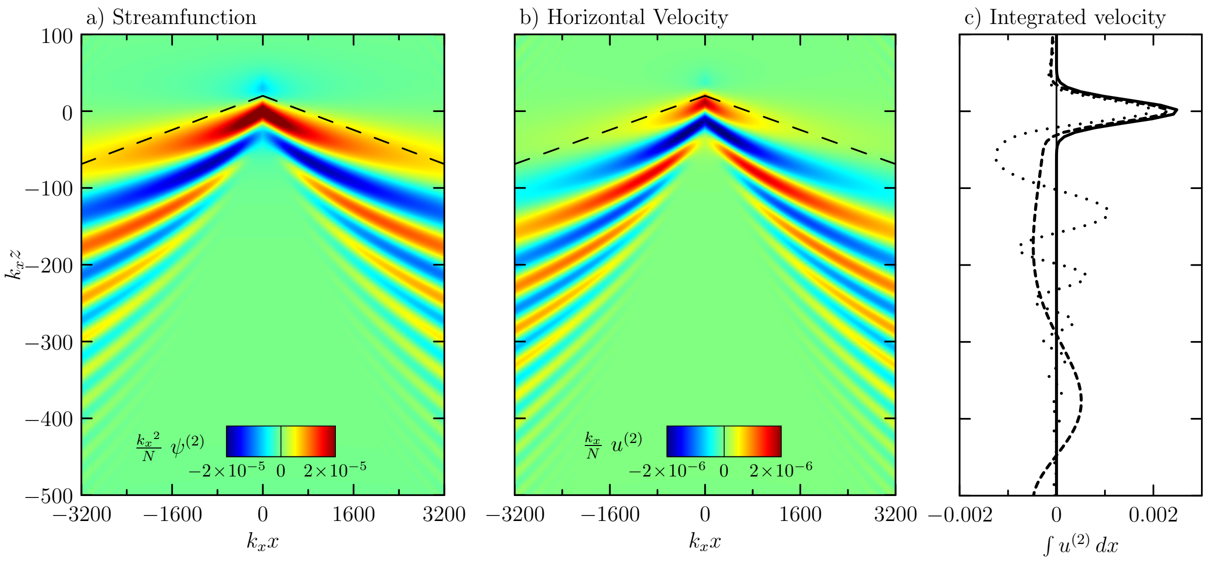

Figure 4.2: Predicted stream function (a) and horizontal velocity field (b) of the long wave induced by a Gaussian wave group centered at the origin with $k_z = -k_x$, $k_x\sigma_x = k_x\sigma_z = 20$ and $k_x\, A_0 = 0.01$. The diagonal dashed lines in panels a and b indicate the predicted slope of phase lines of the long wave according to (4.46). Panel c shows the horizontal integral of the horizontal velocity predicted by theory (solid line) and computed numerically in a finite sized domain with $-500 \le k_x z \le 100$ and $-3217 \le k_x x \le 3217$ (dotted line) and with $-5500 \le k_x z \le 500$ and $-25736 \le k_x x \le 25736$ (dashed line).

group is $L_i \simeq 1440 k_x^{-1}$, which is a reasonable estimate of the lateral extent of the induced long waves to either side of the wave group at $z = 0$. Below the wave group the induced long waves extend much further laterally, spreading in a manner qualitatively similar to that of a bow wake.

Crucially, these lee waves have zero net horizontal momentum associated with them. Even though the induced long wave has alternating positive and negative horizontal velocity field, as anticipated from the results in §4.4.2 these cancel upon integration except at the level of the wave group itself. This can be shown by horizontally integrating (4.57):

$$\int_{-\infty}^{\infty} u^{(2)}\, dx = N|\mathbf{k}|(\sqrt{\pi}\sigma_x) \int_0^{\infty} \widehat{|\mathcal{A}|^2} \cos(\hat{m}\tilde{z})\, d\hat{m} = \frac{1}{2} N|\mathbf{k}|(\sqrt{\pi}\sigma_x)\ |\mathcal{A}|^2. \tag{4.60}$$

This is equal to the horizontal integral of the horizontally integrated divergent-flux flow given generally by (4.33) and (4.42), and given explicitly by (4.43) for a wave group that is Gaussian in the vertical and horizontal. The result is plotted as the thick solid line in figure 4.2c.

Although the horizontally integrated flow is strictly positive, the local horizontal flow about the wave group itself changes sign in the vertical. In particular, from (4.59) a wave group with bivariate Gaussian amplitude envelope has an induced horizontal velocity profile along its horizontal center given by:

$$u^{(2)}(\tilde{x}=0,\tilde{z}) = \frac{1}{2}N\frac{k_x k_z}{|\mathbf{k}|^2}A_0^2\frac{\sigma_x}{\sigma_z^2}\Big[-\frac{\tilde{z}}{\sigma_z} + \Big(2\big(\frac{\tilde{z}}{\sigma_z}\big)^2 - 1\Big)\, D(\tilde{z}/\sigma_z)\Big], \tag{4.61}$$

in which $D(x) = e^{-x^2}\int_0^x e^{t^2}\,dt = (1/2)\int_0^\infty e^{-t^2/4}\sin(xt)\,dt$ is Dawson's integral (Press et al. 2007). Because $D(x)$ is an odd function, it is evident that $u^{(2)}$ is zero at the vertical center of the wave group and begins positive above and negative below, if the wave group propagates upward and to the right. This result has potentially important consequences for the modulational stability of moderately large amplitude internal wave groups. The stability of horizontally periodic Boussinesq internal waves was assessed through the derivation of a non-linear Schrödinger equation in which the non-linear term was strictly positive as a consequence of the wave-induced mean flow being positive (Sutherland 2006b). Though beyond the scope of this chapter, future work will consider the weakly non-linear influence on a wave group of an induced horizontal flow that changes sign over its vertical extent.

Finally, we comment on the implementation of these results in numerical simulations. For this purpose, the Fourier transforms in (4.58) and (4.59) must be estimated by computing Fourier series in a finite sized domain. Because the lee wave, shown for example in figure 4.2b, has significant amplitude far from the wave group, this means that the inverse transform must be computed on a very wide and deep domain in order to reproduce properly the horizontally integrated horizontal flow. To illustrate this, in figure 4.2c we also plot the horizontally integrated, horizontal flow found by inverse transforming (4.59) on two different sized domains. In a domain with the horizontal and vertical extent of the fields plotted in figure 4.2a and b, the horizontally integrated horizontal velocity is moderately smaller than that predicted by (4.43) about the level of the wave group and at greater depths it alternates between positive and negative flows whose magnitude decreases with vertical distance away from the wave group. These result because the lee wave is significant at the sides of the domain. If the domain is much wider (over 200 times the wave-group width), the computed horizontally integrated flow is closer to the prediction (4.43) and there is better cancellation of the positive and negative flows with depth.

Although accurate numerical calculation of the integrated horizontal velocity requires a large domain, the stream function, horizontal velocity, and other fields associated with the long wave change negligibly about the location of the wave group if the domain is sufficiently wide (i.e. about $4L_i$) and sufficiently deep so that the trailing waves have negligible amplitude at the bottom of the domain. All of this is to say that numerical simulations of a wave group that include the predicted lee wave as an initial condition would have to be performed on (perhaps impractically) large domains in order to give an accurate representation of the momentum transport expressed through the horizontally integrated horizontal flow. This insight guides the design of the numerical simulations used to test the predictions of theory.

4.5 Numerical simulations

4.5.1 Numerical model and initial conditions

The evolution of internal wave groups in a uniformly stratified fluid is simulated using a code that solves the fully non-linear, Boussinesq Navier Stokes equations in two dimensions (Sutherland and Peltier 1994). Instead of directly solving the momentum equations, the code evolves the span-wise vorticity field $\zeta \equiv (\nabla \times \mathbf{u}) \cdot \hat{\mathbf{j}}$, where $\hat{\mathbf{j}}$ is the unit vector in the y-direction (into the plane), so ζ is not a vector here. The evolution equation of the span-wise vorticity is found from taking the curl of the momentum equations. As discussed in §4.4.2, instead of considering density perturbations, we evolve the vertical displacement field $\xi \equiv -(\bar{\rho}')^{-1}\rho$ through manipulation of the internal energy equation (4.6).

Explicitly, ξ and ζ are advanced in time according to the (non-dimensional) equations obtained from (4.6) and (4.8) with added viscous damping and thermal diffusion terms:

$$\begin{aligned} \frac{\partial \xi}{\partial t} &= -u\frac{\partial \xi}{\partial x} - w\frac{\partial \xi}{\partial z} + w + \frac{1}{\mathrm{RePr}}\mathcal{D}\xi, \\ \frac{\partial \zeta}{\partial t} &= -u\frac{\partial \zeta}{\partial x} - w\frac{\partial \zeta}{\partial z} + \frac{g}{\rho_0}\frac{\partial \rho}{\partial x} + \frac{1}{\mathrm{Re}}\mathcal{D}\zeta, \end{aligned} \tag{4.62}$$

in which $\mathcal{D}$ represents a diffusivity operator and we set the Prandtl number to be $\mathrm{Pr} = 1$ and the Reynolds number $\mathrm{Re} \equiv (N/{k_x}^2)/\nu = 10^6$. The effects of diffusivity are included to ensure numerical stability, but their influence is set to be negligible as far as the evolution of the wave group and induced mean flow is concerned. To minimize the influence of diffusivity on the wave group and wave-induced flow, in the simulations reported upon here, Laplacian diffusivity acts only on disturbances with horizontal wave numbers much larger than the wave number of the localized wave group k_x. The equations are solved in a horizontally periodic domain with free-slip upper and lower boundaries. The fields themselves are discretized by Fourier modes in the horizontal and by discrete evenly spaced grid points in the vertical. In this horizontal Fourier space, in which $\partial_x \to ik$, the diffusivity operator is expressed by:

$$\mathcal{D} = \begin{cases} 0 & k \leq k_\star \\ -k^2 + \partial_{zz} & k > k_\star. \end{cases} \tag{4.63}$$

In the simulations reported on here we set the cut-off wave number to be $k_\star = 2k_x$.

Given ζ, the stream function is found by inverting Poisson's equation $\zeta = -\nabla^2\psi$, which is equivalent to inverting a tri-diagonal matrix in horizontal Fourier space. From ψ, the velocity components are found using (4.7). The simulation is initialized by a Gaussian wave group whose vertical displacement field in general is given in real-space by:

$$\xi(x, z, t = 0) = A(x, z, 0)\ \cos(k_x x + k_z z). \tag{4.64}$$

In simulations of vertically localized and horizontally periodic wave groups centered initially at the origin, the amplitude envelope is $A(x, z, 0) = A_0 \exp[z^2/(2{\sigma_z}^2)]$ and the width of the domain is set to be $\lambda_x = 2\pi/k_x$. In simulations of horizontally and vertically localized wave groups the amplitude envelope is given as in (4.34) by $A(x, z, 0) = A_0 \exp[x^2/(2{\sigma_x}^2) + z^2/(2{\sigma_z}^2)]$ and the width of the domain is set to be very much larger than σ_x. In either case, assuming small amplitude quasi-monochromatic wave groups, linear theory is used to initialize the corresponding vorticity field through:

$$\zeta(x, z, t = 0) = A_\zeta\ \cos(k_x x + k_z z), \tag{4.65}$$

in which $A_\zeta \equiv N({k_x}^2 + {k_z}^2)^{1/2} A$.

Here we report on simulations of the wave group examined in §4.4. Explicitly, using ${k_x}^{-1}$ and N^{-1} to define the characteristic length and time scales, we set $k_z = -k_x$ and $A_0 = 0.01{k_x}^{-1}$. According to the dispersion relation, the wave has constant-phase lines oriented at 45° to the vertical and the wave group propagates upward to the right at group velocity $(c_{gx}, c_{gz}) = N/(2\sqrt{2}k_x)\ (1, 1)$. The vertical extent of the wave group is $\sigma_z = \sigma \equiv 20{k_x}^{-1}$ ($\epsilon_z = 0.05$) and in horizontally localized wave group simulations we also set $\sigma_x = \sigma$ ($\epsilon_x = 0.05$).

According to (4.45), the horizontal extent of the induced long wave is expected to be on the order of $L_i = 3200\sqrt{2}/\pi\ {k_x}^{-1} \simeq 1440{k_x}^{-1}$ on either side of the wave group. With this in mind, in simulations of horizontally localized wave groups the horizontal extent of the domain is set to be $1024\lambda_x = 6434{k_x}^{-1}$. We will show that this is sufficiently wide that the periodic boundary conditions do not affect the wave group or the induced mean flow about the level of the wave group as it translates upwards.

For straightforward comparison of the numerical results with theory, the wave group is situated initially with its centre at the origin. Thus, after time $Nt = 200$, the wave group is expected to be centered about $(x, z) \simeq (70.7, 70.7)k_x^{-1}$ after propagating diagonally a distance of approximately 5σ. At this location, after the transient start-up time resulting from choosing the initial ambient to be stationary, we may reasonably compare the measured flow induced by the wave group with the predictions of steady state theory. This is demonstrated explicitly below in the examination of the horizontally periodic wave group. The upper and lower boundaries of the domain are situated at $z = 200{k_x}^{-1}$ and $z = -100{k_x}^{-1}$, sufficiently far so that these do not influence the wave group evolution over the duration of a simulation.

For horizontally periodic, vertically localized wave groups, Sutherland (2006b) showed that one should also superimpose on the perturbation fields the horizontal component of the wave-induced flow, given by (4.33) for rightward-propagating waves: $u_{\text{DF}}(z, t = 0) = -\langle\xi\zeta\rangle_{t=0} = (1/2)N|\mathbf{k}||A_0(z)|^2$, in which $A_0(z) = A(z, t = 0)$ is the initial amplitude envelope of the vertical displacement field. This is not a steady background flow but the transient induced mean horizontal flow at $t = 0$, which at later times translates vertically at the vertical group velocity with the wave group. If a simulation is initialized with zero mean horizontal flow then, by momentum conservation, the vertically integrated mean horizontal momentum must be zero for all time. So the zero mean flow initial condition is actually specifying a wave group initially situated at the level of a steady background flow with flow profile $\bar{u} = -u_{\text{DF}}(z, t = 0)$. In these simulations, as time progresses and the wave moves vertically away from its initial position, the steady background flow is revealed about the initial position of the wave group while the opposite signed transient flow is observed to translate vertically with the wave group which, neglecting dispersion, is given by $\overline{u}_{\text{DF}} \equiv (1/2)N|\mathbf{k}||A_0(\tilde{z})|^2$, with $\tilde{z} = z - c_{gz}t$.

For horizontally and vertically localized wave groups, it is not appropriate to superimpose on the wave field the divergent-flux induced flow u_{DF}, because this is a divergent flow. Instead of making assumptions about the divergent-flux and response flow a priori, here we initialize without a wave-induced flow altogether and observe how the induced flow evolves as the wave group propagates. We will see that for both horizontally periodic and horizontally localized wave groups, the horizontal velocity field evolves so that there is a horizontally integrated horizontal flow that translates with the wave group while a nearly equal and opposite but non-translating flow appears about the initial vertical location of the wave group.

4.5.2 Horizontally periodic wave group simulation

First, a simulation with a horizontally periodic wave group is performed with zero initial mean horizontal flow. This provides a basis for comparison with horizontally localized wave groups. The results are shown in figure 4.3. The initial condition in figure 4.3a shows contours of the horizontal velocity field to the left and to the right shows the vertical profile of the horizontally integrated horizontal flow:

$$I_u \equiv \int_{-L_x}^{L_x} u \, dx, \tag{4.66}$$

in which the horizontal extent of the domain is the horizontal wavelength: $\lambda_x = 2L_x$. Because the wave group is horizontally periodic and we have not superimposed a mean background flow initially, $I_u(z, t = 0) = 0$ for all z.

At later times, the wave group is seen to propagate upwards at the predicted vertical group speed, being centered around $z \simeq 70k_x^{-1}$ at time $Nt = 200$. During its propagation, the horizontally integrated flow develops into a "double-jet" profile. A negative jet centered around $z = 0$ is evident at $Nt = 100$ and remains centered there at $Nt = 200$. Meanwhile a positive jet appears, being centered around $z = 35{k_x}^{-1}$ at $Nt = 100$ and around $z = 70{k_x}^{-1}$ at $Nt = 200$. At this last time, the lower positive jet conforms almost exactly to the predicted horizontally integrated divergent-flux induced flow, defined by (4.42). Explicitly, the dashed line shows:

$$I_{u,\mathrm{DF}} = \lambda_x \left\{ \frac{1}{2} N |\mathbf{k}| {A_0}^2 \exp\left[-(z - c_{gz}t)^2 / {\sigma_z}^2 \right] \right\}. \tag{4.67}$$

This simple prediction assumes the wave group translates at the group velocity from its initial position at the origin and does not disperse. Indeed the small discrepancy between I_u and $I_{u,\mathrm{DF}}$ at $Nt = 200$ about $z = 70{k_x}^{-1}$ is the result of dispersion. If $I_{u,\mathrm{DF}}$ is computed using $|A(z,t)|^2$ rather than $|A(z - c_{gz}t, t = 0)|^2$, the curves exactly overlap about $z = 70{k_x}^{-1}$.

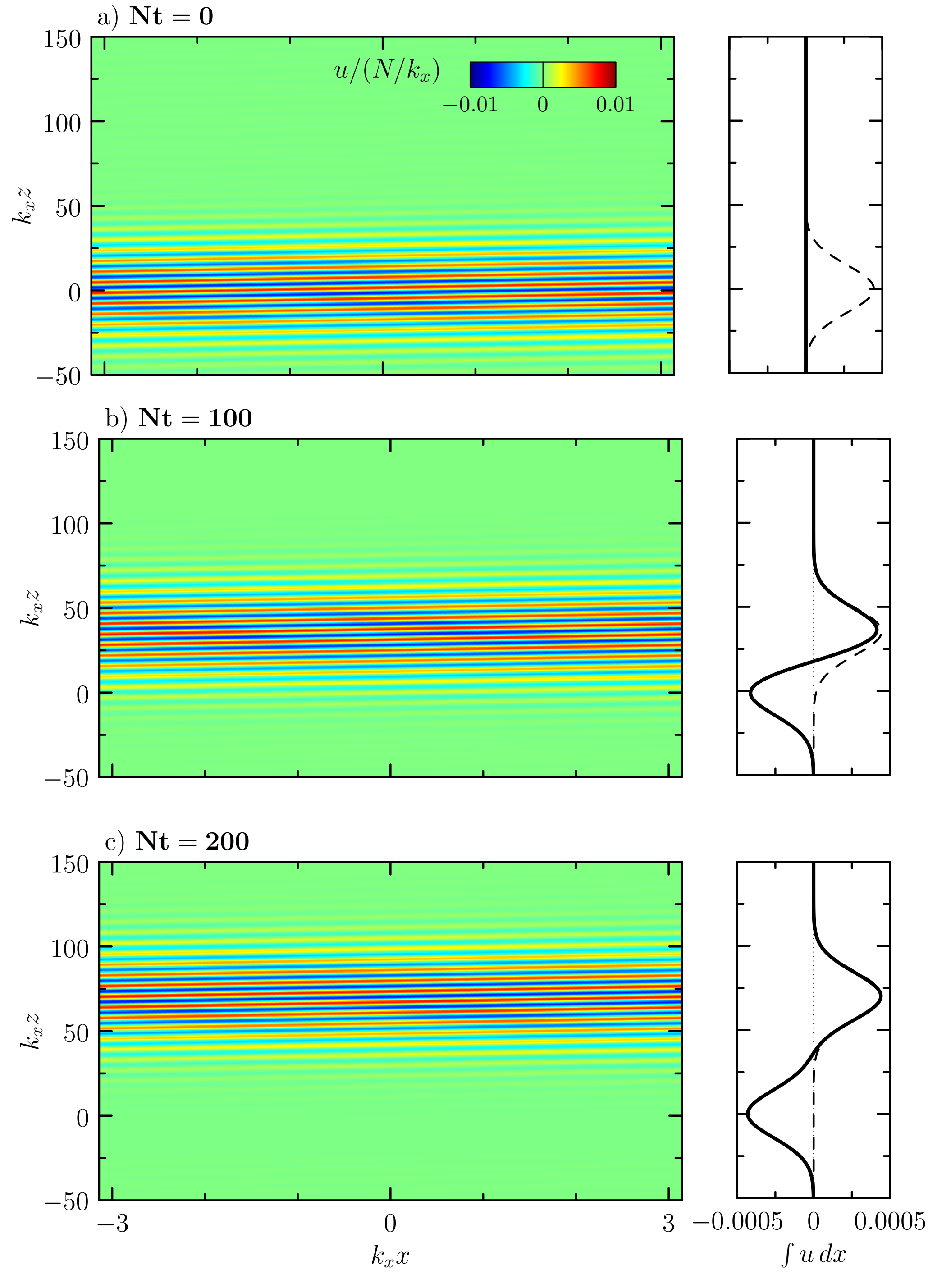

Figure 4.3: Numerical simulation of a horizontally periodic wave group at times $Nt =$ (a) 0, (b) 100 and (c) 200. The left panels show the horizontal velocity field, the right panels show the horizontally integrated horizontal flow I_u (black line). The dashed line plots the predicted integrated horizontal induced flow given by (4.67).

Momentum conservation for a Boussinesq fluid predicts that the domain integrated horizontal flow $\int I_u\, dz$ is unchanging in time. In our simulations, we indeed find that $\int I_u\, dz = 0$ at each time step. In particular, at $Nt = 200$ the positive momentum associated with the lower positive jet is exactly cancelled by the upper negative jet situated around $z = 0$. This result reaffirms the assertion by Sutherland (2006b) that simulations of horizontally periodic, vertically localized wave groups in otherwise stationary fluid should nonetheless have a non-zero mean flow, $\bar{u}(z, t = 0) = u_{\rm DF}$, imposed at the outset. To require zero mean flow, as we have done in the simulation shown in figure 4.3, means that one is actually simulating a wave group centered about a (steady) background negative jet whose speed is equal and opposite to the (transient) divergent-flux induced flow so that the sum of both equals zero at each height z. When the wave group propagates vertically away, the wave-induced flow moves with the waves and reveals itself as a positive, through vertically translating horizontal jet. Simultaneously, the steady negative background jet is revealed.

Herein, the primary purpose of figure 4.3 is to demonstrate that the wave-induced flow has fully separated from the background flow at $Nt = 200$. And so at this time, in a frame of reference moving at the group velocity the wave group and its induced flow can be regarded as being in steady state.

4.5.3 Horizontally localized wave group: non-local wave-induced flow

We now consider the simulation of a horizontally as well as vertically localized wave group. Diagnostics at $Nt = 200$ are shown in figure 4.4. This is the time at which the horizontally periodic wave group and its induced mean flow were shown to have reached steady state in a reference frame translating vertically at speed c_{gz}. Although the domain extended over $-3200 < k_x x < 3200$, here the fields are plotted only for $-100 \leq k_x x \leq 100$.

As expected, the horizontal and vertical velocity fields in figure 4.4a and b show that the wave group has translated to the origin with little dispersion. Because the magnitude of the wave-induced flows is predicted to be of order amplitude squared, the signal is too weak to be seen on the colour scale shown in these two plots. Indeed, (4.48) predicts the magnitude of the induced horizontal flow to be $A_{0ur}/(N/k_x) \sim (\pi^{5/2}/128) \times 10^{-5} \simeq 1.4 \times 10^{-6}$. To reveal the induced flows, we perform a horizontal Fourier transform of both fields over the entire domain and set to zero all Fourier components with horizontal wave numbers between $0.5k_x$ and $1.5k_x$. Inverse transforming gives the resulting wave

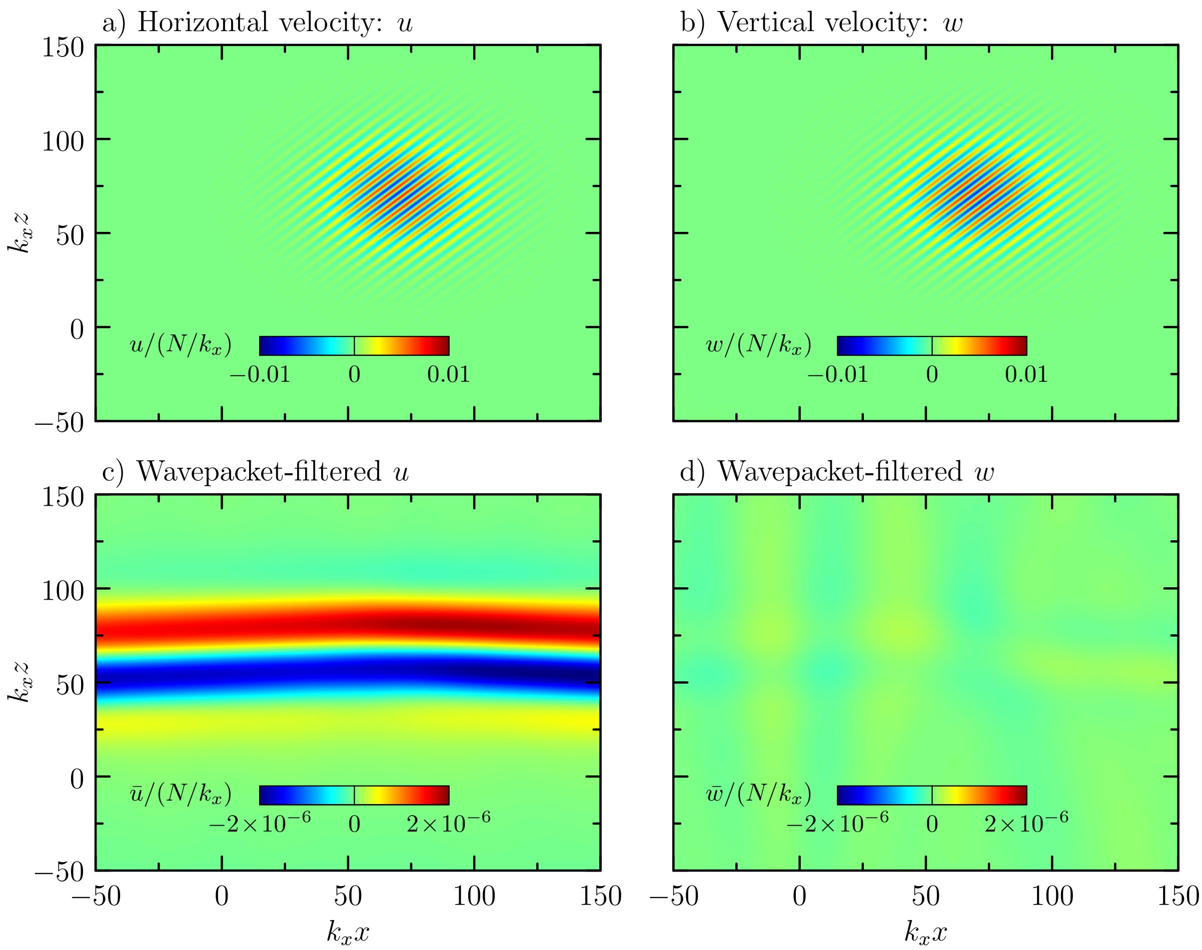

Figure 4.4: Horizontally and vertically localized Gaussian wave group at $Nt = 200$ showing the (a) horizontal and (b) vertical velocity fields and the wave group-filtered (c) horizontal and (d) vertical velocity fields.

group-filtered horizontal and vertical velocity fields $\overline{u}$ and $\overline{w}$ shown in figures 4.4c and d, respectively. These fields, plotted with a colour scale spanning a much smaller range of non-dimensional speeds, e.g. $||\overline{u}|| < 2 \times 10^{-6} N/k_x$, show that the magnitude of the horizontal response flow is indeed well-predicted by (4.48).

Even though the momentum-flux divergence associated with the wave group is predicted to generate a local u and w-dependent divergent-flux induced flow according to (4.33), consistent with (4.41) the response flow results in a total wave-induced flow moving the fluid almost entirely in the x-direction. In figure 4.4c, $\overline{u}$ appears to be nearly independent of x. However, the plots of $\overline{u}$ over the entire horizontal computational domain in figure 4.5 shows that $\overline{u}$ exhibits a pattern similar to a bow wake. Somewhat more directly, it resembles the pattern of internal waves created by a translating cylinder (Stevenson and Thomas 1969, Voisin 1994), although in the case of a vertically translating cylinder the horizontal flow field is an odd function in x centered about the cylinder and in our case it is an even function of x centered about the wave group.

The result in figure 4.4c clearly shows that the momentum-flux divergence associated with the wave group acts as translating localized forcing that excites horizontally long internal waves. The slope of the phase-lines associated with these waves is consistent with the assumptions leading to the order-of-magnitude prediction (4.45) for the lateral extent of the wave-induced flow. The vertical wavelength of the long waves is on the order $\sigma_z = 20{k_x}^{-1}$ and the slope of the constant-phase lines predicted by (4.46) to have magnitude $|k_{xr}/k_{zr}| = \pi\epsilon_z/4\sqrt{2} \simeq 0.028$ is consistent with the slope evident in figure 4.5d.

Tracking the constant phase line of the long wave emanating from the front of the wave group at time $Nt = 200$ (figure 4.5d), we see that the disturbance field becomes negligibly small at a vertical level corresponding to the trailing edge of the wave group. The lateral extent of the disturbance is $k_x|x| \simeq 1000$, close to the value $k_x L_i \simeq 1440{k_x}^{-1}$ predicted by (4.45). The disturbance field further in the lee of the wave group continues to emanate outward. Yet this can be understood as the passive propagation of long waves after their forcing is turned off.

The long waves are the result of the wave-induced flow associated with the localized wave group. Despite the somewhat complex structure of the long waves, horizontally integrating the (unfiltered) horizontal velocity field reveals horizontal vertical profiles shown in the right panels of figure 4.5, similar to those produced by a horizontally periodic wave group. Again, as time progresses, the initially zero flow evolves to reveal a superposition of a steady negative 'jet' centered around $z = 0$ and a vertically translating positive 'jet'. (We have put the word 'jet' in quotations here because the flow is in fact x-dependent, though over long horizontal distances compared with the wave group width.) Furthermore, the vertical structure of the 'jet' is well predicted by theory. From (4.27) and (4.42), we predict:

$$I_{u,\mathrm{DF}} = \sqrt{\pi}\sigma_x \left\{ \frac{1}{2} N|\mathbf{k}|{A_0}^2 \exp\left[-(z - c_{gz}t)^2/{\sigma_z}^2\right] \right\}. \tag{4.68}$$

The right-hand panels in figure 4.5 show that this prediction closely overlaps with the integrated horizontal flow calculated from the simulations in the vicinity of the wave group after it has translated sufficiently far from its initial position and left the negative 'jet' in its wake. Although the wave-induced velocities from momentum-flux divergence (4.33) are of order $\alpha^2\epsilon^0$, the resulting velocities associated with the long wave corresponding to (4.68) are of order $\alpha^2\epsilon^1$, as shown in (4.48) setting $\epsilon = \epsilon_x = \epsilon_z$.

Comparing the structure of the predicted horizontal velocity shown in figure 4.2b (for a wave group centered at the origin) with the numerically computed horizontal velocity associated with the induced long wave shown in figure 4.5d, it is clear that a wave group in an otherwise stationary ambient induces a long wave with the structure and amplitude predicted by theory. While the horizontally integrated horizontal flow is positive over the vertical extent of the wave group, the induced horizontal flow measured along a vertical profile through the centre of the wave group changes from positive on the leading flank to negative on the trailing flank as illustrated in figure 4.6. This shows vertical profiles of $\overline{u}(\tilde{x} = 0, z)$ at four different times and compares the results with the theoretical prediction given by (4.61). Because the ambient is stationary at $Nt = 0$, the measured wave group-filtered horizontal flow is zero at this time. However, after less than one buoyancy period the vertical profile of the wave group-filtered horizontal flow through the centre of the wave group conforms closely to the predicted flow (figure 4.6b). The measurements and prediction are close to overlapping at $Nt = 10$ (figure 4.6c) and much later at $Nt = 200$ (figure 4.6d). This shows that a wave group generated in an ambient initially at rest rapidly induces a horizontal flow field across its breath whose structure can be predicted by steady-state theory.

4.6 Conclusions

This chapter has examined, theoretically and numerically, the structure of the flow induced by a small-amplitude, two-dimensional, Boussinesq, horizontally and vertically localized internal gravity wave group. This induced flow is not the result of wave-breaking, but is a transient flow that varies broadly in space - compared to the width of the wave group - and which is coupled with the wave group as it moves at its group velocity.

Through a theoretical wave-group approach that seeks a steady wave-induced flow in a frame of reference that moves with the group velocity of the wave group (based on the analogy with the surface-wave case in chapters 2 and 3), we find that the leading-order total wave-induced horizontal flow is a horizontally uniform flow whose horizontal integral is equal to the horizontal integral of the horizontal component of the divergent-flux induced flow for internal waves u_{DF}.

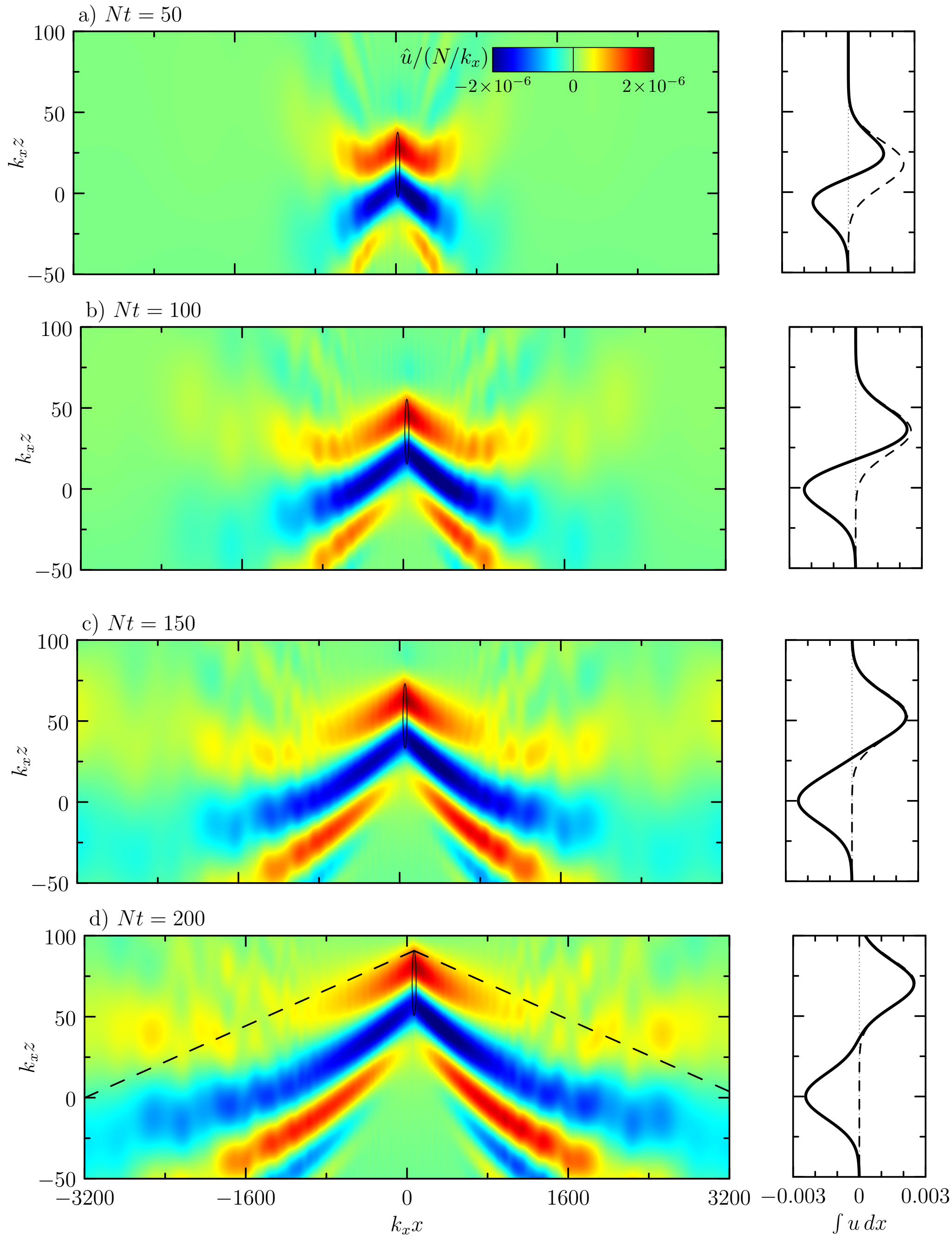

Figure 4.5: Wave group-filtered horizontal flow (left) associated with the Gaussian wave group at Nt = (a) 50, (b) 100, (c) 150 and (d) 200 shown over the entire horizontal extent of the domain. The size of the localized wave group is indicated by the ellipse in each of the left-hand images. The diagonal dashed lines in the left-hand image of (d) are drawn with the slope of the long wave phase lines predicted by (4.46). The horizontally integrated horizontal velocity computed from the unfiltered horizontal velocity field is plotted by the solid lines in the corresponding panels to the right. The dashed line shows the prediction (4.68) for the horizontally integrated induced horizontal flow.

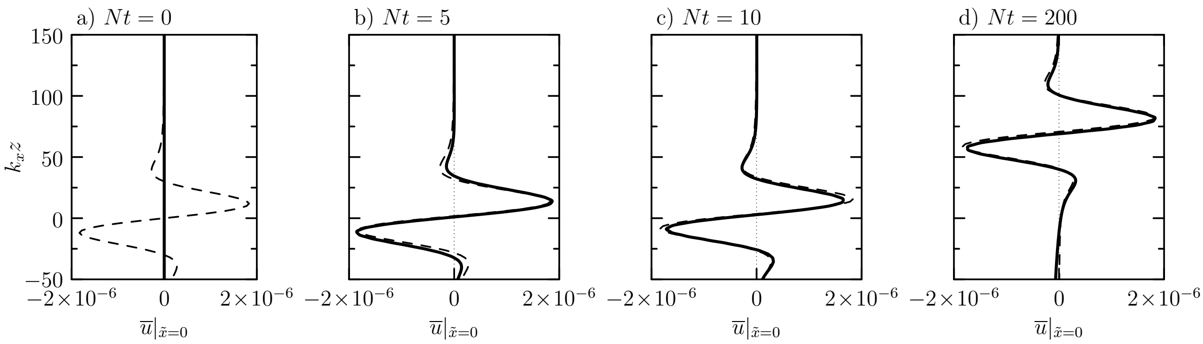

Figure 4.6: Vertical profiles of the measured horizontal velocity (solid lines) at $\tilde{x} = 0$, corresponding to the horizontal position of the centre of the wave group, shown at non-dimensional times $Nt =$ (a) 0, (b) 5, (c) 10 and (d) 200. These are compared with the predicted horizontal flow (dashed lines) given by (4.61).

Simulations show that an internal wave group indeed excites a long horizontal disturbance. But in a sufficiently wide horizontal domain, it is clear that the disturbance field is not horizontally uniform to the far reaches of the domain. In an incompressible fluid, information about the presence of the wave group can only be transmitted laterally at the speed of horizontally long internal waves. The structure and extent of the long disturbance was anticipated by Bretherton (1969b). Furthermore, the analysis reveals the link between the momentum transport by the wave group and the long wave. Consistent with theory, we find that the horizontally integrated horizontal flow associated with the long waves is well represented by the horizontal integral of u_{DF}. This result and the requirement that the horizontally long internal waves propagate with vertical phase speed equal to the vertical group velocity of the internal wave group gives a prediction, not just for the wave number, but also the amplitude of the long waves. Crucially, the characteristic horizontal scale of the induced long wave is much larger than the horizontal scale associated with the group itself: the response is non-local.

This study has focused on small-amplitude, Boussinesq internal wave groups confined to two dimensions. If the span-wise extent of the wave group is finite, adding a third dimension to the problem, then it is possible for a component of the response flow to circulate laterally around the wave group in what has been called "Bretherton flow" (e.g. figure 3a of Bühler and McIntyre (2005)) and is explored in the next chapter. There is some recent experimental evidence for a recirculating flow resulting from a span-wise localized internal wave beam (Bordes et al. 2012), though viscosity played an important role in that study. The dynamics are expected to be more complicated if the waves are large-amplitude or grow to large amplitude through non-Boussinesq effects (Sutherland 2001, Dosser and Sutherland 2011a,b). Horizontally periodic, vertically localized internal wave groups have been shown to be modulationally unstable if their frequency is larger than that for waves with the fastest vertical group velocity. The amplitude-envelope of these waves narrows and grows and advances vertically at a slower speed as a consequence of being Doppler-shifted by the wave-induced mean flow. Otherwise the waves are modulationally stable and the wave group broadens vertically. Qualitatively, the same weakly non-linear dynamics have been observed for wave groups that are horizontally as well as vertically localized (Sutherland 2001).

This can now be understood to occur due to weakly non-linear interactions between the wave group and the horizontal flow associated with the induced long wave. Weakly non-linear theory has also provided evidence for radiating wave-like disturbances excited by moderately large, fully three-dimensional wave groups (Tabaei and Akylas 2007). Based on the scaling of the response flow, very large computational domains would be needed to resolve such problems without the effects of boundaries playing a determining role. Future work will investigate weakly non-linear effects associated with interactions between a span-wise finite, large-amplitude internal wave groups and the induced long wave it generates. The ultimate goal of such work is to evaluate the transport of momentum and energy, not only by the wave group, but by the horizontally long internal waves it generates.

Chapter 5

The balanced circulation induced by three-dimensional internal gravity wave groups

Unlike the two-dimensional case (chapter 4), in which the group radiates long horizontal waves, the induced flow of a three-dimensional gravity wave group is steady in the reference frame moving with the group. Indeed the physics of the problem simplifies considerably by adding a third dimension and is analogous to the physics of a two-dimensional surface gravity group studied in chapters 2. In the surface gravity wave case, the transport of fluid by the Stokes transport is proportional to the (square of the) local amplitude of the envelope. As the amplitude of the envelope of the group varies, so does the Stokes transport leading to a divergence of fluid on the trailing edge of the group and a convergence on the leading edge. In deep water, the Eulerian return flow is simply the flow field that is required to ensure volume is conserved and the fluid is 'returned'. This chapter shows that, at leading order, the same interpretation holds for three-dimensional internal gravity wave groups, for which the stratification inhibits all induced flow in the vertical direction and the balance between the divergent-flux induced flow (the internal wave analogue of the Stokes transport introduced in chapter 4) and the return flow holds for every horizontal slice. This chapter thus provides an explicit description of the divergent-flux induced flow and the return flow for three-dimensional internal gravity wave groups first described by Bretherton (1969b) in the simplest possible framework.

5.1 Introduction

It has been known since Bretherton (1969b) that a three-dimensional internal gravity wave group induces a mean flow that consists of two components: a local response through the centre of the group and a non-local flow around the group, sometimes known as the 'Bretherton flow' (Bühler and McIntyre 2005). Although Bretherton (1969b) does not find explicit expressions for the mean flow around the group, he concludes that it must be entirely horizontal, non-divergent and, according to the circulation theorem, irrotational except where the wave energy density is non-zero (i.e. at the centre of the group). At each horizontal level separately then, the mean flow can be found as the two-dimensional incompressible motion around a concentrated patch of vorticity. Finally, Bretherton (1969b) remarks that the velocities are expected to fall off as the inverse square of the distance to the centre of the group, as in the field due to a two-dimensional dipole.

By appealing to the much simpler, and perhaps more physically intuitive, argument of divergent-flux induced flow introduced in chapter 4, this chapter shows how the induced mean flow by three-dimensional internal gravity waves can be understood using a simple mass balance argument. Unlike Bretherton (1969b), this chapter also provides explicit expressions for the induced velocity field distinguishing two components: the divergent-flux induced flow and the return flow.

Referring the reader to chapter 4 for a more extensive introduction, this short chapter is laid out as follows. §5.2 introduces the three-dimensional governing equations, which are solved by means of a combined separation of scales and perturbation expansion in §5.3. Finally, conclusions are drawn in §5.4.

5.2 Governing equations

We begin by making the usual Boussinesq approximation, that is, we ignore variation of density in the conservation equations except where it is responsible for the existence of the buoyancy force itself. In a three-dimensional coordinate system in which x and y denote the horizontal coordinates and z denotes the vertical coordinate, the corresponding momentum equations are:

$$\frac{D\mathbf{u}}{Dt} = -\frac{1}{\rho_0}\nabla p - g\frac{\rho}{\rho_0}\hat{\mathbf{k}}, \tag{5.1}$$

where $\mathbf{u} = (u, v, w)$ denotes the velocity vector with components in the direction of the respective unit vectors $\hat{\mathbf{i}}$, $\hat{\mathbf{j}}$ and $\hat{\mathbf{k}}$, p denotes the pressure, and gravity g acts in the negative z direction. In the Boussinesq approximation ρ_0 is the (constant) characteristic density. The total density of the fluid is the sum of background density $\overline{\rho}(z)$ and small variations from the background ρ, so that $\rho_T(x, y, z) = \overline{\rho}(z) + \rho(x, y, z)$. The fluid is assumed to be incompressible. Together with mass conservation this requires the flow to be non-divergent:

$$\nabla \cdot \mathbf{u} = 0. \tag{5.2}$$

We further assume the ambient state is uniformly stratified with a corresponding positive and constant squared buoyancy frequency:

$$N^2 = -\frac{g}{\rho_0}\frac{d\overline{\rho}}{dz}. \tag{5.3}$$

Neglecting diffusion of heat and salinity, internal energy conservation gives the following evolution equation for the perturbation density ρ:

$$\frac{D\rho}{Dt} = -w\frac{d\overline{\rho}}{dz}. \tag{5.4}$$

In an uniformly stratified Boussinesq fluid it is convenient to re-express ρ in terms of the vertical displacement field ξ through:

$$\xi = -\frac{\rho}{\overline{\rho}'(z)}, \tag{5.5}$$

where the prime denotes a z-derivative. Then (5.4) can be rewritten as:

$$\frac{D\xi}{Dt} = w. \tag{5.6}$$

By taking the curl of the momentum equation (5.1), the pressure terms can be eliminated and we obtain an equation for the baroclinic generation of vorticity $\zeta = \nabla \times \mathbf{u}$:

$$\frac{D\zeta}{Dt} = \zeta \cdot \nabla\mathbf{u} - N^2\Big(\frac{\partial\xi}{\partial y}\hat{\mathbf{i}} - \frac{\partial\xi}{\partial x}\hat{\mathbf{j}}\Big), \tag{5.7}$$

where we have used the vector identity $\mathbf{u} \cdot \nabla\mathbf{u} = (\nabla(\mathbf{u} \cdot \mathbf{u}))/2 - \mathbf{u} \times (\nabla \times \mathbf{u})$, the fact that the flow is incompressible (5.2) and we have expressed ρ in terms of ξ. Equations (5.6) and (5.7) can be combined, by taking x and y derivatives of (5.6) and substituted into (5.7) after taking its temporal derivative, to give:

$$\underbrace{\begin{bmatrix} 0 & -\partial_t^2\partial_z & (\partial_t^2+N^2)\partial_y \\ \partial_t^2\partial_z & 0 & -(\partial_t^2+N^2)\partial_x \\ -\partial_t^2\partial_y & \partial_t^2\partial_x & 0 \end{bmatrix}}_{=\mathbf{L}} \mathbf{u} = \nabla\cdot\underbrace{\Big[-\partial_t\big(\mathbf{u}\otimes\zeta+\zeta\cdot\nabla\mathbf{u}\big)-N^2\big(\partial_x(\mathbf{u}\xi)\hat{\mathbf{j}}-\partial_y(\mathbf{u}\xi)\hat{\mathbf{i}}\big)\Big]}_{\mathbf{F}}, \tag{5.8}$$

where the linear matrix operator $\mathbf{L}$ acts on the velocity vector $\mathbf{u}$ and the terms in the right-hand side vector $\mathbf{F}$ are non-linear in the amplitude. The symbol $\otimes$ denotes the tensor product. Equation (5.8) is referred to as the mean flow forcing equation and it can readily be compared to its two-dimensional analogue (4.10) in chapter 4.

5.3 The divergent-flux induced flow and the return flow

5.3.1 Perturbation expansion

Wave groups translate in (x,y,z)-space at the group velocity $\mathbf{c}_g = (c_{gx}, c_{gy}, c_{gz})$. In order to represent a three-dimensional group, we assume that the characteristic widths of the group σ_x, σ_y and σ_z are of the same order of magnitude. Likewise, the peak wave numbers in the three directions k_x, k_y and k_z are assumed to be of comparable magnitude. We have $\sigma \equiv \sigma_x \sim \sigma_y \sim \sigma_z$ and $|k_x| \sim |k_y| \sim |k_z|$, so that $\epsilon \equiv \epsilon_x \sim \epsilon_y \sim \epsilon_z$, where $\epsilon_n = 1/(k_n\sigma_n)$ for $n = x, y, z$. We then introduce the slow variables X, Y and Z describing the translation of the wave group:

$$X = \epsilon(x - c_{gx}t), \quad Y = \epsilon(y - c_{gy}t), \quad Z = \epsilon(z - c_{gz}t), \quad T = \epsilon^2 t, \tag{5.9a,b,c,d}$$

where dispersion of the group occurs on the very slow (cf. $O(\epsilon^2)$) time scale T. We introduce a second small parameter $\alpha = |\mathbf{k}|A_0$, where A_0 is the amplitude of vertical displacements at the centre of the group and $\mathbf{k} = (k_x, k_y, k_z)$ is the wave number vector. At leading order ($\alpha^1\epsilon^0$) the vertical displacement field is:

$$\xi^{(1)} = \xi^{(1)}_{(0)} = \mathrm{Re}\big[A(X,Y,Z,T)e^{i(k_x x + k_y y + k_z z - \omega t)}\big], \tag{5.10}$$

where the superscript denotes the order in α, the subscript the order in ϵ and we set higher order terms in ϵ to be zero without loss of generality.

5.3.2 Periodic wave solutions (review)

The linear dispersion equation can be obtained by solving the linearized versions of (5.2) and (5.8) simultaneously. Taking two equations from (5.8) and (5.2), we have three linearly independent equations at $O(\alpha)$:

$$\underbrace{\begin{bmatrix} 0 & -\partial_t^2\partial_z & (\partial_t^2 + N^2)\partial_y \\ \partial_t^2\partial_z & 0 & -(\partial_t^2 + N^2)\partial_x \\ \partial_x & \partial_y & \partial_z \end{bmatrix}}_{=\mathbf{M}} \mathbf{u} = \mathbf{0}_{(3\times 1)}. \tag{5.11}$$

For a non-trivial solution, we require $\det(\mathbf{M}) = 0$, from which we obtain the linear dispersion relationship:

$$\frac{\omega^2}{N^2} = \frac{k_x^2 + k_y^2}{k_x^2 + k_y^2 + k_z^2}. \tag{5.12}$$

The periodic solution for $\mathbf{u}^{(1)}$ corresponding to (5.10) with $A = a_0$ can be obtained from combining (5.6) and (5.11):

$$\mathbf{u}^{(1)} = -i\omega \frac{k_z^2}{k_x^2 + k_y^2} \begin{pmatrix} -k_x k_z \\ -k_y k_z \\ (k_x^2 + k_y^2)/k_z^2 \end{pmatrix} a_0 e^{i(k_x x + k_y y + k_z z - \omega t)}, \tag{5.13}$$

where the real component is understood. It can be verified by substituting (5.10) with $A = a_0$ and (5.13) into the right-hand side of (5.8) that plane periodic Boussinesq internal waves are an exact solution of the fully non-linear equations of motion, a well-known result (see for example Sutherland (2010)).

5.3.3 Leading-order induced mean flow

Returning to the forcing equation (5.8) and assuming that the Eulerian flow field at second-order in α varies on the slow scales X, Y and Z, it can be shown that the individual terms have the following orders in α and ϵ:

$$\underbrace{\begin{bmatrix} 0 & \underbrace{-\partial_t^2\partial_z}_{\epsilon^3} & (\underbrace{\partial_t^2}_{\epsilon^2}+\underbrace{N^2}_{\epsilon^0})\underbrace{\partial_y}_{\epsilon^1} \\ \underbrace{\partial_t^2\partial_z}_{\epsilon^3} & 0 & -(\underbrace{\partial_t^2}_{\epsilon^2}+\underbrace{N^2}_{\epsilon^0})\underbrace{\partial_x}_{\epsilon^1} \\ -\underbrace{\partial_t^2\partial_y}_{\epsilon^3} & \underbrace{\partial_t^2\partial_x}_{\epsilon^3} & 0 \end{bmatrix}}_{=\mathbf{L}} \underbrace{\mathbf{u}^{(2)}}_{\alpha^2} = -\underbrace{\nabla\cdot\overline{\left[\partial_t\left(\mathbf{u}^{(1)}\otimes\zeta^{(1)}+\zeta^{(1)}\cdot\nabla\mathbf{u}^{(1)}\right)\right]}}_{\alpha^2\epsilon^2}+\ldots$$

$$-\underbrace{\nabla\cdot\overline{\left[N^2\left(\partial_x(\mathbf{u}^{(1)}\xi^{(1)})\hat{\mathbf{j}}+\partial_y(\mathbf{u}^{(1)}\xi^{(1)})\hat{\mathbf{i}}\right)\right]}}_{\alpha^2\epsilon^2}, \tag{5.14}$$

where we are only interested in mean flow terms and thus average over the fast scales on the right hand side, as denoted by the over-line. We thus have at leading order ($O(\alpha^2\epsilon^1)$) for the induced mean flow $\mathbf{u}^{(2)}$:

$$\partial_X w^{(2)}(X,Y,Z)=0, \quad \partial_Y w^{(2)}(X,Y,Z)=0, \tag{5.15a,b}$$

which implies that $w^{(2)}=0$, as volume is conserved ($\nabla\cdot\mathbf{u}=0$). In words, stratification inhibits all mean flows in the z-direction at leading order. In general we have the total induced mean flow $\mathbf{u}^{(2)}$ as the sum of the divergent-flux induced flow $\mathbf{u}_{\text{DF}}$ (see chapter 4) and the return flow $\mathbf{u}_{\text{RF}}$:

$$\mathbf{u}^{(2)}=\mathbf{u}_{\text{DF}}+\mathbf{u}_{\text{RF}}. \tag{5.16}$$

We therefore have for the vertical direction $w_{\text{RF}}=-w_{\text{DF}}$; all flow is inhibited by stratification. The induced mean flow is confined to the horizontal plane and has to satisfy two-dimensional conservation of volume:

$$\nabla_{\text{H}}\cdot\mathbf{u}_{\text{H}}^{(2)}=\nabla_{\text{H}}\cdot\left(\mathbf{u}_{\text{DF,H}}+\mathbf{u}_{\text{RF,H}}\right)=0, \tag{5.17}$$

where we let the subscript H denote (two-dimensional operations in) the horizontal plane: $\nabla_{\text{H}}=(\partial_x,\partial_y)$ and $\mathbf{u}_{\text{H}}^{(2)}=(u^{(2)},v^{(2)})$.

5.3.3.1 Divergent-flux induced flow

We only consider the temporal and advective components of the momentum equation (5.1), to arrive at a definition of the divergent-flux induced flow (see chapter 4):

$$\frac{\partial\mathbf{u}_{\text{DF}}}{\partial t}\equiv\overline{-\nabla\cdot(\mathbf{u}^{(1)}\otimes\mathbf{u}^{(1)})}, \tag{5.18}$$

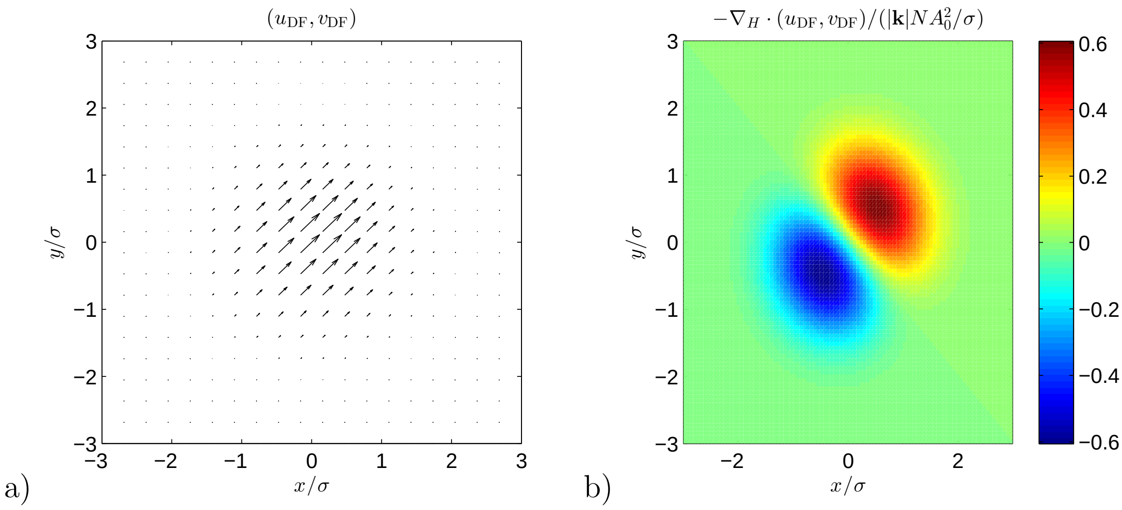

Figure 5.1: The divergent-flux induced flow in a horizontal plane through the centre of the group ($z = c_{gz}t$) showing (a) the velocity field $(u_{\rm DF}, v_{\rm DF})$ and (b) its convergence $-\nabla_{\rm H} \cdot (u_{\rm DF}, v_{\rm DF})$ showing that the divergent-flux induced flow transports fluid in the direction of (the horizontal component of) the group velocity.

where we have used $\nabla \cdot \mathbf{u} = 0$ to write the equation in conservative form. The over-lines denote averaging over the fast scales. We now recast (5.18) in terms of the slow variables, keeping terms of order ϵ alone. In particular, $\partial_t \sim -\epsilon c_{gx}\partial_X - \epsilon c_{gy}\partial_Y - \epsilon c_{gz}\partial_Z$:

$$\mathbf{c}_g u_{\rm DF} = \overline{u^{(1)}\mathbf{u}^{(1)}}, \quad \mathbf{c}_g v_{\rm DF} = \overline{v^{(1)}\mathbf{u}^{(1)}}, \quad \mathbf{c}_g w_{\rm DF} = \overline{w^{(1)}\mathbf{u}^{(1)}}. \tag{5.19a,b,c}$$

Using the polarization relationships (5.13), we obtain from (5.19) the divergent-flux induced velocity vector field pointing in the direction of the group velocity vector $\mathbf{c}_g$:

$$\mathbf{u}_{\rm DF} = \frac{1}{2}N|\mathbf{k}||A|^2\Big(1, \frac{c_{gy}}{c_{gx}}, \frac{c_{gz}}{c_{gx}}\Big). \tag{5.20}$$

Figure 5.1 shows the components of (5.20) and the convergence and divergence of this velocity field in a two-dimensional horizontal plane through the centre of the group (with a positive sign corresponding to an excess of fluid and a negative sign to a deficit).

5.3.3.2 Return flow

From the result in §5.3.3, we immediately obtain $w_{\rm RF} = -w_{\rm DF}$ and solving for the return flow field amounts to solving the two-dimensional Laplace equation (5.17) with sources and sinks given by the divergence of the two-dimensional divergence-flux induced flow field $\mathbf{u}_{\rm SD,H} = (u_{\rm SD}, v_{\rm SD})$ with the individual components given by (5.20). We do so in local complex coordinates in the horizontal plane. The complex potential at $\mathcal{Z} = x + iy$ of a source with strength $M(\mathcal{Z}^*)$ located at $\mathcal{Z}^* = x^* + iy^*$ is given by:

$$\Phi_{\mathrm{H}}(\mathcal{Z}) = \phi_{\mathrm{H}}(\mathcal{Z}) + i\psi_{\mathrm{H}}(\mathcal{Z}) = \frac{M(\mathcal{Z}^*)\log(\mathcal{Z} - \mathcal{Z}^*)}{2\pi}. \tag{5.21}$$

The source strength for a unit area dx^*dy^* is given by:

$$dM(\mathcal{Z}^*) = -\nabla^*_{\mathrm{H}} \cdot \big(u_{\mathrm{DF}}(x^*, y^*), v_{\mathrm{DF}}(x^*, y^*)\big)dx^*dy^*. \tag{5.22}$$

Summing over all the sources, we have for the complex potential:

$$\Phi_{\mathrm{RF,H}} = -\int_{-\infty}^{\infty}\int_{-\infty}^{\infty} \frac{\nabla^* \cdot \big(u_{\mathrm{DF}}(x^*, y^*), v_{\mathrm{DF}}(x^*, y^*)\big)}{2\pi} \log\left(\sqrt{(x - x^*)^2 + (y - y^*)^2}\right)dx^*dy^*. \tag{5.23}$$

Explicitly evaluating the stream function and the velocity components for an isotropic ($\sigma = \sigma_x = \sigma_y = \sigma_z$) Gaussian wave group $A(x, y, z, t) = A_0\exp(-((x - c_{gx}t)^2 + (y - c_{gy}t)^2 + (z - c_{gz}t)^2)/(2\sigma^2))$, we have for the velocity components:

$$\begin{aligned} u_{\mathrm{RF}} &= \frac{|\mathbf{k}|NA_0^2}{2\pi}\int_{-\infty}^{\infty}\int_{-\infty}^{\infty} \frac{(\hat{x} - \hat{x}^*)\Big((\hat{x} - \hat{x}^*) + \frac{k_x}{k_y}(\hat{y} - \hat{y}^*)\Big)}{(\hat{x} - \hat{x}^*)^2 + (\hat{y} - \hat{y}^*)^2} e^{-(\hat{x}^*)^2 - (\hat{y}^*)^2} d\hat{x}^*d\hat{y}^*, \\ v_{\mathrm{RF}} &= \frac{|\mathbf{k}|NA_0^2}{2\pi}\int_{-\infty}^{\infty}\int_{-\infty}^{\infty} \frac{(\hat{y} - \hat{y}^*)\Big((\hat{x} - \hat{x}^*) + \frac{k_x}{k_y}(\hat{y} - \hat{y}^*)\Big)}{(\hat{x} - \hat{x}^*)^2 + (\hat{y} - \hat{y}^*)^2} e^{-(\hat{x}^*)^2 - (\hat{y}^*)^2} d\hat{x}^*d\hat{y}^*, \end{aligned}$$

where $\hat{x} = (x - c_{gx}t)/\sigma$ and $\hat{y} = (y - c_{gy}t)/\sigma$. The corresponding return flow field is illustrated in figure 5.2a. In this figure, the group velocity vector is in the direction of the diagonal $y = x$ line. The return flow is thus predominantly in the opposite direction. The sum of the divergent-flux induced flow $\mathbf{u}_{\mathrm{DF}}$ and the return flow $\mathbf{u}_{\mathrm{RF}}$ is shown in figure 5.2b.

5.4 Conclusions

This chapter has provided an explicit description of the induced mean flow by three-dimensional internal gravity wave groups in uniformly stratified Boussinesq ambients. Although internal gravity waves do not display Stokes drift (defined as the difference between the Lagrangian and Eulerian velocity), the analogy with surface gravity wave groups can be exploited. As for surface gravity wave groups (cf. chapter 2), the wave-induced mean flow consist of two components. Taking advantage of the separation of scales in a quasi-monochromatic wave groups, the advective terms in the momentum equations (sometimes referred to as Reynolds stresses) give rise to a mean flow through the centre of the group in the direction of the group velocity vector that we term the

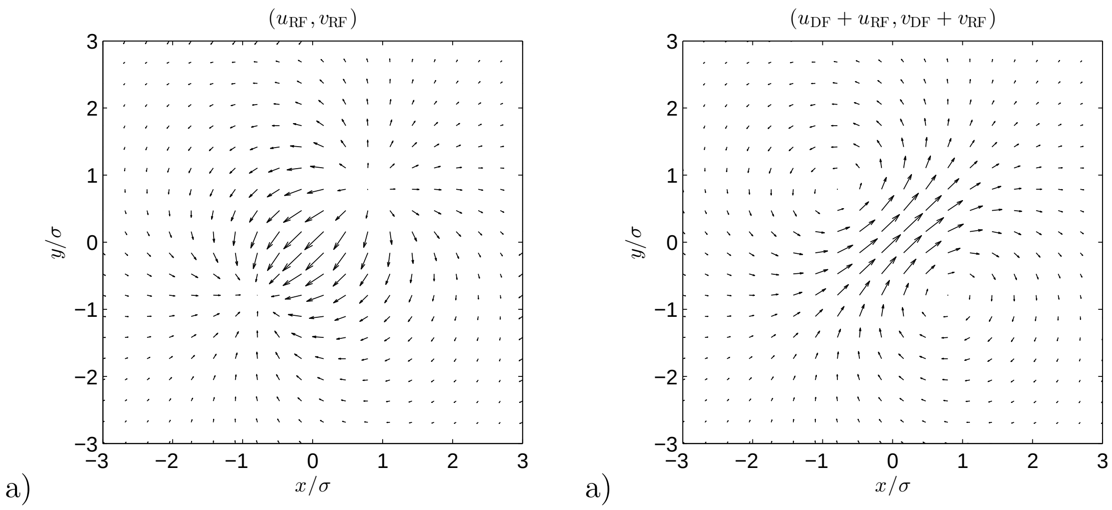

Figure 5.2: The return flow in a horizontal plane through the centre of the group ($z = c_{gz}t$) for a three-dimensional wave group showing the velocity field $(u_{\mathrm{RF}}, v_{\mathrm{RF}})$ and (b) the total induced mean flow field $\mathbf{u}^{(2)} = (u_{\mathrm{DF}} + u_{\mathrm{RF}}, v_{\mathrm{DF}} + v_{\mathrm{RF}})$ at the same location.

"divergent-flux induced flow" (see chapter 4). This divergent-flux induced flow is analogous to the Stokes transport for surface gravity waves and it is local to the group. Because the divergent-flux induced flow is divergent itself (it transports volume), a second component of the induced mean flow is needed: the return flow. The return flow acts to restore the mass imbalance by transporting fluid in the opposite direction around the group. It is thus non-local in the same way as the return flow for surface gravity wave groups in deep water. Stratification simply acts to confine this balanced circulation to a horizontal plane.

Comparing the results in this chapter to the results in the previous chapter (chapter 4) on two-dimensional internal wave groups, a clear contrast becomes evident. Whereas the response to three-dimensional groups is a balanced circulation, two-dimensional groups induce a quasi-steady long internal wave ahead and in its lee. Realistically then, one should expect both a long internal wave and a recirculating region about a wave group of sufficiently wide but nonetheless finite span-wise extent. It is not immediately clear how such a mixed response could be predicted using a perturbation expansion of the type considered herein. Such geometries, that perhaps form realistic descriptions of internal gravity waves generated by flow over a mountain range, provide scope for future work.

Finally, explicit evaluation of the mean flow passing through the wave group can be used to develop weakly non-linear equations for the evolution of moderately large amplitude internal wave groups. This methodology has been successfully employed by Sutherland (2006b) and Dosser and Sutherland (2011a,b) who derived non-linear Schrödinger equations for horizontally periodic, vertically localized two-dimensional internal wave groups allowing these authors to assess the modulational stability of such groups. Extending these results to three-dimensional wave groups using the explicit description of the induced mean flow derived herein provides scope for future work.

Part III

Interfacial gravity waves

Chapter 6

Stokes drift and return flow for two-dimensional interfacial wave groups

This chapter extends the framework developed for surface gravity waves in chapters 2 and 3 to two-dimensional interfacial gravity wave groups in a stably stratified two-layer fluid. It considers the leading-order terms in a separation of scales expansion for a quasi-monochromatic interfacial wave group. As for finite depth surface gravity waves, the return flow can be driven by both the divergence of the Stokes transport and the set-up or set-down of the interface. For pure interfacial wave groups in a two-dimensional channel three cases are examined in turn: the case of two infinitely deep fluids, the case of two fluids of finite and equal depth and the asymmetric case of a finite depth fluid overlying an infinitely deep fluid. Finally, the induced mean flow of coupled free surface and interfacial waves is considered distinguishing the barotropic and the baroclinic solutions to the dispersion relationship. Both the non-Boussinesq case and the Boussinesq case, in which the density difference between the fluids is small, are considered.

6.1 Introduction

Interfacial gravity waves can occur on the interface between two fluids of different density with the lighter fluid overlying the denser one in a stable configuration. Two different configurations can be distinguished: a case without a free surface for which only interfacial waves exist, and a case with a free surface for which interfacial and free surface waves interact. Examples of interfacial waves in the natural environment can be found when density changes are relatively abrupt, such as at the thermocline in tropical seas or lakes and at the atmospheric inversion. For example, Akylas et al. (2007) studied the interfacial solitary waves that may arise from the interaction of a propagating internal tidal beam with the thermocline, motivated by field observations in the Bay of Biscay by New and Pingree (1990, 1992). More generally, long non-linear internal solitary-like waves are ubiquitous features of coastal oceans, as has been shown by in situ and remote sensing observations (see Helfrich and Melville (2006) for a review). Another often cited example of interfacial waves playing a role is the fast-moving band of clouds that appears typically in early morning hours in late October over North-Western Australia and is sometimes known as the Morning Glory. Although the dynamics are more complicated, the clouds mark the crest of a solitary wave that propagates along the morning-time atmospheric inversion (Noonan and Smith 1985, Christie 1992, Menhofer et al. 1997).

Perhaps the most appealing example of interfacial waves is in the so-called dead water effect, first described by the Norwegian Arctic explorer by Fridtjof Nansen (1861-1930). The dead water effect occurs when a layer of fresh water overlies a layer of salt water and a ship's propeller is located approximately at the interface between the fluids. Instead of driving the ship forwards, the propeller drives internal waves, which are hardly visible at the free surface and can bring the ship to a standstill. It most commonly occurs where glacier runoff flows into salt water, such as in fjords. It was observed and documented by Nansen (1897) when sailing his ship the Fram in the Nordenskiöld Archipelago near the Taymyr Peninsula (Russia). More generally, oceanic internal waves are not directly visible to the observer at the ocean's surface or only through small amplitude disturbances that are visible on satellite images (Klemas 2012).

Using the framework developed in the previous chapters, this chapter explores the structure of the Stokes drift, Stokes transport and the return flow for pure interfacial wave groups and coupled free surface interfacial wave groups (see figure 6.1). Two incompressible fluids of different density are considered in a two-dimensional semi-infinite domain. The fluids are assumed to not mix. Both large density differences (non-Boussinesq) and the limit of small density differences (Boussinesq) are considered. Although the individual fluids may be modelled as irrotational, shear between the two layers may lead to an instability through the formation of Kelvin-Helmholtz billows. Such instabilities are in fact thought to be an important mechanism for interfacial wave breaking and, consequently, mixing in the ocean (see Helfrich and Melville (2006) for a review including of field measurements). Provided the effects of gravity are sufficiently strong, the effects of shear are stabilized (see for example Fringer and Street (2003) for a study of shear instability in interfacial waves). This chapter is therefore restricted to the regime of shear-stable interfacial waves. Instead, this chapter pursues a perturbation expansion in the small

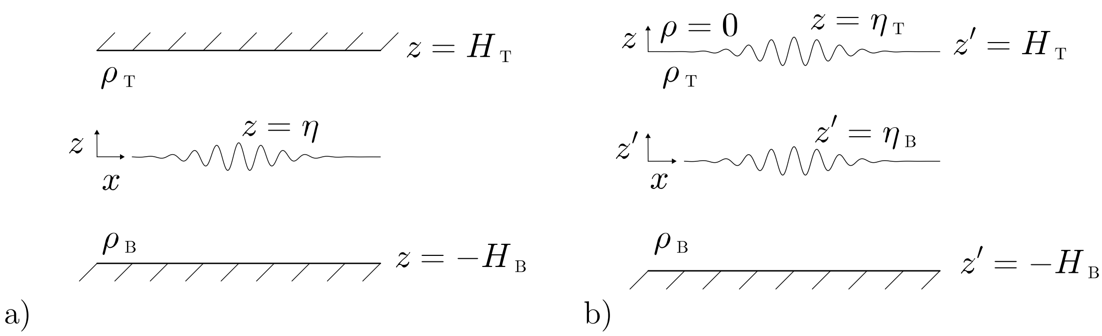

Figure 6.1: Illustration of definitions for (a) closed-lid interfacial wave groups and (b) coupled free surface and interfacial wave groups in a two-layer fluid.

parameter $\alpha = k_0|A_0|$, where k_0 is the peak wave number and $|A_0|$ is the wave group amplitude combined with a separation of scales expansion for quasi-monochromatic wave groups in the small parameter $\epsilon = 1/(k_0\sigma)$, where σ is the horizontal scale of the wave group. As in the previous chapters, only effects up to $O(\alpha^2)$ are considered. We thus abstract from the significant literature on non-linear evolution of interfacial waves and the formation of solitary wave solutions.

This chapter is laid out as follows. §6.2 examines interfacial waves in a two-dimensional channel with a closed lid, first introducing its governing equations and boundary conditions (§6.2.1), followed by its solutions for an infinite depth channel (§6.2.2), a channel with two layers of equal finite depth (§6.2.3) and, finally, a channel with a layer of finite depth overlying a layer of infinite depth (§6.2.4). §6.3 then considers coupled interfacial and surface waves in a two-layer fluid with a free surface, beginning with introduction of its governing equations and boundary conditions (§6.3.1) followed by a discussion of the two familiar categories of linear solutions (§6.3.2): the barotropic or surface mode and baroclinic or internal mode. The induced mean flows for wave groups in the barotropic and the baroclinic mode are then discussed in detail in §6.3.3 and §6.3.4, respectively. Finally, conclusions are drawn in §6.4.

6.2 Closed-lid interfacial waves

6.2.1 Governing equations and boundary conditions

For a two-dimensional domain (see figure 6.1a), the governing equations $\nabla^2\phi_T = 0$ for $z > \eta$ and $\nabla^2\phi_B = 0$ for $z < \eta$ are solved subject to three boundary conditions at the interface $z = \eta(x, t)$. The vertical coordinate z is measured upwards from the undisturbed interface level $z = 0$. The two-dimensional velocity potentials in each layers are defined so that: $u_{\mathrm{T}} = \partial\phi_{\mathrm{T}}/\partial x$, $w_{\mathrm{T}} = \partial\phi_{\mathrm{T}}/\partial z$ in the top layer and $u_{\mathrm{B}} = \partial\phi_{\mathrm{B}}/\partial x$, $w_{\mathrm{B}} = \partial\phi_{\mathrm{B}}/\partial z$ in the bottom layer, with u and w denoting the horizontal and vertical velocity, respectively. The boundary conditions are, respectively, a kinematic boundary condition for the velocities in the top layer, a kinematic boundary condition for the velocities in the bottom layer and a dynamic boundary condition setting the pressure at either side of the interface to be equal (cf. Bernoulli's equation):

$$\frac{\partial \eta}{\partial t} + u_{\mathrm{T}}\frac{\partial \eta}{\partial x} - w_{\mathrm{T}} = 0, \quad \frac{\partial \eta}{\partial t} + u_{\mathrm{B}}\frac{\partial \eta}{\partial x} - w_{\mathrm{B}} = 0 \quad \text{on} \quad z = \eta(x,t), \tag{6.1a,b}$$

$$\rho_{\mathrm{T}}\Big(\frac{\partial \phi_{\mathrm{T}}}{\partial t} + \frac{1}{2}|\nabla\phi_{\mathrm{T}}|^2 + g\eta\Big) = \rho_{\mathrm{B}}\Big(\frac{\partial \phi_{\mathrm{B}}}{\partial t} + \frac{1}{2}|\nabla\phi_{\mathrm{B}}|^2 + g\eta\Big) \quad \text{on} \quad z = \eta(x,t). \tag{6.2}$$

Finally, $w_{\mathrm{T}} \to 0$ as $z \to H_{\mathrm{T}}$ and $w_{\mathrm{B}} \to 0$ as $z \to -H_{\mathrm{B}}$, reflecting the two closed boundaries at the top and bottom of the channel.

6.2.1.1 Linearized equations

The linearized (in α) boundary conditions (6.1-6.2) are:

$$\frac{\partial \eta^{(1)}}{\partial t} - w_{\mathrm{T}}^{(1)}\big|_{z=0} = 0, \quad \frac{\partial \eta^{(1)}}{\partial t} - w_{\mathrm{B}}^{(1)}\big|_{z=0} = 0, \tag{6.3a,b}$$

$$\rho_{\mathrm{T}}\frac{\partial \phi_{\mathrm{T}}^{(1)}}{\partial t}\bigg|_{z=0} + g\rho_{\mathrm{T}}\eta^{(1)} = \rho_{\mathrm{B}}\frac{\partial \phi_{\mathrm{B}}^{(1)}}{\partial t}\bigg|_{z=0} + g\rho_{\mathrm{B}}\eta^{(1)}, \tag{6.4}$$

which can be combined, eliminating η, to give:

$$\rho_{\mathrm{T}}\frac{\partial^2 \phi_{\mathrm{T}}^{(1)}}{\partial t^2}\bigg|_{z=0} - \rho_{\mathrm{B}}\frac{\partial^2 \phi_{\mathrm{B}}^{(1)}}{\partial t^2}\bigg|_{z=0} - g(\rho_{\mathrm{B}} - \rho_{\mathrm{T}})\frac{\partial \phi_{\mathrm{B}}^{(1)}}{\partial z}\bigg|_{z=0} = 0. \tag{6.5}$$

We note from (6.3) that the leading-order vertical velocities are equal at the interface: $w_{\mathrm{T}}^{(1)}(z=0) = w_{\mathrm{B}}^{(1)}(z=0)$.

6.2.1.2 The mean flow forcing equation

At second-order (in α), we obtain from the boundary conditions (6.1-6.2):

$$\frac{\partial \eta^{(2)}}{\partial t} - \frac{\partial \phi_{\mathrm{T}}^{(2)}}{\partial z} = -\overline{\frac{\partial}{\partial x}\Big(u_{\mathrm{T}}^{(1)}\eta^{(1)}\Big)}, \quad \frac{\partial \eta^{(2)}}{\partial t} - \frac{\partial \phi_{\mathrm{B}}^{(2)}}{\partial z} = -\overline{\frac{\partial}{\partial x}\Big(u_{\mathrm{B}}^{(1)}\eta^{(1)}\Big)} \quad \text{on} \quad z = 0, \tag{6.6a,b}$$

$$
\begin{aligned}
g(\rho_{\mathrm{B}}-\rho_{\mathrm{T}})\eta^{(2)}+\rho_{\mathrm{B}}\frac{\partial\phi_{\mathrm{B}}^{(2)}}{\partial t}-\rho_{\mathrm{T}}\frac{\partial\phi_{\mathrm{T}}^{(2)}}{\partial t}=&\frac{1}{2}\overline{\left(\rho_{\mathrm{T}}|\nabla\phi_{\mathrm{T}}^{(1)}|^2-\rho_{\mathrm{B}}|\nabla\phi_{\mathrm{B}}^{(1)}|^2\right)}+...\\
&+\overline{\left(\rho_{\mathrm{T}}\frac{\partial^2\phi_{\mathrm{T}}^{(1)}}{\partial z\partial t}-\rho_{\mathrm{B}}\frac{\partial^2\phi_{\mathrm{B}}^{(1)}}{\partial z\partial t}\right)\eta^{(1)}}\quad\text{on}\quad z=0,
\end{aligned}
\tag{6.7}
$$

where we have restricted our interest to mean flow terms by averaging over the fast scales, as denoted by the over-lines. Furthermore, we have used the identities $\partial_z^2\phi_{\mathrm{T}}=-\partial_x^2\phi_{\mathrm{T}}$ and $\partial_z^2\phi_{\mathrm{B}}=-\partial_x^2\phi_{\mathrm{B}}$ (from Laplace). Before taking stock and considering the orders in α and ϵ of the different terms, we must consider the linear (in α) solutions. Three cases are considered in turn: two layers of infinite depth, (§6.2.2), two layers of finite and equal depth (§6.2.3) and one layer of finite depth overlying a layer of infinite depth (§6.2.4).

6.2.2 Solutions for two layers of infinite depth ($H\to\infty$)

6.2.2.1 Linear solutions

We assume linear (in α) velocity potentials of the form:

$$
\phi_{\mathrm{T}}^{(1)}=B_{\mathrm{T}}(X,Z,T)e^{-k_0z}e^{i(k_0x-\omega_0t)}+O(\alpha^1\epsilon^1),\quad \phi_{\mathrm{B}}^{(1)}=B_{\mathrm{B}}(X,Z,T)e^{k_0z}e^{i(k_0x-\omega_0t)}+O(\alpha^1\epsilon^1),
\tag{6.8a,b}
$$

where $X=\epsilon(x-c_{g,0}t)$, $Z=\epsilon z$ and $T=\epsilon^2t$. The corresponding interfacial elevation is assumed to be:

$$
\eta^{(1)}=A(X,T)e^{i(k_0x-\omega_0t)}+O(\alpha^1\epsilon^1).
\tag{6.9}
$$

Satisfying the linearized boundary conditions (6.3-6.4) at $O(\alpha^1\epsilon^0)$, we recover the standard periodic wave solutions for interfacial waves:

$$
\phi_{\mathrm{T}}^{(1)}=\frac{iA(X)\omega_0}{k_0}e^{-k_0z}e^{i(k_0x-\omega_0t)}+O(\alpha^1\epsilon^1),\quad \phi_{\mathrm{B}}^{(1)}=-\frac{iA(X)\omega_0}{k_0}e^{k_0z}e^{i(k_0x-\omega_0t)}+O(\alpha^1\epsilon^1),
\tag{6.10a,b}
$$

and the deep-water linear dispersion relationship $\omega_0^2=g'k_0$, where $g'=g(\rho_{\mathrm{B}}-\rho_{\mathrm{T}})/(\rho_{\mathrm{B}}+\rho_{\mathrm{T}})$ is now the reduced gravity. Table 6.1 summarizes the linear solutions, as evaluated at the undisturbed interface level $z=0$.

6.2.2.2 Second-order solutions: mean flow

It is evident that the leading-order linear solutions in the two-layers are simply equivalent to the leading-order deep-water surface gravity wave solutions (see chapter 2) with gravity g replaced by the effective gravity g' in the dispersion relationship. Accordingly, we can

	infinite and equal depth $(H_\mathrm{T} = H_\mathrm{B} = H \to \infty)$	finite and equal depth $(H_\mathrm{T} = H_\mathrm{B} = H)$	finite over infinite depth $(H_\mathrm{T} = H,\, H_\mathrm{B} \to \infty)$
$\eta^{(1)}(x,t)$	$A(X)e^{i(k_0x-\omega_0t)}$	$A(X)e^{i(k_0x-\omega_0t)}$	$A(X)e^{i(k_0x-\omega_0t)}$
$u^{(1)}_\mathrm{B}(x,z=0,t)$	$\omega_0A(X)e^{i(k_0x-\omega_0t)}$	$\frac{\omega_0}{\tanh(k_0H)}A(X)e^{i(k_0x-\omega_0t)}$	$\omega_0A(X)e^{i(k_0x-\omega_0t)}$
$u^{(1)}_\mathrm{T}(x,z=0,t)$	$-\omega_0A(X)e^{i(k_0x-\omega_0t)}$	$-\frac{\omega_0}{\tanh(k_0H)}A(X)e^{i(k_0x-\omega_0t)}$	$-\frac{\omega_0}{\tanh(k_0H)}A(X)e^{i(k_0x-\omega_0t)}$
$w^{(1)}_\mathrm{B}(x,z=0,t)$	$-i\omega_0A(X)e^{i(k_0x-\omega_0t)}$	$-i\omega_0A(X)e^{i(k_0x-\omega_0t)}$	$-i\omega_0A(X)e^{i(k_0x-\omega_0t)}$
$w^{(1)}_\mathrm{T}(x,z=0,t)$	$-i\omega_0A(X)e^{i(k_0x-\omega_0t)}$	$-i\omega_0A(X)e^{i(k_0x-\omega_0t)}$	$-i\omega_0A(X)e^{i(k_0x-\omega_0t)}$
$\partial^2\phi^{(1)}_\mathrm{B}(x,z=0,t)/\partial z\partial t$	$-\omega_0^2A(X)e^{i(k_0x-\omega_0t)}$	$-\omega_0^2A(X)e^{i(k_0x-\omega_0t)}$	$-\omega_0^2A(X)e^{i(k_0x-\omega_0t)}$
$\partial^2\phi^{(1)}_\mathrm{T}(x,z=0,t)/\partial z\partial t$	$-\omega_0^2A(X)e^{i(k_0x-\omega_0t)}$	$-\omega_0^2A(X)e^{i(k_0x-\omega_0t)}$	$-\omega_0^2A(X)e^{i(k_0x-\omega_0t)}$

Table 6.1: Linear $(O(\alpha^1\epsilon^0))$ solutions for interfacial waves with a closed lid in an infinite depth two-layer fluid, a finite depth two-layer fluid and a finite depth fluid overlying an infinite depth fluid evaluated at the undisturbed interface level $z = 0$. Each finite depth layer has depth H.

derive leading-order expressions for the Stokes drift and Stokes transport in the two respective layers:

$$u_{\mathrm{SD,T}} = \omega_0 k_0|A(X)|^2e^{-2k_0z},\ u_{\mathrm{SD,B}} = \omega_0 k_0|A(X)|^2e^{2k_0z},\ Q_{\mathrm{ST}} \equiv Q_{\mathrm{ST,T}} = Q_{\mathrm{ST,B}} = \frac{1}{2}\omega_0|A(X)|^2. \tag{6.11a,b,c}$$

In words, the Stokes drift and Stokes transport are equal and in the same direction in both layers and entirely equivalent to the surface gravity wave problem of Stokes (1847) considered in chapter 2.

In order to take stock of the different orders of the terms in the mean flow forcing equations (6.6-6.7) and make use of the symmetry, we first define difference and sum terms $\phi^2_- = \phi^{(2)}_\mathrm{B} - \phi^{(2)}_\mathrm{T}$ and $\phi^2_+ = \phi^{(2)}_\mathrm{B} + \phi^{(2)}_\mathrm{T}$, noting these new terms are only defined at $z = 0$. Using the definition of the Stokes transport in (6.11c) and the linear polarization relationships in table 6.1, we then have from (6.6-6.7):

$$\frac{\partial}{\partial z}\Big(\underbrace{\phi^{(2)}_-}_{O(\alpha^2\epsilon^0)}\Big) = \frac{\partial}{\partial z}\Big(\underbrace{\phi^{(2)}_\mathrm{B} - \phi^{(2)}_\mathrm{T}}_{O(\alpha^2)}\Big) = \underbrace{2\frac{\partial Q_{\mathrm{ST}}}{\partial x}}_{O(\alpha^2\epsilon)} + O(\alpha^2\epsilon^3) \quad \text{on} \quad z = 0, \tag{6.12}$$

$$\frac{1}{2}g(\rho_\mathrm{B} - \rho_\mathrm{T})\underbrace{\frac{\partial\phi^{(2)}_+}{\partial z}}_{O(\alpha^2\epsilon^2)} + (\rho_\mathrm{B} - \rho_\mathrm{T})\underbrace{\frac{\partial^2\phi^{(2)}_+}{\partial t^2}}_{O(\alpha^2\epsilon^3)} + (\rho_\mathrm{B} + \rho_\mathrm{T})\underbrace{\frac{\partial^2\phi^{(2)}_-}{\partial t^2}}_{O(\alpha^2\epsilon^2)} = \underbrace{0}_{O(\alpha^2\epsilon^1)} + O(\alpha^2\epsilon^3) \quad \text{on} \quad z = 0, \tag{6.13}$$

$$\frac{\partial}{\partial z}\Big(\underbrace{\phi^2_+}_{O(\alpha^2\epsilon^1)}\Big) = \frac{\partial}{\partial z}\Big(\underbrace{\phi^{(2)}_\mathrm{B} + \phi^{(2)}_\mathrm{T}}_{O(\alpha^2\epsilon^1)}\Big) = \underbrace{2\frac{\partial\eta^{(2)}}{\partial t}}_{O(\alpha^2\epsilon^2)} + O(\alpha^2\epsilon^3) \quad \text{on} \quad z = 0, \tag{6.14}$$

where we have assumed that the mean-flow terms evolve on the slow scales X and Z and change shape on the even slower scale T. In turn, we have from (6.12) that $\phi^{(2)}_- = O(\alpha^2\epsilon^0)$, from (6.13) that $\phi_+^{(2)} = O(\alpha^2\epsilon^1)$ and from (6.14) that $\eta^{(2)} = O(\alpha^2\epsilon^1)$. Leading-order solutions for the mean flow can thus be found by solving Laplace subject to the boundary conditions:

$$\left.\frac{\partial \phi_{\mathrm{T}}^{(2)}}{\partial z}\right|_{z=0} = -\frac{\partial Q_{\mathrm{ST}}}{\partial x}, \quad \left.\frac{\partial \phi_{\mathrm{B}}^{(2)}}{\partial z}\right|_{z=0} = \frac{\partial Q_{\mathrm{ST}}}{\partial x}, \tag{6.15a,b}$$

in addition to the boundary conditions at the top and bottom of the channel $w_{\mathrm{T}} \to 0$ as $z \to \infty$ and $w_{\mathrm{B}} \to 0$ as $z \to -\infty$. The solutions are:

$$\phi_{\mathrm{RF,B}} = -\frac{1}{2\pi}|a_0|^2\omega_0\sigma \int_0^\infty f(k\sigma)e^{kz}\sin(k(x - c_{g,0}t))dk + O(\alpha^2\epsilon^2), \tag{6.16}$$

$$\phi_{\mathrm{RF,T}} = -\frac{1}{2\pi}|a_0|^2\omega_0\sigma \int_0^\infty f(k\sigma)e^{-kz}\sin(k(x - c_{g,0}t))dk + O(\alpha^2\epsilon^2), \tag{6.17}$$

where $f(k\sigma)$ denotes the envelope in Fourier-space:

$$f(k\sigma) = \frac{\displaystyle\int_{-\infty}^{\infty} |A(x)|^2 e^{-ikx}dx}{\sigma|a_0|^2}. \tag{6.18}$$

For a Gaussian group $A = a_0\exp(((x - c_{g,0}t)/\sigma)^2/2)$, we have $f(k\sigma) = \sqrt{\pi}\exp(-(k\sigma)^2/4)$.

For the leading-order mean set-down, we have:

$$g'\frac{\partial \eta^{(2)}}{\partial t} = -\left.\frac{\partial^2 \phi_-^{(2)}}{\partial t^2}\right|_{z=0}. \tag{6.19}$$

and thus $\eta^{(2)} = 0$ at $O(\alpha^2\epsilon)$ from (6.16-6.17). Comparing the leading-order solutions for the return flow and the mean set-down, these are found to be equivalent to the deep-water surface gravity wave problem (see chapter 2) with the exception of the set-down, which is non-zero at $O(\alpha^2\epsilon^1)$ for two-dimensional deep-water surface gravity waves. The compensating effect of both layers restores symmetry, eliminating the set-down. The next potentially non-zero term would arise as the group changes shape due to dispersion, an effect not considered here.

We have assumed when neglecting higher-order terms in (6.12-6.14) that $(\rho_{\mathrm{B}} - \rho_{\mathrm{T}})/(\rho_{\mathrm{B}} + \rho_{\mathrm{T}}) = O(1)$. In other words, density differences are large and the waves are non-Boussinesq. It is evident from (6.13) that the order of the third term increases relative to the other terms in the Boussinesq limit, for example $(\rho_{\mathrm{B}} - \rho_{\mathrm{T}})/(\rho_{\mathrm{B}} + \rho_{\mathrm{T}}) = O(\epsilon)$. As this particular term is zero here due to symmetry, the solutions (6.16-6.17) remain valid in the Boussinesq limit.

6.2.3 Solutions for two layers of equal finite depth (H)

6.2.3.1 Linear solutions

Taking account of the effect of finite depth but restricting our attention to two layers of equal depth H, we assume linear (in α) velocity potentials of the form:

$$\phi_{\mathrm{T}}^{(1)} = B_{\mathrm{T}}(X,Z,T)\frac{\cosh(k_0(H-z))}{\sinh(k_0 H)}e^{i(k_0x-\omega_0t)} + O(\alpha^1\epsilon^1), \tag{6.20}$$

$$\phi_{\mathrm{B}}^{(1)} = B_{\mathrm{B}}(X,Z,T)\frac{\cosh(k_0(H+z))}{\sinh(k_0 H)}e^{i(k_0x-\omega_0t)} + O(\alpha^1\epsilon^1), \tag{6.21}$$

where $X = \epsilon(x - c_{g,0}t)$, $Z = \epsilon z$ and $T = \epsilon^2 t$. The corresponding interfacial elevation is assumed to be:

$$\eta^{(1)} = A(X,T)e^{i(k_0x-\omega_0t)} + O(\alpha^1\epsilon^1). \tag{6.22}$$

Satisfying the boundary conditions (6.3-6.4) at $O(\alpha^1\epsilon^0)$, we recover the standard periodic wave solutions for finite-depth interfacial waves:

$$\phi_{\mathrm{T}}^{(1)} = \frac{iA(X)\omega_0}{k_0}\frac{\cosh(k_0(H-z))}{\sinh(k_0 H)}e^{i(k_0x-\omega_0t)} + O(\alpha^1\epsilon^1), \tag{6.23}$$

$$\phi_{\mathrm{B}}^{(1)} = -\frac{iA(X)\omega_0}{k_0}\frac{\cosh(k_0(H+z))}{\sinh(k_0 H)}e^{i(k_0x-\omega_0t)} + O(\alpha^1\epsilon^1), \tag{6.24}$$

and the linear dispersion relationship $\omega_0^2 = g'k_0\tanh(k_0H)$, where $g' = g(\rho_{\mathrm{B}}-\rho_{\mathrm{T}})/(\rho_{\mathrm{B}}+\rho_{\mathrm{T}})$ is the reduced gravity. Table 6.1 summarizes the linear solutions, as evaluated at the undisturbed interface level $z = 0$.

6.2.3.2 Second-order solutions: mean flow

It is evident that the leading-order linear solutions in the two-layers of finite depth are simply equivalent to the leading-order finite-depth surface gravity wave solutions (see chapter 3) with gravity g replaced by the effective gravity g' in the dispersion relationship. Accordingly, we can derive leading-order expressions for the Stokes drift and the Stokes transport in the two layers:

$$u_{\mathrm{SD,T}} = \frac{\omega_0 k_0}{2}\frac{\cosh(2k_0(H-z))}{\sinh^2(k_0H)}|A(X)|^2, \quad u_{\mathrm{SD,B}} = \frac{\omega_0 k_0}{2}\frac{\cosh(2k_0(H+z))}{\sinh^2(k_0H)}|A(X)|^2, \tag{6.25a,b}$$

$$Q_{\mathrm{ST}} \equiv Q_{\mathrm{ST,T}} = Q_{\mathrm{ST,B}} = \frac{\omega_0}{2\tanh(k_0H)}|A(X)|^2. \tag{6.26}$$

As expected, the Stokes drift and transport are equal and in the same direction in both layers and entirely equivalent to the surface gravity wave problem considered in chapter 3.

In order to take stock of the different orders of the terms in the mean flow forcing equations (6.6-6.7) and make use of symmetry again, we define $\phi_-^2 = \phi_{\mathrm{B}}^{(2)} - \phi_{\mathrm{T}}^{(2)}$ and $\phi_+^2 = \phi_{\mathrm{B}}^{(2)} + \phi_{\mathrm{T}}^{(2)}$, as for the deep-water interfacial waves considered in §6.2.2. The ordering in (6.12) remains unchanged and we still have $\phi_-^{(2)} = O(\alpha^2\epsilon^0)$. We have from (6.7), using the definition of the Stokes transport in (6.26) and the linear polarization relationships in table 6.1:

$$\underbrace{\frac{1}{2}g(\rho_{\mathrm{B}}-\rho_{\mathrm{T}})\frac{\partial\phi_+^{(2)}}{\partial z}}_{O(\alpha^2\epsilon^1)} + \underbrace{(\rho_{\mathrm{B}}-\rho_{\mathrm{T}})\frac{\partial^2\phi_+^{(2)}}{\partial t^2}}_{O(\alpha^2\epsilon^2)} + \underbrace{(\rho_{\mathrm{B}}+\rho_{\mathrm{T}})\frac{\partial^2\phi_-^{(2)}}{\partial t^2}}_{O(\alpha^2\epsilon^2)} = \underbrace{\overline{\frac{1}{2}\frac{\partial}{\partial t}\Big(\rho_{\mathrm{T}}|\nabla\phi_{\mathrm{T}}^{(1)}|^2 - \rho_{\mathrm{B}}|\nabla\phi_{\mathrm{B}}^{(1)}|^2\Big)}}_{O(\alpha^2\epsilon^1)} + \ldots$$
$$+ \underbrace{\overline{\frac{\partial}{\partial t}\Big(\rho_{\mathrm{T}}\frac{\partial^2\phi_{\mathrm{T}}^{(1)}}{\partial z\partial t} - \rho_{\mathrm{B}}\frac{\partial^2\phi_{\mathrm{B}}^{(1)}}{\partial z\partial t}\Big)\eta^{(1)}}}_{O(\alpha^2\epsilon^1)} \quad \text{on} \quad z=0, \tag{6.27}$$

where the right hand side was zero at $O(\alpha^2\epsilon^1)$ for two deep layers, but is non-zero for finite depth (cf. table 6.1). We then have at leading-order:

$$g(\rho_{\mathrm{B}}-\rho_{\mathrm{T}})\frac{\partial\eta^{(2)}}{\partial t} = -(\rho_{\mathrm{B}}-\rho_{\mathrm{T}})\frac{\partial}{\partial t}\left[\frac{1}{4}\Big(\frac{1}{\tanh^2(k_0H)} - 1\Big)\omega_0^2|A|^2\right], \tag{6.28}$$

which can be solved to give:

$$\eta^{(2)} = -\frac{1}{2}\frac{1}{\sinh(2k_0H)}\frac{g'}{g}k_0|A|^2 + O(\alpha^2\epsilon^2). \tag{6.29}$$

From (6.6a-6.6b) we then have to leading-order:

$$\frac{\partial\phi_{\mathrm{T}}^{(2)}}{\partial z}\bigg|_{z=0} = \big(-1+\delta_{\mathrm{FD}}(k_0H)\big)\frac{\partial Q_{\mathrm{ST}}}{\partial x}, \quad \frac{\partial\phi_{\mathrm{B}}^{(2)}}{\partial z}\Big|_{z=0} = \big(1+\delta_{\mathrm{FD}}(k_0H)\big)\frac{\partial Q_{\mathrm{ST}}}{\partial x}, \tag{6.30a,b}$$

where Q_{ST} is given by (6.26) and $\delta_{\mathrm{FD}}(k_0H) = c_{g,0}\omega_0/(g\sinh(2k_0H))$. Explicitly, the term arising from the mean set-down $\delta_{\mathrm{FD}}(k_0H)$ can be written as:

$$\delta_{\mathrm{FD}}(k_0H) = \frac{k_0H\mathrm{sech}^2(k_0H) + \tanh(k_0H)}{2\sinh(2k_0H)}, \tag{6.31}$$

where, to avoid confusion, we note that δ does not denote a Dirac delta function in this chapter. In the deep-water limit $k_0H \to \infty$, $\delta_{\mathrm{FD}}(k_0H) \to 0$ and we recover the deep-water return flow forcing equations for two layers (6.16-6.17). In the limit $k_0H \to 0$,

$\delta_{\text{FD}}(k_0H) \to 1/2$. We note (6.31) is equivalent to the analogous definition (3.23) for finite-depth surface gravity waves in chapter 3. Explicitly, we have for the return flow satisfying Laplace and the top and bottom boundary conditions:

$$\phi_{\text{RF,B}} = -\frac{|a_0|^2\omega_0\sigma\big(1+\delta_{\text{FD}}(k_0H)\big)}{2\pi\tanh(k_0H)}\int_0^\infty f(k\sigma)\frac{\cosh(k(z+H))}{\sinh(kH)}\sin(k(x-c_{g,0}t))dk+O(\alpha^2\epsilon^2), \tag{6.32}$$

$$\phi_{\text{RF,T}} = -\frac{|a_0|^2\omega_0\sigma\big(1-\delta_{\text{FD}}(k_0H)\big)}{2\pi\tanh(k_0H)}\int_0^\infty f(k\sigma)\frac{\cosh(k(H-z))}{\sinh(kH)}\sin(k(x-c_{g,0}t))dk+O(\alpha^2\epsilon^2). \tag{6.33}$$

As previously, we have assumed when neglecting higher-order terms in (6.27) that $(\rho_{\text{B}}-\rho_{\text{T}})/(\rho_{\text{B}}+\rho_{\text{T}}) = O(1)$. In other words, density differences are large and the waves are non-Boussinesq. It is evident from (6.27) that the order of the third term increases relative to the other terms in the Boussinesq limit. However, we note that this term will be zero due to symmetry and the solutions (6.32-6.33) remain valid in the Boussinesq limit.

6.2.4 Solutions for a layer of finite depth (H) overlying a layer of infinite depth ($H_{\text{B}} \to \infty$)

6.2.4.1 Linear solutions

Taking account of the effect of finite depth in the top layer of depth H, but retaining an infinitely deep bottom layer, we assume linear (in α) velocity potentials of the form:

$$\phi_{\text{T}}^{(1)} = B_{\text{T}}(X,Z,T)\frac{\cosh(k_0(H-z))}{\sinh(k_0H)}e^{i(k_0x-\omega_0t)} + O(\alpha^1\epsilon^1), \tag{6.34}$$

$$\phi_{\text{B}}^{(1)} = B_{\text{B}}(X,Z,T)e^{k_0z}e^{i(k_0x-\omega_0t)} + O(\alpha^1\epsilon^1), \tag{6.35}$$

where $X = \epsilon(x-c_{g,0}t)$, $Z = \epsilon z$ and $T = \epsilon^2 t$. The corresponding interfacial elevation is assumed to be:

$$\eta^{(1)} = A(X,T)e^{i(k_0x-\omega_0t)} + O(\alpha^1\epsilon^1). \tag{6.36}$$

Satisfying the boundary conditions (6.3-6.4) at $O(\alpha^1\epsilon^0)$, we recover the standard periodic wave solutions:

$$\phi_{\text{T}}^{(1)} = \frac{iA(X)\omega_0}{k_0}\frac{\cosh(k_0(H-z))}{\sinh(k_0H)}e^{i(k_0x-\omega_0t)} + O(\alpha^1\epsilon^1), \tag{6.37}$$

$$\phi_{\mathrm{B}}^{(1)} = -\frac{iA(X)\omega_0}{k_0} e^{k_0 z} e^{i(k_0 x - \omega_0 t)} + O(\alpha^1 \epsilon^1), \tag{6.38}$$

and the linear dispersion relationship $\omega_0^2 = gk_0(\rho_{\mathrm{B}} - \rho_{\mathrm{T}})\sinh(k_0 H)/(\rho_{\mathrm{T}}\cosh(k_0 H) + \rho_{\mathrm{B}}\sinh(k_0 H))$. In the Boussinesq limit $\Delta\rho = \rho_{\mathrm{B}} - \rho_{\mathrm{T}} \to 0$, the linear dispersion relationship simplifies to $\omega_0^2 = g' k_0(1 - \exp(-2k_0 H))/2$, where $g' = g(\rho_{\mathrm{B}} - \rho_{\mathrm{T}})/(\rho_{\mathrm{B}} + \rho_{\mathrm{T}})$ is the reduced gravity. The final column in table 6.1 summarizes the linear solutions, as evaluated at the undisturbed interface level $z = 0$.

6.2.4.2 Second-order solutions: mean flow

It is evident that the leading-order linear solutions in the two-layers are simply equivalent to the leading-order surface gravity wave solutions for finite depth (see chapter 3) in the top layer and for deep-water (see chapter 2) in the bottom layer with gravity g replaced by the effective gravity g' in the dispersion relationship. The leading-order expressions for the Stokes drift and the Stokes transport in the two layers are self-evident:

$$u_{\mathrm{SD,T}} = \frac{\omega_0 k_0}{2}\frac{\cosh(2k_0(H-z))}{\sinh^2(k_0 H)}|A(X)|^2, \quad u_{\mathrm{SD,B}} = \omega_0 k_0 e^{2k_0 z}|A(X)|^2, \tag{6.39a,b}$$

$$Q_{\mathrm{ST,T}} = \frac{\omega_0}{2\tanh(k_0 H)}|A(X)|^2, \quad Q_{\mathrm{ST,B}} = \frac{\omega_0}{2}|A(X)|^2. \tag{6.40a,b}$$

The Stokes drift and transport are still in the same direction in both layers, but no longer equal and symmetry is lost.

Without defining the difference and sum terms (in the absence of symmetry), we have directly from (6.6-6.7), using the definition of the Stokes transport in (6.40) and the linear polarization relationships in table 6.1:

$$\underbrace{\left.\frac{\partial \phi_{\mathrm{T}}^{(2)}}{\partial z}\right|_{z=0}}_{O(\alpha^2\epsilon)} - \underbrace{\frac{\partial \eta^{(2)}}{\partial t}}_{O(\alpha^2\epsilon)} = -\underbrace{\frac{\omega_0}{2\tanh(k_0 H)}\frac{\partial |A(X)|^2}{\partial x}}_{O(\alpha^2\epsilon)} + O(\alpha^2\epsilon^3), \tag{6.41}$$

$$\underbrace{\left.\frac{\partial \phi_{\mathrm{B}}^{(2)}}{\partial z}\right|_{z=0}}_{O(\alpha^2\epsilon)} - \underbrace{\frac{\partial \eta^{(2)}}{\partial t}}_{O(\alpha^2\epsilon)} = \underbrace{\frac{\omega_0}{2}\frac{\partial |A(X)|^2}{\partial x}}_{O(\alpha^2\epsilon)} + O(\alpha^2\epsilon^3), \tag{6.42}$$

$$g(\rho_{\rm B}-\rho_{\rm T})\underbrace{\eta^{(2)}}_{O(\alpha^2)}+\rho_{\rm B}\underbrace{\frac{\partial\phi_{\rm B}^{(2)}}{\partial t}\bigg|_{z=0}}_{O(\alpha^2\epsilon)}-\rho_{\rm T}\underbrace{\frac{\partial\phi_{\rm T}^{(2)}}{\partial t}\bigg|_{z=0}}_{O(\alpha^2\epsilon)}=\underbrace{\frac{1}{4}\rho_{\rm T}\omega_0^2\left(\frac{1}{\tanh^2(k_0H)}-1\right)|A(X)|^2}_{O(\alpha^2)}. \tag{6.43}$$

From (6.43), we obtain for the leading-order mean surface elevation:

$$\eta^{(2)}=\frac{\rho_{\rm T}\sinh(k_0H)}{\rho_{\rm T}\cosh(k_0H)+\rho_{\rm B}\sinh(k_0H)}\left(\frac{1}{\tanh^2(k_0H)}-1\right)k_0|A(X)|^2. \tag{6.44}$$

In the Boussinesq limit, we obtain from (6.44):

$$\eta^{(2)}=\frac{1}{2}\frac{1}{\exp(2k_0H)-1}k_0|A(X)|^2. \tag{6.45}$$

From comparison with the set-down for closed-lid interfacial waves in a two-layer fluid where the layers are of equal depth H (6.29), we note the mean surface displacement no longer becomes smaller in the limit of small density differences ($g'/g\to 0$). Moreover, we have a set-up instead of a set-down. The set-up is driven by the lack of symmetry between the Stokes transport forcing on either side of the interface. The contribution from the top layer is no longer cancelled out by the contribution from the bottom layer and remains in (6.43). Finally, we have for the return flow forcing to leading order:

$$\frac{\partial\phi_{\rm T}^{(2)}}{\partial z}\bigg|_{z=0}=-\frac{\omega_0}{2\tanh(k_0H)}\Big(1+\delta_{\rm FD}^*(k_0H,\rho_{\rm B},\rho_{\rm T})\tanh(k_0H)\Big)\frac{\partial|A(X)|^2}{\partial x}, \tag{6.46}$$

$$\frac{\partial\phi_{\rm B}^{(2)}}{\partial z}\bigg|_{z=0}=\frac{\omega_0}{2}\Big(1-\delta_{\rm FD}^*(k_0H,\rho_{\rm B},\rho_{\rm T})\Big)\frac{\partial|A(X)|^2}{\partial x}. \tag{6.47}$$

where $\delta_{\rm FD}^*=\rho_{\rm T}\omega_0c_{g,0}(\tanh^{-2}(k_0H)-1)/2g(\rho_{\rm B}-\rho_{\rm T})$. In the Boussinesq limit:

$$\delta_{\rm FD}^*(k_0H)=\frac{1}{8}e^{-2k_0H}\big(-1+e^{2k_0H}+2k_0H\big)\mathrm{csch}^2(k_0H), \tag{6.48}$$

which is not equal to $\delta_{\rm FD}$ defined for the symmetric case in (6.31). Figure 6.2a compares the two solutions. Solving Laplace in both layers subject to the bottom and top boundary conditions and (6.46-6.47) then gives:

$$\phi_{\rm RF,B}=-\frac{|a_0|^2\omega_0\sigma}{2\pi}\big(1-\delta_{\rm FD}^*(k_0H)\big)\int_0^\infty f(k\sigma)e^{kz}\sin(k(x-c_{g,0}t))dk, \tag{6.49}$$

$$\phi_{\rm RF,T}=-\frac{|a_0|^2\omega_0\sigma\big(1+\delta_{\rm FD}^*(k_0H)\tanh(k_0H)\big)}{2\pi\tanh(k_0H)}\int_0^\infty f(k\sigma)\frac{\cosh(k(H-z))}{\sinh(kH)}\sin(k(x-c_{g,0}t))dk. \tag{6.50}$$

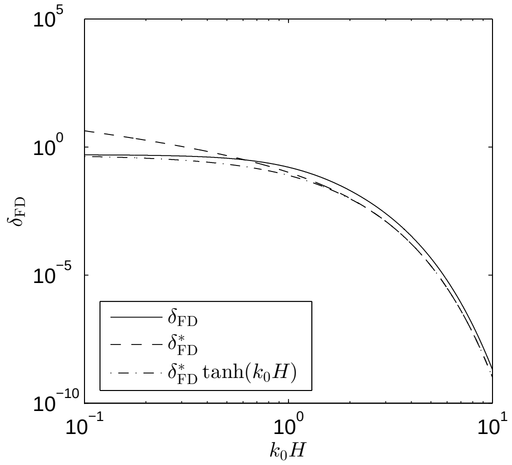

a)

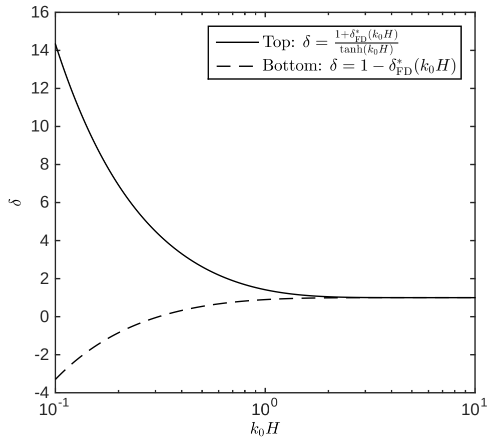

b)

Figure 6.2: Finite depth coefficients for the return flow in the Boussinesq limit of a two-layer fluid with a closed lid. Panel a compares $\delta_{\rm FD}(k_0H)$ (6.31) for the symmetric case with $\delta^*_{\rm FD}(k_0H)$ (6.48) and $\delta^*_{\rm FD}(k_0H)\tanh(k_0H)$ for the asymmetric case. Panel b compares the final depth corrections in the solutions for the return flow in the two layers (6.49-6.50).

Figure 6.2b compares the prefactors in (6.49-6.50) showing a larger magnitude in the top layer. Focussing on the top-layer, the magnitude of the return flow is increased relative to the solution in §6.2.3 by the asymmetry, which causes a positive set-up and thus a larger return flow in the top layer and a smaller one in the bottom layer. Finally, it is evident from figure 6.2b that the role of the set-up dominates that of the Stokes transport in the bottom layer for sufficiently small k_0H. In fact, the return flow then reverses and becomes positive, in the same direction as the Stokes drift. For $k_0H \approx 0.30$ the "return flow" in the bottom layer is zero. For the top layer, we still have $\delta^*_{\rm FD}(k_0H)\tanh(k_0H) \to 1/2$ as $k_0H \to 0$.

6.3 Coupled free surface and interfacial waves

6.3.1 Governing equations and boundary conditions

Now consider the two-dimensional domain (see figure 6.1b) consisting of two layers of fluid of different density, but with a free surface. The fluid on the bottom has density $\rho_{\rm B}$ and thickness $H_{\rm B}$ and the fluid on top has density $\rho_{\rm T}$ and thickness $H_{\rm T}$. The vertical coordinate z is measured upwards from the undisturbed free surface; the vertical coordinate z' is also measured upwards, but from the undisturbed interface between the two fluids, so that $z' = z + H_{\rm T}$. Assuming irrotationality and incompressibility, the governing equations in both fluids are Laplace: $\nabla^2\phi_{\rm B} = 0$ and $\nabla^2\phi_{\rm T} = 0$. The standard free surface boundary conditions are:

$$\frac{D}{Dt}\Big(\eta_{\mathrm{T}}-z\Big)=0,\quad \frac{\partial\phi_{\mathrm{T}}}{\partial t}+\frac{1}{2}|\nabla\phi_{\mathrm{T}}|^2+g\eta_{\mathrm{T}}=0\quad\text{on } z=\eta_{\mathrm{T}}(x,t),\tag{6.51a,b}$$

stating, respectively, that a particle that is located at the free surface stays there (kinematic boundary condition) and that the pressure on the free surface is constant and equal to zero (dynamic boundary condition). The interfacial boundary conditions are:

$$\frac{D}{Dt}\Big(\eta_{\mathrm{B}}-z\Big)=0,\quad \frac{D}{Dt}\Big(\eta_{\mathrm{B}}-z'\Big)=0\quad\text{on } z'=\eta_{\mathrm{B}}(x,t),\tag{6.52a,b}$$

$$\rho_{\mathrm{B}}\Big(\frac{\partial\phi_{\mathrm{B}}}{\partial t}+\frac{1}{2}|\nabla\phi_{\mathrm{B}}|^2+g\eta_{\mathrm{B}}\Big)=\rho_{\mathrm{T}}\Big(\frac{\partial\phi_{\mathrm{T}}}{\partial t}+\frac{1}{2}|\nabla\phi_{\mathrm{T}}|^2+g\eta_{\mathrm{B}}\Big)\quad\text{on } z'=\eta_{\mathrm{B}}(x,t),\tag{6.53}$$

where (6.52) ensures particles located at the interface remain there on both sides of the interface and (6.53) equates the pressures on both sides. Explicitly, $D/Dt=\partial_t+u_{\mathrm{T}}\partial_x+w_{\mathrm{T}}\partial_z$ for the top layer and $D/Dt=\partial_t+u_{\mathrm{B}}\partial_x+w_{\mathrm{B}}\partial_z$ for the bottom layer. Finally, the bottom boundary requires $w_{\mathrm{B}}\to 0$ as $z'\to -H_{\mathrm{B}}$.

6.3.2 Linearized equations and solutions

The linearized (in α) free surface boundary conditions (6.51) are:

$$\frac{\partial\eta_{\mathrm{T}}^{(1)}}{\partial t}-w_{\mathrm{T}}^{(1)}=0,\quad \frac{\partial\phi_{\mathrm{T}}^{(1)}}{\partial t}+g\eta_{\mathrm{T}}=0\quad\text{on}\quad z=0,\tag{6.54a,b}$$

which can be combined eliminating $\eta_{\mathrm{T}}^{(2)}$:

$$\frac{1}{g}\frac{\partial^2\phi_{\mathrm{T}}^{(1)}}{\partial t^2}+\frac{\partial\phi_{\mathrm{T}}^{(1)}}{\partial z}=0\quad\text{on}\quad z=0.\tag{6.55}$$

The linearized (in α) interfacial boundary conditions (6.52-6.53) are:

$$\frac{\partial\eta_{\mathrm{B}}^{(1)}}{\partial t}-w_{\mathrm{B}}^{(1)}=0,\quad \frac{\partial\eta_{\mathrm{B}}^{(1)}}{\partial t}-w_{\mathrm{T}}^{(1)}=0,\quad \rho_{\mathrm{B}}\frac{\partial\phi_{\mathrm{B}}^{(1)}}{\partial t}+g\eta_{\mathrm{B}}^{(1)}=\rho_{\mathrm{T}}\frac{\partial\phi_{\mathrm{T}}^{(1)}}{\partial t}+g\eta_{\mathrm{B}}^{(1)}\quad\text{on}\quad z'=0,\tag{6.56a,b,c}$$

which can be combined to eliminate $\eta_{\mathrm{B}}^{(2)}$:

$$\rho_{\mathrm{T}}\frac{\partial^2\phi_{\mathrm{T}}^{(1)}}{\partial t^2}\bigg|_{z=0}-\rho_{\mathrm{B}}\frac{\partial^2\phi_{\mathrm{B}}^{(1)}}{\partial t^2}\bigg|_{z=0}-g(\rho_{\mathrm{B}}-\rho_{\mathrm{T}})\frac{\partial\phi_{\mathrm{B}}^{(1)}}{\partial z}\bigg|_{z=0}=0\quad\text{on}\quad z'=0.\tag{6.57}$$

Henceforth, we restrict our attention to an infinitely deep bottom layer ($H_{\mathrm{B}} \to \infty$) and a top layer of finite depth H_{T}. Evidently, if the top layer is also of infinite depth, the coupling between the surface and the interface is lost immediately and we return to the closed-lid case. We seek linear (in α) solutions of the form:

$$\phi_{\mathrm{B}}^{(1)}(x,z,t) = B_{\mathrm{B}}(X,Z,T)e^{k_0 z'}e^{i(k_0 x-\omega_0 t)} + O(\alpha^1\epsilon^1), \tag{6.58}$$

$$\phi_{\mathrm{T}}^{(1)}(x,z,t) = \big(B_{\mathrm{T}}^{+}(X,Z,T)e^{k_0 z} + B_{\mathrm{T}}^{-}(X,Z,T)e^{-k_0 z}\big)e^{i(k_0 x-\omega_0 t)} + O(\alpha^1\epsilon^1), \tag{6.59}$$

where $X = \epsilon(x - c_{g,0}t)$, $Z = \epsilon z$, $T = \epsilon^2 t$. Furthermore, in order for the dynamics of the two layers to be coupled at zeroth order in ϵ it must be the case that H_{T} scales on k_0^{-1} and not on the slow scale σ. We further define:

$$\eta_{\mathrm{B}}^{(1)}(x,t) = A_{\mathrm{B}}(X,T)e^{i(k_0 x-\omega_0 t)} + O(\alpha^1\epsilon^1), \quad \eta_{\mathrm{T}}^{(1)}(x,t) = A_{\mathrm{T}}(X,T)e^{i(k_0 x-\omega_0 t)} + O(\alpha^1\epsilon^1). \tag{6.60}$$

Substituting the trial solutions (6.58-6.60) into the linear boundary conditions (6.54-6.56), we find the standard linear dispersion relationship after considerable manipulation:

$$\big(D-1\big)\Big((\rho_{\mathrm{B}}-\rho_{\mathrm{T}})\sinh(k_0 H_{\mathrm{T}}) - D\big(\rho_{\mathrm{T}}\sinh(k_0 H_{\mathrm{T}}) + \rho_{\mathrm{B}}\cosh(k_0 H_{\mathrm{T}})\big)\Big) = 0, \tag{6.61}$$

where $D \equiv \omega_0^2/gk_0$. It is clear that the dispersion relationship (6.61) has two solutions: $D = \omega_0^2/gk_0 = 1$, known as the barotropic or surface mode, and the baroclinic or internal mode:

$$D \equiv \frac{\omega_0^2}{gk_0} = \frac{(\rho_{\mathrm{B}}-\rho_{\mathrm{T}})\sinh(k_0 H_{\mathrm{T}})}{\rho_{\mathrm{T}}\sinh(k_0 H_{\mathrm{T}}) + \rho_{\mathrm{B}}\cosh(k_0 H_{\mathrm{T}})}. \tag{6.62}$$

It can be shown that in the Boussinesq limit (6.62) reduces to the linear dispersion relationship for the analogous problem with a closed lid (§6.2.4). The (non-Boussinesq) linear solutions for the barotropic mode are:

$$\eta_{\mathrm{T}}^{(1)} = A_{\mathrm{T}}e^{i(k_0 x-\omega_0 t)} + O(\alpha^1\epsilon^1), \quad \eta_{\mathrm{B}}^{(1)} = A_{\mathrm{T}}e^{-k_0 H_{\mathrm{T}}}e^{i(k_0 x-\omega_0 t)} + O(\alpha^1\epsilon^1), \tag{6.63a,b}$$

$$\phi_{\mathrm{T}}^{(1)} = -i\frac{\omega_0 A_{\mathrm{T}}}{k_0}e^{k_0 z}e^{i(k_0 x-\omega_0 t)} + O(\alpha^1\epsilon^1), \quad \phi_{\mathrm{B}}^{(1)} = -i\frac{\omega_0 A_{\mathrm{T}}}{k_0}e^{k_0 z}e^{i(k_0 x-\omega_0 t)} + O(\alpha^1\epsilon^1), \tag{6.64a,b}$$

where it is immediately evident that the velocity potential is continuous across the interface and the solutions are entirely equivalent to the deep-water surface gravity waves solutions examined in chapter 2. The fluid motion is barotropic: its surfaces of constant density and constant pressure coincide.

The solutions for the baroclinic mode, in which the interface is no longer a surface of constant pressure, are:

$$\eta_{\mathrm{T}}^{(1)} = A_{\mathrm{T}} e^{i(k_0 x - \omega_0 t)} + O(\alpha^1 \epsilon^1), \quad \eta_{\mathrm{B}}^{(1)} = -A_{\mathrm{T}} \frac{\rho_{\mathrm{T}}}{\rho_{\mathrm{B}} - \rho_{\mathrm{T}}} e^{k_0 H_{\mathrm{T}}} e^{i(k_0 x - \omega_0 t)} + O(\alpha^1 \epsilon^1), \quad (6.65\text{a,b})$$

$$\phi_{\mathrm{B}}^{(1)} = i \frac{\omega_0 A_{\mathrm{T}}}{k_0} \frac{\rho_{\mathrm{T}}}{\rho_{\mathrm{B}} - \rho_{\mathrm{T}}} e^{k_0 H_{\mathrm{T}}} e^{k_0 z'} e^{i(k_0 x - \omega_0 t)} + O(\alpha^1 \epsilon^1), \quad (6.66)$$

$$\phi_{\mathrm{T}}^{(1)} = -i \frac{\omega_0 A_{\mathrm{T}}}{k_0} \left(\frac{1 + D^{-1}}{2} e^{k_0 z} + \frac{D^{-1} - 1}{2} e^{-k_0 z} \right) e^{i(k_0 x - \omega_0 t)} + O(\alpha^1 \epsilon^1), \quad (6.67)$$

where $D^{-1} = (\rho_{\mathrm{T}} \sinh(k_0 H_{\mathrm{T}}) + \rho_{\mathrm{B}} \cosh(k_0 H_{\mathrm{T}}))/(\rho_{\mathrm{B}} - \rho_{\mathrm{T}}) \sinh(k_0 H_{\mathrm{T}})$ corresponding to the baroclinic solution to the dispersion relationship. Table 6.2 summarizes the linear solutions, as evaluated at the undisturbed free surface level ($z = 0$) and the undisturbed interface level $z' = 0$ for both the barotropic and the baroclinic mode. The final column in table 6.2 shows the solutions for the baroclinic mode at the undisturbed interface level $z' = 0$ in the Boussinesq limit, in which $\Delta\rho = \rho_{\mathrm{B}} - \rho_{\mathrm{T}}$ is small and $\rho_{\mathrm{T}} \approx \rho_{\mathrm{B}} \approx \rho_0$, a reference density. In the Boussinesq limit (6.65-6.67) reduce to:

$$\eta_{\mathrm{B}}^{(1)} = A_{\mathrm{B}} e^{i(k_0 x - \omega_0 t)} + O(\alpha^1 \epsilon^1), \quad \eta_{\mathrm{T}}^{(1)} = -\frac{\Delta\rho}{\rho_0} e^{-k_0 H_{\mathrm{T}}} A_{\mathrm{B}} e^{i(k_0 x - \omega_0 t)} + O(\alpha^1 \epsilon^1), \quad (6.68\text{a,b})$$

$$\phi_{\mathrm{B}}^{(1)} = -i \frac{\omega_0 A_{\mathrm{B}}}{k_0} e^{k_0 z'} e^{i(k_0 x - \omega_0 t)} + O(\alpha^1 \epsilon^1), \; \phi_{\mathrm{T}}^{(1)} = i \frac{\omega_0 A_{\mathrm{B}}}{k_0} \frac{\cosh(k_0 z)}{\sinh(k_0 H_{\mathrm{T}})} e^{i(k_0 x - \omega_0 t)} + O(\alpha^1 \epsilon^1), \quad (6.69\text{a,b})$$

where it is now convenient to express all quantities in terms of the internal wave amplitude A_{B}. From comparison with the analogous closed-lid solutions (6.37-6.38), it is clear and not altogether surprising that the small displacement of the free surface does not contribute to the velocity potential in the top layer in the Boussinesq limit, in line with the commonly made closed-lid approximation in oceanographic applications that is also consistent with field observations of interfacial waves in the ocean (e.g. Kao et al. (1985)).

6.3.3 Second-order solutions: mean flow for the barotropic mode

6.3.3.1 Stokes transport

With equivalent expressions for the velocity fields as the deep-water surface gravity waves in chapter 2, the expressions for Stokes drift and Stokes transport for the barotropic mode must also be equivalent to the deep-water surface gravity wave case. Writing the Stokes

	Barotropic mode $z=0$	Barotropic mode $z'=0$	Baroclinic mode (non-Boussinesq) $z=0$	Baroclinic mode (non-Boussinesq) $z'=0$	Baroclinic mode (Boussinesq) $z'=0$
$\eta_{\mathrm{T}}^{(1)}$	A_{T}	A_{T}	A_{T}	A_{T}	$-(\Delta\rho/\rho_0)e^{-k_0H_{\mathrm{T}}}A_{\mathrm{B}}$
$\eta_{\mathrm{B}}^{(1)}$	$e^{-k_0H_{\mathrm{T}}}A_{\mathrm{T}}$	$e^{-k_0H_{\mathrm{T}}}A_{\mathrm{T}}$	$-\frac{\rho_{\mathrm{T}}}{\rho_{\mathrm{B}}-\rho_{\mathrm{T}}}e^{k_0H_{\mathrm{T}}}A_{\mathrm{T}}$	$-\frac{\rho_{\mathrm{T}}}{\rho_{\mathrm{B}}-\rho_{\mathrm{T}}}e^{k_0H_{\mathrm{T}}}A_{\mathrm{T}}$	A_{B}
$u_{\mathrm{T}}^{(1)}$	ω_0A_{T}	$\omega_0e^{-k_0H_{\mathrm{T}}}A_{\mathrm{T}}$	$\omega_0D^{-1}A_{\mathrm{T}}$	$\omega_0\Big(D^{-1}\cosh(k_0H_{\mathrm{T}})-\sinh(k_0H_{\mathrm{T}})\Big)A_{\mathrm{T}}$	$-(\omega_0/\tanh(k_0H_{\mathrm{T}}))A_{\mathrm{B}}$
$u_{\mathrm{B}}^{(1)}$	–	$\omega_0e^{-k_0H_{\mathrm{T}}}A_{\mathrm{T}}$	–	$-\omega_0\frac{\rho_{\mathrm{T}}}{\rho_{\mathrm{B}}-\rho_{\mathrm{T}}}e^{k_0H_{\mathrm{T}}}A_{\mathrm{T}}$	ω_0A_{B}
$w_{\mathrm{T}}^{(1)}$	$-i\omega_0A_{\mathrm{T}}$	$-i\omega_0e^{-k_0H_{\mathrm{T}}}A_{\mathrm{T}}$	$-i\omega_0A_{\mathrm{T}}$	$-i\omega_0\Big(\cosh(k_0H_{\mathrm{T}})-D^{-1}\sinh(k_0H_{\mathrm{T}})\Big)A_{\mathrm{T}}$	$-i\omega_0A_{\mathrm{B}}$
$w_{\mathrm{B}}^{(1)}$	–	$-i\omega_0e^{-k_0H_{\mathrm{T}}}A_{\mathrm{T}}$	–	$i\omega_0\frac{\rho_{\mathrm{T}}}{\rho_{\mathrm{B}}-\rho_{\mathrm{T}}}e^{k_0H_{\mathrm{T}}}A_{\mathrm{T}}$	$-i\omega_0A_{\mathrm{B}}$
$\frac{\partial^2\phi_{\mathrm{T}}^{(1)}}{\partial z\partial t}$	$-\omega_0^2A_{\mathrm{T}}$	$-\omega_0^2e^{-k_0H_{\mathrm{T}}}A_{\mathrm{T}}$	$-\omega_0^2A_{\mathrm{T}}$	$-\omega_0^2\Big(\cosh(k_0H_{\mathrm{T}})-D^{-1}\sinh(k_0H_{\mathrm{T}})\Big)A_{\mathrm{T}}$	$-\omega_0^2A_{\mathrm{B}}$
$\frac{\partial^2\phi_{\mathrm{B}}^{(1)}}{\partial z\partial t}$	–	$-\omega_0^2e^{-k_0H_{\mathrm{T}}}A_{\mathrm{T}}$	–	$\omega_0^2\frac{\rho_{\mathrm{T}}}{\rho_{\mathrm{B}}-\rho_{\mathrm{T}}}e^{k_0H_{\mathrm{T}}}A_{\mathrm{T}}$	$-\omega_0^2A_{\mathrm{B}}$

Table 6.2: Linear ($O(\alpha^1\epsilon^0)$) solutions for coupled interfacial and surface waves evaluated at the undisturbed free surface ($z=0$) and the undisturbed interface ($z'=0$). All terms are to be multiplied by $\exp(i(k_0x-\omega_0t))$. For the baroclinic mode $D^{-1}=(\rho_{\mathrm{T}}\sinh(k_0H_{\mathrm{T}})+\rho_{\mathrm{B}}\cosh(k_0H_{\mathrm{T}}))/((\rho_{\mathrm{B}}-\rho_{\mathrm{T}})\sinh(k_0H_{\mathrm{T}}))$.

transport explicitly for each layer, we have for the barotropic mode to leading-order:

$$Q_{\mathrm{ST,T}}=\overline{\int_{-H_{\mathrm{T}}+\eta_{\mathrm{B}}(x,t)}^{\eta_{\mathrm{T}}(x,t)}u_{\mathrm{T}}^{(1)}dz}=\frac{1}{2}\omega_0\Big(1-e^{-2k_0H_{\mathrm{T}}}\Big)|A_{\mathrm{T}}|^2, \tag{6.70}$$

$$Q_{\mathrm{ST,B}}=\overline{\int_{-\infty}^{\eta_{\mathrm{B}}(x,t)}u_{\mathrm{B}}^{(1)}dz'}=\frac{1}{2}\omega_0e^{-2k_0H_{\mathrm{T}}}|A_{\mathrm{T}}|^2, \tag{6.71}$$

where the over-lines denote averaging over the fast time scales. Evidently, we have $Q_{\mathrm{ST,T}}+Q_{\mathrm{ST,B}}=\omega_0|A_{\mathrm{T}}|^2/2$, the deep-water solution without two densities.

6.3.3.2 Return flow

From the free surface boundary conditions (6.51):

$$\underbrace{\frac{\partial\phi_{\mathrm{T}}^{(2)}}{\partial z}}_{O(\alpha^2\epsilon^1)}+\frac{1}{g}\underbrace{\frac{\partial^2\phi_{\mathrm{T}}^{(2)}}{\partial t^2}}_{O(\alpha^2\epsilon^2)}=\underbrace{\frac{\partial}{\partial x}\overline{\Big(u_{\mathrm{T}}^{(1)}\eta_{\mathrm{T}}^{(1)}\Big)}}_{O(\alpha^2\epsilon^1)}-\frac{1}{g}\underbrace{\frac{\partial}{\partial t}}_{O(\epsilon)}\Bigg(\underbrace{\overline{\frac{\partial^2\phi_{\mathrm{T}}^{(1)}}{\partial t\partial z}\eta_{\mathrm{T}}^{(1)}+\frac{1}{2}|\nabla\phi_{\mathrm{T}}^{(1)}|^2}}_{=0\ \text{at}\ O(\alpha^2\epsilon^0)}\Bigg)\quad\text{on}\quad z=0, \tag{6.72}$$

where we have used the linear polarization relationships in table 6.2, restricted our attention to mean flow terms and assumed these evolve on the slow scales. We thus have to leading order:

$$\frac{\partial\phi_{\mathrm{T}}^{(2)}}{\partial z}\Big|_{z=0}=\frac{\partial}{\partial x}\Big(u_{\mathrm{T}}^{(1)}\big|_{z=0}\eta_{\mathrm{T}}^{(1)}\Big)=\frac{1}{2}\omega_0\frac{\partial|A_{\mathrm{T}}|^2}{\partial x}. \tag{6.73}$$

We have from the interfacial boundary conditions (6.52-6.53) and the polarization relationships in table 6.2:

$$\underbrace{\left.\frac{\partial \phi_{\mathrm{T}}^{(2)}}{\partial z}\right|_{z'=0}}_{O(\alpha^2\epsilon)} - \underbrace{\frac{\partial \eta_{\mathrm{B}}^{(2)}}{\partial t}}_{O(\alpha^2\epsilon^2)} = \underbrace{\frac{\omega_0}{2} e^{-2k_0 H_{\mathrm{T}}} \frac{\partial |A(X)|^2}{\partial x}}_{O(\alpha^2\epsilon)} + O(\alpha^2\epsilon^3), \tag{6.74}$$

$$\underbrace{\left.\frac{\partial \phi_{\mathrm{B}}^{(2)}}{\partial z}\right|_{z'=0}}_{O(\alpha^2\epsilon)} - \underbrace{\frac{\partial \eta_{\mathrm{B}}^{(2)}}{\partial t}}_{O(\alpha^2\epsilon^2)} = \underbrace{\frac{\omega_0}{2} e^{-2k_0 H_{\mathrm{T}}} \frac{\partial |A(X)|^2}{\partial x}}_{O(\alpha^2\epsilon)} + O(\alpha^2\epsilon^3), \tag{6.75}$$

$$g(\rho_{\mathrm{B}} - \rho_{\mathrm{T}}) \underbrace{\eta_{\mathrm{B}}^{(2)}}_{O(\alpha^2\epsilon)} + \rho_{\mathrm{B}} \underbrace{\left.\frac{\partial \phi_{\mathrm{B}}^{(2)}}{\partial t}\right|_{z'=0}}_{O(\alpha^2\epsilon)} - \rho_{\mathrm{T}} \underbrace{\left.\frac{\partial \phi_{\mathrm{T}}^{(2)}}{\partial t}\right|_{z'=0}}_{O(\alpha^2\epsilon)} = \underbrace{0}_{O(\alpha^2\epsilon^0)}, \tag{6.76}$$

where the right hand side scales as $O(\alpha^2\epsilon^0)$, but is identical to zero here. Summing up, we can ignore the slow modulation of the interface $\eta_{\mathrm{B}}^{(2)}$ and calculate the return flow at leading order according to:

$$\left.\frac{\partial \phi_{\mathrm{T}}^{(2)}}{\partial z}\right|_{z'=0} = \frac{1}{2}\omega_0 e^{-2k_0 H_{\mathrm{T}}} \frac{\partial |A_{\mathrm{T}}|^2}{\partial x}, \quad \left.\frac{\partial \phi_{\mathrm{B}}^{(2)}}{\partial z}\right|_{z'=0} = \frac{1}{2}\omega_0 e^{-2k_0 H_{\mathrm{T}}} \frac{\partial |A_{\mathrm{T}}|^2}{\partial x}. \tag{6.77a,b}$$

It is evident that all we have done is to compartmentalize the Stokes transport and the return flow forced by the divergence of the Stokes transport at the two boundaries: the solutions are entirely equivalent to the deep-water gravity wave case in chapter 2.

6.3.4 Second-order solutions: mean flow for the baroclinic mode

It is evident from the linear solutions for the baroclinic mode in the Boussinesq limit (6.68-6.69) that we return to the analogous closed-lid problem already examined in §6.2.4. Here we investigate how this is modified by non-Boussinesq effects.

6.3.4.1 Stokes transport

Writing the Stokes transport explicitly for each layer, we have to leading-order for the baroclinic mode:

$$
\begin{aligned}
Q_{\mathrm{ST,T}} = \overline{\int_{-H_{\mathrm{B}}+\eta_{\mathrm{B}}(x,t)}^{\eta_{\mathrm{T}}(x,t)} u_{\mathrm{T}}^{(1)} dz} &= \overline{u_{\mathrm{T}}^{(1)}|_{z=0}\eta_{\mathrm{T}}^{(1)}} - \overline{u_{\mathrm{T}}^{(1)}|_{z'=0}\eta_{\mathrm{B}}^{(1)}} \\
&= \frac{1}{2}\omega_0\Big(\delta_{\mathrm{ST,T,F}}(k_0H_{\mathrm{T}},\rho_{\mathrm{B}},\rho_{\mathrm{T}}) + \delta_{\mathrm{ST,T,I}}(k_0H_{\mathrm{T}},\rho_{\mathrm{B}},\rho_{\mathrm{T}})\Big)|A_{\mathrm{B}}|^2, \\
&= \frac{1}{2}\omega_0\delta_{\mathrm{ST,T}}(k_0H_{\mathrm{T}},\rho_{\mathrm{B}},\rho_{\mathrm{T}})|A_{\mathrm{B}}|^2,
\end{aligned} \tag{6.78}
$$

$$
Q_{\mathrm{ST,B}} = \overline{\int_{-\infty}^{\eta_{\mathrm{B}}(x,t)} u_{\mathrm{B}}^{(1)} dz'} = \frac{1}{2}\omega_0|A_{\mathrm{B}}|^2, \tag{6.79}
$$

where the over-lines denote averaging over the fast time scales and we express the Stokes transport in terms of the (square) of the internal wave amplitude A_{B}. The non-dimensional terms $\delta_{\mathrm{ST,T,F}}(k_0H_{\mathrm{T}},\rho_{\mathrm{B}},\rho_{\mathrm{T}})$ and $\delta_{\mathrm{ST,T,I}}(k_0H_{\mathrm{T}},\rho_{\mathrm{B}},\rho_{\mathrm{T}})$ reflect the contributions from the free surface (F) and the interface (I) to the Stokes transport in the top layer, respectively. For the bottom layer, we only have one contribution (cf. $\delta_{\mathrm{ST,B}} = \delta_{\mathrm{ST,B,I}} = 1$). Explicitly, we have:

$$
\delta_{\mathrm{ST,T,F}}(k_0H_{\mathrm{T}},\rho_{\mathrm{B}},\rho_{\mathrm{T}}) = \frac{\Delta\rho}{\rho_{\mathrm{T}}}\frac{\rho_{\mathrm{T}}\sinh(k_0H_{\mathrm{T}}) + \rho_{\mathrm{B}}\cosh(k_0H_{\mathrm{T}})}{\rho_{\mathrm{T}}\sinh(k_0H_{\mathrm{T}})}e^{-2k_0H_{\mathrm{T}}}, \tag{6.80}
$$

$$
\delta_{\mathrm{ST,T,I}}(k_0H_{\mathrm{T}},\rho_{\mathrm{B}},\rho_{\mathrm{T}}) = \frac{\Delta\rho}{\rho_{\mathrm{T}}}\Big(D^{-1}\cosh(k_0H_{\mathrm{T}}) - \sinh(k_0H_{\mathrm{T}})\Big)e^{-k_0H_{\mathrm{T}}}, \tag{6.81}
$$

where $\Delta\rho = \rho_{\mathrm{B}} - \rho_{\mathrm{T}}$ and $D^{-1} = (\rho_{\mathrm{T}}\sinh(k_0H_{\mathrm{T}}) + \rho_{\mathrm{B}}\cosh(k_0H_{\mathrm{T}}))/((\rho_{\mathrm{B}} - \rho_{\mathrm{T}})\sinh(k_0H_{\mathrm{T}}))$. In the Boussinesq limit $\Delta\rho/\rho_0 \to 0$ with $\rho_0 = (\rho_{\mathrm{B}} + \rho_{\mathrm{T}})/2$, equations (6.80-6.81) simplify considerably:

$$
\delta_{\mathrm{ST,T,F}}(k_0H_{\mathrm{T}},\Delta\rho/\rho_0) = 2\frac{\Delta\rho}{\rho_0}\frac{\cosh(k_0H_{\mathrm{T}}) - \sinh(k_0H_{\mathrm{T}})}{\sinh(k_0H_{\mathrm{T}})}, \tag{6.82}
$$

$$
\delta_{\mathrm{ST,T,I}}(k_0H_{\mathrm{T}}) = \frac{1}{\tanh(k_0H_{\mathrm{T}})}, \tag{6.83}
$$

and it is clear that the effect of the internal wave (6.83) is dominant for small density ratios $\Delta\rho/\rho_0$. Finally, $\delta_{\mathrm{ST,T}}$ is defined as the sum of both terms: $\delta_{\mathrm{ST,T}} = \delta_{\mathrm{ST,T,F}} + \delta_{\mathrm{ST,T,I}}$. Figure 6.3 compares the relative magnitude of the two contributions for different values of $\Delta\rho/\rho_{\mathrm{T}}$, with the sum of both terms illustrated in figure 6.4. We note from (6.79) that the Stokes drift coefficient in the bottom layer is not a function of k_0H_{T} and small relative to

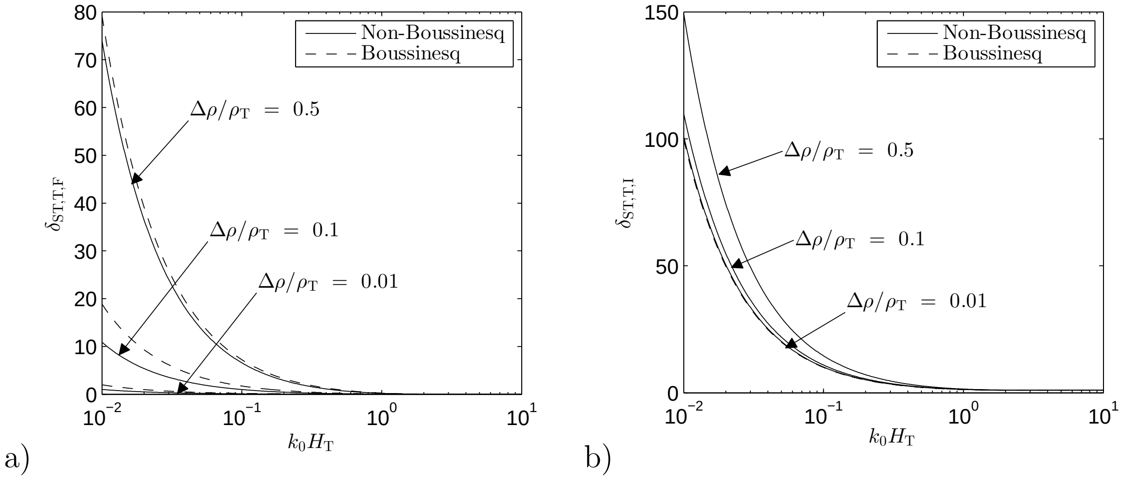

Figure 6.3: Stokes transport coefficients for the top layer with a free surface for different densities comparing the non-Boussinesq coefficients (6.80-6.81) and the Boussinesq coefficients (6.82-6.83). Panel (a) shows the contribution from the free surface wave group ($\delta_{\mathrm{ST,T,F}}$) and panel (b) from the interfacial wave group ($\delta_{\mathrm{ST,T,I}}$). Note that the dashed line for the Boussinesq case in panel b closely overlaps with the non-Boussinesq line for $\Delta\rho/\rho_{\mathrm{T}} = 0.01$.

the Stokes drift coefficient in the top layer except for large $k_0 H_{\mathrm{T}}$ (cf. $\delta_{\mathrm{ST,B}} = \delta_{\mathrm{ST,B,I}} = 1$).

6.3.4.2 Return flow

From the free surface boundary conditions (6.51) at second-order (in α), we obtain the familiar return flow forcing equation (cf. chapter 3):

$$\Big(\underbrace{\frac{\partial}{\partial z}}_{O(\epsilon)} + \underbrace{\frac{1}{g}\frac{\partial^2}{\partial t^2}}_{O(\epsilon^2)}\Big)\underbrace{\phi_{\mathrm{T}}^{(2)}}_{O(\alpha^2)} = \overline{\underbrace{\frac{\partial}{\partial x}\big(u_{\mathrm{T}}^{(1)}\eta_{\mathrm{T}}^{(1)}\big)}_{O(\alpha^2\epsilon^1)} \underbrace{-\frac{1}{g}\frac{\partial}{\partial t}\Big(\frac{\partial^2\phi_{\mathrm{T}}^{(1)}}{\partial t\partial z}\eta_{\mathrm{T}}^{(1)} + \frac{1}{2}(\nabla\phi_{\mathrm{T}}^{(1)})^2\Big)}_{O(\alpha^2\epsilon^1)}} \text{ at } z = 0, \tag{6.84}$$

where we have two contributions on the right hand side: one from the divergence of a Stokes transport term and one from the mean set-down of the surface wave group. To leading-order we have for the free surface set-down:

$$\underbrace{\eta_{\mathrm{T}}^{(2)}}_{O(\alpha^2\epsilon^0)} = \underbrace{-\frac{1}{g}\Big(\frac{\partial^2\phi_{\mathrm{T}}^{(1)}}{\partial t\partial z}\eta_{\mathrm{T}}^{(1)} + \frac{1}{2}\big(\nabla\phi_{\mathrm{T}}^{(1)}\big|_{z=0}\big)^2\Big)}_{O(\alpha^2\epsilon^0)}. \tag{6.85}$$

From table 6.2, we can express the set-down of the free surface as:

$$\eta_{\mathrm{T}}^{(2)} = \delta_{\mathrm{F}}(k_0 H_{\mathrm{T}}, \rho_{\mathrm{B}}, \rho_{\mathrm{T}}) k_0 |A_{\mathrm{B}}|^2, \tag{6.86}$$

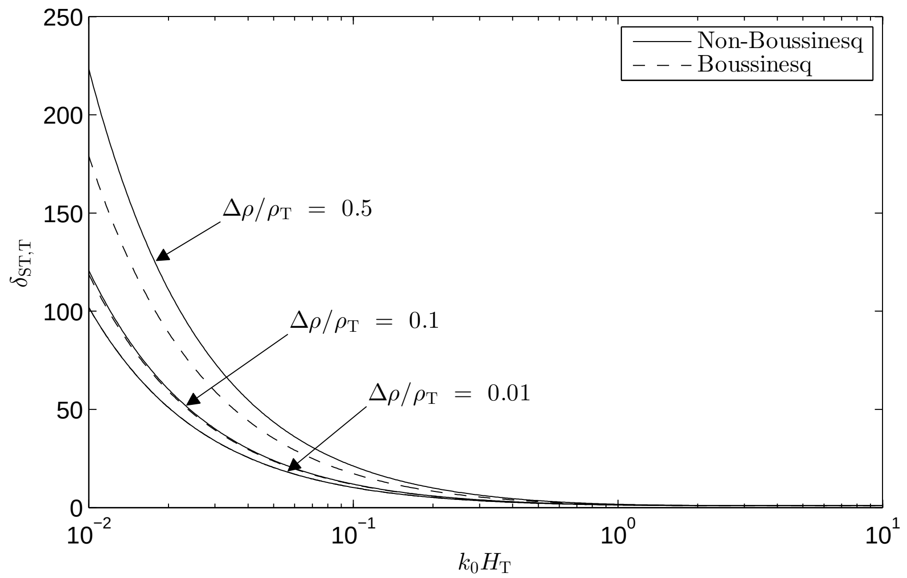

Figure 6.4: Total Stokes transport coefficients ($\delta_{\mathrm{ST,T}}$) for the top layer with a free surface for different densities comparing the sum of the non-Boussinesq coefficients (6.80-6.81) and the sum of the Boussinesq coefficients (6.82-6.83). Note that the difference between the Boussinesq and non-Boussinesq solutions is only visible for the largest value of $\Delta\rho/\rho_{\mathrm{T}}$.

where $\delta_{\mathrm{F}} = (D - D^{-1})(\Delta\rho/\rho_{\mathrm{T}})^2 \exp(-2k_0H_{\mathrm{T}})/4$, which in the Boussinesq limit reduces to:

$$\delta_{\mathrm{F}}(\Delta\rho/\rho_0, k_0H_{\mathrm{T}}) = -\frac{1}{4}\frac{\Delta\rho}{\rho_0}\frac{\cosh(k_0H_{\mathrm{T}}) - \sinh(k_0H_{\mathrm{T}})}{\sinh(k_0H_{\mathrm{T}})}. \tag{6.87}$$

Figure 6.5a then shows the variation of this generally small set-down with k_0H_{T} for different relative densities. We now consider the two terms on the right hand side of (6.84) in turn:

$$\overline{\frac{\partial}{\partial x}\big(u_{\mathrm{T}}^{(1)}\big|_{z=0}\eta_{\mathrm{T}}^{(1)}\big)} = \frac{1}{2}\omega_0\delta_{\mathrm{ST,T,F}}(k_0H_{\mathrm{T}}, \rho_{\mathrm{B}}, \rho_{\mathrm{T}})\frac{\partial|A_{\mathrm{B}}|^2}{\partial x}, \tag{6.88}$$

$$\overline{-\frac{1}{g}\frac{\partial}{\partial t}\Big(\frac{\partial^2\phi_{\mathrm{T}}^{(1)}}{\partial t\partial z}\Big|_{z=0}\eta_{\mathrm{T}}^{(1)} + \frac{1}{2}\big(\nabla\phi_{\mathrm{T}}^{(1)}\big|_{z=0}\big)^2\Big)} = \frac{1}{2}\omega_0\delta_{\mathrm{RF,F}}(k_0H_{\mathrm{T}}, \rho_{\mathrm{B}}, \rho_{\mathrm{T}})\frac{\partial|A_{\mathrm{B}}|^2}{\partial x}, \tag{6.89}$$

where $\delta_{\mathrm{ST,T,F}}(k_0H_{\mathrm{T}}, \rho_{\mathrm{B}}, \rho_{\mathrm{T}})$ is defined in (6.80) and $\delta_{\mathrm{RF,F}}(k_0H_{\mathrm{T}}, \rho_{\mathrm{B}}, \rho_{\mathrm{T}}) = -2k_0c_{g,0}\delta_{\mathrm{F}}/\omega_0$, which, in the Boussinesq limit, simplifies to:

$$\delta_{\mathrm{RF,F}}(\Delta\rho/\rho_0, k_0H_{\mathrm{T}}) = \frac{1}{2}\frac{\Delta\rho}{\rho_0}\frac{-1 + 2k_0H_{\mathrm{T}} + \exp(2k_0H_{\mathrm{T}})}{\big(\exp(2k_0H_{\mathrm{T}}) - 1\big)^2}. \tag{6.90}$$

We define $\delta_{\mathrm{RF,T,F}} = \delta_{\mathrm{ST,T,F}} + \delta_{\mathrm{RF,F}}$, so that to leading order:

$$\frac{\partial\phi_{\mathrm{T}}^{(2)}}{\partial z}\Big|_{z=0} = \frac{1}{2}\omega_0\delta_{\mathrm{RF,T,F}}(k_0H_{\mathrm{T}}, \rho_{\mathrm{B}}, \rho_{\mathrm{T}})\frac{\partial|A_{\mathrm{B}}|^2}{\partial x}. \tag{6.91}$$

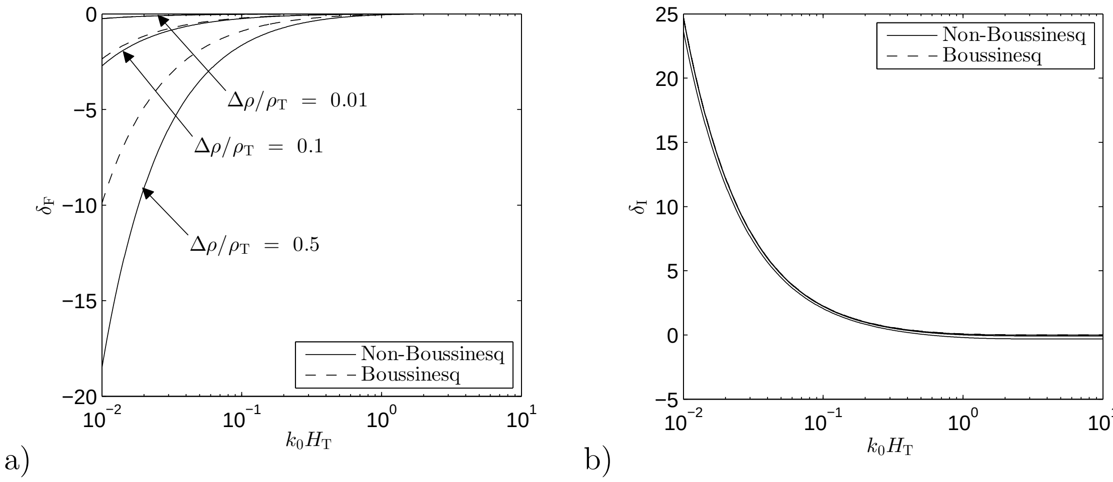

Figure 6.5: Mean surface (a) set-down and interfacial set-up (b) coefficients δ_F and δ_I for different densities comparing the non-Boussinesq coefficients and the Boussinesq coefficients (6.87). Note that the difference between the Boussinesq case and the non-Boussinesq cases in panel b is very small and not clear from visual inspection.

Figure 6.6a shows the contribution to the return flow forcing in the top layer at the mean surface level due to the free surface set-down $\delta_{RF,F}(k_0H_T, \rho_B, \rho_T)$ (6.90). Comparison with the total return flow forcing at the mean surface level $\delta_{RF,T,F}(k_0H_T, \rho_B, \rho_T)$ shown in figure 6.6b, the contribution from the set-down is marginal except for shallow depths, as in the surface gravity wave case in chapter 3. For shallow water depths, both contributions to the return flow, namely the divergence of the Stokes transport and the free surface set-down, are of equal order of magnitude.

We have from the interfacial boundary conditions (6.52-6.53) and the polarization relationships in table 6.2:

$$\underbrace{\left.\frac{\partial \phi_T^{(2)}}{\partial z}\right|_{z'=0}}_{O(\alpha^2\epsilon)} - \underbrace{\frac{\partial \eta_B^{(2)}}{\partial t}}_{O(\alpha^2\epsilon)} = \underbrace{-\frac{1}{2}\omega_0\delta_{ST,T,I}(k_0H_T, \rho_B, \rho_T)\frac{\partial |A_B|^2}{\partial x}}_{O(\alpha^2\epsilon)} + O(\alpha^2\epsilon^3), \tag{6.92}$$

$$\underbrace{\left.\frac{\partial \phi_B^{(2)}}{\partial z}\right|_{z'=0}}_{O(\alpha^2\epsilon)} - \underbrace{\frac{\partial \eta_B^{(2)}}{\partial t}}_{O(\alpha^2\epsilon)} = \underbrace{\frac{1}{2}\omega_0\frac{\partial |A_B|^2}{\partial x}}_{O(\alpha^2\epsilon)} + O(\alpha^2\epsilon^3), \tag{6.93}$$

$$g(\rho_B - \rho_T)\underbrace{\eta_B^{(2)}}_{O(\alpha^2\epsilon^0)} + \rho_B\underbrace{\left.\frac{\partial \phi_B^{(2)}}{\partial t}\right|_{z'=0}}_{O(\alpha^2\epsilon)} - \rho_T\underbrace{\left.\frac{\partial \phi_T^{(2)}}{\partial t}\right|_{z'=0}}_{O(\alpha^2\epsilon)} = \underbrace{g(\rho_B - \rho_T)\delta_I k_0|A_B|^2}_{O(\alpha^2\epsilon^0)}. \tag{6.94}$$

where $\delta_{ST,T,I}(k_0H_T, \rho_B, \rho_T)$ is given by (6.81) and $\delta_I(k_0H_T, \rho_B, \rho_T)$ is, after considerable

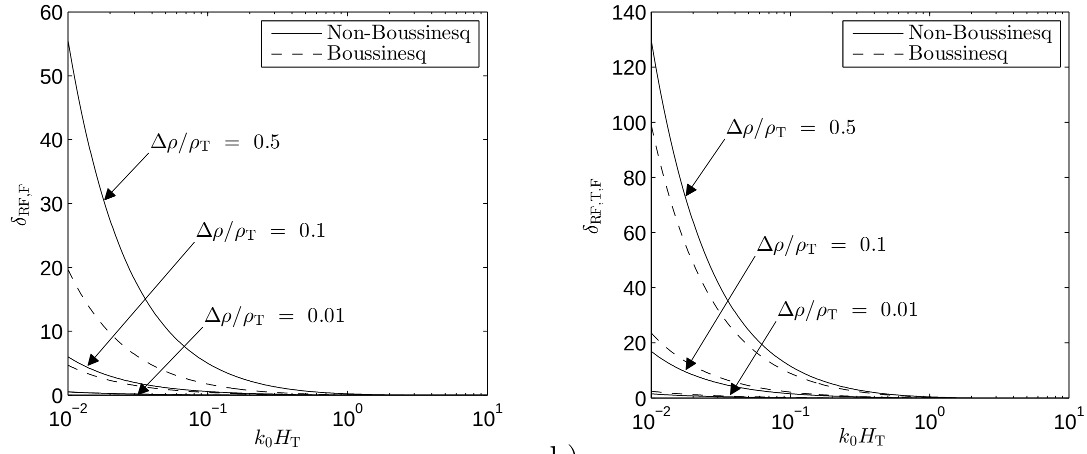

a) b)

Figure 6.6: Return flow forcing coefficients for the free surface boundary condition for different densities comparing the non-Boussinesq coefficients and the Boussinesq coefficients. Panel a shows the contribution from the free surface wave set-down ($\delta_{\mathrm{RF,F}}$) and panel b shows the coefficient for the total return flow forcing at the free surface, namely the sum of the set-down and the Stokes drift coefficients: $\delta_{\mathrm{RF,T,F}} = \delta_{\mathrm{ST,T,F}} + \delta_{\mathrm{RF,F}}$ (cf. (6.91)).

manipulation, given by (from table 6.2):

$$\delta_{\mathrm{I}} = -\frac{-\rho_{\mathrm{B}}^3 - 2\rho_{\mathrm{B}}^2\rho_{\mathrm{T}} - 2\rho_{\mathrm{B}}\rho_{\mathrm{T}}^2 + 3\rho_{\mathrm{T}}^3 + \left(\rho_{\mathrm{B}}^3 + 2\rho_{\mathrm{B}}\rho_{\mathrm{T}}^2 - 3\rho_{\mathrm{T}}^3\right)\cosh(k_0 H_{\mathrm{T}}) + 2\rho_{\mathrm{B}}(\rho_{\mathrm{B}} - \rho_{\mathrm{T}})\rho_{\mathrm{T}}\sinh(2k_0 H_{\mathrm{T}})}{2\left(\rho_{\mathrm{B}} + \rho_{\mathrm{T}}\right)^2\left(\rho_{\mathrm{T}} + \rho_{\mathrm{B}}\coth(k_0 H_{\mathrm{T}})\right)\sinh^2(k_0 H_{\mathrm{T}})}, \tag{6.95}$$

which reduces to $\delta_{\mathrm{I}} = (\exp(2k_0 H_{\mathrm{T}}) - 1)^{-1}/2$ in the Boussinesq limit, a value equivalent to the set-up of the analogous closed-lid case (cf. (6.45)). Summing up, we have for the leading-order interfacial set-up:

$$\eta_{\mathrm{B}}^{(2)} = \delta_I(k_0 H_{\mathrm{T}}, \rho_{\mathrm{B}}, \rho_{\mathrm{T}}) k_0 |A_{\mathrm{B}}|^2. \tag{6.96}$$

Figure 6.5 compares the set-down at the free surface (panel a) and the set-up at the interface (panel b), the latter being much larger in magnitude for small density differences and in fact not a function of $\Delta\rho/\rho_0$ in the Boussinesq limit.

Finally, we have for the return flow forcing at the interface to leading order:

$$\left.\frac{\partial \phi_{\mathrm{T}}^{(2)}}{\partial z}\right|_{z'=0} = -\frac{\omega_0}{2}\Big(\underbrace{\delta_{\mathrm{ST,T,I}}(k_0 H, \rho_{\mathrm{B}}, \rho_{\mathrm{T}}) + \delta_{\mathrm{RF,I}}(k_0 H, \rho_{\mathrm{B}}, \rho_{\mathrm{T}})}_{\delta_{\mathrm{RF,T,I}}(k_0 H, \rho_{\mathrm{B}}, \rho_{\mathrm{T}})}\Big)\frac{\partial |A_{\mathrm{B}}|^2}{\partial x}, \tag{6.97}$$

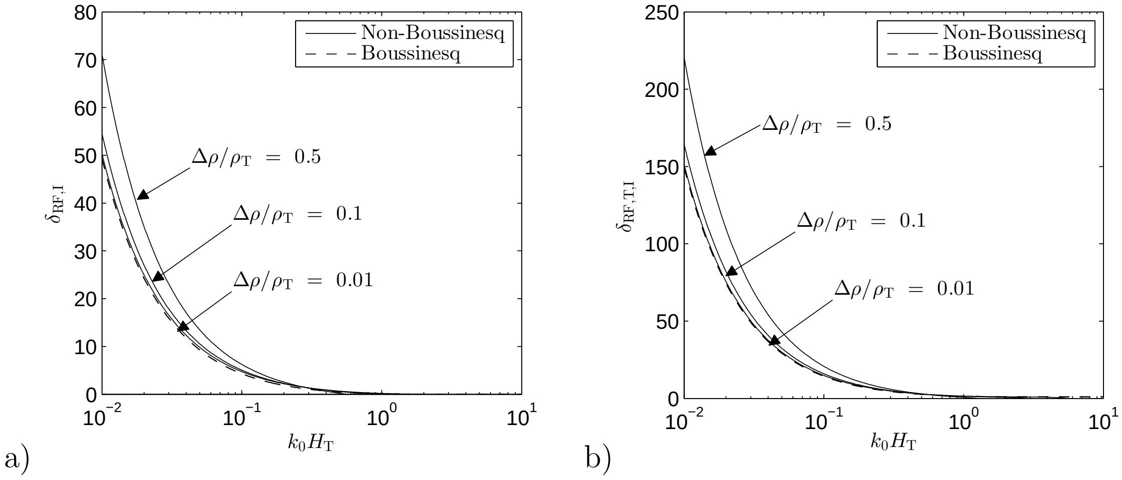

Figure 6.7: Return flow forcing coefficients for top layer at the interfacial boundary condition for different densities comparing the non-Boussinesq coefficients and the Boussinesq coefficients. Panel a shows the contribution from the interfacial wave set-down ($\delta_{\mathrm{RF,I}}$) and panel b shows the coefficient for the total return flow forcing to the top layer at the interface, namely the sum of the set-down and the Stokes drift coefficients: $\delta_{\mathrm{RF,T,I}} = \delta_{\mathrm{ST,T,I}} + \delta_{\mathrm{RF,I}}$. Note that the dashed line for the Boussinesq case in panel b closely overlaps with the non-Boussinesq line for $\Delta\rho/\rho_{\mathrm{T}} = 0.01$.

$$\left.\frac{\partial \phi_{\mathrm{B}}^{(2)}}{\partial z}\right|_{z'=0} = \frac{\omega_0}{2}\Big(1 - \delta_{\mathrm{RF,I}}(k_0 H, \rho_{\mathrm{B}}, \rho_{\mathrm{T}})\Big)\frac{\partial |A_{\mathrm{B}}|^2}{\partial x}. \tag{6.98}$$

where $\delta_{\mathrm{RF,I}} = 2c_{g,0}\delta_{\eta\mathrm{B}}/\omega_0$. In the Boussinesq limit, $\delta_{\mathrm{RF,I}}$ converges to the analogous quantity for the closed-lid case δ^*_{FD} defined in (6.48). Figure 6.7 shows the magnitude of the coefficients $\delta_{\mathrm{RF,I}}$ and $\delta_{\mathrm{RF,T,I}}$. For the non-Boussinesq case, the top layer now experiences forcing from both interfaces and we can solve for the return flow to give explicitly using superposition:

$$\phi_{\mathrm{RF,T}} = -\tfrac{|a_0|^2\omega_0\sigma}{2\pi}\int_0^\infty \frac{f(k\sigma)\sin(k(x - c_{g,0}t)}{\sinh(kH)}\Big(\delta_{\mathrm{RF,T,F}}\cosh\big(k(z + H_{\mathrm{T}})\big) + \delta_{\mathrm{RF,T,I}}\cosh(kz)+)\Big)dk. \tag{6.99}$$

where the return flow field is dominated by the interfacial forcing in the Boussinesq limit and contributions from the free surface do not play a role unless the density difference is large. The relative magnitude of the forcing coefficients is evident from figure 6.8.

6.4 Conclusions

This chapter has examined the induced mean flow of two-dimensional interfacial gravity groups in a two-layer fluid through a separation of scales expansion for quasi-monochromatic

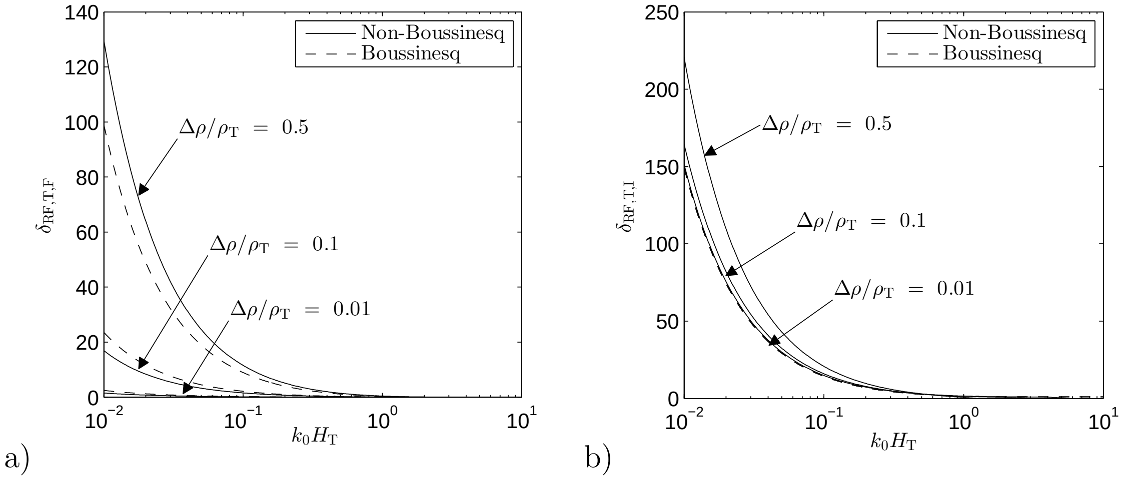

Figure 6.8: Total return flow forcing coefficients for the top layer showing (a) forcing from the mean free surface level ($z = 0$) and (b) forcing from the mean interface level ($z' = 0$). Note that the dashed line for the Boussinesq case in panel b closely overlaps with the non-Boussinesq line for $\Delta\rho/\rho_{\mathrm{T}} = 0.01$.

wave groups, considering both the case of a closed lid and the case of a free surface on top. In the Boussinesq limit, the effect of the free surface on the linear dynamics can be ignored, a not surprising and well-known result that is also confirmed to apply to the mean flow herein. As for surface gravity wave groups, the induced mean flow consist of two components: the Stokes drift and transport on the one hand and the return flow on the other.

For a two-layer fluid with a closed lid, three cases are considered in turn. For two infinitely deep layers, the leading-order solutions for the return flow field on both sides are equivalent to the deep-water surface gravity wave solutions in chapter 2. As a result of symmetry of the return flows on both sides of the interface, there is no mean set-down of the interface, as for deep-water surface wave groups. For two layers of finite and equal depth, we obtain a set-down of the interface analogous to the finite depth surface gravity wave problem in chapter 3. The magnitude of the set-down is now proportional to the density difference between the layers. Both the divergence of the Stokes transport and the set-down of the interface contribute to the magnitude of the return flow, reducing the magnitude of the return flow in the top layer and increasing the return flow in the bottom layer by, at most, 50% relative to the case without a set-down, as for the surface gravity wave case. The third case of a finite depth fluid overlying an infinitely deep fluid is markedly different. The asymmetry now leads to a mean set-up of the interface instead of a set-down. As a result, the return flow is enhanced in the top layer and reduced in the bottom layer. If the top layer is sufficiently shallow, the set-up becomes sufficiently large to eliminate the return flow in the bottom layer. For even shallower depths, the "return flow" in the bottom layer becomes positive.

Evidently, the limits of validity of a Stokes expansion are reached for sufficiently small depth, when the ratio of the layer depth and interfacial wave amplitude H/a_0 is no longer large, as discussed for surface gravity waves in chapter 3. Based on analogous work for surface waves, Yuan et al. (2007) provide validity regimes for different interfacial wave theories.

Chapter 7

Conclusions

This thesis has examined the structure and magnitude of the induced mean flow by surface, internal and interfacial wave groups. In all three cases, the advective terms in the momentum equation, sometimes referred to as Reynolds stresses, calculated based on linear theory gave rise to one component of the mean flow, termed the 'divergent-flux induced flow' herein. The divergent-flux induced flow is also known as the pseudo-momentum (per unit mass). In the simplest possible framework, a mass balance argument can be used to show that a second component of the mean flow is required, as the divergent-flux induced flow is itself divergent.

Surface gravity waves - part I

For surface gravity waves the divergent-flux induced flow is known as the Stokes transport and, for deep water, it is concentrated near the surface. As has been shown in chapter 2, the return flow in infinitely deep water can be understood as the balancing flow that is required by the divergence of the Stokes transport to ensure mass conservation is satisfied. From a practical perspective, its magnitude can be found by placing a series of potential-flow sources and sinks at the undisturbed water level with their strength corresponding to the local divergence of the Stokes transport. The effects of frequency dispersion, causing the group to change shape as it travels, can be ignored for realistic sea states, as has been shown by considering subsequent order in a separation of scales expansion and by comparing to the Fourier-space solutions of Longuet-Higgins and Stewart (1962). In loose terms, the Stokes drift transports fluid from the trailing edge of the group to its leading edge and the return flow transports this fluid back. A transition depth can then be defined above which net horizontal Lagrangian transport is positive and dominated by the Stokes drift and below which net horizontal Lagrangian transport is negative and dominated by the return flow. Chapters 2 and 3 show how this depth scale depends on the peak wave number and bandwidth of the spectrum.

For the return flow of surface gravity waves to be unaffected by the presence of the bottom boundary condition requires the depth to be really rather large. Whereas the variation of the linear wave dynamics with depth scales on the inverse of the wave number k_0, the variation of the return flow with depth scales on the half-width of the group σ. The non-dimensional parameter $\epsilon = 1/(k_0\sigma)$ that compares their relative magnitudes is typically small. Moreover, the functional dependence of the return flow on the non-dimensional depth z/σ is much slower than the exponential decay of the linear wave dynamics with $k_0 z$, as explored in chapter 2. Taking into account finite depth, calculations in chapter 3 show that for a typical peak wave period of $T_0 = 10$ s, the bottom boundary has a significant effect of the magnitude of return flow up to depths of approximately 1.0 km. For smaller depths, the two-dimensional return flow can in fact be modelled as a block flow that is uniform with depth, a "shallow" water approximation with respect to the return flow. Relative to the Stokes drift, which is truly concentrated near the surface, the magnitude of the horizontal transport by the return current always remains small, except for water depths of less than 100 m for a typical peak wave period of $T_0 = 10$ s (and $\epsilon = 0.16$). For small water depths, not only the divergence of the Stokes transport, but also the set-down of the free surface provides "forcing" for the return flow with a maximum enhancement of 50% for the shallowest of water depths.

Chapter 3 also explores the effect of directional spreading on the magnitude of the return flow and associated particle transport. It is physically intuitive that, as soon the return flow can flow around as well as underneath the group itself, the magnitude of the velocities at any point reduces significantly. For sufficiently shallow water depth, the two-dimensional picture in chapter 2, in which the Stokes transport and the return flow form an irrotational balance in the vertical plane, is rotated by 90 degrees. The return flow becomes uniform with depth, but can be modelled by a distribution of potential-flow sources and sinks in the horizontal plane. The local Stokes drift through the centre of the group is complemented by a non-local return flow distributed over a large area.

Internal gravity waves - part II

Although the non-linearity of internal gravity waves in a continuously stratified medium arises from the non-linear governing equations and not from the non-linear boundary conditions, as for the surface gravity wave case, and internal waves do not display Stokes drift, the structure of its induced mean flow is remarkably similar. This especially applies to the case of three-dimensional internal gravity waves (chapter 4). At leading order in a separation of scales expansion for a quasi-monochromatic wave group, stratification acts to restrict the induced mean flow entirely to the horizontal plane. The return flow can then be found by solving for a two-dimensional potential flow field, subject to a distribution of sources and sinks of fluid provided by the divergence of the divergent-flux induced flow, thereby providing explicit descriptions for the return flow field predicted by Bretherton (1969b). The analogies with the two-dimensional surface gravity case in deep-water in chapter 2 are evident, and the solutions are in fact entirely equivalent to the return flow for shallow-depth three-dimensional surface gravity wave groups. Provided the depth is sufficiently shallow relative to the scale of the group, variation of the return flow is then also confined to the horizontal plane.

Unlike the case of surface gravity waves and three-dimensional internal gravity waves, a balanced circulation consisting of the divergent-flux induced flow and a return flow cannot exist for two-dimensional internal gravity wave groups. Stratification inhibits mean flows in the vertical direction and there are not enough physical degrees of freedom for a balance to form. Instead, the group generates a second type of waves that are long relative to the size of the group. On the scale of the group these waves thus appear to be a mean flow. In reality they travel out in front and in the lee of the travelling wave group, thereby confirming the results of Bretherton (1969b). The problem can be approximated as steady, as the horizontal velocity of the source of the long waves (the group itself) is much smaller than the speed of the long waves it generates. Although the entire flow field can be predicted by going to higher order in the separation of scales expansion, reproducing the results of Bretherton (1969b) and comparing to the results of fully non-linear numerical simulations, many physical insights can be derived at lower order from the concept of divergent-flux induced flow. For example, the amount of momentum contained in these long waves can be understood by considering the momentum associated with the divergent-flux induced flow.

Interfacial gravity waves - part III

Finally, chapter 6 has examined the induced mean flow of two-dimensional interfacial gravity groups in a two-layer fluid distinguishing the case in which the top fluid is exposed to a free surface and the closed-lid case. In the Boussinesq limit of small density differences between the layers, the effect of the free surface on the linear dynamics can be ignored, a not surprising and well-known result. This also applies to the mean flow. As for surface gravity wave groups, the induced mean flow consist of two components:

the Stokes drift and transport on the one hand and the return flow on the other. In fact, the behaviour of the induced mean flow of interfacial gravity wave groups is analogous to that of surface gravity waves with the exception that Stokes drift and transport and the return flow can now occur on both sides of the interface. As a result, symmetry or the lack thereof has a large role to play.

The symmetric cases of two infinitely deep fluids and two fluids of finite depth overlying each other, not surprisingly, correspond closely to the case of deep-water surface gravity waves of chapter 2 and the case of finite-depth surface gravity waves of chapter 3, respectively. In the last case, the set-down of the interface enhances the return flow in the bottom layer and reduces it in the top layer (by 50% at most, as for surface gravity waves). In the asymmetric case of a finite-depth light fluid overlying an infinite-depth dense fluid, which is perhaps most realistic of real cases in the physical environment (cf. the oceanic thermocline), the response is markedly different. The asymmetry now leads to a mean set-up of the interface instead of a set-down. As a result, the return flow is enhanced in the top layer and reduced in the bottom layer. If the top layer is sufficiently shallow, the set-up becomes sufficiently large to eliminate the return flow in the bottom layer altogether. For even shallower depths, the "return flow" even becomes positive.

Implications and future work

What reunites the three types of gravity waves examined in this thesis is that the behaviour of their induced mean flows is fundamentally altered by the geometry in which they occur. For surface gravity waves groups, the structure of the return flow is altered by the introduction of a third degree of freedom through even very small degrees of directional spreading. Moreover, the degree of directional spreading crucially determines the magnitude of the return flow and the magnitude of the corresponding particle transport of Lagrangian particles. For internal gravity wave groups, the effect of going from three to two dimensions is even more dramatic, preventing a balanced circulation and exciting long waves that travel out in front of the group and in its lee on a much longer spatial scale than the group itself.

Although two-dimensional geometries are relevant for certain physical situations, such as the internal waves generated by a spatially uniform flow over a long mountain range or surface gravity wave groups in uni-directional seas, two-dimensional geometries are too restrictive to understand wave-induced flow in the physical environment. Although the transition between two-dimensional and three-dimensional geometries can be easily understood for surface gravity waves by introducing a small amount of directional spreading (as in chapter 3), the exact nature of this transition is less clear for internal gravity waves. Realistically, one might expect both a long internal wave and a recirculating region to be induced about an internal wave group of sufficiently wide but nonetheless finite span-wise extent. Currently, leading-order separation of scales expansions (chapters 4 and 5) can only predict either behaviour separately, in line with Bretherton (1969b). Examining how this approach can be adapted to model cases in which both types of responses occur provides scope for future work.

For surface gravity waves, the depth is shown to have a very important effect on the size of the mean flow through the centre of the group, with the infinite depth approximation only applicable to extremely deep seas and resulting in a mean flow that is too small for most other depths. Depth is thus also an important factor in determining the non-linear evolution and potential instability of surface wave groups through their interaction with the mean flow. Although instabilities of this kind have received attention for surface gravity waves, relatively little is known about this type of instability for internal and interfacial waves. With simple expressions for wave-induced mean flow in place, these results can be used to develop weakly non-linear equations for the evolution of moderately large amplitude internal wave groups. This methodology has been successfully employed by Sutherland (2006a), Dosser and Sutherland (2011a) and Dosser and Sutherland (2011b), who derived non-linear Schrödinger equations for horizontally periodic, vertically localized two-dimensional internal wave groups, and thus provides scope for further work on the non-linear evolutions of two and three-dimensional internal wave groups and the interaction with their mean flows.

Finally, application of the wave-induced mean flow framework developed in this thesis, in which the mean flow is understood as the inseparable pair of divergent-flux induced flow and its response flow necessary for conservation of mass, to other types of geophysical waves provides scope for future work. For example, the induced mean flows of Kelvin waves (e.g. Weber et al. (2014)) and Rossby waves (e.g. Marshall et al. (2013)) have recently received attention. Crucially, the approach developed herein only lends itself for problems in which a separation exists between the fast scales of the individual waves and slow scales of the envelope that modulates the quasi-monochromatic wave train. It cannot be applied to waves for which such a separation does not exist, such as the shallow-water solitary waves described by a Korteweg-de Vries equation. Ultimately, the product of the physical understanding developed in this thesis may contribute to improved parameterization of Stokes drift and internal gravity wave drag to be used in General Circulation Models of the earth's climate.

Appendix A

Fenton's (1985) 5th order Stokes expansion

For deep water, the Stokes expansion in wave steepness α for the velocity potential and the surface elevation in deep water up to fifth order are respectively given by (Fenton 1985):

$$\phi(x,z,t) = \sqrt{\frac{g}{k^3}}\left[\alpha e^{kz}\sin(\theta) - \tfrac{1}{2}\alpha^3 e^{kz}\sin(\theta) + \tfrac{1}{2}\alpha^4 e^{2kz}\sin(2\theta) + \alpha^5\left(-\tfrac{37}{24}e^{kz}\sin(\theta) + \tfrac{1}{12}e^{3kz}\sin(3\theta)\right)\right], \quad \text{(A.1)}$$

$$\eta(x,t) = \frac{1}{k}\left[\left(\alpha - \tfrac{3}{8}\alpha^3 - \tfrac{211}{192}\alpha^5\right)\cos(\theta) + \left(\tfrac{1}{2}\alpha^2 + \tfrac{1}{3}\alpha^4\right)\cos(2\theta) + \left(\tfrac{3}{8}\alpha^3 + \tfrac{99}{128}\alpha^5\right)\cos(3\theta) + \tfrac{1}{3}\alpha^4\cos(4\theta) + \tfrac{125}{384}\alpha^5\cos(5\theta)\right], \quad \text{(A.2)}$$

where $\theta = kx - \omega t$ and $\alpha = kH/2$. Note that Fenton's (1985) series (A.1) and (A.2) are normalized so that $\max(\eta) - \min(\eta) = H$, where H denotes the full, non-linear wave height and not the (smaller) underlying linear wave height. The non-linear dispersion equation is given by (Fenton 1985):

$$\omega = \sqrt{gk}\Big(1 + \frac{1}{2}\alpha^2 + \frac{1}{8}\alpha^4\Big), \quad \text{(A.3)}$$

so that the errors in the dynamic and kinematic free surface boundary conditions are both $O(\alpha^6)$.

Appendix B

Two-dimensional surface wave return flow far-field asymptotics

B.0.1 Wave number space

B.0.1.1 Without dispersion

The horizontal component of the return flow without dispersion (2.24a) can be expressed in terms of the non-dimensional integral:

$$\frac{u_{\mathrm{RF}}(x,z,t)}{-\frac{1}{2\sqrt{\pi}}\frac{|a_0|^2\omega_0}{\sigma}} = \mathrm{Re}\Big[\int_0^\infty f(\hat{k})e^{\hat{k}(\hat{z}+i(\hat{x}-\hat{t}))}d\hat{k}\Big], \tag{B.1}$$

where $\hat{k} = k\sigma$, $\hat{z} = z/\sigma$, $\hat{x} = x/\sigma$ and $\hat{t} = c_{g,0}t/\sigma$ and $f(\hat{k}) = \hat{k}\exp(-\hat{k}^2/4)$. The asymptotic behaviour of the horizontal component of the return flow without dispersion (B.1) at large distances away from the centre of the group, either $|x-c_{g,0}t| \to \infty$, $z \to -\infty$ or both, can be found by integrating by parts twice:

$$\begin{aligned}
\mathrm{Re}\Big[\int_0^\infty f(\hat{k})e^{\hat{k}(\hat{z}+i(\hat{x}-\hat{t}))}d\hat{k}\Big] &= \mathrm{Re}\left[\left[\tfrac{f(\hat{k})e^{\hat{k}(\hat{z}+i(\hat{x}-\hat{t}))}}{\hat{z}+i(\hat{x}-\hat{t})}\right]_0^\infty - \int_0^\infty \frac{f'(\hat{k})e^{\hat{k}(\hat{z}+i(\hat{x}-\hat{t}))}}{\hat{z}+i(\hat{x}-\hat{t})}d\hat{k}\right], \\
&= \mathrm{Re}\left[-\left[\frac{f'(\hat{k})e^{\hat{k}(\hat{z}+i(\hat{x}-\hat{t}))}}{\big(\hat{z}+i(\hat{x}-\hat{t})\big)^2}\right]_0^\infty + \int_0^\infty \frac{f''(\hat{k})e^{\hat{k}(\hat{z}+i(\hat{x}-\hat{t}))}}{\big(\hat{z}+i(\hat{x}-\hat{t})\big)^2}d\hat{k}\right], \\
&= -\frac{(\hat{x}-\hat{t})^2-\hat{z}^2}{\big((\hat{x}-\hat{t})^2+\hat{z}^2\big)^2} + \mathrm{Re}\left[\int_0^\infty \frac{f''(\hat{k})e^{\hat{k}(\hat{z}+i(\hat{x}-\hat{t}))}}{\big(\hat{z}+i(\hat{x}-\hat{t})\big)^2}d\hat{k}\right],
\end{aligned} \tag{B.2}$$

where we have used $f(\hat{k}) \to 0$ as $\hat{k} \to 0$, $f(\hat{k}) \to 0$ as $\hat{k} \to \infty$, $f'(\hat{k}) \to 1$ as $\hat{k} \to 0$ and $f'(\hat{k}) \to 0$ as $\hat{k} \to \infty$. The Riemann-Lebesque lemma now guarantees that the right-hand integrals in the final equation of (B.2) converges to zero as $|\hat{x}-\hat{t}| \to \infty$. For $\hat{z} \to -\infty$ convergence to zero is guaranteed by the nature of the exponential, so that we have in the far-field ($|\hat{x}-\hat{t}| \to \infty$ or $z \to -\infty$):

$$u_{\mathrm{RF}}(x,z,t) = \frac{1}{2\sqrt{\pi}} \frac{|a_0|^2\omega_0}{\sigma} \frac{(\hat{x}-\hat{t})^2 - \hat{z}^2}{\left((\hat{x}-\hat{t})^2 + \hat{z}^2\right)^2}. \tag{B.3}$$

From (B.3) we can obtain an expression for the horizontal particle displacement by the return flow in the far-field as a function of time and the initial particle position (x_0,z_0):

$$\frac{\int_{-\infty}^{t} u_{\mathrm{RF}}(x_0,z_0,t)dt}{\sigma} = \frac{1}{2\sqrt{\pi}} \frac{|a_0|^2\omega_0}{c_{g,0}\sigma} \frac{\hat{x}_0-\hat{t}}{\left((\hat{x}_0-\hat{t})^2 + \hat{z}_0^2\right)^2}. \tag{B.4}$$

It is also evident from (B.4) that the net particle transport (by taking the limit $\hat{t} \to \infty$) by the far field ($\hat{z}_0 \to -\infty$) of the return flow is zero.

B.0.1.2 With leading-order dispersion

Including the leading-order effect of dispersion, an expression for the corresponding horizontal velocity of the return flow can be found by differentiating the velocity potential (2.33) with respect to x. The expression thus obtained has the same functional form as (B.1) for a group without dispersion, but with a different function f, which is now given by $f(\hat{k}) = \hat{k}\exp(-\hat{k}^2/4)/(1-\hat{k}\epsilon/4)$. It can be shown that the new f has the same properties: $f(\hat{k}) \to 0$ as $\hat{k} \to 0$, $f(\hat{k}) \to 0$ as $\hat{k} \to \infty$, $f'(\hat{k}) \to 1$ as $\hat{k} \to 0$ and $f'(\hat{k}) \to 0$ as $\hat{k} \to \infty$. As a result the asymptotic argument in §B.0.1.1 remains valid and we have for the far-field:

$$u_{\mathrm{RF}}(x,z,t) = \frac{|\tilde{a}_0|^2\tilde{\sigma}\omega_0}{2\sqrt{\pi}} \frac{(x-c_{g,0}t)^2 - z^2}{\left((x-c_{g,0}t)^2 + z^2\right)^2}, \tag{B.5}$$

with $|\tilde{a}_0| = |a_0|(1+\gamma_0^2 t^2/\sigma^4)^{-1/4}$ replacing $|a_0|$ and $\tilde{\sigma} = (1+\gamma_0^2 t^2/\sigma^4)^{1/2}$ replacing σ in B.3. We note that $|\tilde{a}_0|^2\tilde{\sigma} = |a_0|^2\sigma$ and that leading-order dispersion does not affect the far-field solution.

B.0.2 Real space

Although the solution can be shown to be identical, it may be more physically intuitive to consider the flow field of a series of sources and sinks, in which case we can construct an expression in terms of a summation (over the different sources and sinks) in physical and not wave number space. The contribution to the horizontal velocity field at (x,z) of a dipole with its source located at ($l + c_{g,0}t$,0) and its sink at ($-l + c_{g,0}t$,0) and strength M per unit length dl is given by:

$$du_{\text{RF}} = \frac{M}{\pi}\Big[\frac{x - l - c_{g,0}t}{(x - l - c_{g,0}t)^2 + z^2} - \frac{x + l - c_{g,0}t}{(x + l - c_{g,0}t)^2 + z^2}\Big]dl, \tag{B.6}$$

Instead of integrating (B.6), we first assume the source and sink are far away from our point of interest (x, z) relative to the distance between the source and sink pair, namely $|x - c_{g,0}t| \gg 2l$, $z \gg 2l$ or both. In this limit (B.6) becomes:

$$du_{\text{RF}} = \frac{2l}{\pi}\frac{(x - c_{g,0}t)^2 - z^2}{\big((x - c_{g,0}t)^2 + z^2\big)^2}M(l)dl, \tag{B.7}$$

where the strength is given by $M = (\omega_0|a_0|^2/\sigma)(l/\sigma)\exp(-(l/\sigma)^2)$. Normalizing by the group half-width σ so that $\hat{l} = l/\sigma$, $\hat{x} = x/\sigma$, $\hat{t} = c_{g,0}t/\sigma$, we have for the far-field behaviour of a Gaussian group:

$$u_{\text{RF}}(x, z, t) = \frac{2}{\pi}\frac{|a_0|^2\omega_0}{\sigma}\frac{(\hat{x} - \hat{t})^2 - \hat{z}^2}{\big((\hat{x} - \hat{t})^2 + \hat{z}^2\big)^2}\underbrace{\int_0^\infty \hat{l}^2 e^{-\hat{l}^2} d\hat{l}}_{=\sqrt{\pi}/4} = \frac{1}{2\sqrt{\pi}}\frac{|a_0|^2\omega_0}{\sigma}\frac{(\hat{x} - \hat{t})^2 - \hat{z}^2}{\big((\hat{x} - \hat{t})^2 + \hat{z}^2\big)^2}, \tag{B.8}$$

which is equivalent to (B.3).

Appendix C

Mean flow forcing for surface waves of infinite and finite depth

Table C.1 summarizes the lowest-order linear ($O(\alpha^1\epsilon^0)$) solutions for finite and infinite depth that contribute to the forcing of the mean flow (3.20).

	infinite depth ($k_0 d \to \infty$)	finite depth
$\eta^{(1)}$	$Ae^{i(k_0x-\omega_0t)}$	$Ae^{i(k_0x-\omega_0t)}$
$\phi^{(1)}$	$-\frac{\omega_0 A}{k_0}e^{i(k_0x-\omega_0t)}$	$-\frac{\omega_0 A}{k_0\tanh(k_0d)}e^{i(k_0x-\omega_0t)}$
$u^{(1)}$	$\omega_0 Ae^{i(k_0x-\omega_0t)}$	$\frac{\omega_0}{\tanh(k_0d)}Ae^{i(k_0x-\omega_0t)}$
$w^{(1)}$	$-i\omega_0 Ae^{i(k_0x-\omega_0t)}$	$-i\omega_0 Ae^{i(k_0x-\omega_0t)}$
$\frac{\partial^2\phi^{(1)}}{\partial z\partial t}$	$-\omega_0^2 Ae^{i(k_0x-\omega_0t)}$	$-\omega_0^2 Ae^{i(k_0x-\omega_0t)}$
$\frac{\partial Q_{\mathrm{ST}}}{\partial x} = \overline{\frac{\partial}{\partial x}\left(u^{(1)}\eta^{(1)}\right)}$	$\epsilon\frac{\omega_0}{2}\frac{\partial\lvert A\rvert^2}{\partial X}$	$\epsilon\frac{\omega_0}{2\tanh k_0d}\frac{\partial A^2}{\partial X}$
$\frac{\partial\eta^{(2)}}{\partial t} = -\frac{1}{g}\frac{\partial}{\partial t}\overline{\left(\frac{\partial^2\phi^{(1)}}{\partial z\partial z}\eta^{(1)} + \frac{1}{2}\lvert\nabla\phi^{(1)}\rvert^2\right)}$	0	$\epsilon\frac{c_{g,0}\omega_0^2}{4g\sinh^2(k_0d)}\frac{\partial\lvert A\rvert^2}{\partial X}$

Table C.1: Linear polarization relationships ($O(\alpha^1\epsilon^0)$) evaluated at $z=0$ (only real parts understood) and resulting leading-order ($O(\alpha^2\epsilon^1)$) mean flow forcing terms for finite and infinite depth.

Appendix D

The deep-water return flow as a summation of sources and sinks

D.1 Two-dimensional summation of sources and sinks

From the potential of a source with strength M in a two-dimensional infinite half-space located at $x = x^*$ and $z = 0$, $\phi_{\mathrm{RF}} = (M/\pi)\ln(\sqrt{(x-x^*)^2 + z^2})$, we obtain for the horizontal velocity of a dipole with strength m per unit length and its source and sink located at $x = x^*$ and $x = -x^*$, respectively:

$$du_{\mathrm{RF}} = \frac{m}{\pi}\Big[\frac{x-x^*}{(x-x^*)^2+z^2} - \frac{x+x^*}{(x+x^*)^2+z^2}\Big]dx^*, \tag{D.1}$$

from which the return flow field can be found by integrating with respect to x^* from $x^* = 0$ to $x^* \to \infty$. The far-field limit, valid for either $|x| \gg \sigma$, $|z| \gg \sigma$ or both, is:

$$u_{\mathrm{RF}} = \frac{2}{\pi}\frac{x^2-z^2}{(x^2+z^2)^2}\int_0^\infty m(x^*)x^*dx^* = \frac{1}{2\sqrt{\pi}}\frac{\omega_0|a_0|^2}{\sigma}\frac{\hat{x}^2-\hat{z}^2}{(\hat{x}^2+\hat{z}^2)^2}, \tag{D.2}$$

where we have used $\hat{x} = x/\sigma$ and $\hat{z} = z/\sigma$ and the second identity holds for a Gaussian spectrum:

$$m = \frac{\partial Q_{\mathrm{ST}}(x^*)}{\partial x^*} = \frac{\omega_0|a_0|^2}{\sigma}\frac{x^*}{\sigma}\exp(-(x^*/\sigma)^2). \tag{D.3}$$

D.2 Three-dimensional summation of sources and sinks ($\sigma_x = \sigma_y$)

From the potential of source with strength in a three-dimensional infinite half-space located at (x^*,y^*), $\phi_{\mathrm{RF}} = -(M/(2\pi))/\sqrt{(x-x^*)^2+(y-y^*)^2+z^2}$, we obtain for the horizontal velocity of a dipole with its source located at (x^*,y^*) and its sink at ($-x^*$,y^*):

$$du_{\mathrm{RF}} = \frac{m}{2\pi}\Big[\frac{x-x^*}{\big((x-x^*)^2+(y-y^*)^2+z^2\big)^{3/2}} - \frac{x+x^*}{\big((x+x^*)^2+(y-y^*)^2+z^2\big)^{3/2}}\Big]dx^*dy^*, \tag{D.4}$$

from which the return flow field can be found by integrating with respect to x^* from $x^*=0$ to $x^*\to\infty$ and with respect to y^* from $y^*\to-\infty$ to $y^*\to\infty$. The far-field limit valid for $|x|\gg\sigma$, $|y|\gg\sigma$ and $|z|\gg\sigma$ is:

$$u_{\mathrm{RF}} = \frac{2x^2-y^2-z^2}{(x^2+y^2+z^2)^{5/2}}\int_0^\infty\int_0^\infty \frac{2m(x^*,y^*)x^*dx^*dy^*}{\pi} = \frac{\omega_0|a_0|^2}{4\sigma}\frac{2\hat{x}^2-\hat{y}^2-\hat{z}^2}{(\hat{x}^2+\hat{y}^2+\hat{z}^2)^{5/2}}, \tag{D.5}$$

where the second identity holds for a Gaussian spectrum:

$$m(x^*,y^*) = \frac{\partial Q_{\mathrm{ST}}(x^*,y^*)}{\partial x^*}\frac{\omega_0|a_0|^2}{\sigma}\frac{x^*}{\sigma}\exp(-(x^*/\sigma)^2-(y^*/\sigma)^2). \tag{D.6}$$

Appendix E

The shallow-water limit for surface waves

E.1 Two-dimensional shallow-water limit

In the shallow-water limit $k_0 d \to 0$, the linear signal (3.18) becomes:

$$\eta^{(1)} = A(X)e^{i(k_0 x - \omega_0 t)}, \quad u^{(1)} = \frac{gk_0}{\omega_0}A(X)e^{i(k_0 x - \omega_0 t)}, \quad w^{(1)} = -i\frac{gk_0}{\omega_0}k_0(d+z)A(X)e^{i(k_0 x - \omega_0 t)}, \tag{E.1a,b,c}$$

with the linear dispersion equation $\omega_0 = \sqrt{gd}k_0$. The velocity field in (E.1) still satisfies conservation of volume. The Stokes drift and transport are given by:

$$u_{\text{SD}} = \frac{|A(X)|^2}{2}\sqrt{\frac{g}{d^3}}, \quad Q_{\text{ST}} = \frac{|A(X)|^2}{2}\sqrt{\frac{g}{d}}. \tag{E.2a,b}$$

It is evident that the limit $k_0 d \to 0$ must be taken with great care and that, in such a limit, we must also have $\alpha \to 0$. In physical terms, finite amplitude waves cannot exist on a infinitely thin fluid. From (3.25), we have:

$$u_{\text{RF}} = -\frac{3}{2}\frac{|A(X)|^2}{2}\sqrt{\frac{g}{d^3}}. \tag{E.3}$$

The only net contribution to Lagrangian transport then results from the mean set-down $(\partial\eta^{(2)}/\partial t)$ and we have $u_{\text{L}} = u_{\text{SD}} + u_{\text{RF}} = -(|A(X)|^2/4)\sqrt{g/d^3}$, a negative uniform flow. This result is perhaps intuitive, as in the limit of shallow depth the group and phase velocities become equal. In physical terms, individual waves then no longer move through the group taking particles with them and hence cannot drive the irrotational circulation of Stokes drift and return flow associated with deep-water wave groups.

E.2 Three-dimensional shallow-water limit

As before, the leading-order Stokes drift and transport are readily extended to three dimensions:

$$u_{\mathrm{SD}} = \frac{|A(X,Y)|^2}{2}\sqrt{\frac{g}{d^3}}, \quad Q_{\mathrm{ST}} = \frac{|A(X,Y)|^2}{2}\sqrt{\frac{g}{d}}. \tag{E.4a,b}$$

Taking note of the return flow "forcing equation" (3.20), conservation of volume can be satisfied in a two-dimensional (x, y) domain to give:

$$u_{\mathrm{RF}} = -\frac{1}{2\pi d}\int_{-\infty}^{\infty}\int_{-\infty}^{\infty}\frac{m(x^*,y^*)(x+x^*)}{(x+x^*)^2+(y+y^*)^2}dx^*dy^*, \tag{E.5}$$

where $m(x^*, y^*)$ is the source strength of a distribution of sources (ans sinks) located at $z = 0$. We have used $\delta_{\mathrm{FD}}(k_0 d) \to 1/2$ as $k_0 d \to 0$. Their strength is given by:

$$m(x^*,y^*) = \frac{3}{2}\frac{\partial Q_{\mathrm{ST}}(x^*,y^*)}{\partial x^*} = \frac{3}{2}\sqrt{\frac{g}{d}}\frac{|a_0|^2}{\sigma}\frac{x^*}{\sigma}\exp(-((x^*/\sigma)^2+(y^*/\sigma)^2)), \tag{E.6}$$

where we have used a summation of dipoles to solve Laplace subject to the boundary condition at $z = 0$ (3.20) (see appendix D). The second identity in (E.6) holds for a Gaussian group with $\sigma \equiv \sigma_x = \sigma_y$.

Appendix F

Three-dimensional surface gravity wave return flow with $\sigma_x \neq \sigma_y$

F.0.1 Infinite depth ($\sigma_x \neq \sigma_y$)

The assumption $\sigma_x = \sigma_y$ (and $\delta_{3\text{D}} = 1$) has been relaxed in §3.4.3 to examine the effects of realistic degrees of directional spreading. The corresponding solution for the return flow velocity potential with $\delta_{3\text{D}} \neq 1$ is:

$$\phi_{\text{RF}} = \frac{i\omega_0|a_0|^2}{8\pi^2}\int_{-\infty}^{\infty}\int_{-\infty}^{\infty}\frac{\hat{k}f(\hat{k},\hat{l})}{\sqrt{\hat{k}^2+\hat{l}^2\delta_{3\text{D}}^2}}e^{\sqrt{\hat{k}^2+\hat{l}^2\delta_{3\text{D}}^2}\hat{z}+i(\hat{k}\hat{x}+\hat{l}\hat{y})}d\hat{k}d\hat{l}, \tag{F.1}$$

where $\hat{x} = x/\sigma_x$, $\hat{y} = y/\sigma_y$, $\hat{z} = z/\sigma_x$ and $f(\hat{k},\hat{l})$ is now a bivariate function defined as:

$$f(\hat{k},\hat{l}) = \frac{\displaystyle\int_{-\infty}^{\infty}\int_{-\infty}^{\infty}|A(x,y)|^2 e^{-i(kx+ly)}dxdy}{\sigma_x\sigma_y|a_0|^2}, \tag{F.2}$$

where $\hat{k} = k\sigma_x$ and $\hat{l} = l\sigma_y$. We have $f(\hat{k},\hat{l}) = \pi\exp(-(\hat{k}^2+\hat{l}^2)/4)$ for a bivariate Gaussian group $A(x,y) = a_0\exp(-(\hat{x}^2+\hat{y}^2)/2)$.

F.0.2 Finite depth $\sigma_x \neq \sigma_y$

For finite depth, the corresponding solution for the return flow is:

$$\phi_{\mathrm{RF}} = \frac{i\omega_0|a_0|^2(1+\delta_{\mathrm{FD}}(k_0 d))}{8\pi^2 \tanh(k_0 d)} \int_{-\infty}^{\infty}\int_{-\infty}^{\infty} \frac{\hat{k} f(\hat{k},\hat{l})}{\sqrt{\hat{k}^2+\hat{l}^2\delta_{\mathrm{3D}}^2}} \frac{\cosh\left(\sqrt{\hat{k}^2+\hat{l}^2\delta_{\mathrm{3D}}^2}(\hat{z}+\hat{d})\right)}{\sinh\left(\sqrt{\hat{k}^2+\hat{l}^2\delta_{\mathrm{3D}}^2}\hat{d}\right)} e^{i(\hat{k}\hat{x}+\hat{l}\hat{y})} d\hat{k} d\hat{l}, \tag{F.3}$$

with $\hat{d} = d/\sigma_x$. In the shallow return flow limit, we obtain:

$$u_{\mathrm{RF}} = -\frac{\omega_0|a_0|^2(1+\delta_{\mathrm{FD}}(k_0 d))}{8\pi^2 \tanh(k_0 d) d} \int_{-\infty}^{\infty}\int_{-\infty}^{\infty} \frac{\hat{k}^2 f(\hat{k},\hat{l})}{\hat{k}^2+\hat{l}^2\delta_{\mathrm{3D}}^2} e^{i(\hat{k}\hat{x}+\hat{l}\hat{y})} d\hat{k} d\hat{l}. \tag{F.4}$$

Appendix G

Non-linear forcing of long internal waves

Here we compute the leading-order non-zero expression for $\nabla \cdot \mathbf{F}$ in (4.10), in which $\mathbf{F}$ is given explicitly by:

$$\mathbf{F} \equiv \Big[\frac{\partial}{\partial t}\big[\zeta^{(1)}\ \mathbf{u}^{(1)}\big] + N^2 \frac{\partial}{\partial x}\big[\xi^{(1)}\ \mathbf{u}^{(1)}\big]\Big], \tag{G.1}$$

and the velocity, vorticity and vertical displacement fields $\mathbf{u}^{(1)}$, $\zeta^{(1)}$ and $\xi^{(1)}$ are given in terms of the quasi-monochromatic internal wave group. Further to (4.29), we neglect dispersion, expressed through the dependence of the amplitude envelope upon the slow variable T. Thus for the vertical displacement field we suppose at leading order:

$$\xi^{(1)} = \xi^{(1)}_{(0)} \equiv A(X, Z)e^{i\theta}, \tag{G.2}$$

in which it is understood that the actual field is the real part of the right-hand side, $\theta \equiv k_x x + k_z z - \omega t$, and $(X, Z) = (\epsilon(x - c_{gx}t), \epsilon(z - c_{gz}t))$ represent the slow spatial variables associated with the amplitude envelope that translates at the group velocity of the wave group. Here we have assumed the slow vertical and horizontal scales are comparable in magnitude so that $\epsilon \equiv \epsilon_x = \epsilon_z$. For convenience in this appendix, we also drop the superscript, (1), with the understanding that all the fields under consideration are $O(\alpha)$ and so write the perturbation expansion in ϵ for each of the fields as $\zeta = \zeta_{(0)} + \epsilon\zeta_{(1)} + \ldots$, etc.

From the linearized equations of motion for internal waves, we express the $O(\epsilon^0)$ fields in terms of the vertical displacement amplitude envelope, as listed in the second column of table G.1. At $O(\epsilon)$, we assume that ξ is an imposed field and so set $\xi^{(1)}_{(1)} \equiv 0$ (and $\xi^{(1)}_{(n)} \equiv 0$ for $n \geq 1$). To get the remaining fields we extract terms involving exactly one derivative of the amplitude envelope. So, for example, from the differential relations $w = \partial_t \xi = \partial_x \psi$

field	$O(\epsilon^0)$	$O(\epsilon^1)$
vertical displacement	$\xi_{(0)} = Ae^{i\theta}$	$\xi_{(1)} = 0$
stream function	$\psi_{(0)} = -(N/\|\mathbf{k}\|)Ae^{i\theta}$	$\psi_{(1)} = -i(N/\|\mathbf{k}\|^3)[k_x A_X + k_z A_Z]e^{i\theta}$
horizontal velocity	$u_{(0)} = i(Nk_z/\|\mathbf{k}\|)Ae^{i\theta}$	$u_{(1)} = (Nk_x/\|\mathbf{k}\|^3)[-k_z A_X + k_x A_Z]e^{i\theta}$
vertical velocity	$w_{(0)} = -i(Nk_x/\|\mathbf{k}\|)Ae^{i\theta}$	$w_{(1)} = (Nk_z/\|\mathbf{k}\|^3)[-k_z A_X + k_x A_Z]e^{i\theta}$
vorticity	$\zeta_{(0)} = -N\|\mathbf{k}\|Ae^{i\theta}$	$\zeta_{(1)} = i(N/\|\mathbf{k}\|)[k_x A_X + k_z A_Z]e^{i\theta}$

Table G.1: Expressions for different fields at $O(\alpha\epsilon^0)$ (second column) and $O(\alpha\epsilon^1)$ (third column) given in terms of the amplitude envelope A of the vertical displacement field, as found through the linearized equations for internal waves. It is understood that the actual fields are the real parts of the tabulated expressions.

we find:

$$-c_{gx}A_X e^{i\theta} - c_{gz}A_Z e^{i\theta} = -(N/|\mathbf{k}|)A_X e^{i\theta} + ik_x\psi_{(1)}, \tag{G.3}$$

in which the subscripts to A denote partial derivatives. Solving for $\psi_{(1)}$ and simplifying using $c_{gx} = Nk_z^2/|\mathbf{k}|^3$ and $c_{gz} = -Nk_xk_z/|\mathbf{k}|^3$ gives:

$$\psi_1 = -i(N/|\mathbf{k}|^3)[k_x A_X + k_z A_Z]e^{i\theta}. \tag{G.4}$$

This and the corresponding expressions for the other $O(\epsilon)$ fields of interest are given in the third column of table G.1.

Next we consider the leading-order, $O(\alpha^2\epsilon^1)$, contributions from each of the four products of pairs of fields in the expression for $\mathbf{F}$ in (G.1). In doing so, we explicitly extract the real part of each expression and keep only the slowly varying result (i.e. those terms in the product for which $e^{i\theta}$ multiplies its complex conjugate). At $O(\alpha^2\epsilon^0)$ the result gives zero. At next order in ϵ we consider the product of $O(\epsilon^0)$ fields with $O(\epsilon^1)$ fields. Thus we find the following:

$$\begin{aligned}
(\overline{\zeta u})^{(2)}_{(1)} &= \frac{\epsilon}{4}(N^2/|\mathbf{k}|^2)\left[2k_xk_z\partial_X + (k_z^2 - k_x^2)\partial_Z\right]|A|^2,\\
(\overline{\zeta w})^{(2)}_{(1)} &= \frac{\epsilon}{4}(N^2/|\mathbf{k}|^2)\left[(k_z^2 - k_x^2)\partial_X - (2k_xk_z)\partial_Z\right]|A|^2,\\
(\overline{\xi u})^{(2)}_{(1)} &= \frac{\epsilon}{4}(Nk_x/|\mathbf{k}|^3)\left[-k_z\partial_X + k_x\partial_Z\right]|A|^2,\\
(\overline{\xi w})^{(2)}_{(1)} &= \frac{\epsilon}{4}(Nk_z/|\mathbf{k}|^3)\left[-k_z\partial_X + k_x\partial_Z\right]|A|^2.
\end{aligned} \tag{G.5}$$

These expressions may be substituted into (G.1) to get the non-linear forcing at $O(\alpha^2\epsilon^3)$. After some simplifying we find:

$$\begin{aligned}
(\nabla\cdot\mathbf{F})^{(2)}_{(3)} = \frac{1}{4}\epsilon^3\frac{N^3}{|\mathbf{k}|^5}\Big[&-k_xk_z(3k_z^3 + k_x^2)\,\partial_{XXX} \;+\; (k_z^4 + 4k_z^2k_x^2 + k_x^4)\,\partial_{XXZ}\\
&+ k_xk_z(5k_z^2 - k_x^2)\,\partial_{XZZ} \;-\; 2k_x^2k_z^2\,\partial_{ZZZ}\Big]|A|^2.
\end{aligned} \tag{G.6}$$

Bibliography

Acheson, D. J. 1976. On over-reflexion. *J. Fluid Mech.* **77** 433–472.

Adcock, T. A. A., P. H. Taylor. 2009. Focusing of unidirectional wave-groups on deep water: an approximate nonlinear Schrödinger equation based model. *Proc. Roy. Soc. A* **465** 3083–3102.

Akylas, T. R., R. H. J. Grimshaw, S. R. Clarke, A.Tabaei. 2007. Reflecting tidal wave beams and local generation of solitary waves in the ocean thermocline. *J. Fluid Mech.* **593** 297–313.

Andrews, D. G., M. E. McIntyre. 1978. An exact theory of nonlinear waves on a Lagrangian-mean flow. *J. Fluid Mech.* **89** 609–646.

Ardhuin, F., L. Marié, N. Rascle, P. Forget, A. Roland. 2009. Observation and estimation of Lagrangian, Stokes, and Eulerian currents induced by wind and waves at the sea surface. *J. Phys. Oceanogr.* **39**(11) 2820–2838.

Banyte, D. M., M. Visbeck, T. Tanhua, T. Fischer, G. Krahmann, J. Karstensen. 2013. Lateral diffusivity from tracer release experiments in the tropical North Atlantic thermocline. *J. Geophys. Res. Oceans* **118** 2719–2733.

Belcher, S. E., A. L. M. Grant, K. E. Hanley, B. Fox-Kemper, L. Van Roekel, P. P. Sullivan, W. G. Large, A. Brown Andy, A. Hines, D. Calvert, A. Rutgersson, H. Pettersson, J. R. Bidlot, P. A. E. M. Janssen, J. A. Polton. 2012. A global perspective on Langmuir turbulence in the ocean surface boundary layer. *Geophys. Res. Lett.* **39**(18).

Boccotti, P. 1983. Some new results on statistical properties of wind waves. *Appl. Ocean Res.* **5** 134–140.

Bordes, G., A. Venaille, S. Joubaud, P. Odier, T. Dauxois. 2012. Experimental observation of a strong mean flow induced by internal gravity waves. *Phys. Fluids* **24** 086602.

Breivik, O., J. Bidlot, P. A. E. M. Janssen. 2014. Approximate Stokes drift profiles in deep water. *J. Phys. Oceanogr.* **44** 2433–2445.

Bretherton, F. P. 1969a. Momentum transport by gravity waves. *Quart. J. Roy. Meteorol. Soc.* **95**(404) 213–243.

Bretherton, F. P. 1969b. On the mean motion induced by gravity waves. *J. Fluid Mech.* **36**(4) 785–803.

Bretherton, F. P., C. J. R. Garrett. 1969. Wavetrains in inhomogeneous moving media. *Proc. R. Soc. London, Ser. A* **302** 529–554.

Brinch-Nielsen, P. U., I. G. Jonsson. 1986. Fourth order evolution-equations and stability analysis for Stokes waves on arbitrary water depth. *Wave Motion* **8**(455).

Bühler, O. 2009. *Waves and Mean Flows*. Cambridge University Press, Cambridge, UK.

Bühler, O., M. E. McIntyre. 2005. Wave capture and wave–vortex duality. *J. Fluid Mech.* **534** 67–95.

Christie, D. R. 1992. The Morning Glory of the Gulf of Carpentaria: a paradigm for non-linear waves in the lower atmosphere. *Aust. Met. Mag.* **41** 21–60.

Craig, W., P. Guyenne, C. Sulem. 2010. A Hamiltonian approach to nonlinear modulation of surface water waves. *Wave Motion* **47**(552).

Craik, A. D. D., S. Leibovich. 1976. A rational model for Langmuir circulations. *J. Fluid Mech.* **73** 401–426.

Dalzell, J. R. 1999. A note on finite depth second-order wave-wave interactions. *Appl. Ocean Res.* **21** 105–111.

Dean, R. G. 1970. Relative validities of water wave theories. *J. Waterway. Div-ASCE* **96**(1) 105–119.

Donelan, M. A., J. Hamilton, W. H. Hui. 1985. Directional spectra of wind-generated waves. *Phil. Trans. R. Soc. Lond. A* **315** 509–562.

Dosser, H. V., B. R. Sutherland. 2011a. Anelastic internal wavepacket evolution and stability. *J. Atmos. Sci.* **68** 2844–2859.

Dosser, H. V., B. R. Sutherland. 2011b. Weakly nonlinear non-Boussinesq internal gravity wavepackets. *Physica D* **240** 346–356.

Dysthe, K.B. 1979. Note on a modification to the nonlinear Schrödinger equation for application to deep water waves. *Proc. R. Soc. Lond. A* **369** 105–114.

Eames, I. 2008. Settling of particles beneath water waves. *J. Phys. Oceanogr.* **38** 2846–2853.

Eames, I., S. E. Belcher, J. C. R. Hunt. 1994. Drift, partial drift and Darwin's proposition. *J. Fluid Mech.* **275** 201–223.

Eames, I., M. E. McIntyre. 1999. On the connection between Stokes drift and Darwin drift. *Math. Proc. Cambridge* **126**.

Ewans, K. C. 1998. Observations of the directional spectrum of fetch-limited waves. *J. Phys. Oceanogr.* **28** 495–512.

Fenton, J. D. 1985. A fifth-order Stokes theory for steady waves. *J. Waterway Port Coastal and Ocean Engineering* **111** 216–234.

Fenton, J. D. 1990. Nonlinear wave theories. B. Le Méhauté, D. M. Hanes, eds., *Ocean Engineering Science*. Wiley, New York.

Fringer, O. B., R. L. Street. 2003. The dynamics of breaking progressive interfacial waves. *J. Fluid Mech.* **494** 319–353.

Gibbs, R. H., P. H. Taylor. 2005. Formation of walls of water in fully nonlinear simulations. *Appl. Ocean Res.* **27**(4) 142–157.

Gramstad, O., K. Trulsen. 2007. Hamiltonian form of the modified nonlinear Schrödinger equation for gravity waves on arbitrary depth. *J. Fluid Mech.* **670** 404–426.

Hasselmann, D. E., M. Dunckel, J. A. Ewing. 1980. Directional wave spectra observed during JONSWAP 1973. *J. Phys. Oceanogr.* **10** 1264–1280.

Hedges, T. S. 1995. Regions of validity of analytical wave theories. *Proc. Inst. Civ. Engnrs. Water, Maritime and Energy* **112** 111–114.

Helfrich, K. R., W. K. Melville. 2006. Long nonlinear internal waves. *Annu. Rev. Fluid Mech.* **38** 395–425.

Hudspeth, R. T., W. Sulisz. 1991. Stokes drift in two-dimensional wave flumes. *J. Fluid Mech.* **230** 209–229.

Hunt, J. C. R., R. J. Perkins, J. C. H. Fung. 1994. Problems in modeling disperse two-phase flows. *Appl. Mech. Rev* **47**(6S) S49–S60.

Janssen, P. A. E. M. 1983. On a fourth-order envelope equation for deep-water waves. *J. Fluid Mech.* **126** 1–11.

Kantha, L. H., C. A. Clayson. 2004. On the effect of surface gravity waves on mixing in the oceanic mixed layer. *Ocean Model.* **6** 101–124.

Kao, T. W., F.-S. Pan, D. Renouard. 1985. Internal solitons on the pycnocline: Generation, propagation, and shoaling and breaking over a slope. *J. Fluid Mech.* **159** 19–53.

Kinsman, B. 1984. *Wind waves: their generation and propagation on the ocean surface*. Dover, New York, USA.

Klemas, V. 2012. Remote sensing of ocean internal waves: an overview. *J. Coastal Res.* **28**(3) 540–546.

Lindzen, R. S. 1981. Turbulence and stress owing to gravity wave and tidal breakdown. *J. Geophys. Res.* **86** 9707–9714.

Longuet-Higgins, M.S. 1969. On the transport of mass by time-varying ocean currents. *Deep Sea Research and Oceanographic Abstracts* **16**(5) 431–447.

Longuet-Higgins, M.S. 1986. Eulerian and Lagrangian aspects of surface waves. *J. Fluid Mech.* **37** 683–707.

Longuet-Higgins, M.S., R.W. Stewart. 1962. Radiation stress and mass transport in gravity waves, with applications to 'surf beats'. *J. Fluid Mech.* **13** 481–504.

Marshall, D. P., B. Vogel, X. Zhai. 2013. Rossby rip currents. *Geophys. Res. Lett.* **40** 4333–4337.

McFarlane, N. A. 1987. The effect of orographically excited gravity wave drag on the general circulation of the lower stratosphere and troposphere. *J. Atmos. Sci.* **44** 1775–1800.

McIntyre, M. E. 1981. On the wave momentum myth. *J. Fluid Mech.* **106** 331–347.

McLandress, C. 1998. On the importance of gravity waves in the middle atmosphere and their parameterization in general circulation models. *J. Atmos. Sol.-Terr. Phys.* **60** 1357–1383.

McWilliams, J. C., J.M. Restrepo. 1999. The wave-driven ocean circulation. *J. Phys. Oceanogr.* **29** 2523–2540.

Menhofer, A., R. K. Smith, M. J. Reeder, D. R. Christie. 1997. “Morning-Glory” disturbances and the environment in which they propagate. *J. Atmos. Sci.* **54** 1712–1725.

Monismith, S. G., E.A. Cowen, H. M. Nepf, J. Magnaudet, L. Thais. 2007. Laboratory observations of mean flows under surface gravity waves. *J. Fluid Mech.* **573** 131–147.

Nansen, F. 1897. *Farthest North: The epic adventure of a visionary explorer*, vol. 1. Skyhorse Publ., New York, USA.

New, A. L., R. D. Pingree. 1990. Large-amplitude internal soliton packets in the central Bay of Biscay. *Deep Sea Res.* **37**(9) 513–524.

New, A. L., R. D. Pingree. 1992. Local generation of internal soliton packets in the central Bay of Biscay. *Deep Sea Res.* **39**(9) 1521–1534.

Noonan, J. A., R. K. Smith. 1985. Linear and weakly nonlinear internal wave theories applied to ‘Morning Glory’ waves. *Geophys. Astrophys. Fluid Dyn.* **33** 123–143.

Palmer, T. N., G. J. Shutts, R. Swinbank. 1986. Alleviation of a systematic westerly bias in general circulation and numerical weather prediction models through an orographic gravity drag parametrization. *Quart. J. Roy. Meteor. Soc.* **112** 1001–1039.

Polton, J. A., D. M. Lewis, S. E. Belcher. 2005. The role of wave-induced Coriolis-Stokes forcing on the wind-driven mixed layer. *J. Phys. Oceanogr.* **35** 444–457.

Press, W. H., S. A. Teukolsky, W. T. Vetterling, B. P. Flannery. 2007. *Numerical Recipes: The Art of Scientific Computing*. 3rd ed. Cambridge University Press, New York, USA.

Rieper, F., U. Achatz, R. Klein. 2013. Range of validity of an extended WKB theory for atmospheric gravity waves: One-dimensional and two-dimensional case. *J. Fluid Mech.* **729** 330–363.

Röhrs, J., K. H. Christensen, L. R. Hole, G. Broström, M. Drivdal, S. Sundby. 2013. Observation-based evaluation of surface wave effects on currents and trajectory forecasts. *Ocean Dyn.* **62**(10–12) 1519–1533.

Scinocca, J. F., T. G. Shepherd. 1992. Nonlinear wave-activity conservation laws and Hamiltonian structure for the two-dimensional anelastic equations. *J. Atmos. Sci.* **49** 5–27.

Sharma, J., R. G. Dean. 1981. Second-order directional seas and associated wave forces. *Proc. Offshore Tech. Conf.* **4** 2505–2514.

Smith, J. A. 2006. Observed variability of ocean wave Stokes drift, and the Eulerian response to passing groups. *J. Phys. Oceanogr.* **36** 1381–1402.

Sobey, R. J. 2012. Steep progressive waves in deep and shallow water. *P. I. Civil. Eng. Engineering and Computational Mechanics* **165**(3) 181–200.

Starr, V. P. 1947. A momentum integral for surface waves in deep water. *J. Mar. Res.* **6** 126–135.

Stevenson, T. N., N. H. Thomas. 1969. Two-dimensional internal waves generated by a travelling oscillating cylinder. *J. Fluid Mech.* **36** 505–511.

Stokes, G. G. 1847. On the theory of oscillatory waves. *Trans. Camb. Philos. Soc.* **8** 441–455.

Sutherland, B. R. 2001. Finite-amplitude internal wavepacket dispersion and breaking. *J. Fluid Mech.* **429** 343–380.

Sutherland, B. R. 2006a. Internal wave instability: Wave-wave vs wave-induced mean flow interactions. *Phys. Fluids.* **18** Art. No. 074107. Doi:10.1063/1.2219102.

Sutherland, B. R. 2006b. Weakly nonlinear internal wavepackets. *J. Fluid Mech.* **569** 249–258.

Sutherland, B. R. 2010. *Internal Gravity Waves*. Cambridge University Press, Cambridge, UK.

Sutherland, B. R., W. R. Peltier. 1994. Turbulence transition and internal wave generation in density stratified jets. *Phys. Fluids A* **6** 1267–1284.

Swan, C. 1990. Convection within an experimental wave flume. *J. Hydraul. Res.* **28** 273–282.

Tabaei, A., T. R. Akylas. 2007. Resonant long-short wave interactions in an unbounded rotating stratified fluid. *Stud. Appl. Math.* **119** 271–296.

Tamura, H., Y. Miyazawa, L. Y. Oey. 2012. The Stokes drift and wave induced-mass flux in the north pacific. *J. Geophys. Res.* **117**.

Thorpe, S. A. 2004. Langmuir circulation. *Annu. Rev. Fluid Mech.* **36** 55–79.

Tromans, P. S., A. H. R. Anaturk, P. M. Hagemeijer. 1991. New model for the kinematics of large ocean waves - application as a design wave. *Proceedings of the 1st International Offshore and Polar Engineering Conference* 64–71.

Ursell, F. 1953. The long-wave paradox in the theory of gravity waves. *P. Camb. Philos. Soc.* **49**(4) 685–694.

van Dyke, M. 1982. *An album of fluid motion*. The Parabolic Press, Stanford, USA.

Voisin, B. 1994. Internal wave generation in uniformly stratified fluids. Part 2. moving point sources. *J. Fluid Mech.* **261** 333–374.

Wallet, A., F. Ruellan. 1950. *Houille Blanche* **5** 483–489.

Weber, J.E.H., K. H. Christensen, G. Broström. 2014. Stokes drift in internal equatorial Kelvin waves: continuous stratification versus two-layer models. *J. Phys. Oceanogr.* **44** 591–599.

Yuan, Y., J. Li, Y. Cheng. 2007. Validity ranges of interfacial wave theories in a two-layer fluid system. *Acta Mechanica Sinica* **23**(6) 597–607.

Yuen, H. C., B. M. Lake. 1975. Nonlinear deep water waves: theory and experiment. *Phys. Fluids* **18** 956–960.